

IntechOpen

# Hypersonic and Supersonic Flight

Advances in Aerodynamics,  
Materials, and Vehicle Design

*Edited by Konstantin Volkov*





---

Hypersonic and Supersonic  
Flight - Advances in  
Aerodynamics, Materials,  
and Vehicle Design

*Edited by Konstantin Volkov*

Published in London, United Kingdom

---

Hypersonic and Supersonic Flight - Advances in Aerodynamics, Materials, and Vehicle Design  
<http://dx.doi.org/10.5772/intechopen.104045>  
Edited by Konstantin Volkov

#### Contributors

Ghedjatti Ilyes, Yuan Shiwei, Wang Haixing, Pradeep Kumar Sulur Loganathan, Marta Kianicová, Juluru Sandeep, Xin Gao, Chengwei Zhao, Konstantin Volkov

© The Editor(s) and the Author(s) 2023

The rights of the editor(s) and the author(s) have been asserted in accordance with the Copyright, Designs and Patents Act 1988. All rights to the book as a whole are reserved by INTECHOPEN LIMITED. The book as a whole (compilation) cannot be reproduced, distributed or used for commercial or non-commercial purposes without INTECHOPEN LIMITED's written permission. Enquiries concerning the use of the book should be directed to INTECHOPEN LIMITED rights and permissions department ([permissions@intechopen.com](mailto:permissions@intechopen.com)).

Violations are liable to prosecution under the governing Copyright Law.



Individual chapters of this publication are distributed under the terms of the Creative Commons Attribution 3.0 Unported License which permits commercial use, distribution and reproduction of the individual chapters, provided the original author(s) and source publication are appropriately acknowledged. If so indicated, certain images may not be included under the Creative Commons license. In such cases users will need to obtain permission from the license holder to reproduce the material. More details and guidelines concerning content reuse and adaptation can be found at <http://www.intechopen.com/copyright-policy.html>.

#### Notice

Statements and opinions expressed in the chapters are those of the individual contributors and not necessarily those of the editors or publisher. No responsibility is accepted for the accuracy of information contained in the published chapters. The publisher assumes no responsibility for any damage or injury to persons or property arising out of the use of any materials, instructions, methods or ideas contained in the book.

First published in London, United Kingdom, 2023 by IntechOpen  
IntechOpen is the global imprint of INTECHOPEN LIMITED, registered in England and Wales, registration number: 11086078, 5 Princes Gate Court, London, SW7 2QJ, United Kingdom

#### British Library Cataloguing-in-Publication Data

A catalogue record for this book is available from the British Library

Additional hard and PDF copies can be obtained from [orders@intechopen.com](mailto:orders@intechopen.com)

Hypersonic and Supersonic Flight - Advances in Aerodynamics, Materials, and Vehicle Design  
Edited by Konstantin Volkov

p. cm.

Print ISBN 978-1-83768-259-1

Online ISBN 978-1-83768-260-7

eBook (PDF) ISBN 978-1-83768-261-4

# We are IntechOpen, the world's leading publisher of Open Access books Built by scientists, for scientists

**6,300+**

Open access books available

**171,000+**

International authors and editors

**190M+**

Downloads

**156**

Countries delivered to

Our authors are among the  
**Top 1%**

most cited scientists

**12.2%**

Contributors from top 500 universities



**WEB OF SCIENCE™**

Selection of our books indexed in the Book Citation Index  
in Web of Science™ Core Collection (BKCI)

Interested in publishing with us?  
Contact [book.department@intechopen.com](mailto:book.department@intechopen.com)

Numbers displayed above are based on latest data collected.  
For more information visit [www.intechopen.com](http://www.intechopen.com)





# Meet the editor



Dr. Volkov is a senior lecturer in thermofluids at Kingston University, London, UK. He holds a Ph.D. in Fluid Mechanics. After completing his Ph.D., Dr. Volkov worked at the Baltic State Technical University, Russia, University of Central Lancashire, UK, and University of Surrey, UK. His areas of expertise include the design and optimization of energy systems and modelling and simulation of turbulent multi-phase flows. He is a chartered engineer and member of the Institute of Physics, Institution of Mechanical Engineers, Combustion Institute, and Higher Education Academy.





# Contents

<b>Preface</b>	<b>XI</b>
<b>Chapter 1</b> High-Temperature Effects on Supersonic Flow around a Wedge <i>by Konstantin Volkov</i>	<b>1</b>
<b>Chapter 2</b> Design and CFD Analysis on the Reduction of Thermal Effect in Re-entry Vehicle by Using Retractable Aerospike <i>by Pradeep Kumar Sulur Loganathan</i>	<b>21</b>
<b>Chapter 3</b> Design and Performance of Hypersonic Intake for Scramjet Engine <i>by Juluru Sandeep</i>	<b>47</b>
<b>Chapter 4</b> Clean and Sustainable Hydrogen-Electric Propulsion <i>by Xin Gao and Chengwei Zhao</i>	<b>63</b>
<b>Chapter 5</b> Cyclic Oxidation of Diffusion Aluminide Coatings <i>by Marta Kianicová</i>	<b>91</b>
<b>Chapter 6</b> Perspective Chapter: Effect of Laser Key Parameters on the Ignition of Boron Potassium Nitrate with a Changing Working Distance <i>by Ghedjatti Ilyes, Yuan Shiwei and Wang Haixing</i>	<b>147</b>



# Preface

Hypersonic flight vehicles could enable a range of future aviation and space missions. However, the extreme environmental conditions associated with high Mach number flight pose a major challenge for vehicle aerodynamics, materials and structures, and flight control, particularly within the hybrid ramjet/scramjet/rocket propulsion systems. The complexity of hypersonic vehicles requires closer coupling of aerodynamics and design principles with new materials development to achieve expanded levels of performance and structural durability.

The book focuses on a synthesis of the fundamental disciplines and practical applications involved in the investigation, description, and analysis of super and hypersonic aircraft flight including applied aerodynamics, aircraft propulsion, flight performance, stability, and control. A particular focus of the book is the development of theoretical, computational, and experimental methods in aerodynamics. Computational methods are widely used by practicing aerodynamicists, and the book covers computational fluid dynamics (CFD) techniques used to improve understanding of the physical models that underlie computational methods.

Chapter 1 compares the results of numerical calculations obtained with different gas models, ideal perfect gas, and high-temperature air with each other and with theoretical values from the theory of oblique shock waves. At the high intensity of the shock wave, which occurs at high supersonic and hypersonic flow velocities, the properties of the gas differ from the properties of a perfect gas. This leads to significant differences in the distributions of flow characteristics behind the shock wave front, corresponding to the models of a perfect and real gas. An approach and a calculation module have been developed that allow taking into account equilibrium chemical reactions in the air at high temperatures. To demonstrate the capabilities of the developed model, the problem of supersonic flow around a wedge with an attached shock wave is used. A comparison is made of the space-time distributions of flow characteristics calculated using the perfect and real gas models. The developed computational module allows the inclusion in the design systems of advanced aircraft shapes, as well as integration with both commercial and open-source CFD packages.

Chapter 2 considers the shape optimization of two spike classes. A spike with a slender spike tip reduces drag and enables longer ranges for economical flight. The chapter discusses the thermal and vibration effects on the space re-entry vehicle returning to the Earth's temperature. These spike materials can withstand the high temperature produced on the space re-entry vehicle due to aero thermodynamic heating caused by shock waves. They have vibration-absorbing properties and good durability so they can be utilized as heat-shielding materials for long-time processes, reducing the cost of material used for the heat shield. Employment of an aero-spike in the re-entry vehicle effectively reduces the cost due to structural damages, representing an innovative and effective design concept for future developments.

Chapter 3 addresses a detailed procedure for the design of hypersonic intake and techniques to mitigate unstating conditions of a scramjet engine. The desire to achieve hypersonic speeds at low cost has led to the development of air-breathing engines known as supersonic combustion ramjet engines or scramjet engines. The design of intake depends on the number of ramps and the angle of the ramp, which decides the strength of shock for compression. All the scramjet intakes designed based on oblique shock theory will start efficiently in the designed conditions, but the main problem is unstating the performance of intake at off-design conditions. At off-design conditions, the incident shock may not satisfy shock on lip condition or required pressure for combustion and may lead to flow separation due to shock boundary layer interaction. The chapter also emphasizes the performance parameters of scramjet engines and explains the importance of shock wave and boundary layer interaction and its effects on starting intake as well as methods to control it.

Chapter 4 draws attention to the possible feasibilities and challenges of hydrogen–electric propulsion in hypersonic and supersonic flight. Current trends suggest that aircraft capable of full hydrogen fuel cell propulsion remain the goal of long-term research. The chapter reviews and discusses challenges related to the application of hydrogen fuel cells in aviation. It also discusses general design and hybridization concepts of hydrogen–electric propulsion for general aircraft and their hypersonic and supersonic considerations; merits of hydrogen–electric propulsion on thermofluid process integrations; potential merits of hydrogen–electric propulsion projected through thermofluids structural engineering and re-engineering; storage options; and challenges in design and operation.

Chapter 5 focuses on the comparison of the cyclic oxidation of protective aluminide coatings deposited on two types of nickel superalloys. Diffusion aluminide coatings belong to the wide category of coatings used for high-temperature applications. Structural materials of particular components degrade during service due to fatigue, creep, oxidation, corrosion, and erosion. All samples with and without aluminide coatings were exposed to cyclic oxidation. Two types of superalloys were deposited by aluminide coating and Si-modified aluminide coating. Samples from MAR 247 LC superalloy with both aluminide Al and AlSi coatings appear to be the most acceptable selection of combinations relating to superalloys/coating.

Chapter 6 discusses the effect of laser key parameters on the ignition of boron potassium nitrate with a changing working distance. The need to realize more effective ignition systems and exploit their full potential in aerospace propulsion applications has led to significant developments in laser and power systems. Understanding the physics and chemistry behind the combined system of laser power source and optics, and the considered medium as well as the interaction in between, led to a better apprehension of how an optimal and viable solution can be achieved in terms of ignition delays, burning times, and combustion temperatures, considering laser wavelength, power and energy densities, and the focal length displacement over a changing working distance. This is of paramount importance when operating amid difficult conditions in aerospace propulsion applications or during outer space missions, particularly those involving manned missions, not only in terms of performance and efficiency but also safety, engineering, and economic feasibility.

The book aims to expand the hypersonic knowledge base and promote continued hypersonic technology progress through computations and experimental testing. It promotes open discussion between research institutions, academia, and industry from around the globe on research and development of enabling technologies. The book covers many aspects of theory and practice which deliver essential contributions and provide input and support to cooperative efforts.

**Dr. Konstantin Volkov**  
Department of Mechanical Engineering,  
Kingston University,  
London, UK



## Chapter 1

# High-Temperature Effects on Supersonic Flow around a Wedge

*Konstantin Volkov*

### Abstract

The development of the flow pattern that arises during the interaction of a shock wave with a wedge is discussed. Mathematical modeling of the flow around the wedge is carried out with Euler equations. These equations describe the unsteady flow of an inviscid compressible fluid around a wedge in a two-dimensional domain. To take into account high-temperature effects on super- and hypersonic flows, the model developed takes into account equilibrium chemical reactions in the air, ionization, and dissociation processes. The initial parameters of the flow are set equal to the parameters of the flow behind the shock wave in accordance with the Rankine–Hugoniot relations. The solutions to the problem obtained with the model of ideal perfect gas and the model taking into account high-temperature effects in the air are compared. The influence of high-temperature effects on the distribution of flow quantities is discussed.

**Keywords:** aerodynamics, super- and hypersonic flow, computational fluid dynamics, shock wave, physical and chemical processes, wedge

### 1. Introduction

The complexity of various technical problems associated with the design and development of hypersonic aircraft leads to the need for research in the field of aerodynamics and heat transfer using mathematical modeling. Hypersonic aircraft is characterized by flat aerodynamic shapes of streamlined surfaces [1]. As a propulsion system, it is supposed to use a ramjet engine with supersonic combustion integrated with the body [2]. A characteristic feature of aircraft with an air intake formed by the planes of the aircraft and elements of the power plant is the presence of extended structural elements in the form of a wedge with a small opening angle and a blunting of a small radius, subject to the most intense aerodynamic heating [3, 4].

The supersonic flow around a wedge is one of the well-studied problems in computational fluid dynamics (CFD) [5]. This interaction results in the formation of an impact configuration with two triple points [6]. The flow disturbance starts from the wedge tip when the shock wave touches it. Depending on the Mach number and the

angle of the wedge, regular reflection (shock is attached to wedge) or non-regular reflection (a reflected shock wave has a curvilinear front) is generated. Depending on inlet flow conditions (angle of wedge and inlet Mach number), the main and reflected waves meet at a triple point. Between this point and the wedge, two waves merge into one wave, forming a Mach configuration [7, 8]. Downstream of the triple point, a tangential discontinuity is formed on which pressure and normal velocity remain continuous, while density and tangential velocity suffer a discontinuity.

CFD tools are applied to simulate regular and non-regular shock reflection in [9, 10]. In other studies, shock reflection from a line of symmetry is discussed when two wedges are placed in a supersonic flow [11]. This formulation of the problem allows to exclude boundary layer effects [12].

The inviscid compressible flow around a wedge is carried out in [13]. When the angle of flow turning, equal to the angle of inclination of the wedge, is less than the maximum, the problem has two solutions. In the solution with an oblique shock of lesser intensity (a “weak” shock), the uniform flow between the shock and the wedge is almost always supersonic [14]. The exception is a small neighborhood of the maximum angle of rotation. For a perfect gas, this neighborhood does not exceed fractions of a degree for all Mach numbers of the oncoming flow. After a shock of greater intensity (a “strong” shock), the flow of a perfect gas is always subsonic.

For supersonic and hypersonic flows of an inviscid gas, there is the possibility of the existence of two solutions (strong and weak). Depending on the angle of incidence and the input value of the Mach number, two typical configurations are formed: two-hop (regular) and three-hop (Mach), and in a certain range of parameters, both options. The possibility of hysteresis with a change in the angle of incidence of the shock has been shown in both physical and numerical experiments [12].

The experimental results of the flow around aircraft model in a hypersonic shock tube are presented in [15]. The results of the numerical simulation of the thermal state of a sharp wedge with a blunt edge in a high-speed airflow are presented in [16]. Accounting for viscosity and turbulence complicates the situation due to such effects as separation and reattachment of the boundary layer [17].

When a strong shock wave moves and interacts with a body, the temperature and pressure of the gas behind its front increase. The perfect gas model does not provide the required accuracy of the numerical solution, since the molecular weight and heat capacities are not constant. In high-temperature air, these quantities are functions of pressure and temperature. In this case, it is necessary to take into account the processes of dissociation and ionization taking place in a gas. In practice, various models are used that take into account high-temperature processes in gases, as well as analytical dependencies and interpolation of tabular values. From a computational point of view, the model proposed in [18] (Kraiko model) for air and taking into account the reactions between 13 components are interesting and successful. The main advantage of this model is that it takes into account the dissociation and ionization of air at high temperatures. In the temperature range up to 20,000 K and pressures from 0.001 to 1000 atm, the error of the model does not exceed  $\pm 2\%$ , usually falling within the band of  $\pm 1\%$ . Accounting for non-equilibrium chemical reactions is discussed in [19] based on a one-temperature model.

In this study, calculations are performed with the model of perfect gas and the model taking into account high-temperature effects. The results of numerical calculations obtained with different models are compared with each other and with theoretical values from the theory of oblique shock waves.



## 2. Formulation of problem

The governing equations are solved in the domain shown in **Figure 1**. The wedge angle is  $\beta$ . The length of the domain is 3.2, and its height is 2.2. The wedge is located at a distance of 0.2 from the origin. The shock is at the point  $x = 0$  at time  $t = 0$ . There is no gas motion ahead of the shock wave ( $u = v = 0$ ), and the pressure and temperature are  $p = 101325$  Pa and  $T = 288.2$  K. The flow velocity is fixed at 1000 and 3000 m/s. The flow quantities behind the shock wave are found from the Rankine-Hugoniot conditions. The gas does not cross the centerline. Free outflow conditions are applied to the upper and right boundaries.

For this problem, there is an exact solution in the framework of the theory of oblique shock waves [1]. With the help of this problem, the capabilities of the scheme for reproducing shock waves are checked, which make it possible to assess the discrepancy between CFD calculation and the exact solution. As a parameter characterizing the proximity of the numerical solution to the analytical one, the Mach number is considered, which changes abruptly when passing through the shock wave.

## 3. Oblique shock wave

When a supersonic flow flows around a wedge, under certain restrictions on the half-angle of the wedge and the Mach number, an oblique shock occurs. When flowing around a cone, the shock front has a conical surface.

The angle of the wedge,  $\beta$ , is equal to the angle of flow turning at the shock. The angle between the shock front and the direction of the undisturbed flow is the shock slope angle,  $\sigma$ . The velocity of the undisturbed flow,  $v_1$ , is decomposed into the normal and tangential components to the shock surface,  $v_{n1}$  and  $v_{\tau1}$ . Therefore

$$v_{n1} = v_1 \sin \sigma, v_{\tau1} = v_1 \cos \sigma.$$

Flow quantities before and behind shock wave are interconnected by relationships following from the laws of conservation of mass, momentum, and energy:  
 conservation of mass

$$\rho_1 v_{n1} = \rho_2 v_{n2}; \tag{1}$$

conservation of momentum in the direction normal to the shock

$$\rho_1 v_{n1}^2 + p_1 = \rho_2 v_{n2}^2 + p_2; \tag{2}$$

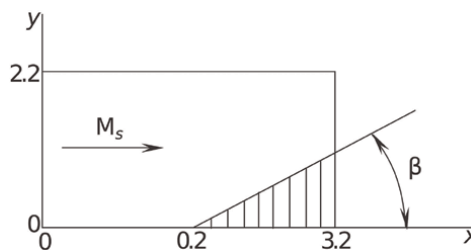


**Figure 1.**  
 Computational domain.

conservation of momentum in the direction tangential to the shock (the pressure gradient in the direction tangential to the surface of the shock is equal to zero)

$$\rho_1 v_{n1} v_{\tau 1} = \rho_2 v_{n2} v_{\tau 2}; \quad (3)$$

conservation of energy

$$\rho_1 v_{n1} \left( \varepsilon_1 + \frac{v_1^2}{2} + \frac{p_1}{\rho_1} \right) = \rho_2 v_{n2} \left( \varepsilon_2 + \frac{v_2^2}{2} + \frac{p_2}{\rho_2} \right). \quad (4)$$

Here,  $\varepsilon$  is specific internal energy. In relation (4), the terms in parentheses represent the sum of the specific internal and specific kinetic energy before and behind the shock. The change in this quantity is associated with the work performed on a given mass of gas by external forces, of which only surface pressure forces are taken into account. Taking into account the mass conservation condition (1), the requirement of equality of the tangential velocity components on the shock is  $v_{\tau 1} = v_{\tau 2}$ . Dividing both parts of Eq. (4) on the shock by the mass flux through the shock,  $\rho_1 v_{n1} = \rho_2 v_{n2}$ , the relation has the form

$$h_1 + \frac{v_1^2}{2} = h_2 + \frac{v_2^2}{2},$$

where  $h = \varepsilon + p/\rho$  is specific enthalpy.

The given conservation laws are valid for any gas model (perfect, real, dissociating, or ionized) when passing through an oblique shock wave since they express the general relations of the conservation laws without reference to any relations connecting thermodynamic variables to each other, and relations determining the form thermodynamic functions.

To close the conditions of dynamic compatibility at the shock, it is necessary to give specific dependencies that determine the specifics of the thermodynamic state of the gas. The enthalpy and molar mass are functions of pressure and temperature,  $h = h(p, T)$  and  $\mu = \mu(p, T)$ . The equation of state of an ideal gas is taken, which has a composition corresponding to this state

$$p = \frac{\rho R_0 T}{\mu(p, T)},$$

where  $R_0$  is the universal gas constant. The thermodynamic quantities before the shock are known ( $h_1 = c_p T_1$ ,  $\mu_1 = 0.029$  kg/mol for air), and the relations relating to the thermodynamic parameters behind the shock are introduced into the model from additional conditions describing the thermodynamic model of high-temperature air [3, 4].

To determine thermodynamic quantities of high-temperature flow behind a shock wave ( $v_{\tau 1} = v_{\tau 2}$ ), the following equations are applied

$$h_2 = h_2(p_2, T_2), \mu_2 = \mu_2(p_2, T_2), p_2 = \frac{\rho_2 R_0 T_2}{\mu_2}.$$

For a perfect gas, simple transformations allow one to find the thermodynamic quantities behind the shock [5]

$$\frac{p_2}{p_1} = \left( \frac{2\gamma}{\gamma+1} M_1^2 \sin^2 \sigma - \frac{\gamma-1}{\gamma+1} \right);$$

$$\frac{\rho_2}{\rho_1} = \left[ \frac{2}{(\gamma+1)M_1^2 \sin^2 \sigma} + \frac{\gamma-1}{\gamma+1} \right]^{-1};$$

$$\frac{T_2}{T_1} = \frac{\rho_1 p_2}{\rho_2 p_1};$$

$$\frac{M_2}{M_1} = \left\{ \frac{T_1}{T_2} \left[ \cos^2 \sigma + \sin^2 \sigma \left( \frac{\gamma-1}{\gamma+1} + \frac{2}{(\gamma+1)M_1^2 \sin^2 \sigma} \right)^2 \right] \right\}^{1/2}.$$

Here,  $\sigma$  is the shock angle.

Using the replacement  $\rho_2 = p_2 \mu_2 / (R_0 T_2)$ , the conditions of dynamic compatibility on the shock take the form

$$p_2 \mu_2(p_2, T_2) v_{n2} - C_1 R_0 T_2 = 0;$$

$$C_1 v_{n2} + p_2 - C_2 = 0;$$

$$h_2(p_2, T_2) + \left( \frac{v_{n2}^2 + v_{\tau 2}^2}{2} \right) - C_3 = 0.$$

Here,  $C_1 = \rho_1 v_{n1}$ ,  $C_2 = \rho_1 v_{n1}^2 + p_1$ ,  $C_3 = h_1 + v_1^2/2$ ,  $v_{\tau 2} = v_{\tau 1}$ .

To solve a nonlinear system of equations, Newton's method is used, which consists of solving a sequence of linear problems

$$U^{n+1} = U^n - J^{-1}F,$$

where

$$U = \begin{pmatrix} p_2 \\ T_2 \\ v_{n2} \end{pmatrix}, F = \begin{pmatrix} p_2 \mu_2(p_2, T_2) v_{n2} - C_1 R_0 T_2 \\ C_1 v_{n2} + p_2 - C_2 \\ h_2(p_2, T_2) + 0.5(v_{n2}^2 + v_{\tau 2}^2) - C_3 \end{pmatrix}.$$

Jacobian has the form

$$J = \frac{\partial F}{\partial U} = \begin{pmatrix} v_{n2} \left[ \mu_2(p_2, T_2) + p_2 \frac{\partial \mu_2}{\partial p_2} \right] & p_2 v_{n2} \frac{\partial \mu_2}{\partial T_2} - C_1 R_0 & p_2 \mu_2 \\ \frac{1}{\partial h_2} & 0 & C_1 \\ \frac{\partial h_2}{\partial p_2} & \frac{\partial h_2}{\partial T_2} & v_{n2} \end{pmatrix}.$$

The inverse matrix is written as

$$J^{-1} = \frac{1}{|J|} \begin{pmatrix} J_{11} & J_{12} & J_{13} \\ J_{21} & J_{22} & J_{23} \\ J_{31} & J_{32} & J_{33} \end{pmatrix}.$$

Here

$$\begin{aligned}
 J_{11} &= -C_1 \frac{\partial h_2}{\partial T_2}, \\
 J_{12} &= C_1 R_0 v_{n2} + p_2 \mu_2 \frac{\partial h_2}{\partial T_2} - p_2 v_{n2}^2 \frac{\partial \mu_2}{\partial T_2}, \\
 J_{13} &= p_2 v_{n2} C_1 \frac{\partial \mu_2}{\partial T_2} - C_1^2 R_0, \\
 J_{21} &= C_1 \frac{\partial h_2}{\partial p_2} - v_{n2}, \\
 J_{22} &= v_{n2}^2 \left( \mu_2 + p_2 \frac{\partial \mu_2}{\partial p_2} \right) - p_2 \mu_2 \frac{\partial h_2}{\partial p_2}, \\
 J_{23} &= p_2 \mu_2 - C_1 v_{n2} \left( \mu_2 + p_2 \frac{\partial \mu_2}{\partial p_2} \right); \\
 J_{31} &= \frac{\partial h_2}{\partial T_2}, \\
 J_{32} &= \frac{\partial h_2}{\partial p_2} \left( p_2 v_{n2} \frac{\partial \mu_2}{\partial T_2} - C_1 R_0 \right) - v_{n2} \left( \mu_2 + p_2 \frac{\partial \mu_2}{\partial p_2} \right) \frac{\partial h_2}{\partial T_2}, \\
 J_{33} &= C_1 R_0 - p_2 v_{n2} \frac{\partial \mu_2}{\partial T_2}.
 \end{aligned}$$

The matrix determinant is found from the relation

$$\begin{aligned}
 |J| &= p_2 v_{n2} C_1 \left( \frac{\partial h_2}{\partial p_2} \frac{\partial \mu_2}{\partial T_2} - \frac{\partial \mu_2}{\partial p_2} \frac{\partial h_2}{\partial T_2} \right) + \mu_2 \frac{\partial h_2}{\partial T_2} (p_2 - C_1 v_{n2}) + \\
 &+ C_1 R_0 \left( v_{n2} - C_1 \frac{\partial h_2}{\partial p_2} \right) - p_2 v_{n2}^2 \frac{\partial \mu_2}{\partial T_2}.
 \end{aligned}$$

The initial approximation is taken from the solution for a perfect gas.

To find partial derivatives of enthalpy and molecular weight with respect to pressure and temperature, finite difference formulas are used

$$\begin{aligned}
 \frac{\partial h}{\partial p} &= \frac{h(p + \Delta p, T) - h(p - \Delta p, T)}{2\Delta p}; \\
 \frac{\partial h}{\partial T} &= \frac{h(p, T + \Delta T) - h(p, T - \Delta T)}{2\Delta T}; \\
 \frac{\partial \mu}{\partial p} &= \frac{\mu(p + \Delta p, T) - \mu(p - \Delta p, T)}{2\Delta p}; \\
 \frac{\partial \mu}{\partial T} &= \frac{\mu(p, T + \Delta T) - \mu(p, T - \Delta T)}{2\Delta T}.
 \end{aligned}$$

Here,  $\Delta p = k_p p^n$  и  $\Delta T = k_T T^n$ . The coefficients  $k_p$  and  $k_T$  are in the range of 0.005–0.01.

#### 4. Governing equations

The Euler equations are used to describe the unsteady flow of inviscid compressible gas. The Euler equations are written as

$$\frac{\partial}{\partial t} \oint_V \mathbf{U} dV + \oint_{\partial V} \mathbf{F} \cdot d\mathbf{S} = 0, \quad (5)$$

where  $t$  is time,  $\mathbf{U}$  is vector of conservative flow quantities at point  $\mathbf{x}$  at time  $t$ ,  $\mathbf{F}$  is vector of fluxes,  $V$  is control volume with boundary  $\partial V$ ,  $d\mathbf{S} = \mathbf{n} dS$  is vector of area element  $dS$  to the boundary  $\partial V$  with external normal  $\mathbf{n}$ . The vector of conservative flow quantities and vector of fluxes in equation (5) have the form

$$\mathbf{U} = \begin{pmatrix} \rho \\ \rho \mathbf{v} \\ \rho e \end{pmatrix}, \mathbf{F} = \begin{pmatrix} \rho \mathbf{v} \\ \rho \mathbf{v} \mathbf{v} + p \mathbf{I} \\ (\rho e + p) \mathbf{v} \end{pmatrix}.$$

The specific total energy is equal to the sum of the internal energy  $\varepsilon$  (it includes the energies of translational motion, rotational, vibrational, and electronic excitation of atomic and molecular components of the gas mixture), and kinetic energy

$$e = \varepsilon + \frac{1}{2} |\mathbf{v}|^2.$$

Here,  $\rho$  is density,  $p$  is pressure,  $\mathbf{v}$  is velocity vector,  $\mathbf{I}$  is unit tensor. For a thermally perfect gas, specific heat capacity and molar mass remain constant. In high-temperature air, when the processes of dissociation and ionization become noticeable, the dependences of these characteristics on the parameters of the medium become more complicated; in particular, the dependence on pressure and temperature begins to play a role (as a result of a change in the molecular composition).

Eq. (6) is supplemented by the equation of state

$$p = \rho \frac{R_0}{M_\Sigma(p, T)} T,$$

where  $R_0$  is universal gas constant,  $M_\Sigma$  is molecular weight. The specific enthalpy is  $h = \varepsilon + p/\rho$ . The specific total energy is defined as

$$e = h + \frac{1}{2} |\mathbf{v}|^2 - \frac{p}{\rho}.$$

The specific enthalpy is

$$h = h_0 + \int_{T_0}^T c_p dT,$$

where  $h_0$  is enthalpy of formation of a substance at temperature  $T_0$ .

The molecular weight,  $M_\Sigma$ , the gas constant  $R = R_0/M_\Sigma$ , the heat capacity at constant pressure,  $c_p$ , and the heat capacity at constant volume,  $c_v$ , of perfect gas is constant. Therefore, Mayer's relationship ( $c_p - c_v = R$ ) is applicable. The ratio of specific heat capacities is  $\gamma = c_p/c_v$ , and the relations  $h = c_p T$  and  $\varepsilon = c_v T$  are applied to find the enthalpy and internal energy.

## 5. Numerical method

The finite volume method is used to find numerical solutions to governing equations. Eq. (6) is solved numerically with the finite volume method. The flow domain is divided into closed control volumes. The mesh value found at the center of the control volume,  $V_i$ , is the average integral value

$$\mathbf{U}_i = \frac{1}{V_i} \int_{V_i} \mathbf{U} dV.$$

The integral over the boundary of the control volume  $i$  is a sum of the products of flux vector at the centers of face  $j$  and face area,  $S_{ij}$ . Then, Eq. (6) is written in semi-discrete form

$$\frac{d\mathbf{U}_i}{dt} + \frac{1}{V_i} \sum_j^{N_i} \mathbf{F}_{ij} S_{ij} = 0, \quad (6)$$

where  $V_i$  is the volume of the control volume  $i$ ,  $\mathbf{F}_{ij}$  is the flow vector from cell  $i$  to cell  $j$  at the center of the face of the control volume,  $S_{ij}$  is the face area  $j$  of the control volume  $i$ .

To discretize time derivative in Eq. (7), an explicit third-order Runge–Kutta scheme is used. There are different approaches to calculate convective flows on the edge of the control volume. In this case, standard schemes for calculating flows, for example, the widely used Roe scheme, lead to a loss of accuracy and divergence of the computational procedure. The Godunov scheme and the Rusanov scheme are used to discretize convective flows. The second order of approximation in space is applied. Flow quantities are interpolated from the center of the cells to the edge of control volume, and limiters are applied to restrict the gradient of the solution and to ensure the monotonicity of the scheme.

The fluxes in finite volume scheme (7) are calculated in the direction of the normal to the boundary. The flux through the edge of control volume is found as

$$\mathbf{F}_{j+1/2} = \frac{1}{2} [\mathbf{F}(\mathbf{U}_L) + \mathbf{F}(\mathbf{U}_R)] - \frac{1}{2} |A| (\mathbf{U}_R - \mathbf{U}_L),$$

where  $|A| = R|\Lambda|L$  and  $\Lambda = \text{diag}\{v_n - a, v_n, v_n + a\}$  is diagonal matrix with Jacobian eigenvalues on the main diagonal.

For an approximate accounting of complex physical and chemical processes in real gases, a methodology has been developed for the effective adiabatic exponent, which makes it possible to decompose the complete problem of modeling high-speed flows into stages. This ensures the creation of a universal computing complex, structured into a number of autonomous segments, with the possibility of independent modification of their functional content, improvement of algorithms, and computer implementation.

The heat capacity at constant pressure is calculated using numerical differentiation (second-order central difference discretization)

$$c_p(p, T) = \left( \frac{\partial h}{\partial T} \right)_p = \frac{h(p, T + \Delta T) - h(p, T - \Delta T)}{2\Delta T},$$

where  $\Delta T = 0.01T$ .

## 6. Transformation of variables

The fluid flow described by the Euler equations is determined by the vector of conservative variables

$$\mathbf{U} = \{\rho, \rho u_x, \rho u_y, \rho e\},$$

where  $\rho$  is density,  $\rho u_x$ ,  $\rho u_y$  are momentums in  $x$  and  $y$  directions,  $\rho e = \rho \left[ \varepsilon + \frac{(u_x^2 + u_y^2)}{2} \right]$  is total energy.

In addition to the vector of conservative variables, the vector of physical (primitive) variables is used

$$\mathbf{Q} = \{\rho, u_x, u_y, p\},$$

where  $\rho$  is density,  $u_x$ ,  $u_y$  are velocities in  $x$  and  $y$  directions,  $p$  is pressure.

Physical variables are expressed in terms of conservative variables. The direct transformation operation is not straightforward. However, the reverse transformation requires the solution of equations

$$\begin{cases} \rho e = \rho \varepsilon(p, T) + \rho \frac{v^2}{2} \\ p = \rho \frac{R_0}{M_\Sigma(p, T)} T \end{cases} \Rightarrow \begin{cases} \varepsilon(p, T) = \frac{(\rho e)}{\rho} - \frac{v^2}{2} \\ p M_\Sigma(p, T) - \rho R_0 T = 0 \end{cases}$$

Unknown quantities are  $p, T$ ,  $\varepsilon = h - p/\rho$ . These equations are non-linear. To solve non-linear equations, Newton's method is applied. The variables at the new iteration are found from values at the previous iteration

$$p^{n+1} = p^n + \Delta p, T^{n+1} = T^n + \Delta T,$$

where  $\Delta p$ ,  $\Delta T$  are increments of pressure and temperature. The superscript  $n$  denotes the iteration number.

The quantities  $\varepsilon$  and  $M_\Sigma$  are expanded in a Taylor series keeping terms of first order

$$\begin{aligned} \varepsilon^{n+1}(p, T) &= \varepsilon^n + \frac{\partial \varepsilon}{\partial p} \Delta p + \frac{\partial \varepsilon^n}{\partial T} \Delta T; \\ M_\Sigma^{n+1}(p, T) &= M_\Sigma^n + \frac{\partial M_\Sigma^n}{\partial p} \Delta p + \frac{\partial M_\Sigma^n}{\partial T} \Delta T. \end{aligned}$$

Then, equations take the form

$$\begin{aligned} \frac{\partial \varepsilon^n}{\partial p} \Delta p + \frac{\partial \varepsilon^n}{\partial T} \Delta T &= \frac{(\rho e)}{\rho} - \frac{v^2}{2} - \varepsilon^n; \\ \left( M_\Sigma^n + p^n \frac{\partial M_\Sigma^n}{\partial p} \right) \Delta p + \left( p^n \frac{\partial M_\Sigma^n}{\partial T} - \rho R_0 \right) \Delta T &= \rho R_0 T^n - p^n M_\Sigma^n. \end{aligned}$$

The increments of the pressure and temperature,  $\Delta p$  and  $\Delta T$ , are obtained. The iterations finish when  $\Delta p$  and  $\Delta T$  satisfy the accuracy conditions. The derivatives of  $\varepsilon$  and  $M_{\Sigma}$  are found with the central difference formulas of the second order

$$\begin{aligned}\frac{\partial \varepsilon^n}{\partial p} &= \frac{\varepsilon(p^n + \delta_p, T^n) - \varepsilon(p^n - \delta_p, T^n)}{2\delta_p}; \\ \frac{\partial \varepsilon^n}{\partial T} &= \frac{\varepsilon(p^n, T^n + \delta_T) - \varepsilon(p^n, T^n - \delta_T)}{2\delta_T}; \\ \frac{\partial M_{\Sigma}^n}{\partial p} &= \frac{M_{\Sigma}(p^n + \delta_p, T^n) - M_{\Sigma}(p^n - \delta_p, T^n)}{2\delta_p}; \\ \frac{\partial M_{\Sigma}^n}{\partial T} &= \frac{M_{\Sigma}(p^n, T^n + \delta_T) - M_{\Sigma}(p^n, T^n - \delta_T)}{2\delta_T}.\end{aligned}$$

Here,  $\delta_p = k_p p^n$ ,  $\delta_T = k_T T^n$ . The coefficients  $k_p$  and  $k_T$  are chosen from the interval 0.005–0.01.

## 7. Results and discussion

A supersonic flow around a wedge with a half-angle  $\beta=30^\circ$  by a perfect and high-temperature gas is simulated. The inlet pressure and inlet temperature (flow quantities before the shock) are  $10^5$  Pa and 290 K. The working substance is air ( $\gamma=1.4$  and  $\mu=0.029$  kg/mol). The inlet Mach number varies from 2 to 16. For the ideal perfect gas, the solution is available in a tabular form. The results presented in the study correspond to two cases. The difference between them is the velocity behind the shock wave front. It equals  $10^3$  m/s (Case 1) and  $3 \cdot 10^3$  m/s (Case 2). In Case 1, density is  $\rho=5.5$  kg/m<sup>3</sup>, pressure is  $p=16.78$  bar, temperature is  $T=1068$  K for a perfect gas, and density is  $\rho=5.7$  kg/m<sup>3</sup>, pressure is  $p=16.59$  bar, temperature is  $T=1012$  K for high-temperature air. In case 2, density is  $\rho=7.0$  kg/m<sup>3</sup>, pressure is  $p=133.5$  bar, temperature is  $T=6649$  K for perfect gas and density is  $\rho=10.0$  kg/m<sup>3</sup>, pressure is  $p=127.1$  bar, temperature is  $T=4251$  K for high-temperature air. In Case 3, the flow velocity is  $3 \cdot 10^3$  m/s, and the inlet conditions for real and perfect gas are identical (density is  $\rho=7.0$  kg/m<sup>3</sup>, pressure is  $p=134.5$  bar, temperature is  $T=6649$  K).

The mesh contains  $110 \times 160$  nodes. Mesh nodes are clustered near the solid boundaries and shock wave front to take into account gradient regions of flow (**Figure 2**). The minimum residual level is used as a criterion for the convergence of the difference solution to the stationary solution of the problem. Approximately 2200 time steps are taken to achieve the specified residual level (in the calculations  $R = 10^{-10}$ ).

The pressure distributions found from the perfect and real gas models are shown in **Figure 3** at different times. In this case, the shock-wave structure for both models is similar. However, the compressed region for a real gas is slightly smaller than in the case of the perfect gas model. The temperature in case 1 does not exceed 1900 K (**Figure 4**). Temperatures are low, and there are no chemical reactions. Therefore, the molar mass of air remains constant. It should be noted that narrow regions with high temperatures exist where the temperature reaches 2480–3100 K, but this has little effect on the flow pattern.



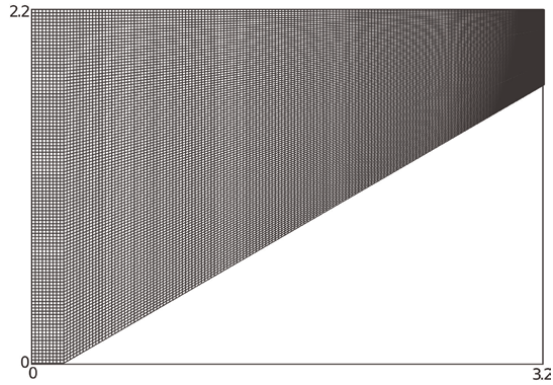


**Figure 2.**  
*Mesh.*

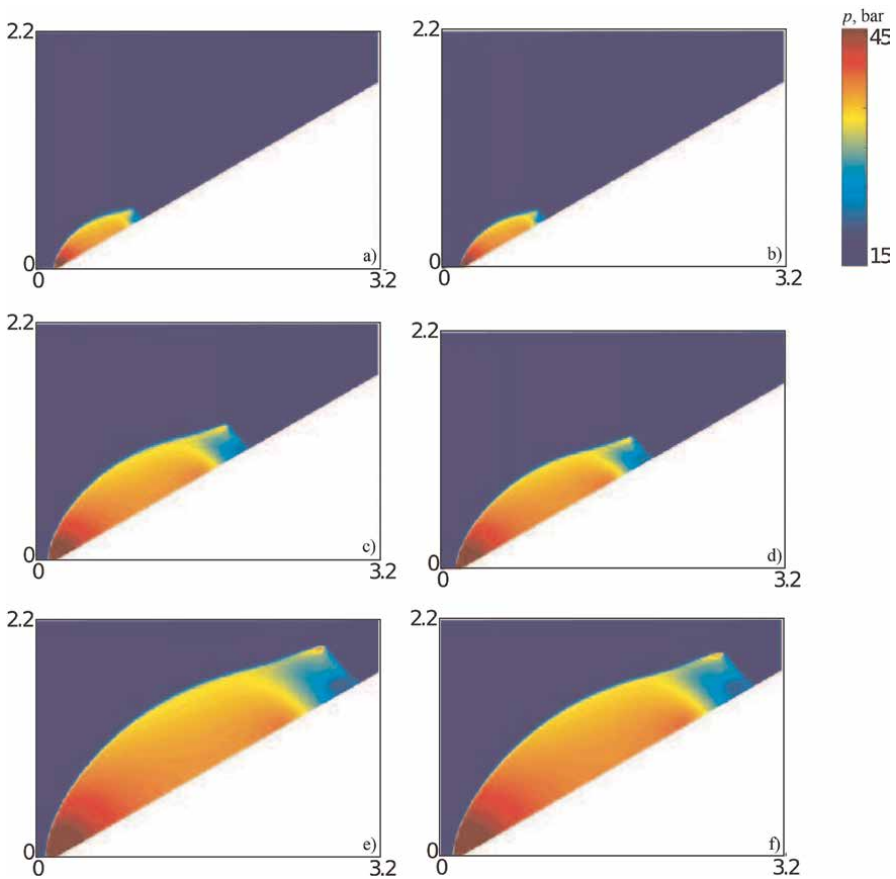


**Figure 3.**  
*Case 1. Pressure contours at time 0.697 (a, b), 1.384 (c, d), 2.054 ms (e, f) for perfect (a, c, e) and real (b, d, f) gas.*

Large flow velocity leads to significant differences in flow quantity distributions computed with the perfect gas model and real gas model (**Figures 5 and 6**). The pressure computed with a real gas model exceeds the pressure computed with a

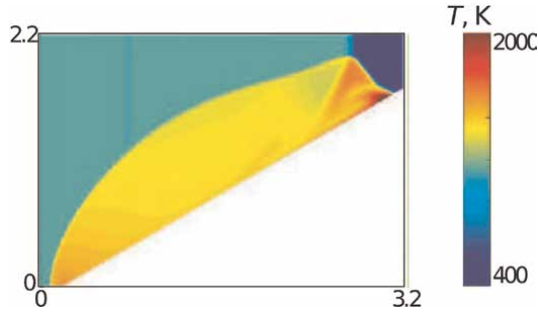


**Figure 4.**  
Case 1. Temperature contours at time 2.054 ms for a perfect gas.

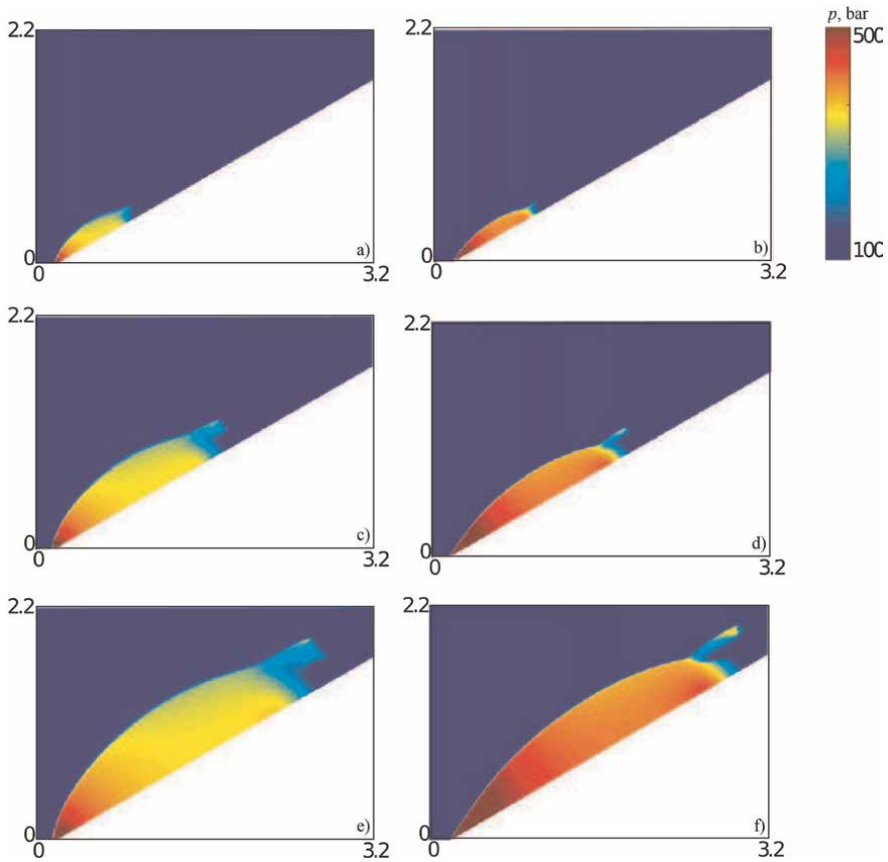


**Figure 5.**  
Case 2. Pressure contours at time (a, b) 0.242), (c, d) 0.476, and (e, f) 0.708 ms for perfect (a, c, e) and real (b, d, f) gas.

perfect gas model. The shock-wave structure in a real gas has a flattened shape in comparison with a perfect gas model. Dissociation and ionization processes in high-speed flow lead to different distributions of temperature. The maximum temperature in a real gas (it is about 11,000 K) is two times lower than the temperature computed with a perfect gas model (it is about 23,000 K). Temperature distributions computed

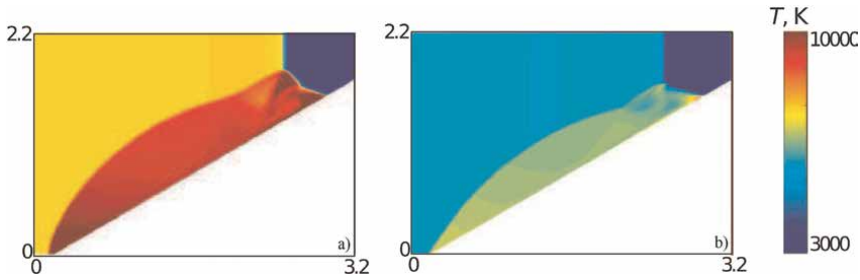


**Figure 6.**  
Case 2. Temperature contours at time 0.708 ms for perfect (a) and real (b) gas.

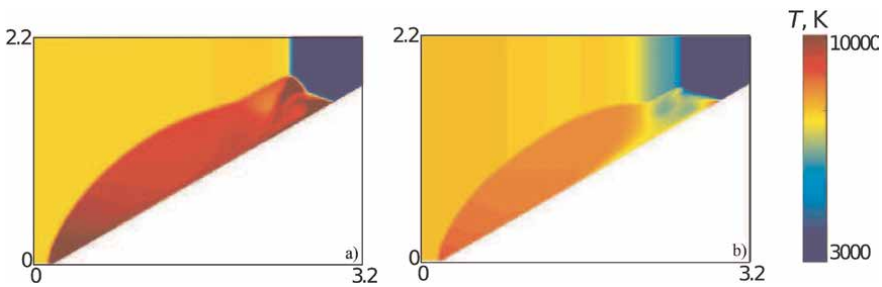


**Figure 7.**  
Case 2. Temperature contours at time 0.749 ms for a perfect gas (a) and at time 0.723 ms (b) for a real gas.

with two models are compared in **Figure 7**. Density distribution is similar to pressure distribution, however, density computed with a perfect gas model is two times smaller than those computed with a real gas model.

The distributions of the flow characteristics along the lower wall of the computational domain are shown in **Figure 8** shows flow quantities distributions along  $x=0$  line. When high-temperature effects in the air are taken into account, pressure undergoes relatively small changes. Dashed lines correspond to a perfect gas model, and solid lines correspond to a real gas model.

Distributions of flow quantities computed at the same inlet conditions show that the shock wave structures computed with different models of air are similar to each other. However, the distribution flow quantities are different (**Figure 9**). In a region of shock, the difference in the values of the parameters is small and similar to that observed in a perfect gas. At the same time, the temperature distributions computed with perfect and real gas models are different (**Figure 10**). Temperature distributions computed with perfect and real gas models are compared in **Figure 11**.

Flow quantities distributions along line  $x = 0$  are presented in **Figure 12**. High-temperature effects in the air have a significant impact on density and temperature distributions. At the same time, pressure distributions are relatively weakly affected by physical and chemical processes. Dashed lines correspond to a perfect gas model, and solid lines correspond to a real gas model.

The influence of wedge angle and inlet Mach number is shown in **Figure 13** ( $\beta=30^\circ$ ). Pressure distribution is not affected by high-temperature effects in air. At the same time, temperature distributions computed with different gas models are

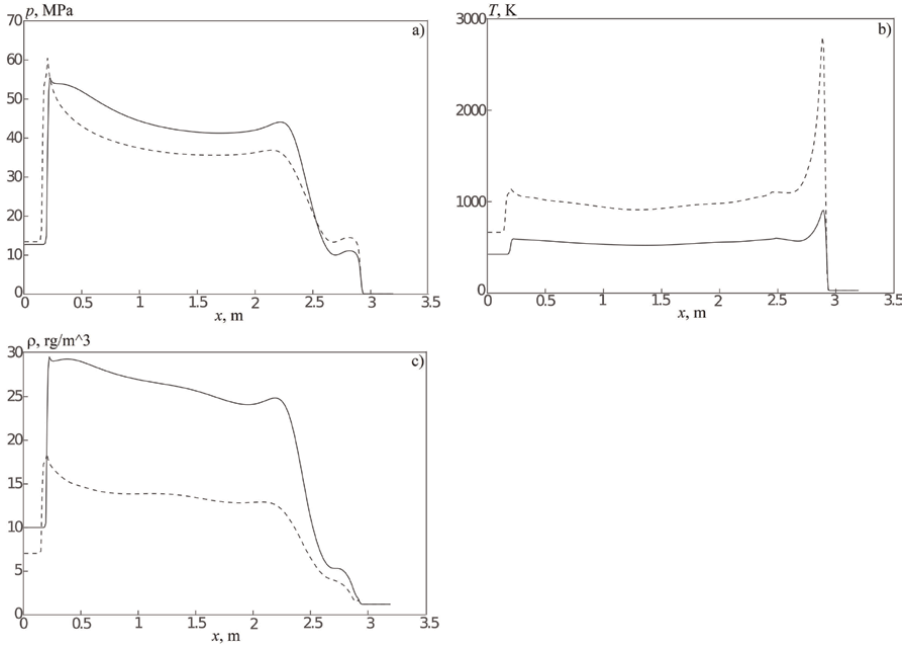


**Figure 8.** Case 2. Pressure (a), temperature (b) and density (c) distributions along  $x = 0$  line.

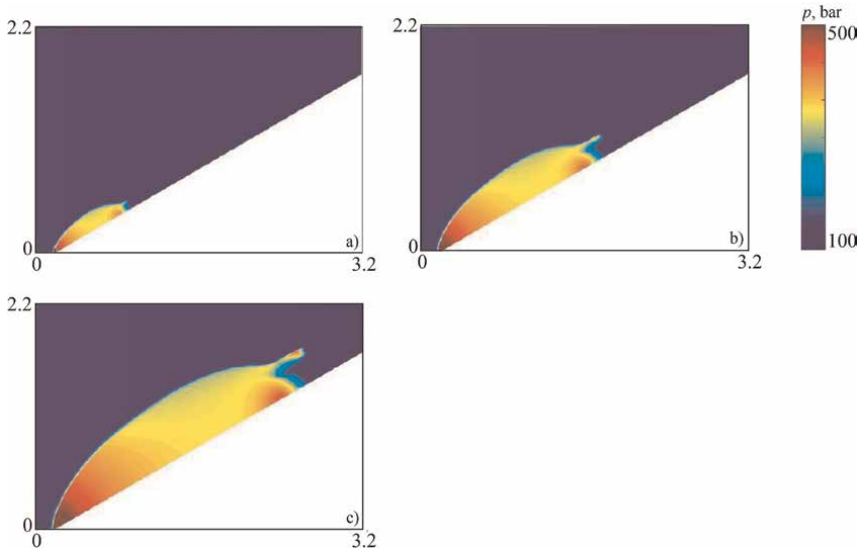


**Figure 9.** Case 3. Pressure contours at time 0.245 (a), 0.478 (b), 0.711 ms (c) for a real gas.

different. Dashed lines correspond to a perfect gas model, and solid lines correspond to a real gas model.

For comparison, **Figure 14** shows the distributions of flow characteristics behind a normal shock as a function of the inlet Mach number. The flow velocity behind a normal shock is subsonic. Therefore, a difference between the flow quantities computed with perfect and real gas models exceeds the mismatch of the flow quantities

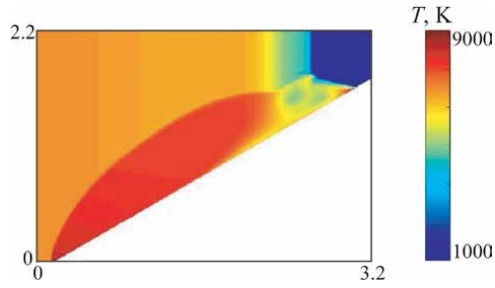


**Figure 10.**  
 Case 3. Temperature contours at time 0.711 ms for a real gas.

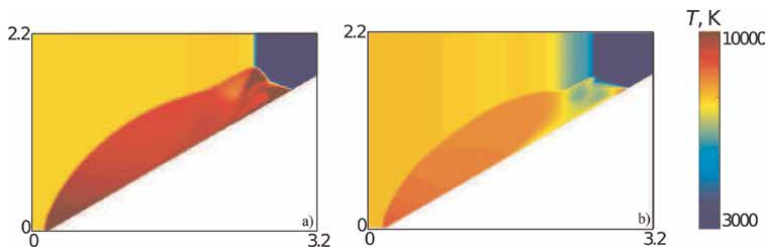


**Figure 11.**  
 Case 2. Temperature contours at time 0.749 ms for a perfect gas (a) and at time 0.723 ms for a real gas (b).

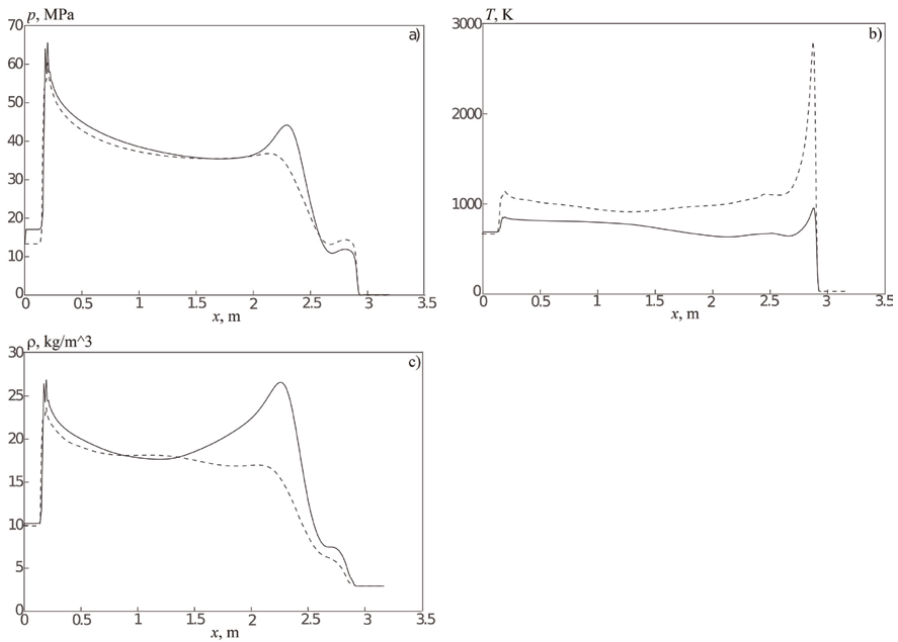


**Figure 12.**  
 Case 3. Pressure (a), temperature (b), and density (c) distributions along  $x = 0$  line for perfect and real gas models.

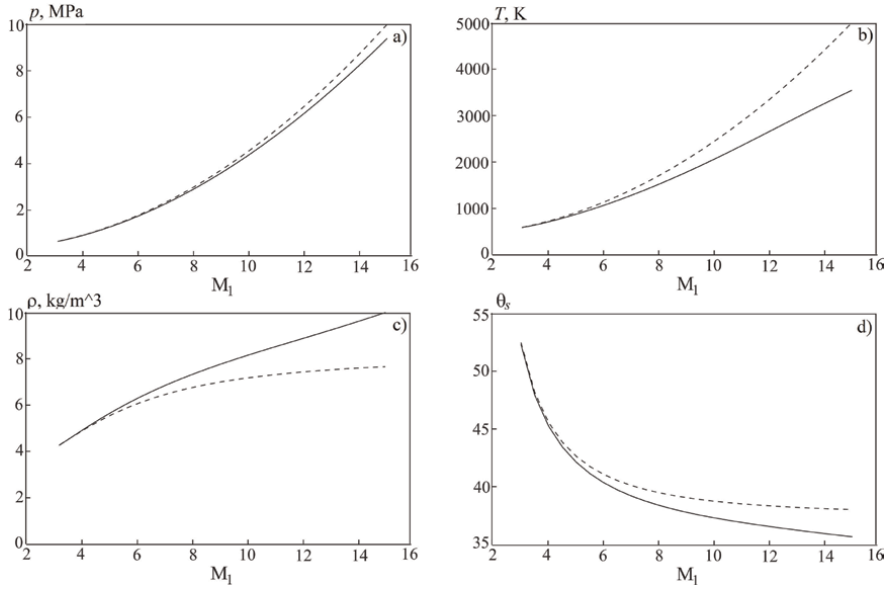


**Figure 13.** Pressure (a), temperature (b), density (c), and shock angle (d) distributions computed with the perfect gas model and high-temperature model based on the Kraiko model [18].

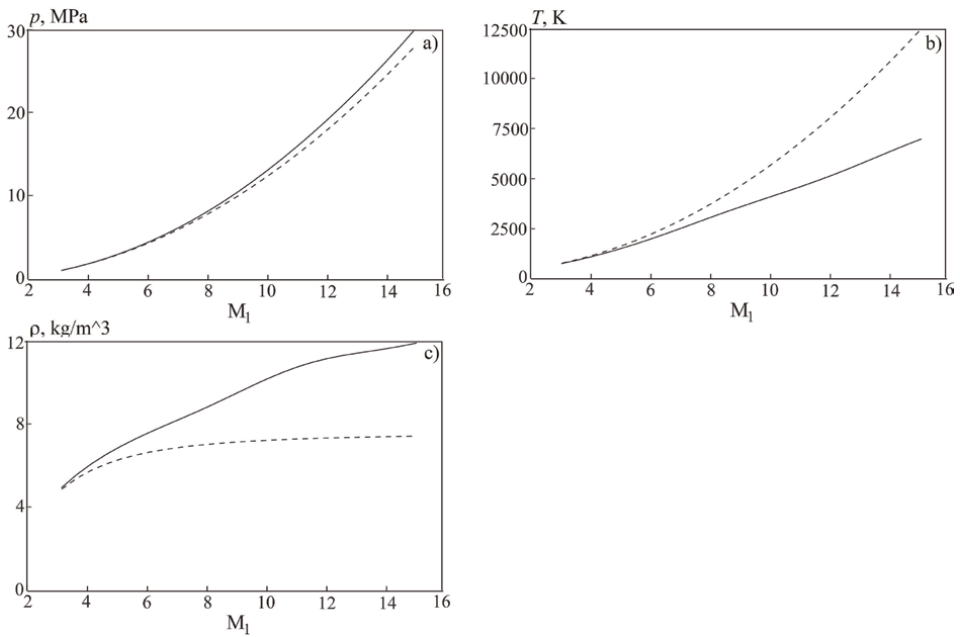


**Figure 14.** Pressure (a), temperature (b), and density (c) distributions behind a normal shock computed with the perfect gas model and Kraiko model [18].

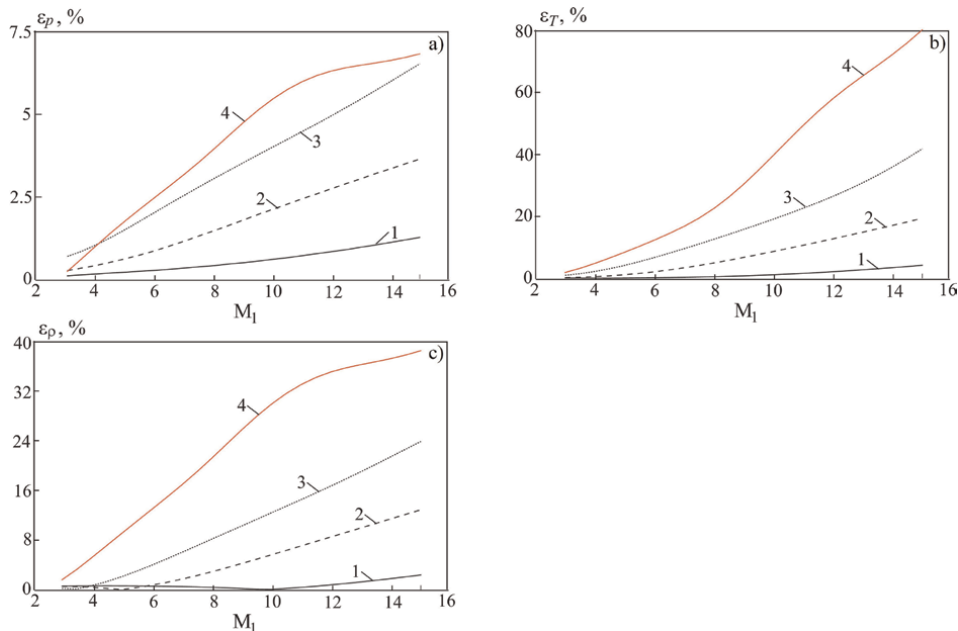


**Figure 15.** Relative error in determining pressure (a), temperature (b) and density (c) at  $\beta = 10^\circ$  (line 1),  $20^\circ$  (line 2),  $30^\circ$  (line 3). Line 4 corresponds to a normal shock wave.

observed behind an oblique shock wave. Dashed lines correspond to a perfect gas model, and solid lines correspond to a real gas model.

The use of the perfect gas model at high Mach numbers of the oncoming flow leads to the inaccurate solutions. The relative error of computations of flow quantities obtained with the perfect gas model and real gas model is shown in **Figure 15**. An increase in the angle of the wedge leads to an increase in the error between solutions computed with various models of air.

## 8. Conclusion

At high intensity of the shock wave, which occurs at high supersonic and hypersonic flow velocities, the properties of the gas differ from the properties of a perfect gas. This leads to significant differences in the distributions of flow characteristics behind the shock wave front, corresponding to the models of a perfect and real gas. An approach and a calculation module have been developed that allow taking into account equilibrium chemical reactions in the air at high temperatures. To demonstrate the capabilities of the developed model, the problem of supersonic flow around a wedge with an attached shock wave is used. A comparison is made of the space-time distributions of flow characteristics calculated using the perfect and real gas models.

The developed computational module allows the inclusion in the design systems of advanced aircraft shapes, as well as integration with both commercial and open-source CFD packages.


## **Author details**

Konstantin Volkov  
Kingston University, London, United Kingdom

\*Address all correspondence to: k.volkov@kingston.ac.uk

## **IntechOpen**

---

© 2022 The Author(s). Licensee IntechOpen. This chapter is distributed under the terms of the Creative Commons Attribution License (<http://creativecommons.org/licenses/by/3.0>), which permits unrestricted use, distribution, and reproduction in any medium, provided the original work is properly cited. 



## References

- [1] Anderson JD. *Modern Compressible Flow: With Historical Perspective*. New York: McGraw-Hill Education; 2003. p. 776
- [2] Kurganov A, Tadmor E. New high resolution central schemes for nonlinear conservation laws and convection-diffusion equations. *Journal of Computational Physics*. 2000;**160**: 241-282
- [3] Volkov KN, Emelyanov VN, Karpenko AG. Numerical simulation of gas dynamic and physical-chemical processes in hypersonic flows past bodies. *Numerical Methods and Programming*. 2017;**18**:387-405
- [4] Emelyanov VN, Karpenko AG, Volkov KN. Simulation of hypersonic flows with equilibrium chemical reactions on graphics processor units. *Acta Astronautica*. 2019;**163**:259-271
- [5] Krasnov NF. *Aerodynamics of Bodies of Revolution*. Moscow: Mashinostroenie; 1964. p. 573
- [6] Kemm F. On the proper setup of the double Mach reflection as a test case for the resolution of gas dynamics codes. *Computers and Fluids*. 2016;**132**: 72-75
- [7] Semenov AN, Berezkina MK, Krasovskaya IV. Classification of shock wave reflections from a wedge. Part 1: Boundaries and domains of existence for different types of reflections. *Technical Physics*. 2009;**54**:491-496
- [8] Semenov AN, Berezkina MK, Krasovskaya IV. Classification of shock wave reflections from a wedge. Part 2: Experimental and numerical simulations of different types of Mach reflections. *Technical Physics*. 2009;**54**:497-503
- [9] Bulat PV, Volobuev IA, Volkov KN, Pronin VA. Numerical simulation of regular and Mach reflection of shock wave from the wall. *Scientific and Technical Journal of Information Technologies, Mechanics and Optics*. 2017;**17**:920-928
- [10] Bulat PV, Volkov KN. Use of WENO schemes for simulation of the reflected shock wave-boundary layer interaction. *Journal of Engineering Physics and Thermophysics*. 2015;**88**:1203-1209
- [11] Adrianov AL, Starykh AL, Uskov VN. *Interference of Stationary Gas Discontinuities*. Novosibirsk: Nauka; 1995. p. 180
- [12] Ivanov MS, Vandromme D, Fomin VM, Kudryavtsev AN, Hadjadj A, Khotyanovsky DV. Transition between regular and Mach reflection of shock waves: New numerical and experimental results. *Shock Waves*. 2001;**11**:199-207
- [13] Elling V, Liu T-P. Supersonic flow onto a solid wedge. *Communications on Pure and Applied Mathematics*. 2008; **LXI**:1347-1448
- [14] Kraiko AN, P'yankov KS, Yakovlev EA. The flow of a supersonic ideal gas with "weak" and "strong" shocks over a wedge. *Journal of Applied Mathematics and Mechanics*. 2014;**78**: 318-330
- [15] Ruleva LB, Solodovnikov SI. Features of preparing a validating experiment in a hypersonic aerodynamic shock tube. *AIP Conference Proceedings*. 2021;**2318**:060001
- [16] Surzhikov ST. Ionization of air in flow around a blunt wedge at relatively low hypersonic speeds. *Journal of*

Physics Conference Series. 2019;**1009**:  
012022

[17] Lipanov AM, Rusyak IG, Korolev SA, Karskanov SA. Numerical solution of the problem of flow past projected bodies for determining their aerodynamic coefficients. *Journal of Engineering Physics and Thermophysics*. 2019;**92**: 477-485

[18] Kraiko AN, Makarov VE. Explicit analytic formulas defining the equilibrium composition and thermodynamic functions of air for temperatures from 200 to 20000 K. *High Temperature*. 1996;**34**:208-219

[19] Petrov MN, Tambova AA, Titarev VA, Utyuzhnikov SV, Chikitkin AV. FlowModellium software package for calculating high-speed flows of compressible fluid. *Computational Mathematics and Mathematical Physics*. 2018;**58**:1932-1954

## Chapter 2

# Design and CFD Analysis on the Reduction of Thermal Effect in Re-entry Vehicle by Using Retractable Aerospike

*Pradeep Kumar Sulur Loganathan*

### Abstract

The shape optimization of two spike classes was investigated in this study. A spike with a sharp and blunt spikes reduces drag and aero-thermodynamic heating and enables longer ranges for economical flight. Conversion of kinetic energy into heat when coming down to earth causes damage—the blunt nose design increases maximum temperature and density at the vehicle's nose. Sharp-fore bodies reduce drag but provide only an area for dispersing heat flux downstream of the shock wave—the increased area of a blunt fore-body aids in efficient heat dissipation. ANSYS Fluent is used to analyze blunt bodies with blunt and sharp spike configurations, as well as the effect of counter flow. The findings suggest drag reductions ranging from 44% to 61%. The twin-spike design is the best among the models studied, with a 44 percent reduction in peak heat flux and a 46 percent reduction in the drag coefficient. Thermal protection systems, commonly used to reduce heat in re-entry vehicles, are costly. The aim of this study is to minimize re-entry heating by introducing a spike in the frontal region of the nose and preventing further vehicle damage at high temperatures.

**Keywords:** aero thermodynamic heating, ablating materials, blunt and sharp spikes

### 1. Introduction

The sporadic creation of the shock layer is one of the features of hypersonic flow. The shock wave is attached to the completely tangent to the nose cone and is known as an attached shock wave when the structural bluntness ratio is equal to zero. The shock separation distance grows when the boundary layer rises more significantly than zero. The shock wave will intensify, and the shock layer will grow thicker. In the shock layer, the BR factor raises static pressure, temperature, and density while lowering velocity [1]. Aero heating in hypersonic flow is also affected by the large-scale separated vortex generated by the shock wave and boundary layer interaction near the head cone. The vortex has a strong pulsation pattern and produces heat skin

depressions due to structural deformation in a thicker boundary layer and a fluctuating temperature distribution. The formation and dissolution of the vortex cause violent vibration [2].

Variations in the thermodynamic nonequilibrium conditions are caused by the dissociation patterns produced by the multiple gas mixtures. The shock wave is located further away from the vehicle surface because it is upstream of the vehicle surface in the airflow. It has been discovered that approximately 30% of the original air composition is dissociated, whereas the percentage in CO<sub>2</sub> flow is around 60%; as a result, energy transfer in the translational-rotational modes in airflow is slower than in CO<sub>2</sub> [3]. An Orion-like re-entry capsule's multidisciplinary design optimization (MDO) produced more effective design solutions than the low-fidelity aero thermodynamic model. Future developments may consider chemical nonequilibrium phenomena to refine aero thermodynamic implications and heat load estimation considerations [4].

The cohesive zone method (CZM) was used to determine the region for delamination propagation in a re-entry vehicle's ceramic matrix composites body flap. Due to the low longitudinal strength under compression and compressive load, no growth is possible for the maximum allowed delamination size as an existing manufacturing defect (5 mm) and under the maximum hinge moment service condition. The development of extensive delamination increased due to the impact of foreign objects. The margin of safety concerning the investigated body flap's delamination growth phenomenon is nearly 20 in the most critical service load conditions [5].

Because compressible flows are hyperbolic, the leading bow shock influences the wake region. The increased energy available for chemical reactions, which leads to the formation of new atomic compositions, is accompanied by an increase in number density over the bow shock. The bow shock temperature decreases for all energy states, and the highest temperature values are found within the shock layer, indicating that chemical reactions can change the thickness of the shockwave structures and the distribution of thermodynamic properties across the domain [6].

To improve oxidation resistance while maintaining thermomechanical stability, adhesion, and homogeneity, a commercial product made of Al-oxide-based refractory varnish was enhanced with silicon-oxide nanoparticles. The carbon-carbon-coated materials resist erosion and oxidation and have excellent morphology with no visible discontinuities [7]. Thermal coating, also known as the thermal protection system (TPS), is required for re-entry vehicles. Thermal barrier coating (TBC) is used to resist large temperature gradients because metals are highly susceptible to corrosion, heating, and wear. We use phenolic and composites, such as silica and ceramics. This module will discuss the challenges encountered during re-entry, desirable vehicle shapes, materials used to prevent aerodynamic heating, types of re-entry vehicles, and brief analysis of their performance [8].

Because of atmospheric drag and aerodynamic heat, the planet's gravity and atmosphere place enormous strain on spaceflight during entry. This project concerns the CFD analysis in ANSYS Fluent of the entry capsule with a payload into the Earth's atmosphere. The shockwave behavior during the module's entry will be investigated [9]. The mechanical properties of silica aerogels with various geometric properties, such as particle size, pore size, and ligament diameter, were calculated using the finite volume method (FVM). According to the FVM simulation results, a power law

correlation exists between relative density and mechanical properties (elastic modulus and yield stress) of silica aerogels. Finally, the findings suggest that it is possible to create silica aerogels with an ultra-low density, high strength, and stiffness if the textural features are well controlled [10].

The evaluation of the re-entry vehicle's aero thermodynamic analysis. The flow field around a blunted cone-flare in hypersonic flow is depicted using computational fluid dynamics results. The heat flux was calculated using a numerical approach to the Navier-Stokes equation and two different Mach numbers [11]. This study studies the effect of thermal loads on the structure and observes how it reacts because of the thermal loads, providing exposure to various coupled-field analyses [12].

The study's goal was to perform a thermostructural analysis of the TPS of a re-entry module known as the Crew module. The thermostructural research includes heat transfer analysis to determine temperature distribution and variation throughout the operation. The thermal and mechanical load analysis is then performed to obtain structural deformations and stresses [13]. This article discusses the nose cone, the forwardmost section of a rocket, guided missile, or aircraft. The cone is shaped to provide the least amount of aerodynamic resistance. Nose cones are also intended for use in and under water and on high-speed land. The nose cone of a satellite vehicle may become the satellite itself after separating from the rocket's final stage, or it may be used to shield the satellite until the orbital speed is achieved before separating from the satellite [14, 15].

## **2. Introduction to aero thermodynamic heating**

Atmospheric entry is the movement of an object from outer space into and through the gases of a planet's, dwarf planets, or natural satellite's atmosphere. Uncontrolled entry, such as the entry of astronomical objects, space debris, or bolides, and controlled entry (or) re-entry of a spacecraft capable of being navigated or following a predetermined course are the two main types of atmospheric entry. EDL refers to the technologies and procedures that allow for the controlled atmospheric entry, descent, and landing of spacecraft. Atmospheric and aerodynamic heating can cause atmospheric breakup capable of completely disintegrating smaller objects. These forces may cause things with lower compressive strength to explode. Before parachutes or air brakes can be deployed, crewed space vehicles must be slowed to subsonic speeds. Such vehicles have kinetic energies ranging from 50 to 1,800 megajoules, and atmospheric dissipation is the only way to expend the kinetic energy. The rocket fuel required to slow the vehicle would be nearly equal to the amount used to accelerate it initially, making the use of retro rockets for the entire Earth re-entry procedure impractical [8].

While adiabatic compression causes the high temperature at the heat shield's surface, the vehicle's kinetic energy is eventually lost due to gas friction (viscosity) after the vehicle has passed by. Other minor energy losses include direct black body radiation from hot gases and chemical reactions between ionized gases [14]. Ballistic warheads and expendable vehicles do not require slowing during re-entry and are designed to maintain speed. Furthermore, slow-speed returns to Earth from near-space, such as parachute jumps from balloons, do not necessitate heat shielding because the gravitational acceleration of an object starting at relative rest within the

atmosphere (or not far above it) cannot generate enough velocity to cause significant atmospheric heating [16].

At the Karman line, 100 km (62.14 mi/54 nautical mi) above the surface, atmospheric entry occurs for Earth. In comparison, Venus atmospheric entry occurs at 250 km (155.3 mi/135 nautical mi), and Mars atmospheric entry occurs at about 80 km (50 mi/43.2 nautical mi). Uncontrolled objects accelerate through space toward the Earth under gravity and are slowed by friction when they come into contact with the Earth's atmosphere. Meteors are often relatively fast relative to the Earth because their orbital path differs from the Earth's before encountering the Earth's gravity [17]. Most controlled objects enter at hypersonic, orbital, or unbounded speeds. Several technologies have been developed to enable atmospheric re-entry and flight at high speeds. Buoyancy is a low-velocity controlled atmospheric entry method suitable for planetary entry where thick atmospheres, strong gravity, or both complicate high-velocity hyperbolic entry, such as the atmospheres of Venus, Titan, and the gas giants [1].

## **2.1 Thermal effects on space re-entry vehicle**

The primary cause of shock-layer heating is not direct friction with the re-entry object. Some heating is also accounted for by friction-based entropy increases of the molecules within the wave [2]. It has little effect when the vehicle travels at subsonic speeds. Still, it significantly impacts the design, material of the vehicle structure, and the incorporated systems at supersonic (beyond  $M = 1.2$ ) and hypersonic (beyond  $M = 5$ ) speeds. The spacecraft re-enters at very high speeds (Mach number greater than 20), which is enough to destroy the vehicle if safety precautions are not taken. Even after the vehicle has reached a high stability temperature, the heating effect remains at its high point at the leading edge [3].

## **2.2 Aerospike**

During the flight, hypersonic vehicles experience significant drag and aerodynamic heating. Many attempts are being made to reduce these impacts to achieve longer ranges, reduced fuel consumption, and safer flights. One method is to employ spikes. A spike is a needle-like body attached to the main Blunt's nose tip [16]. The primary mechanism of drag and heating reduction is twofold: first, a much weaker oblique foreshock replaces the strong detached bow shock ahead of the blunt body; second, it encourages separation of the flow downstream of the foreshock and creates a recirculation zone that screens a large portion of the main body nose surface. The shear layer that encircles the recirculation zone reattaches to the main body surface, creating a shock wave that turns the outer flow at the body shoulder [17].

Several designs are being considered. Spikes, aero discs, and even supersonic projectiles that were thrown ahead of the blunt forebody are among the concepts. Among these strategies, spikes proved to be the most straightforward and successful in minimizing aerodynamic heating [2]. A drag-reducing aerospike minimizes the aerodynamic drag of blunt bodies at supersonic speeds. A detached shock is created ahead of the body by the aerospike. A zone of recirculating flow forms between the shock and the forebody, acting as a more streamlined forebody profile and lowering drag [10].

### **3. Silica aerogel**

#### **3.1 Silica aerogel: A historical overview**

Many people believe that aerogels are recent technological advancements. The first aerogels were made in 1931. Steven. S. Kistler of the College of the Pacific in Stockton, California, set out at the time to prove that a “gel” contained a continuous solid network the same size and shape as the wet gel. The obvious way to test this hypothesis was to remove the liquid from the wet gel without causing any damage to the solid component. As is often the case, the apparent path was fraught with peril. When a wet gel is left to dry on its own, it shrinks, often to a fraction of its original size. This shrinkage was frequently accompanied by severe gel cracking. Kistler correctly predicted that the solid component of the gel was microporous and that the evaporating liquid’s liquid-vapor interface exerted strong surface tension forces that collapsed the pore structure. Kistler then discovered the most crucial aspect of aerogel [13].

The first gels studied by Kistler were silica gels prepared by the acidic condensation of aqueous sodium silicate. However, attempts to prepare aerogels by converting the water in these gels to a supercritical fluid failed. Instead of leaving a silica aerogel behind, the supercritical water redissolved the silica, precipitating as the water was vented. When the French government approached Stanislaus Teichner at Claud Bernard University, Lyon, in the late 1970s, he was looking for a method to store oxygen and rocket fuels in porous materials. What happened next is the subject of a legend passed down among aerogel researchers. Teichner delegated the task of preparing and studying aerogels for this application to one of his graduate students [18].

Particle physics researchers realized in the early 1980s that silica aerogels would be an ideal medium for producing and detecting Cherenkov radiation. Large transparent tiles of silica aerogel were required for these experiments. Two large detectors were built using the TMOS method. One at the Deutsches Elektronen-Synchrotron (DESY) in Hamburg, Germany, used 1700 L of silica aerogel in the TASSO detector, and another at CERN used 1000 L of silica aerogel prepared at the University of Lund in Sweden [19]. The Lund group established the first pilot plant in Sjobo, Sweden, to produce silica aerogel monoliths using the TMOS method. A 3000-L autoclave was included in the plant to handle the high temperatures and pressures encountered in supercritical methanol production (240°C and 80 atmospheres). However, during a production run in 1984, the autoclave developed a leak. The room in which the vessel was kept quickly filled with methanol vapors and exploded. The plant was later rebuilt and still produces silica aerogels through the TMOS process [20].

#### **3.2 Energy absorbing materials**

Simply said, materials absorb kinetic energy by plastic deformation, elastic deformation, brittle fracture, or the fluid dynamics of gases or liquids inside the material. Organic foams, such as expanded polystyrene, polyurethanes, polyethers, or polyethylene, are frequently employed as impact-absorbing materials. These often exhibit plastic or elastomeric behavior [9]. As an inorganic solid, silica aerogels are fragile by nature. At first, glance, using delicate material as cushioning could appear bad. Because silica aerogels typically contain shallow-density elements, the solid

network collapses gradually, distributing the force of impact over a more extended period. Additionally, because silica aerogels are an open-pored substance, the gas inside the solid's central portion is driven outside when the material collapses [15].

### **3.3 Environmental concerns**

Silica aerogels are produced and used in an environmentally friendly manner. During their manufacture, no significantly dangerous wastes are produced. Silica aerogels can be disposed of naturally. They swiftly break down into a fine powder in the environment that resembles one of the most prevalent materials on Earth, sand, almost precisely. Silica aerogels are also absolutely nontoxic and inflammable. They could eliminate a tremendous quantity of unnecessary plastic materials if they ever make their way into general use as protective materials [21].

### **3.4 Potential uses**

Silica aerogels may find utility in various applications due to their appealing energy-absorbing qualities. These could include safeguarding one's safety while driving, safeguarding delicate equipment such as aircraft flight recorders, and safeguarding technological devices such as laptop hard drives [22].

### **3.5 The pore structure of silica aerogel**

Silica aerogels' pore structure is challenging to define in words. Unfortunately, the approaches for describing porosity that is now available only somewhat improve on that. According to a categorization proposed by the International Union of Pure and Applied Chemistry, pores with a diameter of less than 2 nm are called "micropores," those between 2 and 50 nm are called "mesopores," and those more than 50 nm are called "macropores." [23].

## **4. Thermal properties of silica aerogels**

Around 1980, there was a resurgence of interest in aerogel technology as energy efficiency, and the environmental implications of chlorofluorocarbons (CFCs) became more of a concern. The solid insulating value and environmentally benign manufacturing processes of silica aerogels made them an appealing replacement for conventional insulation, which became immediately apparent. Unfortunately, cost-sensitive businesses like housing could not afford the material's production costs [24]. There are three processes by which thermal energy can travel through an insulating material: solid conductivity, gaseous conductivity, and radiative (infrared) transmission. These three factors add up to the material's overall thermal conductivity. A given material's inherent quality is solid conductivity. Solid conductivity is comparatively high for dense silica. However, only a tiny (1–10%) portion of solid silica is present in silica aerogels. As a result, thermal transfer through the silica aerogel's substantial component takes a very circuitous route and is not incredibly efficient. The visual transparency of silica aerogels makes them ideal for insulation applications. The radioactive component of thermal transfer is small and unimportant at low temperatures [25].



#### **4.1 Thermal resistance**

The aerogel particles on the fabric surface increase the fabric's thermal resistance. The thermal resistance of the thickener-coated material was  $0.0118 \text{ m}^2\text{K/W}$ , whereas the thermal resistance of the aerogel-coated fabric (A1) was  $0.0199 \text{ m}^2\text{K/W}$ . In other words, a 2% aerogel coating increased thermal resistance by 68.64%.

### **5. Synthesis of the aerogels**

Melamine (M), Resorcinol (R), and Formaldehyde (F) were polycondensed to form hydrogels with sodium carbonate as a catalyst (C) and deionized water (W) as a solvent. Carbon black (CB) and diatomite were used as conductive and anti-shrinkage additives. The reactants used in the gel preparation had molar ratios of (M + R)/C of 135 and (M + R)/W of 0.052. By adding acetic acid or sodium carbonate, the final pH of the precursors was eventually adjusted to pH 7.4. The samples for the MRF series were created using a pre-polymerization procedure described elsewhere. For 1 hour at  $40^\circ\text{C}$ , a solution containing R, F, C, and (solution A) was stirred. Separately, at  $70^\circ\text{C}$ , a solution containing M, F, W, and C (solution B) was stirred for 30 minutes. Then, solutions A and B were mixed and stirred for 20 minutes at room temperature to allow the precursors to cross-link further [26].

Diatomite (50% w/v) and carbon black (ca.0.9wt %) were added before gelification, and k was required to ensure a homogeneous dispersion. Following the gelatine step, the hydrogels were supercritically dried with  $\text{CO}_2$  after a controlled water-acetone exchange. Finally, the carbon aerogels were carbonized in a nitrogen atmosphere to produce denser carbon aerogels [20].

### **6. Heat ablating materials**

#### **6.1 Phenolics-impregnated carbon ablators (PICA)**

Phenolics-impregnated carbon ablators (PICA), a carbon fiber preform impregnated in phenolics resin, is a modern thermal production system with the advantages of low density coupled with efficient ablative ability at high heat flux. It is a good choice for ablative applications such as high peak heating conditions found on the sample or lunar return missions. Phenolics-impregnated carbon ablators' thermal conductivity is lower than other heat flux ablative materials, such as conventional carbon phenolics [27].

PICA was the primary TPS material for the Stardust Aeroshell and was patented by NASA Ames Research Centre in the 1990s. The sample-return capsule Stardust was the fastest artificial object to re-enter Earth's atmosphere ( $12.4 \text{ km/s}$  ( $28,000 \text{ mph}$ ) at  $135 \text{ km}$  altitude), 70% faster than the Shuttle and the Apollo mission capsules. PICA was critical to the success of the Stardust mission, which returned to Earth in 2006. The heat shield on Stardust ( $0.81 \text{ m}$  base diameter) was made of one monolithic piece that could withstand a nominal peak heating rate of  $1.2 \text{ kW/cm}^2$ . A PICA heat shield was also used for the Mars Science

Laboratory's entry into the Martian atmosphere. During atmospheric entry, the resin and carbon fibers decay at different rates, resulting in distinct zones in the material.

- The virgin material, which has not decomposed.
- The char layer has entirely decomposed the resin. As the carbon fibers decompose, the heat shield contracts.
- The pyrolysis zone is formed by interpolating between the virgin and char layers.
- PICA-NuSil, also known as PICA-N, is a type of PICA. The addition of NuSil reduces the spread of phenolic dust found in PICA and improves the heat shield's integrity by making it more resistant to humidity and erosion [28].

PICA is a simple ablative TPS composed of a porous chopped carbon fiber preform infused with a high-surface area phenolic resin matrix. Because the phenolic infusion is at a low loading level, the final material is highly porous and has a low density. As a result, the ablative material is relatively efficient. The risk of massive cost or long endurance redevelopment for PICA required to support the next decade's priority planetary entry missions is currently rated low to moderate [29].

## **6.2 Ultra-high-temperature ceramic (UHTC) materials**

Ultra-high-temperature ceramic (UHTC) materials are a class of refractory ceramics that offer excellent stability at temperatures above 2000°C. They are being researched as potential thermal production system (TPS) coatings for material subjected to high temperatures and bulk material for heating elements. Borides, carbides, nitrides, and oxides of early transition metals are examples of ultra-high-temperature ceramics [30]. The current effects have concentrated on heavy, early transition metal borides like hafnium diboride ( $\text{HfB}_2$ ) and zirconium diboride ( $\text{ZrB}_2$ ). Hafnium nitride ( $\text{HfN}$ ), zirconium nitride ( $\text{ZrN}$ ), titanium carbide ( $\text{TiC}$ ), titanium nitride ( $\text{TiN}$ ), titanium dioxide ( $\text{TiO}_2$ ), tantalum carbide ( $\text{TaC}$ ), and their associated composites are other ultra-high-temperature ceramic materials under investigation for thermal production system (TPS) applications.

Due to the completion of Space Shuttle missions and the elimination of Air Force space plane development. However, a series of NASA programs in the 1990s aimed at developing a fully reusable hypersonic space plane, such as the National Aerospace Plane, Venture star/X-33, Boeing X-37, and the Air Force's Black star program, UHTCs were also increasingly used in a variety of settings, ranging from nuclear engineering to aluminum production [11]. NASA Ames conducted two flight experiments in 1997 and 2000 to test the real-world performance of UHTC materials in re-entry environments. By mounting them on modified nuclear ordnance Mk12A re-entry vehicles and launching them on Minuteman III ICBMs, the slender Hypersonic Aerothermodynamic Research Probes (SHARP B1 and B2) briefly exposed the UHTC materials to actual re-entry environments.

SHARP-B2 was recovered and included four retractable, sharp wedge-like protrusions called “strakes” that each contained three different UHTC compositions extended into the re-entry flow at different altitudes to improve the characterization of UHTC mechanical strength and better study their performance [15]. The SHARP-B2 test allowed the recovery of four segmented strakes, each with three sections made of a different HfB<sub>2</sub> or ZrB<sub>2</sub> composite. Despite impacting the sea at three times the predicted velocity, the vehicle was successfully recovered. Between 14 and 19 seconds into re-entry, four rear strake segments (HfB<sub>2</sub>) fractured, two mid components (ZrB<sub>2</sub>/SiC) cracked, and no fore strake segments failed [4].

The actual heat flux was 60% lower than predicted, the actual temperatures were much lower, and the heat flux on the rear strakes was much higher than expected. Material failures in composites and pure ceramics were caused by enormous grain sizes, with cracks following macroscopic crystal grain boundaries [16]. Because of their high melting points and good mechanical properties, UHTCs will become vital components as the next generation of spacecraft, and hypersonic flight applications are developed [12]. Only small, simple-shaped bulk UHTC components can be formed due to the limitations of current processing methods. UHTC coatings can be used to solve this problem. As C- and SiC-based composites become more widely used as structural components in aeronautics, protective coatings will be required to protect them from the harshest environments [31].

### **6.3 Toughened uni-piece fibrous reinforced oxidation composites (TUFROCs)**

The toughened uni-piece fibrous reinforced oxidation composite (TUFROC) allows space launch facilities and other frameworks that use earth re-entry vehicles to be much more affordable and sustainable. The TUFROC's exposed surface design and the appropriate material combination will allow a space vehicle to withstand both the mechanical stresses of initial ascent and the extreme heating and stress of re-entry. It provides a thermal production tile attachment system suitable for application to the leading edge of a space vehicle and other uses in extreme heating environments up to 36000°F, possibly higher for short intervals [3].

The variant of TUFROC tested and reported here was 0.4 g/cm<sup>3</sup>. It was created to operate at surface temperatures of around 2000 K. In conjunction with the ROCCI 4 cap, the graded surface treatment provides dimensional stability during high-speed entries. In contrast, the fibrous base insulation offers low thermal conductivity insulation to protect the vehicle structure [7]. The advantage of this low-cost, insulating composite over a re-entry vehicle with a sharp leading edge is increased cross-range capability due to reduced drag. The reinforced carbon-carbon (RCC) has large radii and operates at heat fluxes of less than 70 W/cm<sup>2</sup> during Earth entry. These systems are significantly heavier than TUFROC (1.6 g/cm<sup>3</sup> vs. 0.4 g/cm<sup>3</sup>), orders of magnitude more expensive, and require substantially longer fabrication lead times (**Figures 1–19**) [5].

When a lightweight fibrous TPS, such as TUF1-treated AETB, is applied to a vehicle's wing leading edge, it is susceptible to excessive recession during re-entry. Because of the temperature capability of the two-piece TUFROC TPS technology, lightweight fibrous insulation can be applied to a space vehicle's wing leading edge (**Table 1**) [32].

### 7. 3D view of space re-entry vehicle

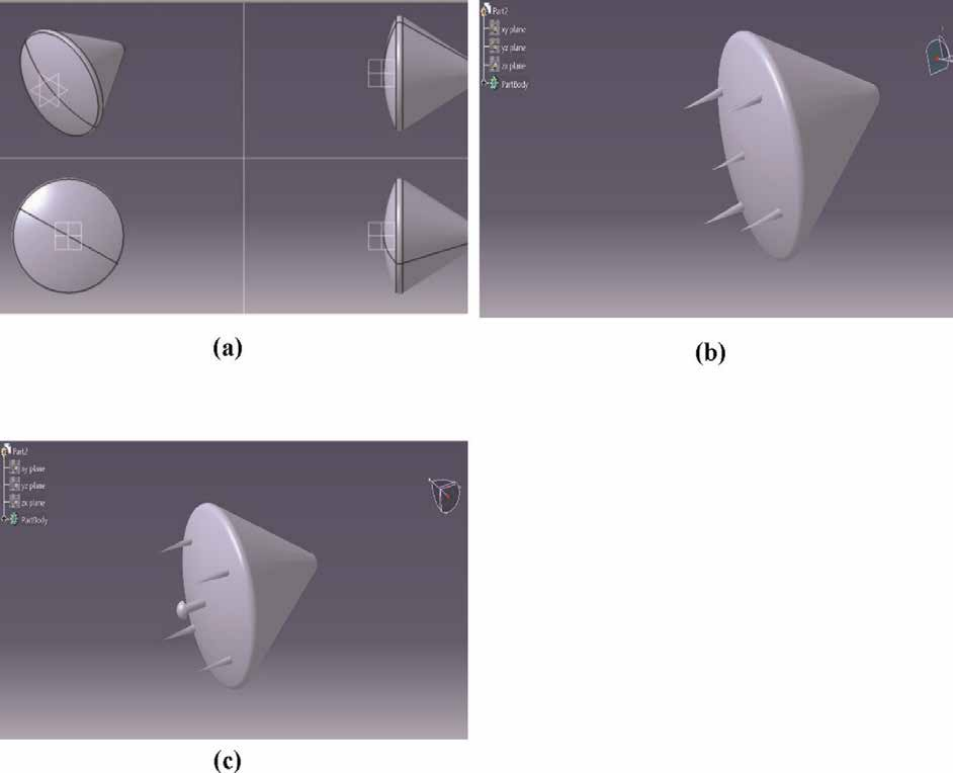


Figure 1. a. 3D view of space re-entry vehicle, b. with sharp spike, c. with blunt spike.

### 8. Result and discussion

#### 8.1 PICA

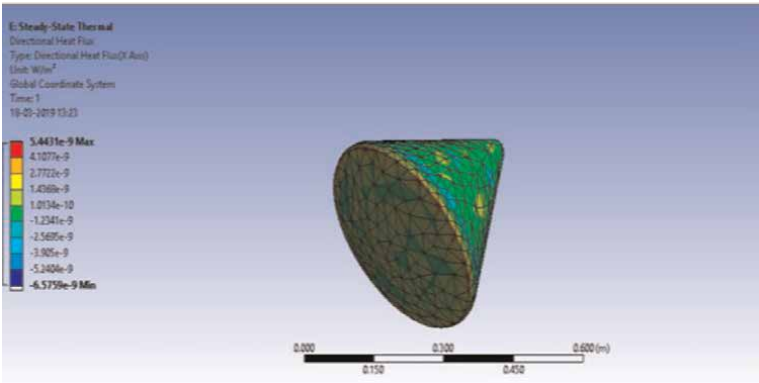
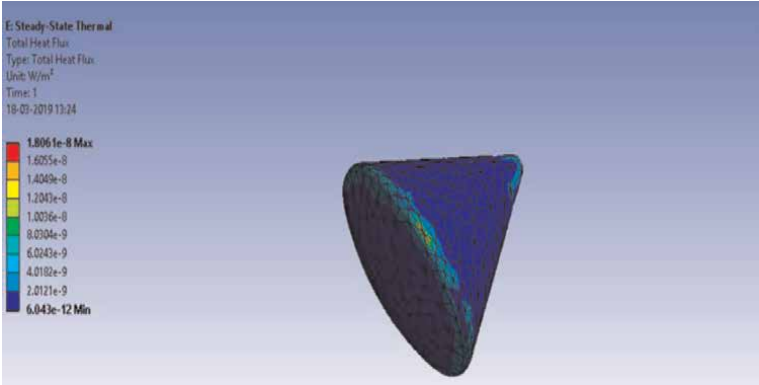
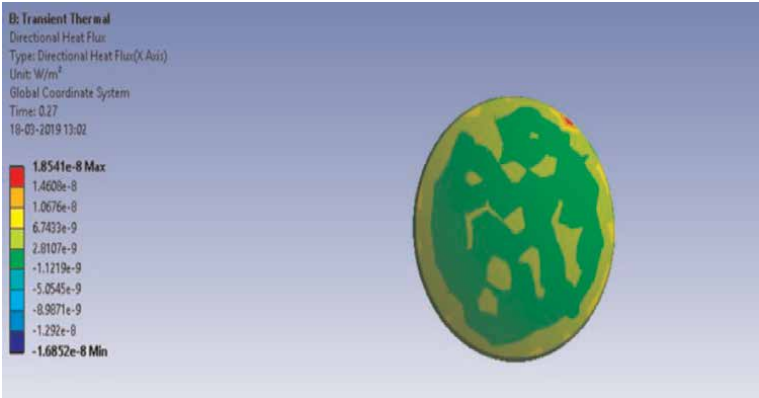


Figure 2. Directional heat flux steady state in PICA.



**Figure 3.**  
*Total heat flux steady state in PICA.*



**Figure 4.**  
*Directional heat flux transient in PICA.*

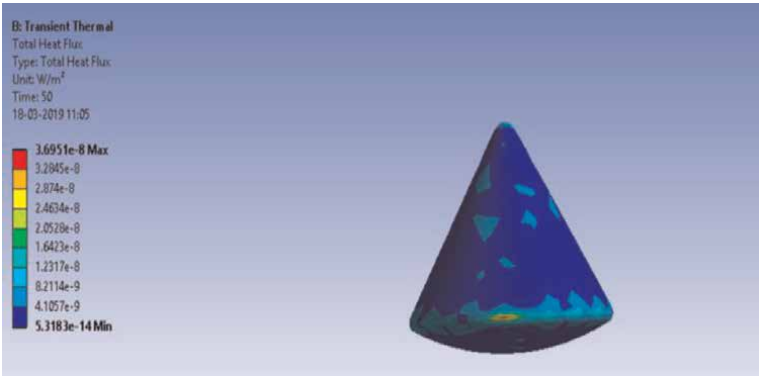


**Figure 5.**  
*Total heat flux transient in PICA.*

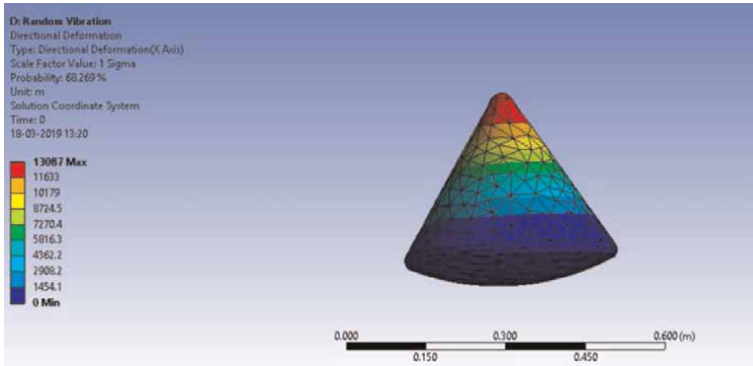


Figure 6.  
Directional deformation—vibration in PICA.

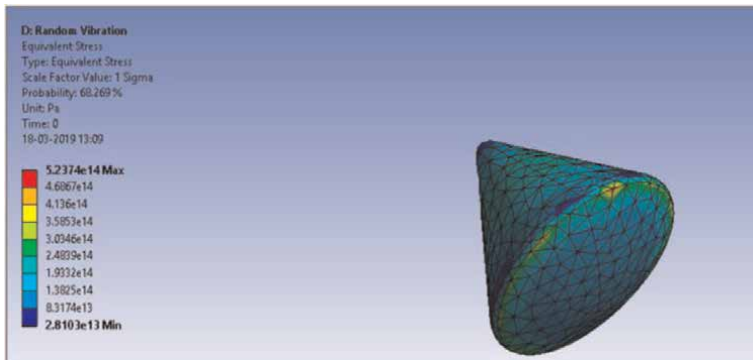


Figure 7.  
Equivalent stress—vibration in PICA.

## 8.2 TUFROC

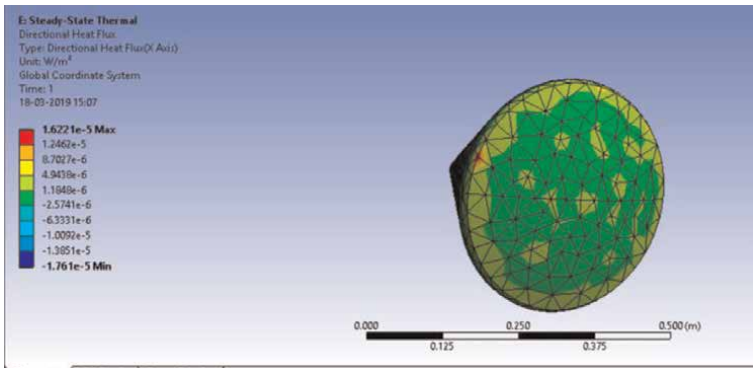
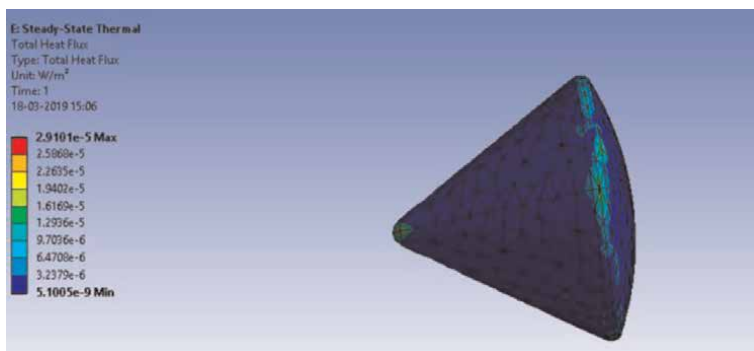
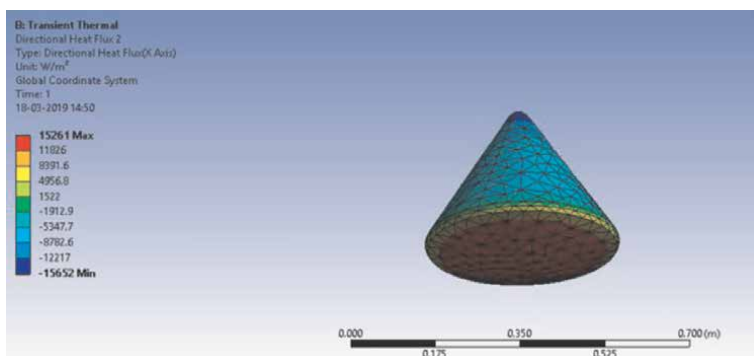


Figure 8.  
Directional heat flux steady state in TUFROC.



**Figure 9.**  
*Total heat flux steady state in TUFROC.*



**Figure 10.**  
*Directional heat flux transient in TUFROC.*

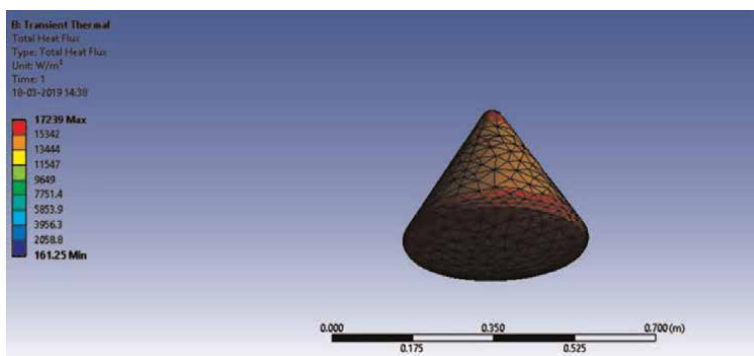


**Figure 11.**  
*Total heat flux transient in TUFROC.*

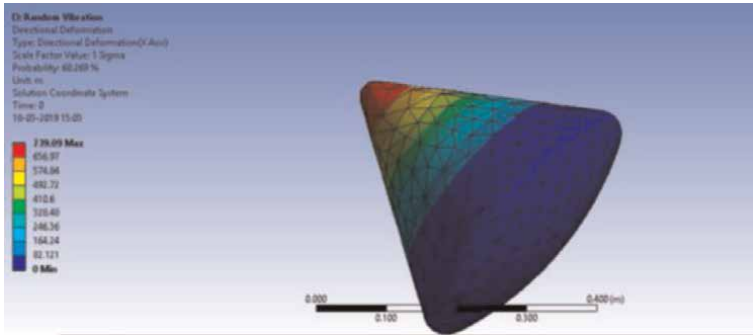


Figure 12.  
Directional deformation—vibration in TUFROC.

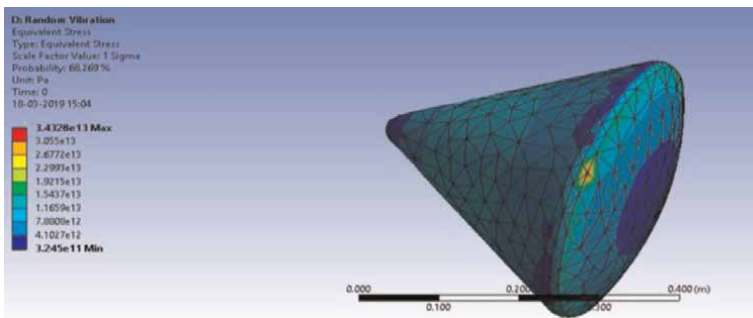


Figure 13.  
Equivalent stress—vibration in TUFROC.

### 8.3 UHTC

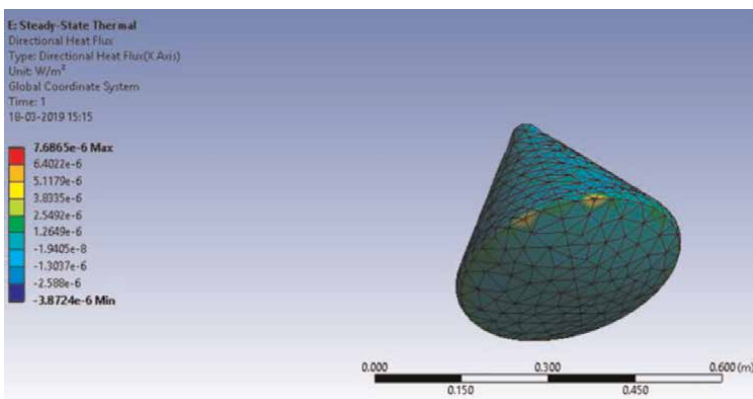


Figure 14.  
Directional heat flux steady state in UHTC.



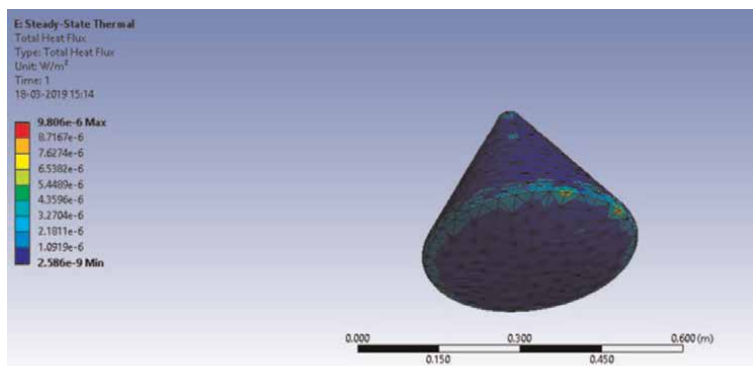


Figure 15.  
Total heat flux steady state in UHTC.

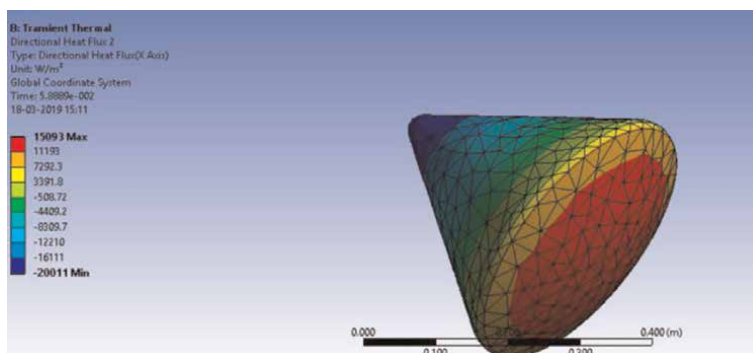


Figure 16.  
Directional heat flux transient in UHTC.

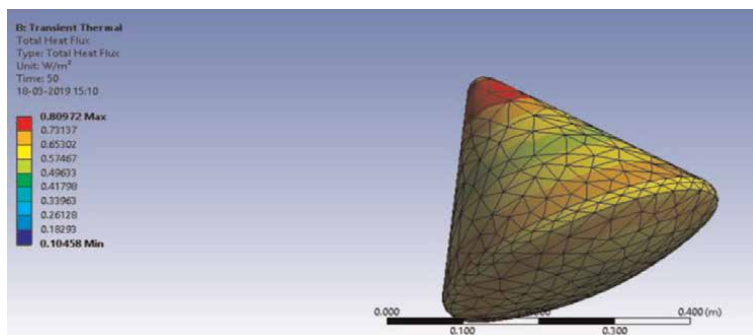
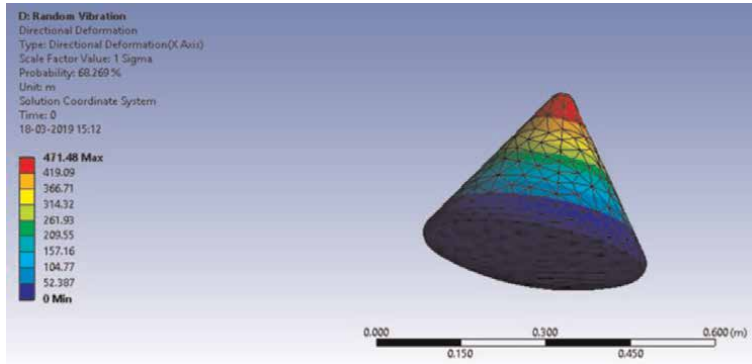
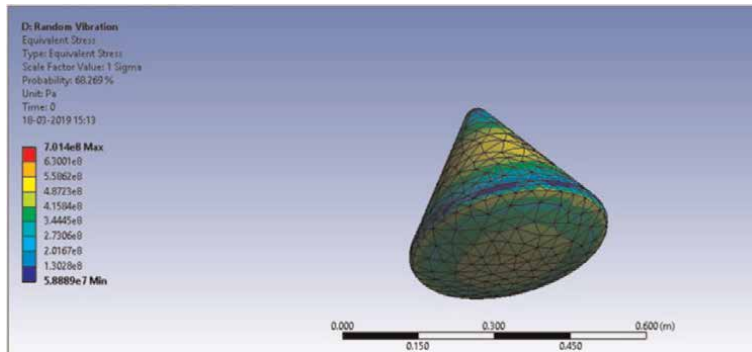


Figure 17.  
Total heat flux transient in UHTC.



**Figure 18.**  
Directional deformation—vibration in UHTC.



**Figure 19.**  
Equivalent stress—vibration in UHTC.

Properties	Ultra-high-temperature ceramic (UHTC) material	Toughened uni-piece fibrous reinforced oxidation composites (TUFROCs)	Silica aerogel
Poisson ratio	0.12–0.14	0.5	0.2
Young’s modulus	360 G pa	70 (or) 7 GPa	$10^6$ – $10^7$ N/m <sup>2</sup>
Density	6.10 g/cm <sup>3</sup>	0.27 g/cm	0.003–0.35 g/cm <sup>3</sup>
Temperature	Above 2000°C	3600°F(1982.22°C)	Above 1200°C
Thermal conductivity	75–105 w/mk	219–221 w/mk	0.5 W/mk
Isotropic resistivity	22 μ Ω cm	12–14 Ωcm	$1e^{23} \times 10^{-8}$ Ωm
Tensile ultimate strength	565 M Pa	4400 Mpa	45 to 155 Mpa
Compressive ultimate strength	6.14–12.5 M Pa	20.7Mpa	1100–1600 Mpa
Specific heat	56–83.8 Wm	1125 J/kg-k	330 K

**Table 1.**  
Mechanical properties of different materials.

## 8.4 Silica aerogel

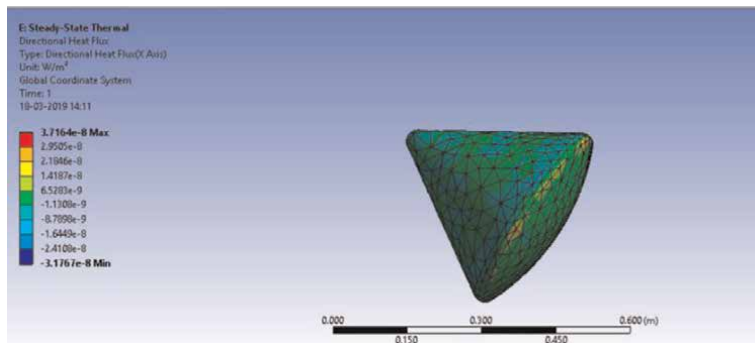


Figure 20.  
Directional heat flux steady state in silica aerogel.

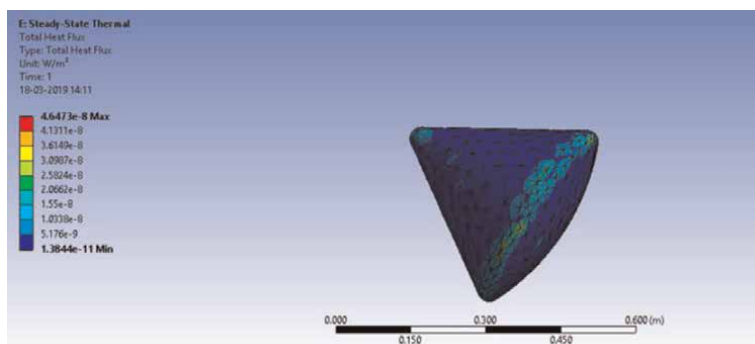


Figure 21.  
Total heat flux steady state in silica aerogel.

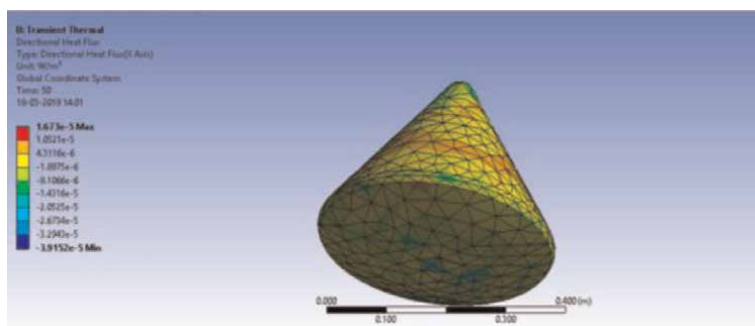
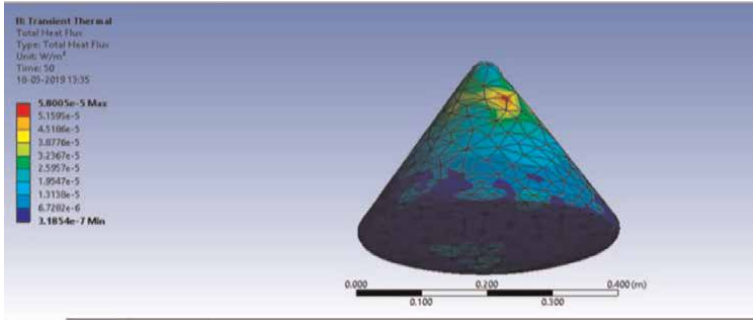
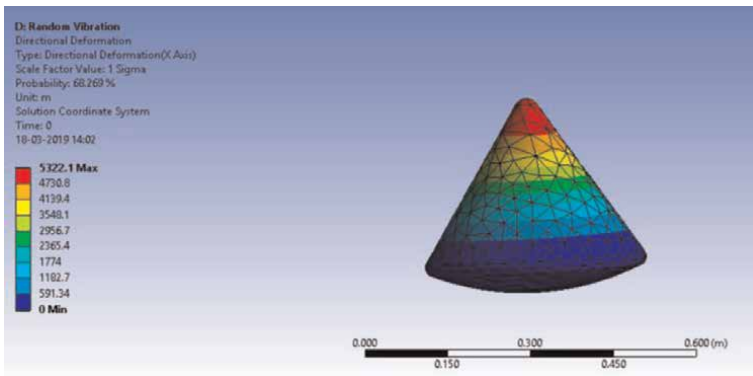


Figure 22.  
Directional heat flux transient in silica aerogel.



**Figure 23.**  
*Total heat flux transient in silica aerogel.*



**Figure 24.**  
*Directional deformation—vibration in silica aerogel.*

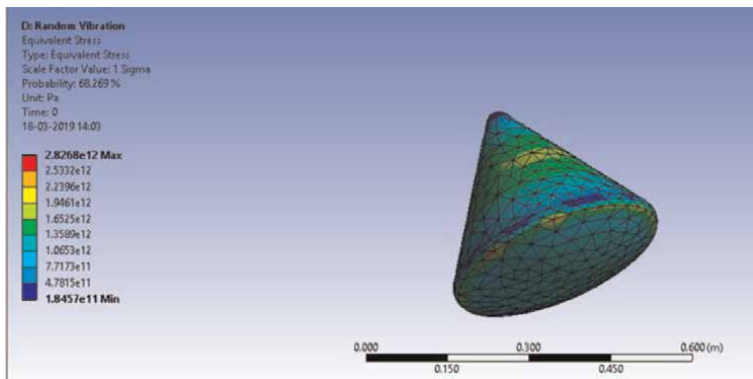


**Figure 25.**  
*Equivalent stress—vibration in silica aerogel.*

## 9. Resultant table

The 3D modeling of the re-entry vehicle, with sharp and sharp-blend, is designed in CATIA which is shown in **Figure 1a, b, and c**. We have done the steady-state thermal analysis, transient thermal analysis, and vibration analysis on the space re-entry vehicle to analyze their thermal and vibration properties. In the first case, we discussed the steady-state thermal analysis for PICA in **Figures 2 and 3**, for TUFROC in **Figures 8 and 9**, for UHTC in **Figures 14 and 15**, and for silica aerogel in **Figures 20 and 21**; from this analysis, the silica aerogel has a low heat transfer value of  $4.6473e^{-8} \text{ W/m}^2$  followed by PICA  $5.8061e^{-8} \text{ W/m}^2$  from **Table 2**, which shows these materials will withstand the high temperature compared to the other materials. The silica aerogel is lightweight and has a high temperature-resisting property next to UHTC and TUFROC. In the second case, we discussed the transient thermal analysis for PICA in **Figures 4 and 5**, for TUFROC in **Figures 10 and 11**, for UHTC in **Figures 16 and 17**, and for silica aerogel in **Figures 22 and 23**; this analysis also shows that silica aerogel has a low heat transfer value of  $5.8005e^{-5} \text{ W/m}^2$  from **Table 3**, followed by PICA  $3.6951e^{-4} \text{ W/m}^2$ , and the UHTC have  $0.80972 \text{ W/m}^2$ .

In the third case, we discussed the vibration analysis for PICA in **Figures 6 and 7**, for TUFROC in **Figures 12 and 13**, for UHTC in **Figures 18 and 19**, and for silica aerogel in **Figures 24 and 25**; from this analysis, the silica aerogel material has a high deformation sustaining the ability of  $5322.1 \text{ W/m}^2$  due to the vibration effects on space re-entry vehicles compared to PICA  $1308 \text{ W/m}^2$  from **Table 4**. This analysis shows that the silica aerogel can protect the parent material from the vibrations that occur during the re-entry into the atmosphere.

S. No	Directional heat flux steady state		Total heat flux steady state	
	Maximum ( $\text{W/m}^2$ )	Minimum ( $\text{W/m}^2$ )	Maximum ( $\text{W/m}^2$ )	Minimum ( $\text{W/m}^2$ )
UHTC	$7.6865e^{-6}$	$-3.8724e^{-6}$	$9.806e^{-6}$	$2.586e^{-9}$
PICA	$5.4431e^{-9}$	$-6.5759e^{-9}$	$5.8061e^{-8}$	$6.043e^{-12}$
TUFROC	$1.6221e^{-5}$	$-1.761e^{-5}$	$2.9101e^{-5}$	$5.1005e^{-9}$
SILICA AEROGEL	$3.7164e^{-8}$	$-3.1767e^{-8}$	$4.6473e^{-8}$	$1.3844e^{-11}$

**Table 2.**  
Heat flux steady-state thermal analysis.

S. No	Directional heat flux transient		Total heat flux transient	
	Maximum ( $\text{W/m}^2$ )	Minimum ( $\text{W/m}^2$ )	Maximum ( $\text{W/m}^2$ )	Minimum ( $\text{W/m}^2$ )
UHTC	15093	-20011	0.80972	0.10458
PICA	$1.8541e^{-4}$	$-1.685e-4$	$3.6951e^{-4}$	$5.3183e^{-14}$
TUFRO	15261	-15652	17239	161.25
SILICA AEROGEL	$1.673e^{-5}$	$-3.9132e^{-9}$	$5.8005e^{-5}$	$3.1854e^{-7}$

**Table 3.**  
Transient thermal analysis.

S. No	Directional deformation vibration		Equivalent stress vibration	
	Maximum (W/m <sup>2</sup> )	Minimum (W/m <sup>2</sup> )	Maximum (W/m <sup>2</sup> )	Minimum (W/m <sup>2</sup> )
UHTC	471.48	52.387	7.014e <sup>8</sup>	5.8889e <sup>7</sup>
PICA	1308	1454.1	5.237e <sup>14</sup>	2.8103e <sup>13</sup>
TUFROC	739.09	82.121	3.4328e <sup>13</sup>	3.245e <sup>11</sup>
Silica aerogel	5322.1	591.34	2.8268e <sup>12</sup>	1.8457e <sup>11</sup>

**Table 4.**  
Random vibration analysis.

## 10. CFD Analysis

### 10.1 Pressure contours

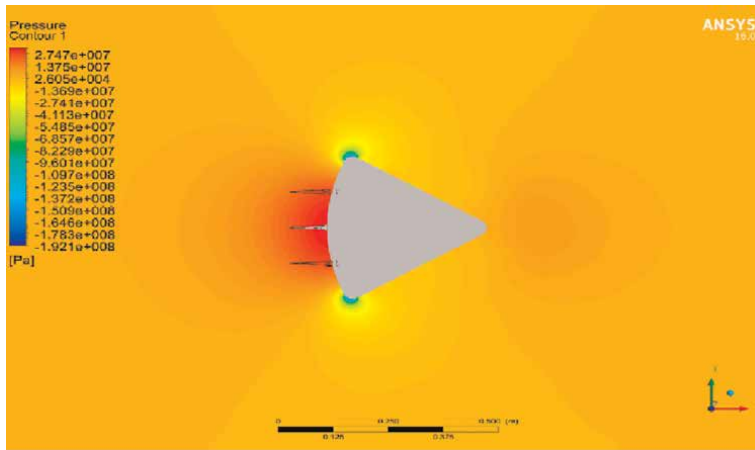


**Figure 26.**  
Sharp spike.

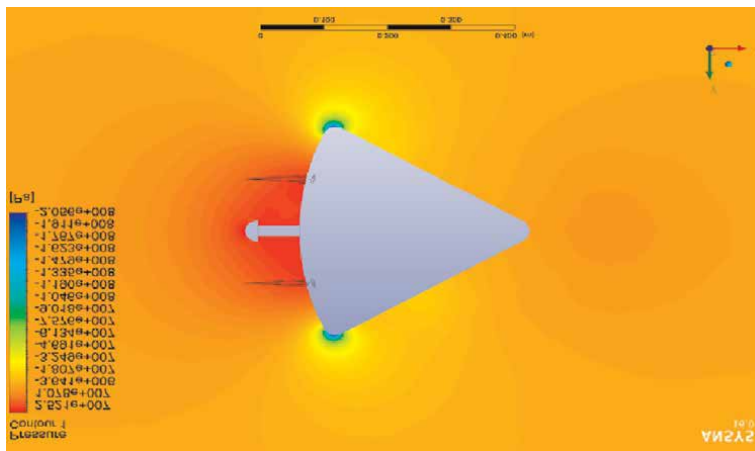


**Figure 27.**  
Sharp with blunt spike.

## 10.2 Velocity contours

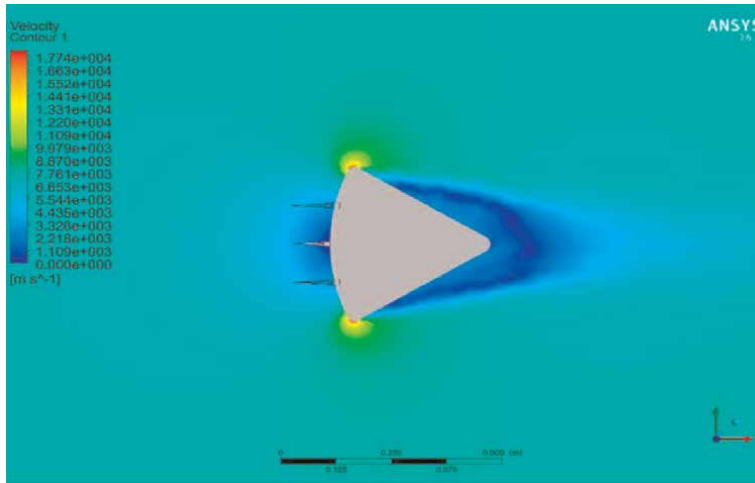


**Figure 28.**  
*Sharp spike.*

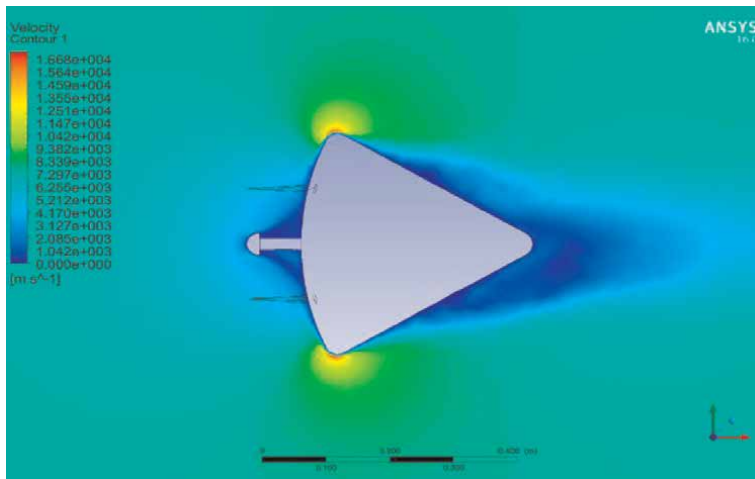


**Figure 29.**  
*Sharp with blunt spike.*

## 10.3 Streamline flow

The flow analysis has done for re-entry vehicles with sharp spike and sharp-blunt spike combinations to examine the pressure shown in **Figures 26** and **27**, velocity shown in **Figures 28** and **29**, and streamline patterns shown in **Figures 30** and **31**. This analysis finds drag coefficient and shockwave formations in these two combinations. The analysis shows that these two combination re-entry vehicles with the aero disk with sharp aerospike have a drag value of 38641.5 N and

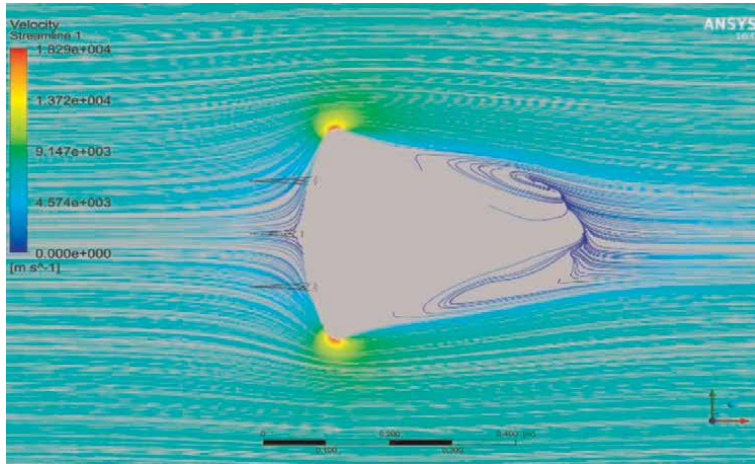


**Figure 30.**  
*Sharp spike.*

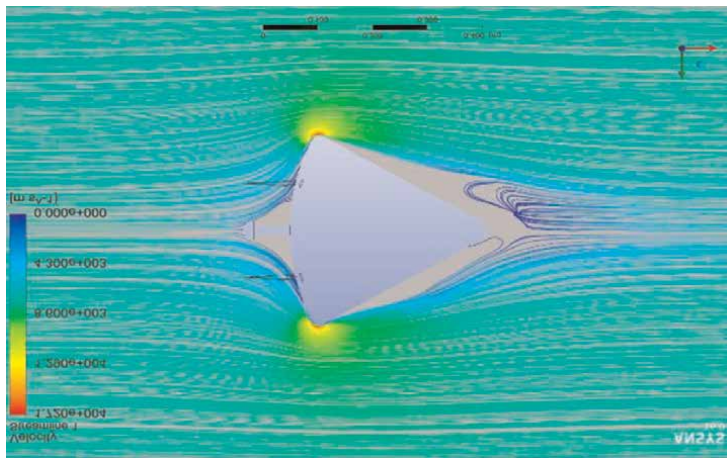


**Figure 31.**  
*Sharp with blunt spike.*

lift the value of 11288.4 N, significantly reducing drag formation and the formation of shock waves. Whereas the spike with sharp-blunt has a drag value of 225718 N and lifts the value of 104559 N, this reduces the drag but is lesser than the previous sharp spike.

## 11. Conclusion

In this work, we have analyzed the thermal and vibration effect on the space re-entry vehicle returning to the Earth's temperature. These materials withstand the high temperature produced on the space re-entry vehicle due to aero thermodynamic heating caused by shock waves. The silica aerogel is a lightweight material that can



withstand very high temperatures and has reduced wear and tear effects on the body of the space re-entry vehicle. Since silica aerogel material is not reacted with any other substance, by keeping silica aerogel as outer layer-1, PICA as layer-2, TUFROC as layer-3, and UHTC as an innermost layer-4, these sandwich-like layered structures will exhibit excellent heating ablating, vibration absorbing properties, and good durability so that it can be utilized as heat shielding materials for long time processes as that can reduce the cost of material used for the heat shield. Using an aerospike in a re-entry vehicle will reduce the strength of the shockwave formation. Thereby, there will be a better reduction in the aerothermodynamics heating. So, employment of aerospike in the re-entry vehicle will effectively reduce the cost due to structural damages and therefore, it will be an innovative and effective design concept for future developments.


## **Author details**

Pradeep Kumar Sular Loganathan  
Department of Aeronautical Engineering, KIT-Kalaignarkarunanidhi Institute of Technology, Tamil Nadu, India

\*Address all correspondence to: [pradeepzero1991@gmail.com](mailto:pradeepzero1991@gmail.com)

## **IntechOpen**

---

© 2022 The Author(s). Licensee IntechOpen. This chapter is distributed under the terms of the Creative Commons Attribution License (<http://creativecommons.org/licenses/by/3.0>), which permits unrestricted use, distribution, and reproduction in any medium, provided the original work is properly cited. 

## References

- [1] Chang FY, Weng HC. Hypersonic thermal flow past a spherically blunted tangent-ogive nose cone. *Journal of Chinese Society of Mechanical Engineering*. 2022;**43**(1):1-10
- [2] Wu J, Zhang Z, Hou A, Xue X, Cao X. Thermal aeroelastic characteristics of inflatable reentry vehicle experiment (IRVE) in hypersonic flow. *International Journal of Aerospace Engineering*. 2021; **2021**:1-17
- [3] Moreira FC, Wolf WR, Azevedo JLF. Thermal analysis of hypersonic flows of carbon dioxide and air in thermodynamic non-equilibrium. *International Journal of Heat and Mass Transfer*. 2021;**165**:1-19
- [4] Di Fiore F, Maggiore P, Mainini L. Multifidelity domain-aware learning for the design of re-entry vehicles. *Structural and Multidisciplinary Optimization*. 2021;**64**(5):3017-3035. DOI: 10.1007/s00158-021-03037-4
- [5] Di Caprio F et al. Damage tolerance evaluation of a C/C-SiC composite body flap of a re-entry vehicle. *Composite Structures*. 2021;**274**:114341
- [6] Farah E, Teschner T-R. Aerodynamic performance investigation through different chemistry modelling approaches for space re-entry vehicles using the DSMC method. In: *UKACM 2022 2022 Annu. Conf. UK Assoc. Comput. Mech. Nottingham, UK*. 2022
- [7] Delfini A et al. Thermal analysis of advanced plate structures based on ceramic coating on carbon/carbon substrates for aerospace Re-Entry Re-Useable systems. *Acta Astronautica*. 2020;**183**:153-161
- [8] Mallick A, Kapadia B, Arnold A. A brief discussion about reentry vehicles. *International Journal of Latest Engineering Management Research*. 2017;**02**(02):50-63
- [9] Ma H, Zheng X, Luo X, Yi Y, Yang F. Simulation and analysis of mechanical properties of silica aerogels: From rationalization to prediction. *Materials (Basel)*. 2018;**11**(2):1-12. DOI: 10.3390/ma11020214
- [10] Balakrishna B, Venkateswarlu S, Reddy PR. Flow analysis of an atmosphere re-entry vehicle. *International Journal of Engineering Research and Development*. 2012;**3**(4):2278-2267
- [11] Wuchina E, Opila E, Opeka M, Fahrenholtz W, Talmy I. UHTCs: Ultra-high temperature ceramic materials for extreme environment applications. *Electrochemical Society Interface*. 2007;**16**(4):30-36. DOI: 10.1149/2.f04074if
- [12] Krishna S, Student PG. Coupled field analysis of nose cone of a re-entry vehicle. *International Journal of Research & Computational Technology*. 2015;**7**(5):14-24
- [13] Bheekhun N, Abu Talib AR, Hassan MR. Aerogels in aerospace: An overview. *Advanced Materials in Science and Engineering*. 2013;**2013**:1-19
- [14] Prasanna Kumar TJ, Dharma Teja R, Rajesh R, Karthi AR. Transient thermal analysis on re-entry vehicle nose cone with tps materials. *International Journal of Aerospace in Mechanical Engineering*. 2016;**3**(6):6-15
- [15] Macias C et al. Synthesis of porous and mechanically compliant carbon aerogels using conductive and structural additives. *Gels*. 2016;**2**(1):1-16. DOI: 10.3390/gels2010004

- [16] Carandente V, Savino R, Iacovazzo M, Boffa C. Aerothermal analysis of a sample-return re-entry capsule. *Fluid Dynamic Material Process.* 2013;**9**(4):461-484. DOI: 10.3970/fdmp.2013.009.461
- [17] Raju M. CFD analysis of mars phoenix capsules at Mach number 10. *Journal of Aeronautical Aerospace Engineering.* 2015;**04**(01):4-7. DOI: 10.4172/2168-9792.1000141
- [18] Shaid A, Furgusson M, Wang L. Thermophysiological comfort analysis of aerogel nanoparticle incorporated fabric for fire fighter's protective clothing. *Chemical Materials Engineering.* 2014; **2**(2):37-43
- [19] Thapliyal PC, Singh K. Aerogels as promising thermal insulating materials: An overview. *Journal of Materials.* 2014;**2014**:1-10. DOI: 10.1155/2014/127049
- [20] Hoseini A, McCague C, Andisheh-Tadbir M, Bahrami M. Aerogel blankets: From mathematical modeling to material characterization and experimental analysis. *International Journal of Heat and Mass Transfer.* 2016;**93**:1124-1131. DOI: 10.1016/j.ijheatmasstransfer.2015.11.030
- [21] Ibrahim M et al., Aerogel-based coating for energy-efficient building envelopes To cite this version: HAL Id : hal-01112594. 2015
- [22] Jelle BP, Baetens R, Gustavsen A. Aerogel insulation for building applications. *Sol-Gel Handbook.* 2015; **3-3**:1385-1412. DOI: 10.1002/9783527670819.ch45
- [23] Patel RP, Purohit NS, Suthar AM. An overview of silica aerogels. *International Journal of ChemTech Research.* 2009; **1**(4):1052-1057
- [24] Cohen E, Glicksman L. Thermal properties of silica aerogel formula. *Journal of Heat Transfer.* 2015;**137**(8):111
- [25] Zhao Z, Wang X, Qiu J, Lin J, Xu D. Three-dimensional graphene-based hydrogel. *Aerogel Materials.* 2014;**36**: 137-151
- [26] Chakraborty S, Pisal AA, Kothari VK, Venkateswara Rao A. Synthesis and characterization of fibre reinforced silica aerogel blankets for thermal protection. *Advanced Materials in Science and Engineering.* 2016; **2016**:1-9
- [27] Tsioulou O, Erpelding J, Lampropoulos A. Development of novel low thermal conductivity concrete using aerogel powder. 2016
- [28] Venkatapathy E et al. Sustaining mature thermal protection systems crucial for future in-situ planetary missions. *Bulletin AAS.* 2021;**53**(4):7. DOI: 10.3847/25c2cf.8dd247ac
- [29] Ford K, Meurisse MJ, Thornton J. Sensitivity Analysis of PICA and PICA-N Using PATO and DAKOTA. 2021
- [30] Arenas JP, Crocker MJ. Recent trends in porous sound-absorbing materials. *Sound & Vibration.* 2010; **44**(7):12-18
- [31] Lynam A, Romero AR, Xu F, Wellman RW, Hussain T. Thermal spraying of ultra-high temperature ceramics: A review on processing routes and performance. *Journal of Thermal Spray Technology.* 2022;**31**(4):745-779. DOI: 10.1007/s11666-022-01381-5
- [32] Lin MF. Thermal properties of carbon toroids. *Journal of the Physical Society of Japan.* 1999;**68**(11):3585-3591. DOI: 10.1143/JPSJ.68.3585



# Design and Performance of Hypersonic Intake for Scramjet Engine

*Juluru Sandeep*

## Abstract

Rockets are the only vehicles to reach hypersonic speeds with non-airbreathing engines carrying both fuel and oxidizer increasing budget of space exploration. So, the desire to achieve hypersonic speeds at low cost has led to the development of air-breathing engines known as supersonic combustion ramjet engines or scramjet engines. The most complex part in the development of the scramjet engine is the intake. Free-stream hypersonic speed flow will be compressed in intake and processed into the combustor as per the required pressure and temperature. The high-pressurized flow can be provided to the combustor based on the strength of shocks attained in the intake due to ramps. So, the design of intake depends on the number of ramps and the angle of ramp, which decides the strength of shock for compression. All the scramjet intakes designed based on oblique shock theory will start efficiently in the designed conditions, but the main problem is unstating the performance of intake at off-design conditions. It is very important to know the flow behavior at off-design conditions to enhance the operating range of the engine. So, in this chapter, a detailed procedure for the design of hypersonic intake and techniques to mitigate the unstating conditions of scramjet engines is discussed.

**Keywords:** intake, shock wave angle, deflection angle, Kantrowitz limit

## 1. Introduction

The major parts of scramjet engine and the flow process is shown in **Figure 1**. Scramjet engine propels the vehicle at hypersonic speeds, that is, at  $M > 5$ . The scramjet combusts the flow at supersonic speeds; thus, the free-stream hypersonic flow has to be reduced to supersonic speeds through air-intake, which compresses the flow [1]. The performance of a scramjet-powered hypersonic vehicle is determined by its air-intake efficiency as the engine depends very much on the quantity and quality (uniformity and total pressure) of the flow required for its smooth performance. As speeds increased, the simple inlets used in the early years could no longer provide efficient compression and still produce meaningful thrust, because the total pressure loss incurred was too great. New techniques are needed to be found in order to

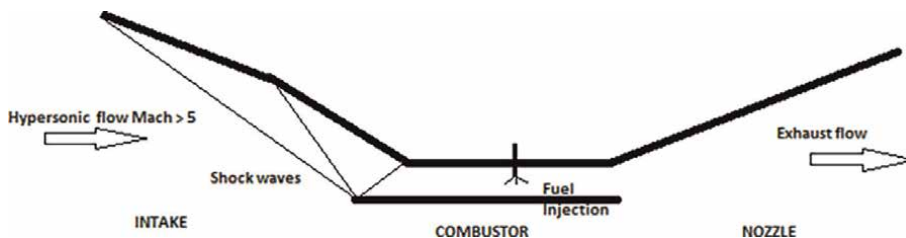


**Figure 1.**  
*Schematic diagram of scramjet engine geometry.*

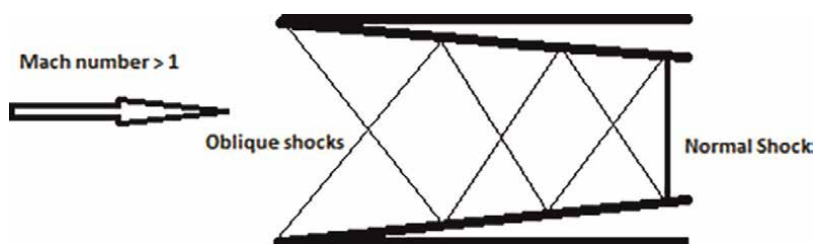


**Figure 2.**  
*Example of an internal compression inlet.*

improve the efficiency of inlets. The use of oblique shocks was a likely answer to the question, but the exact technique for use was not as clear. Emerging from this idea were the internal, external, and mixed compression inlets (**Figures 1 and 2**).

### 1.1 Internal compression inlet

In an internal compression inlet, the shocks are first reflected inwards from a wall toward the centerline of the inlet, similar to that shown in **Figure 2**. This guarantees that at least one shock wave-boundary-layer interaction will occur, not counting those for the normal shock. Some form of boundary layer control is needed to make these inlets effective, but these are uncommon on aircraft because of the complexity required in the design, and the need for multiple operating point designs.

### 1.2 External compression inlet

External compression inlets, like that shown in **Figure 3**, have been the “go-to” solution for many years. They are the simplest in principle but have some complexity in their design, and variable geometry is needed for these inlets. The plates, the bleed, and the mechanisms for the variable geometry ramps tend to increase weight, and are the enemy of performance in all aircrafts. So, while the system worked, improvements could be made to make designs rely less on their heavy features. The bleed and mass spillage also add a fair amount of drag to the inlet, since subsonic air needs to be discharged into a supersonic free stream. In external compression inlets, there is not an oblique shock boundary-layer interaction, rather bleed is needed at the root of the oblique shock to help control the separation that occurs.

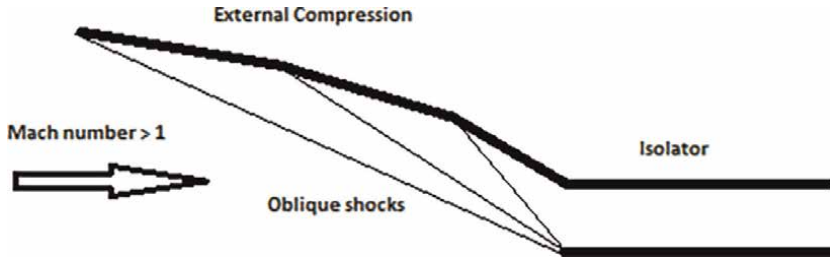


Figure 3.  
Sketch of an external compression inlet.

### 1.3 Mixed compression inlet

A mixed compression inlet, like that shown in **Figure 4**, combines both the internal and external compression inlets. Initially, one or more oblique shocks form that miss the inlet lip (like an external compression inlet). After that, one or more shocks reflect inward toward the centerline of the inlet (like an internal compression inlet). This type of inlet is generally used only for higher Mach number aircraft ( $M = 2.5$  and above) because of the increased design complexity. Very few of these high Mach aircraft have been made, with the SR-71 as the only one ever in production. However, mixed compression inlets have been used for several experimental aircrafts, such as the X-43a and the XB-70. The number of oblique shocks used in inlets has slowly increased over time. At first, a single oblique shock was used, but the Mach number was relatively small, approximately 1.6. As top speeds increased, to Mach numbers above 2, two shocks started to be used as well as variable geometry ramps to adjust shock angles and shock standoff distance. The F-14 and F-15 were some of the first to use a set of three oblique shocks in their inlet capture systems. The theory states that the more oblique shocks in the inlet, the lower the total pressure loss through the compression system.

### 1.4 Hypersonic intakes

Mixed compression intake is used for the design of hypersonic intakes. It is a blend of external and internal compression. The main function of intake is to compress the flow and supply the required pressurized flow to the combustor following a bow shock

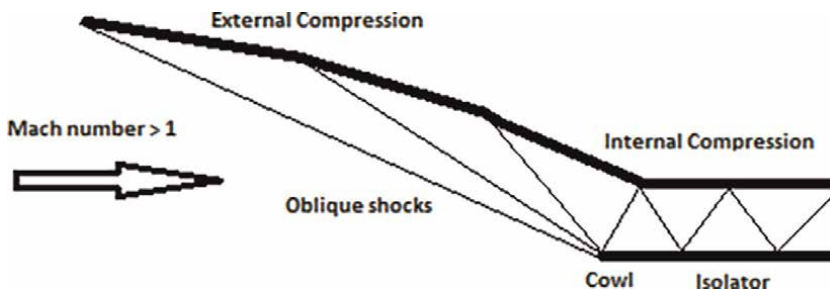


Figure 4.  
Sketch of mixed compression inlet.

at the forebody of the vehicle and the multiple number of oblique shocks through the ramps of internal and external compression. These waves will coalesce at the cowl leading edge for the design of Mach number satisfying shock-on-lip condition. As the flow deflects through the several ramps of external compression, thus the flow is deflected back into the axial direction through reflected shocks and cowl leading edge shock in the internal compression region and isolator. The reflected shocks interact with the boundary layer of the walls, such as ramp, cowl, and isolator. This interaction leads to a flow separation region, and the level of separation is influenced by the strength of the reflected shock and the thickness of the boundary layer along wall surfaces.

Scramjet engine starting Mach number is 5. So, the engine has to be integrated with turbojet and ramjet to achieve Mach 5 speed. The intake of the scramjet engine has to be designed to withstand shock waves due to the hypersonic speed of Mach 5. The intake starts efficiently at the designed condition but at off-design conditions, it leads to the “unstarting problem,” which means the flow turns to subsonic due to normal shock or shock wave boundary-layer interaction. So, the starting and unstarting of hypersonic intake play a vital role in knowing the operating range of the scramjet engine.

### **1.5 Starting of intakes**

The inlet total pressure recovery, including both shock and viscous losses, is the governing factor determining the starting of these inlets; this is in contrast to the generally accepted criterion of considering contraction ratio based only on normal-shock pressure recovery, which is applicable to inlets with relatively thin boundary layers. Although boundary-layer separation in the vicinity of the cowl lip station does not appear to directly govern starting by adversely affecting the contraction ratio, it does significantly affect the inlet pressure recovery by increasing the viscous losses through mixing. The geometric and aerodynamic parameters investigated also affect starting by their effect on the pressure recovery. The total-pressure recovery required for starting these inlets can be predicted reasonably well by a one-dimensional analysis; however, at present, there is no accurate means of predicting the total-pressure recovery, accounting for separation and viscous losses as well as internal shock losses, for a given configuration. Basic data are provided, which can be used to verify future empirical or theoretical methods to predict inlet-pressure recovery, and thus starting conditions.

### **1.6 Unstart of intakes**

Unstarting of intake is the major challenge of hypersonic intake, which is to be addressed. It describes the choked flow due to a very low area ratio of the throat to intake with an increase in Mach number. Mostly, the unstart of the intake is detected through the ejection of the shock system and spillage of mass flow, which leads to reduced pressure recovery and also huge distortion in the flow. This type of flow phenomenon will lead to a catastrophic effect on the scramjet performance.

The unstart of the intake is due to numerous reasons, such as over contraction, off-design conditions, fluctuations in operation of the combustor, and back pressure, or maybe because of the combined result of these factors. One of the major causes for unstarting is flow separation due to shock wave-boundary-layer interaction and develops the boundary-layer thickness in the isolator duct. Generally, supersonic intakes use a bled system, and varying intake geometry by cowl angle is used to start intake. Because of high enthalpy and total temperature in hypersonic flows, the



mechanical designed control methods have to sustain severe structural problems and need cooling techniques.

## **2. Design of hypersonic intake**

The design of hypersonic intake is a very complex method because of multiple shocks in the intake. So, the design procedure should consider the adoption of oblique shock relations. The subsequent intake geometry has to undergo the possibility of starting flow characteristics. If the intake fails to start, then the design has to be changed.

The design of hypersonic intake has to consider the following points:

1. The starting Mach number of intake should be less than the cruise Mach number, and the flow should be uniform while entering into the combustor over a wide range of flight envelope.
2. The intake has to satisfy Oswatitsch and Kantrowitz criteria.
3. The shocks from ramps should be of equal strength with minimum total pressure loss.
4. The design should be flexible to have good performance in off-design conditions also.
5. The geometry has to be easily analyzed using analytical and computational methods.
6. The mass flow spillage should be minimum without affecting starting of intake.
7. The design of intake has to ensure minimum external drag.
8. The aerodynamic stability of intake depends on the forces generated in all directions due to changes in the angle of attack. So, these forces must be as small as possible.
9. The designed intake has to sustain extensive acceleration, large internal pressure, and huge heat transfer without varying geometry of intake.

The known fact is that a better range of intake starting is attained with a less Mach number and has low efficiency with adequate thrust designed for the missile/vehicle to launch from its parent engine than an intake starts with a high Mach number for high efficiency. This emphasizes the efficiency of the intake and its performance parameters will not be the deciding negotiators in the selection of intake for a definite mission. A detailed study of these negotiations and trade-offs should be analyzed along with other engine parameters for designed conditions, which does not lead to the finest performance but somewhat needs design negotiations to enhance the scramjet mission requirements.

The intake is made into three divisions and named ramps, cowl, and isolator. In intake, the compression process taken due to ramps by shocks is known as external

compression and compression due to cowl, and isolator by the reflection of a series of shocks is known as internal compression. The isolator is a constant area duct that functions to reduce the disturbances in the flow caused due to combustion process and mitigates it to further propagation toward the cowl and forebody of intake. So, the design of three components fulfills the design of intake.

The design of the intake gives the efficiency and performance of the intake. The design starts with requirements of scramjet for combustion process, such as the amount of pressure, that is, compression with minimum total pressure loss and drag. Michel K Smart has stated a minimum of 50 is required for scramjet to attain hypersonic speeds [2]. Thus, as this amount of compression cannot be achieved by a single ramp, the number of internal and external shocks will decide the number of ramps for the design of intake. This illustrates the dependence of intake performance on the number of shocks, but the isentropic condition restricts the number of shocks. Furthermore, the number of shocks will increase the number of ramps with lower deflection angles and increase the length of the intake adding drag and weight to the scramjet. Considering above points to simplify the design of intake, it is divided into two sub-steps, (i) deflection and shock wave angles, and (ii) intake geometry.

## 2.1 Deflection angle ( $\theta$ ) and shock wave ( $\beta$ ) angles

The Oswatitsch criterion says to improve the efficiency of the intake and the shocks should be of equal strength to generate an equal pressure ratio throughout multiple shocks [3]. So, the intake compression efficiency depends on deflection and shock wave angles, which are by using gas dynamic relations with the following iterative procedure.

The free-stream Mach number of the scramjet intake is  $M_1$  and the throat Mach number should not be less than half of the free-stream Mach number to evade the flow separation as given by Mahoney [4].

The two stages of intake, external compression and internal compression corresponding flow deflection angles, are calculated separately. The design of both stages is independent excluding the static pressure ratio, which is the combined effect of the compression process in both stages. To attain minimum total pressure loss across a shock, weak shocks with a low static pressure ratio are preferred. This leads to low deflection angles. So, in this iterative procedure, the initial static pressure ratio ( $P_2/P_1$ ) assumed is 0.01 and total pressure ratio ( $P_{t2}/P_{t1}$ ) is 1.0, and the respective shock wave angle, deflection angle, and Mach number across the shock wave are found with the input of the free-stream Mach number using the following oblique shock relations.

The pressure ratio is given by:

$$\frac{P_2}{P_1} = 1 + \frac{2\gamma}{\gamma + 1} (M_{n1}^2 - 1) \quad (1)$$

$$M_{n1} = M_1 \sin \beta \quad (2)$$

Substitute Eq. (2) in Eq. (1).

$$\beta = \sin^{-1} \left[ \sqrt{\frac{\left(\frac{P_2}{P_1} - 1\right) \left(\frac{\gamma+1}{2\gamma}\right) + 1}{M_1^2}} \right] \quad (3)$$

Eq. (3) gives shock wave angle for a given Mach number. To find the deflection angle the  $\theta$ - $\beta$ -M relation is used.

$$\tan\theta = 2\cot\beta \left[ \frac{M_1^2 \sin^2\beta - 1}{M_1^2 (\gamma + \cos^2\beta) + 2} \right] \quad (4)$$

The static pressure ratio from Eq. (1) for the former shock wave is fixed with reference to the Oswatitsch criterion and further used for the subsequent shocks and the properties across each shock wave are calculated by using the above oblique shock relations. This procedure is repeated for all the shocks in the external compression. Once all the calculations for each and every shock wave are done, the Mach number behind the last external shock wave is compared with the defined Mach number after the external compression, that is,  $M_e$ . If both are not matching, then the above procedure has to be iterated continuously by step-by-step increase in the static pressure ratio till the Mach number after external compression matches with  $M_e$ . The turning angles for the external compression are concluded if the above condition is satisfied.

Similarly, the turning angles of the internal compression are also calculated using the same iterative procedure assuming the static pressure ratio obtained after external compression as the initial guess. This iteration process is repeated continuously to match the exit Mach number of internal compression to half of the free-stream Mach number by an increase in the static pressure ratio. The actual static pressure ratio and total pressure ratio of the intake are obtained by multiplying the properties considering all the shock waves of both internal and external compressions. Optimum turning angles are generated for maximizing the total-pressure recovery for given operating conditions.

Now, the second step in the design process of intake is to find the linear dimensions of intake, such as lengths of the ramps and height, which fixes the location of the shocks for the compression. While calculating the lengths, shock-on-lip condition is to be considered, which means the shocks from ramps have to impinge on the cowl at the same point as shown in **Figure 5**. In the **Figure 6**, points a, b, and c are for the external

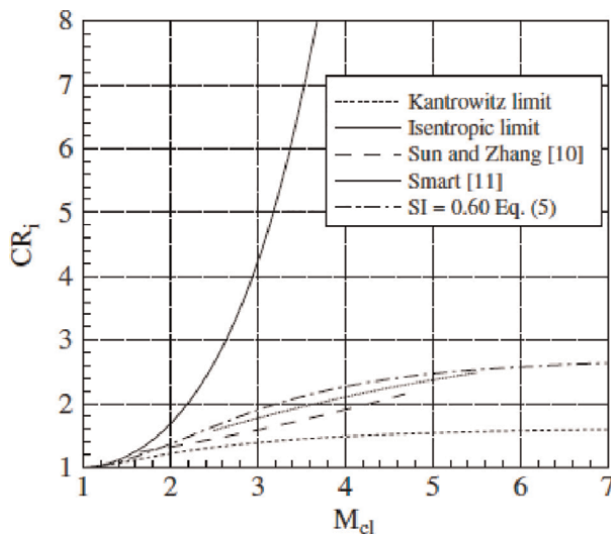


**Figure 5.** Plot against internal contraction ratio and cowl Mach number using empirical relations [5].

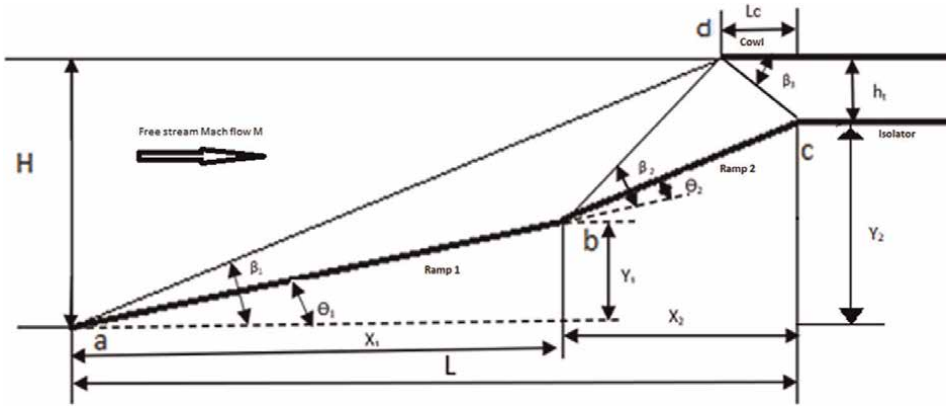


**Figure 6.**  
Schematic diagram of scramjet intake with geometrical parameters.

ramp, and points d and e are for the cowl. The ramps and cowl together will generate two external shocks and one internal shock. However, the number of shock waves is of any number of combinations with respect to external/internal compression satisfying the pressure requirement for combustion.

Deflection angles for first, second ramps, and cowl are denoted by  $\theta_1$ ,  $\theta_2$ ,  $\theta_3$ , and shock wave angles are  $\beta_1$ ,  $\beta_2$ ,  $\beta_3$ , respectively, which are calculated using oblique shock relations as stated in the design procedure.

## 2.2 Linear dimensions of scramjet intake

In the performance of intake, drag estimation is an important parameter and the length of the intake leads to skin friction drag, and also, the external/internal oblique shocks have to intersect at the cowl leading edge point to avail maximum capture area to reduce the spillage drag or losses satisfying shock-on-lip condition. Point d is the leading-edge point of the cowl known as the cowl lip at which the external shocks meet. To reduce the intake length, point d is chosen as the point where the first external oblique shock meets the horizontal line drawn from e. Similarly, all the internal shocks meet at shoulder point c. The trigonometric relations are used to calculate the length of ramps, cowl, and coordinates of the intake geometry, and the procedure is as follows:

From the isentropic limit of contraction ratio, that is,  $CR_{isen}$ .

$$CR_{isen} = \frac{A}{A^*} = \frac{1}{M} \left[ \frac{2}{\gamma + 1} \left( 1 + \frac{\gamma + 1}{2} M^2 \right) \right]^{\frac{\gamma + 1}{2(\gamma - 1)}} \quad (5)$$

From Kantrowitz limit the contraction ratio is  $CR_{kantr}$ .

$$CR_{kantr} = \frac{A}{A^*} = \left[ \frac{(\gamma + 1)M^2}{(\gamma - 1)M^2 + 2} \right]^{0.5} \left[ \frac{(\gamma + 1)M^2}{2\gamma M^2 - (\gamma - 1)} \right]^{\frac{1}{(\gamma - 1)}} \quad (6)$$

In the intakes, the external compression considers the overall contraction ratio with respect to free stream Mach number, and for the internal contraction ratio, Mach number close to cowl is chosen. The internal contraction is given as the ratio of the

cowl cross stream area to the throat area and variation of  $CR_i$  with respect to Mach number is shown in **Figure 5**.

$$CR_i = \frac{A_{cl}}{A_t} \quad (7)$$

Kantrowitz criterion gives an important design parameter of intake, that is, the isolator height using the above relations. It has been categorized into three regions based on the contraction ratio values as follows:

- i. If  $CR > CR_{i\text{isentr}}$  in which the starting of intakes is impossible;
- ii. If  $CR < CR_{K\text{antr}}$  in which the self-starting of intakes is possible according to the Kantrowitz theory;
- iii. The intakes work efficiently once it is started and this is a critical region.

Based on the above CR value for a given Mach number for a 2-dimensional design CR can be considered with respect to height at the respective locations.

$$CR_i = \frac{A_{cl}}{A_t} = \frac{h_{cl}}{h_t} \quad (8)$$

The length of the cowl is given by the following:

$$\tan(\beta_3) = \frac{h_t}{L_c} \quad (9)$$

Assume the value of the length of intake  $L$ , and calculate the height  $H$  using the following relation:

$$\tan(\beta_1) = \frac{H}{L - L_c} \quad (10)$$

$$x_1 = \frac{H - (L - L_c) * \tan(\beta_2 + \theta_1)}{\tan \theta_1 - \tan(\beta_2 + \theta_1)} \quad (11)$$

$$y_1 = x_1 \tan \theta_1 \quad (12)$$

$$x_1 + x_2 = L \quad (13)$$

$$\tan(\theta_1 + \theta_2) = \frac{y_2 - y_1}{x_2} \quad (14)$$

$$y_2 = y_1 + x_2 * \tan(\theta_1 + \theta_2) \quad (15)$$

With the above relations, we can calculate the first and second ramp points, that is,  $(x_1, y_1)$  and  $(x_2, y_2)$ .

### 3. Performance of scramjet intake

Scramjet intake performance is evaluated with respect to its total pressure ratio and kinetic energy efficiency. These two are the performance parameters derived

based on quasi-one-dimensional flow through the Intake. In **Figure 1**, the free-stream flow is indicated by station 0, that is, the captured free-stream flow before the compression, and station 3 in the figure indicates the downstream flow through the internal compression of intake and followed by the isolator connecting to the combustor. The flow properties at all stations are used to calculate performance parameters.

### 3.1 Total-pressure recovery, $\pi_c$

Total-pressure recovery,  $\pi_c$ , is defined as the ratio between the total pressure at station 3 to the total pressure at station 0. It establishes the loss in total pressure due to shock waves in the internal and external compression process. The total pressure recovery parameter indicates the sum of total pressure loss due to each shock wave. Total-pressure recovery is also severely inclined by shock wave-boundary-layer interactions, and to a slighter range by the viscous loss as the flow deteriorates due to the no-slip state at the surface of the ramps, isolator, or cowl walls. The following equation is used to calculate  $\pi_c$ :

$$\pi_c = \frac{p_{t3}}{p_{t0}} \quad (16)$$

### 3.2 Kinetic energy efficiency, $\eta_{KE(ad)}$

Kinetic energy efficiency,  $\eta_{KE(ad)}$ , is defined as the ratio of the kinetic energy of the flow at station 3 to the kinetic energy of the free-stream flow, if it stayed to be expanded isentropically to free-stream pressure. This parameter quantifies the productivity of the compression process with respect to energy supervision. In scramjet engine, the kinetic energy possessed at hypersonic speeds is enough to produce the required thrust by enhancing the flow velocity through the nozzle. The loss in kinetic energy due to compression will obviously affect the thrust and efficiency of the engine. The equation for calculating  $\eta_{KE}$  is:

$$\eta_{KE} = 1 - \left( \frac{2}{\gamma - 1} \right) \left( \frac{1}{M_0^2} \right) \left[ \left( \frac{T_x}{T_0} \right) - 1 \right] \quad (17)$$

$$T_x = T_{03} \left( \frac{p_0}{p_{03}} \right)^{\frac{\gamma-1}{\gamma}} \quad (18)$$

### 3.3 Compression process efficiency, $\eta_{C(ad)}$

The overall efficiency and specific impulse of the engine depend on the efficiency of the compression process,  $\eta_{C(ad)}$ . The overall compression efficiency gives the amount of energy used up during the compression process. It is defined as the ratio of the total energy of the flow at station 3 to the initial energy of the flow captured at station 0 from free stream. This value of  $\eta_{C(ad)}$  is calculated by:

$$\eta_{c(ad)} = 1 - \frac{(\gamma - 1)M_0^2}{2} \left( \frac{1 - \eta_{KE(ad)}}{\frac{T_3}{T_0} - 1} \right) \quad (19)$$

## 4. Challenges in scramjet intake at off-design conditions

The scramjet intake works efficiently at designed conditions but the major challenges that come across at off-design conditions are shock wave-boundary-layer interactions (SBLI), flow spillage, etc. Out of these problems SBLI is very harmful to the structure of intake and starting of intake. So, in this section, a detailed explanation about the formation of SBLI and the methods are suggested to mitigate the flow separation due to SBLI.

### 4.1 Shock wave-boundary-layer interactions

Shock wave-boundary-layer interactions are a phenomenon when a shock wave meets a boundary layer and it can be found in most of high-speed flows. The typical case of SBLI is when a generated shock wave impinges on a surface where the boundary layer is developed as shown in **Figure 7**. As a result, the shock imposes a severe adverse pressure gradient toward the boundary layer causing it to eventually thicken and creating the possibility of separation. In most cases, SBLI also causes flow unsteadiness. The consequences of the phenomena are found to be detrimental, especially in high-speed flows. In hypersonic flows, SBLI causes intense localized heating due to high Mach numbers that can be severe enough to destroy the body of the aero vehicle.

### 4.2 SBLI control mechanisms

It seems almost impossible to avoid the occurrence of SBLI in any practical applications; hence, this leads to the idea of developing control mechanisms by manipulating the flow either before or during the interaction itself. The objectives of the control mechanisms are to prevent shock-induced separation and also stabilize the oscillating shock. The momentum of the turbulent boundary layer appears to be an important factor affecting the upstream turbulence of the shock as well as the resistance of the boundary layer toward separation. Hence, by increasing the incoming boundary layer momentum prior to the interaction with the shock proves to be one of the beneficial mechanisms. This can be done using several boundary layer manipulation techniques listed below.

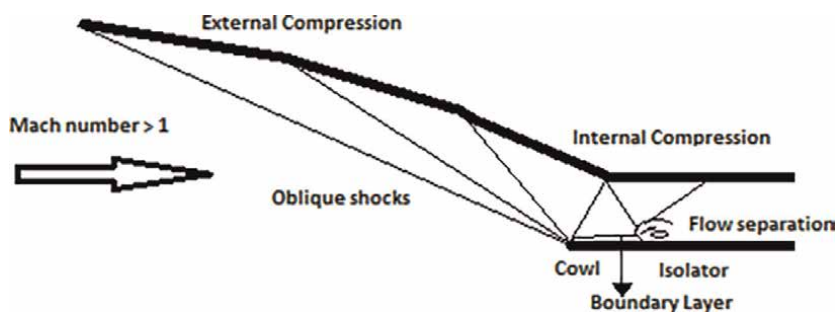


**Figure 7.** Schematic diagram of shock wave-boundary-layer interactions in a typical hypersonic inlet [1].

#### 4.2.1 Bleed system

Currently, this is one of the most popular techniques due to its effectiveness. The introduction of the bleed system is aimed to suppress the boundary-layer separation induced at the impinging of shock wave with boundary layer by removing the low momentum portion of the boundary layer as shown in **Figure 8**. This is achieved through different designs, such as holes, porous wall sections, slots, and scoops, which are distributed at designated locations predicted for boundary-layer separations in which SBLIs are likely to occur. The locations are along the compression ramp, cowl, and sidewall of the intake (**Figure 8**).

Numerical investigation of different bleed models for a mixed compression inlet has been reported by Mizukami et al. [6] and Vivek and Mittal [7]. Gawienowski conducted a series of experiments with different bleed slot sizes and mass flow rates to assess the performance of an external compression intake at supersonic speeds [8]. Pressure recovery and distortion levels were estimated and it was found that increasing the bleed slot area as well as the bleed mass flow increases the intake performance. The selection of bleed hole geometry and its inclination for an effective and efficient bleed system are reported by Syberg et al. [9]. The effect of the different bleed systems at various locations on hypersonic intake is studied by Pandian et al. [10]. Shock wave-boundary-layer with bleed slot interaction studies were reported by Hamed et al. [11]. The bleed system can be introduced in the following ways:

- Mass injection
- This is done by applying fluid injection through a porous plate or several slots positioned upstream of the shock impingement location.
- Distributed suction
- This is applied at a certain distance upstream (usually specified in the scale of the boundary-layer thickness,) of the shock impingement. This will lower the shape parameter; and produces a fuller velocity profile and a more robust boundary layer toward separation.
- Localized suction

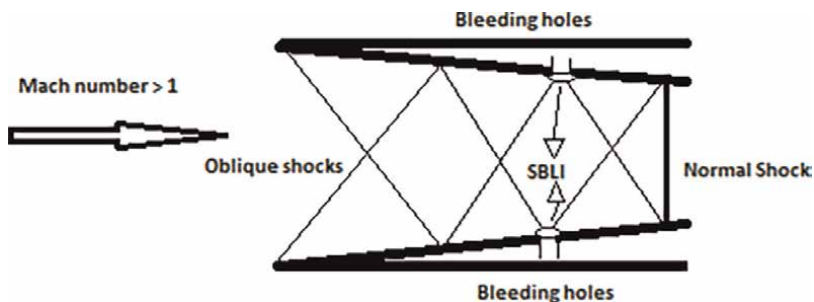


**Figure 8.**  
*Internal compression inlet with bleed holes.*



- This type of suction is applied locally inside the interaction region or in the immediate vicinity. It is done by drilling holes perpendicularly to the surface.

#### 4.2.2 Cowl bending

The cowl of intake is deflected to attain a variable intake geometry angle to enhance the operating range of intake as analyzed by Das and j. k. Prasad [12]. The analysis is carried out to understand the flow phenomenon and performance characteristics of intake with permissible exit flow and back pressure. For permissible exit flow, increasing the deflection angle of the cowl will increase the performance, but due to pressurized flow at the exit, a small change in the angle of the cowl in the direction of  $2^\circ$  enhances the performance. But for subsequent flow separation in the bigger region of the intake because of back pressure, the flow will be distorted at the intake exit.

#### 4.2.3 Vortex generators

The vortex generator devices are placed upstream of the shock and produce counter-rotating vortices that transfer high momentum flow from the outer region into the low momentum flow near the wall. This will produce a more energize boundary layer and high resistance to an adverse pressure gradient. Flow field analysis inside the mixed compression inlet was found to be within acceptable tolerances of the available data by Vivek V. Kumar and Surendra Bogadi [13]. There was little variation in the flow field results between inviscid and laminar flows and it was due to the low molecular viscosity at the altitude considered and consequently a thin boundary layer. The line and contour plots presented in the report have given a considerable amount of information on the nature of the flow field existing within the inlet. The comparison between the mixed inlet and the inlet with MVG shows the thinning of separation occurring in the case of the mixed inlet with MVG. The amount of pressure is also gaining in the case of MVG and thereby proper compression for efficient combustion (**Figure 9**).

#### 4.2.4 Micro-ramps

The micro-ramp is a novel flow control device that is a part of the micro-vortex generator family. It has recently shown great potential in controlling adverse

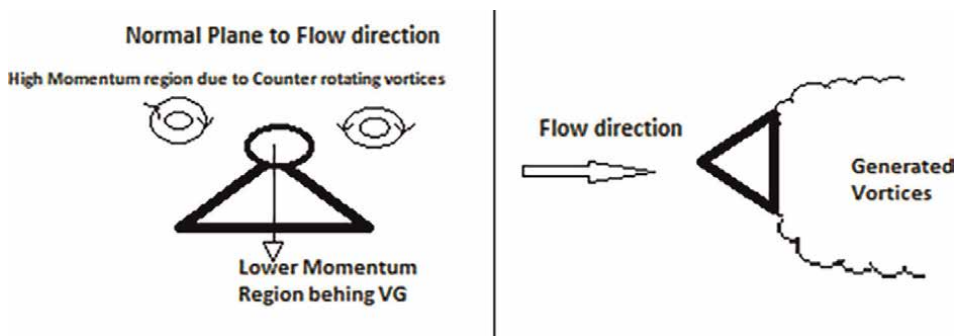


**Figure 9.**  
*Flow over vortex generators in normal plane and along flow direction.*

phenomena. The term micro relates to the device having a height less than the boundary-layer thickness. In most present literature, the height range of the micro-ramp is between 30% and 90% of boundary-layer thickness. Due to the small size, the micro-ramp is embedded inside the boundary layer, hence reducing the parasitic drag compared with the conventional full-size vortex generator.

The study on the effect of the micro-ramp height was done by Babinsky et al. [14]. It was shown that the height has little effect on the fundamental flow development specifically in the region downstream of the device. After comparing experimental results of different heights from both surface flow visualization and pressure ratios, it can be deduced that the main flow features a real most identical. When comparing the stream-wise effect, all of the micro-ramps with different heights also showed similar development in momentum exchange behavior.

The flow development however similar but still vary with height. Ashill et al. [15] also agree with this conclusion and stated that flow by smaller devices develops and evolves more quickly than larger devices. Hence, high momentum fluid is moved to the near-wall regions in a shorter period of time. Therefore, practically it would be beneficial to locate smaller devices in certain regions that require more flow control.

#### *4.2.5 Stream-wise vortices*

Shock wave-boundary-layer interaction control by air jet stream-wise vortices was studied by Ryszard Szwaba [16]. This shows that stream-wise vortices influence the static pressure level downstream of the shock wave, which implies the reduction of separation. The vortices cause the entertainment of higher momentum fluid into the lowest sub-layers of a boundary layer, which counteracts separation.

## **5. Conclusions**

This chapter explains the importance of intake to achieve hypersonic speeds by a scramjet engine. Scramjet is the only air-breathing engine, which mostly depends on the quality of air given for combustion by intake to achieve hypersonic speeds. So, the major focus is given on the design of hypersonic intake for scramjet engine with an analytical method for preliminary design. The chapter also emphasizes on the performance parameters of a scramjet. The importance of shockwave-boundary-layer interaction and its effects on starting of intake are explained with methods to control it.

## **Acknowledgements**

The author is very much thankful to the Department of Aero Engineering, School of Engineering and Technology, and Management of Sandip University for providing the facilities to write this chapter.

## **Appendices and nomenclature**

M     Mach number  
p     Pressure (Pa)

T Temperature (K)  
 $\beta$  Shock wave angle relative to flow direction upstream of shock

## Degrees

$\gamma$  Air-specific heat ratio  
 $\eta_{C(ad)}$  Compression process efficiency  
 $\eta_{KE(ad)}$  Kinetic energy efficiency  
 $\pi_c$  Total-pressure recovery  
 $\theta$  Flow turning angle relative to initial flow direction (degree)  
H Height of intake  
L Length of intake  
 $h_t$  Height of isolator  
 $L_c$  Length of cowl  
 $A_{cl}$  Area near cowl  
CR Contraction ratio  
SBLI Shock wave-boundary-layer interaction

## Subscript

t Stagnation flow condition  
x x-coordinate  
y y-coordinate  
0 Station 0 at free-stream  
3 Station 3 at isolator exit  
\* Entrance of isolator


## Author details

Juluru Sandeep  
Department of Aero Engineering, Sandip University, Nashik, Maharashtra, India

\*Address all correspondence to: [julusandeep@gmail.com](mailto:julusandeep@gmail.com)

## IntechOpen

---

© 2022 The Author(s). Licensee IntechOpen. This chapter is distributed under the terms of the Creative Commons Attribution License (<http://creativecommons.org/licenses/by/3.0>), which permits unrestricted use, distribution, and reproduction in any medium, provided the original work is properly cited. 

## References

- [1] Heiser WH, Pratt DT. Hypersonic Air Breathing Propulsion. AIAA; 1993. pp. 251-257
- [2] Smart MK. How much compression should a scramjet inlet do? AIAA Journal. 2012;**50**(3):610-619
- [3] Oswatitsch K. Pressure Recovery for Missiles with Reaction Propulsion at High Supersonic Speeds (the Efficiency of Shock Diffusers). NACA, TM 1140 (translation). USA: NASA Technical Reports; 1947
- [4] Mahoney JJ. Inlets for Supersonic Missiles. Washington DC: AIAA Education Series; 1993
- [5] Flock AK, Gülhan A. Modified Kantrowitz starting criteria for mixed compression supersonic intakes. AIAA Journal. 2019;**57**(5)
- [6] Mizukami M, Saunders JD. Parametrics on 2D navier-stokes analysis of a Mach 2.68 rectangular bifurcated mixed compression inlet. AIAA Paper, AIAA95-2755. 1995
- [7] Vivek P, Buzz SM. Instability in a mixed-compression air intake. Journal of Propulsion and Power. 2009;**25**(3):819-822
- [8] Gawienowski JJ. The effect of Boundary layer Removal through throat slots on the internal performance of a side inlet at Mach number of 2.0 and 2.3. NASA Technical Memorandum, NASA TM-X-502
- [9] Syberg J, Konesek JL. Bleed system design technology for supersonic inlets. Journal of Aircraft. 1973;**10**(7):407-413
- [10] Pandian S, Jose J, Patil MM, Srinivasa P. Hypersonic Air-Intake performance improvement through different bleed systems. ISABE. 2001; **2001-1039**
- [11] Hamed A, Shih S, Yeuan JJ. Investigation of shock/turbulent boundary layer interactions. Journal of Propulsion and Power. 1994;**10**(1):16
- [12] Das S, Prasad JK. Characteristics of a supersonic air - Intake with bleed. In: International Conference on Aerospace and Science. 2008. pp. 70-73
- [13] Kumar VV, Bogadi S. Effect of micro-vortex generator in hypersonic inlet. International Journal of Applied Research in Mechanical Engineering. 2011;**1**(1)
- [14] Babinsky H, Li Y, Ford CWP. Microramp control of supersonic oblique shock-wave/boundary layer interactions. AIAA. 2009;**47**(3):668-675
- [15] Ashill PR, Fulker JL, Hackett KC. A review of recent developments in flow control. Aeronautical Journal. 2005;**109** (1095):205-232
- [16] Szwaba R, Flaszynski P, Szumski J, Telega J. Shock wave - boundary layer interaction control by air-jet streamwise vortices. In: 8th International Symposium on Experimental and Computational Aerothermodynamics of Internal Flows: Conference Proceedings, Lyon, France. Vol. 2, No. 2. Peer reviewed collective publishing house by Duke University Press; 2007. p. 548

# Clean and Sustainable Hydrogen-Electric Propulsion

*Xin Gao and Chengwei Zhao*

## Abstract

For future hypersonic and supersonic flight, clean, sustainable and energy-efficient propulsion should be addressed in the general background of the sensational clean electric transition of aircraft. This chapter is to draw the attention of the research communities on the possible feasibilities and challenges of hydrogen-electric propulsion in hypersonic and supersonic flight. This chapter is structured with the following aspects, (1) general design and hybridisation concepts of hydrogen-electric propulsion for general aircraft and their hypersonic and supersonic considerations; (2) merits of hydrogen-electric propulsion on thermofluids process integrations; (3) potential merits of hydrogen-electric propulsion projected through thermofluids structural engineering and re-engineering; (4) storage options and their challenges in design and operation; and (5) reliability considerations.

**Keywords:** hydrogen, cryogenic, electric propulsion, fuel cells, system design, operation

## 1. Introduction

Hydrogen has been considered a very promising clean, sustainable energy source for a long time. In recent decades, it has come back into the limelight [1]. Due to the current world situation, accompanied by changes in the climate and the increase in the price of traditional fossil energy sources, aircraft urgently needs a new propulsion technology to reduce polluting emissions and lower fossil fuel consumption [2]. Hydrogen propulsion is, therefore, widely seen as a solution to the current situation because of its renewable nature and the effective reduction of carbon dioxide emissions [3]. There are currently four mainstream hydrogen propulsion: (1) all-electric fuel cell propulsion, (2) fuel cell propulsion and complementary direct-drive hydrogen turbines, (3) hydrogen-fuelled turbofan electric propulsion and (4) pure combustion propulsion [4]. The mission range of the aircraft still determines the efficiency of these concepts. In the medium to long range, fuel cells will be more advantageous [5]. However, fuel cells still face more challenges in being used as an aviation application. Because of its lower power-to-weight ratio, the system's complexity [6] and the inconvenience of hydrogen storage and waste heat management [7] are all issues that need to be addressed. However, current trends suggest that aircraft capable of full hydrogen fuel cell propulsion remains the ultimate goal of long-term research. The

challenges related to the application of hydrogen fuel cells in aviation are described in detail in Section 3, along with current research and future perspectives.

## **2. Fuel cell principles**

A fuel cell is an energy conversion device that converts chemical energy stored in fuels and oxidisers into electrical energy through a redox reaction based on electrochemical principles. The fuel cell itself does not store energy; it is, like the internal combustion engine, a device that converts chemical energy into other forms of energy using 'fuel'. An internal combustion engine produces heat by burning fuel, and thermodynamic energy is converted into kinetic energy. On the other hand, a fuel cell has electrical power through an electrochemical reaction, and the electrical energy produced can be converted into other energy as required, such as mechanical energy through an electric motor. In this respect, it is more like a battery with a fuel tank. However, unlike conventional batteries, it does not require charging time, only refuelling, and it could have a higher energy density than traditional batteries especially on the system level. And the device itself produces no noise or vibrations in the workshop, and this electrochemical reaction does not produce pollutants that are harmful to the climate [8].

### **2.1 Working principle**

The fuel cell consists of four main components: the anode, the cathode, the electrolyte, and the external circuit. Fuel gas and oxidation gas are fed through the anode and cathode of the fuel cell separately. The fuel gas emits electrons at the anode, which are transferred to the cathode via an external circuit and combined with the oxidation gas to form ions. The ions migrate through the electrolyte to the anode under the influence of an electric field and react with the fuel gas, forming a circuit and generating an electric current. At the same time, the fuel cell generates some heat due to its electrochemical reaction and the cell's internal resistance. In addition to conducting electrons, the cathode and anode of the cell act as catalysts for redox reactions (**Figure 1**).

### **2.2 Fuel cell types**

There are numerous classifications of fuel cells, commonly based on the type of electrolyte, including proton exchange membrane fuel cells (PEMFCs), alkaline fuel cells (AFCs), phosphoric acid fuel cells (PAFCs), molten carbonate fuel cells (MCFCs), and solid oxide fuel cells (SOFCs) [9]. In addition, different variants of these types have been developed, such as the direct methanol fuel cell (DMFC), which is based on LT-PEMFC but uses methanol and the high-temperature (HT-)PEMFC, in which the phosphoric acid is stabilised in a polymer membrane. Proton ceramic fuel cells (PCFCs) have many similarities to SOFC but use proton-conducting electrolyte materials [10].

The Proton Exchange Membrane Fuel Cell (PEMFC), also known as the Polymer Electrolyte Membrane Fuel Cell, was invented by General Electric in the late 1950s and used in NASA space missions [11]. The electrolyte is a very thin polymer membrane in this type of cell. This polymer membrane conducts protons but not electrons, thus ensuring ion exchange between the electrodes. Generally, proton exchange membrane fuel cells use platinum on carbon (Pt/C) as the catalyst for the cathode reaction (**Figure 2**).

The different membrane materials determine the specific conditions of use. LT-PEMFCs operate between 65°C and 85°C, which offers the possibility of using water

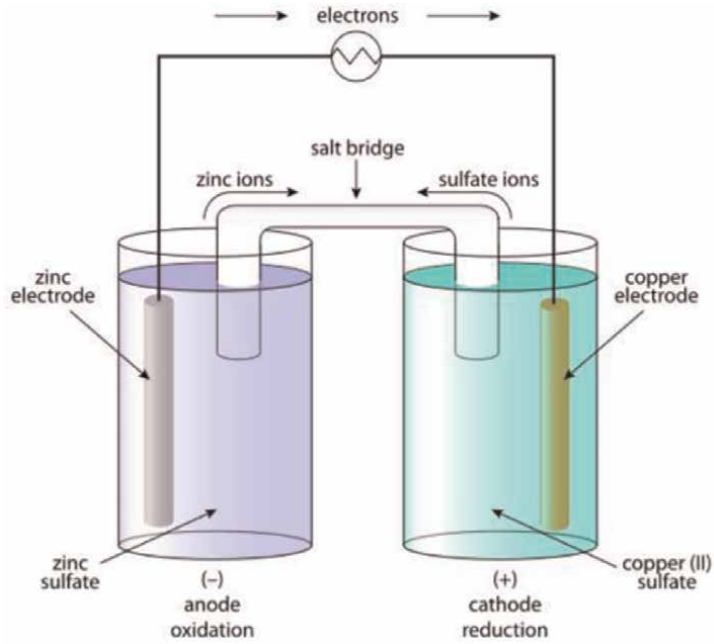


**Figure 1.**  
*Simplified schematic of the working principle of a fuel cell.*

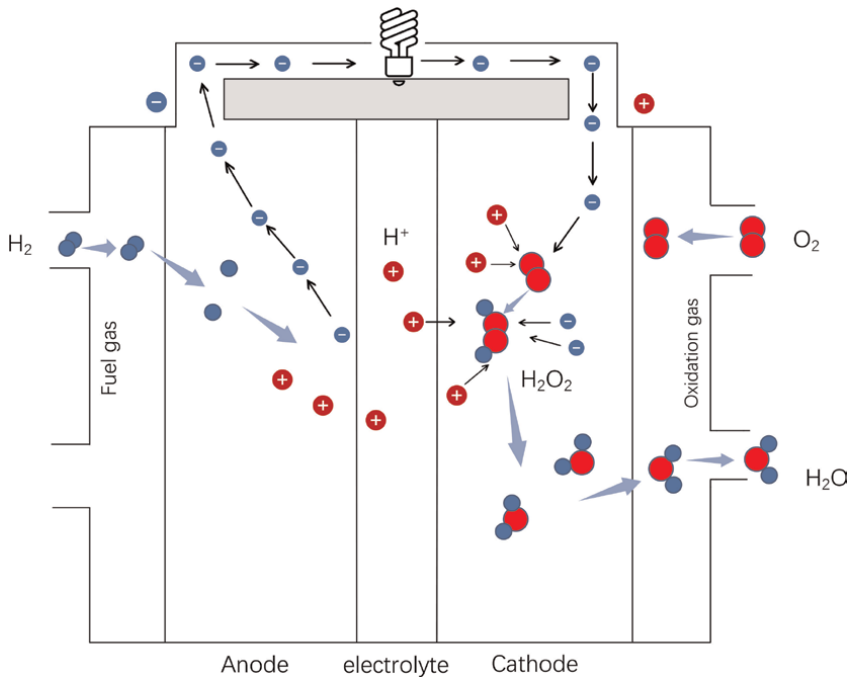


**Figure 2.**  
*Working principle of PEMFC.*

cooling in the fuel cell cooling system. HT-PEMFCs operate between 140°C and 180°C, where the proton conductivity is high enough, and the polymer membrane remains chemically stable. Ceramic membranes used in SOFCs require temperatures of 500–1000°C to achieve sufficiently high ionic conductivity, depending on the electrolyte material and thickness. These operating temperatures determine the materials of the cell and system.

## **2.3 Fuel cell systems**

As the chemical electromotive force of a fuel cell is well below 1 V, the clamping voltage and the electrical power generated can be increased by connecting several cells in series to make the fuel cell fit for everyday use. Each cell is separated by interconnected bipolar plates and sealed with gaskets, thus forming a fuel cell stack. By designing the bipolar plate structure, air and fuel can be evenly distributed within the cell, thus increasing the efficiency of the fuel cell. For low-temperature fuel cells where liquid cooling can be used, the passage of the coolant is also an essential part of the bipolar plate structure. (This is described in more detail in Section 3.2).

The fuel cell stack is the core part of the overall fuel cell system and is used to generate electricity. At the same time, to ensure the fuel cell stack's stability, other components must work together to supply the fuel, air, and coolant to the fuel cell stack in the correct operating environment. Depending on the operating environment, different parts are used, often referred to as BoP (Balance of Plant). These may include pumps, blowers, valves, heat exchangers, humidifiers, filters, chemical reactors, injectors, burners, gas purification, electric actuators, power converters, and everything else required for the operation of the fuel cell system.

## **2.4 Fuel cell characteristics**

Different types of fuel cells have different physical characteristics, and it is crucial to select a suitable type of fuel cell for the best possible application in various fields. In 2009, the German Aerospace Centre (DLR) used a 16 kW high-temperature polymer electrolyte membrane fuel cell (HT-PEMFC) in an Antares motor glider for a test flight [12]. This system was upgraded with a 30 kW low-temperature polymer electrolyte exchange membrane fuel cell (LT-PEMFC). The experience from the appeal platform led to another successful human-crewed test flight in 2016 [13, 14]. Based on the application of fuel cells in aviation, the following section focuses on the characteristics of low-temperature polymer electrolyte membrane fuel cells (LT-PEMFC) and high-temperature polymer electrolyte membrane fuel cells (HT-PEMFC).

### **2.4.1 Lt-PEMFC**

LT-PEMFC typically operates at temperatures between 65°C and 85°C. Its operating temperature is limited because it uses a solid polymer-acid membrane (usually PFSA) which conducts protons when wetted. The character of this hydrated membrane is such that the LT-PEMFC must be operated at a temperature below the boiling point of water. However, the operating temperature must be neither too low (below 65°C) to flood the polymer membrane with condensed water nor too high (above 85°C) to degrade the polymer membrane after dehydration [15]. In addition to the control of temperature, the management of water inside the fuel cell is also a



crucial point. As the product of the hydrogen fuel cell reaction is water, if the water produced through the electrochemical reaction is not managed, too much water will soak into the electrodes, and the reactants will not be able to enter the reaction point. Dehydration of the polymer membrane will reduce ionic conductivity, so proper wetting of the polymer membrane is also required. The wetting of the membrane can be maintained by the water produced in the electrochemical reaction, and the excess water must be removed. To effectively control moisture in the fuel cell, individual gas diffusion layers can be designed into the cell structure to allow the gas reactants to participate more efficiently in the reaction and to direct the drainage of liquid water from the electrodes [16]. In addition, catalysts are required to increase the power density of the fuel cell to make it more efficient. In general, platinum is a perfect catalyst for electrochemical reactions, which can effectively improve the efficiency of fuel cells at low temperatures.

The LT-PEMFC system requires external air to participate in the reaction within the fuel cell, and an air compressor and air filter are usually used to supply air to the positive electrode. The air must be humidified before entering the positive electrode for reaction, either externally using a humidifier or internally within the fuel cell. The most common fuel for LT-PEMFC is hydrogen, which must be supplied at the correct pressure and temperature. For the reactions within the fuel cell to be more efficient, the hydrogen needs to be evenly distributed and adequately humidified. LT-PEMFCs are less tolerant to impurities contained in the fuel. This is mainly due to their relatively low operating temperature, which results in the solid adsorption of impurities on the platinum catalyst at the cathode. To prevent the accumulation of pollutants or contaminants in the fuel at the anode compartment, the fuel needs to be cleaned, which results in a slight loss of fuel (<1%) [17]. Hydrogen produced from natural gas carries sulphur and carbon monoxide, which can seriously affect the lifetime and performance of the LT-PEMFC. Carbon dioxide can also have an adverse effect through the formation of carbon monoxide in the side reactions. Ammonia contamination can also lead to rapid degradation as well as membrane poisoning [18]. Most LT-PEMFC systems today use high-purity hydrogen to achieve a satisfactory lifetime with minimal loading of the platinum catalyst. In principle, however, LT-PEMFC can be operated on modified hydrocarbon fuels and cracked ammonia, provided that the concentrations of sulphur, ammonia and carbon monoxide are all well below 1 ppm. Fuel cells with fuel handling systems have been built and demonstrated [19].

Bipolar plates are another vital part of the LT-PEMFC system and integrate many functions. Bipolar plates are usually designed with a complex hydrodynamic structure that allows them to perform the tasks of homogeneous distribution of fuel and air, separation of air and fuel, management of water and heat inside the fuel cell and conduction of current. Bipolar plates can be made of graphite, metal or composite materials [20]. The choice of bipolar plate material can significantly impact the system's cost, functionality, lifetime, weight and size; for example, metal plates have a higher energy density but a shorter lifetime than graphite. The correct bipolar plate material for each application and an excellent structural design are essential.

The heat management of the LT-PEMFC is also an important aspect. Usually, a liquid cooling system is generally used, where the coolant is a mixture of water and anti-freeze additives. The liquid cooling system usually consists of a coolant pump and a radiator. To prevent ions in the coolant from causing leakage currents in the battery stack, a Raisin filter should also be installed to filter out the ions in the coolant.

## 2.4.2 HT-PEMFC

To solve the problems of LT-PEMFC, the first attempts have been made to increase the operating temperature of PEMFCs. Therefore, it is vital to change the performance of proton exchange membranes so that they can be used in a broader range of temperatures to meet the requirements of both low-temperature cold start and high performance after start-up, which will become an important direction in the future, that is, high-temperature proton exchange membrane fuel cells (HT-PEMFC).

High-temperature proton exchange membrane fuel cells (HT-PEMFCs), which operate at 100–200°C, have more key advantages than ordinary LT-PEMFCs: (1) the catalytic activity of the electrodes is highly active; (2) the catalyst has high resistance to impurity gases; (3) there is only gas phase mass transfer, which is simple and efficient [21]; (4) the hydrothermal management is simple; (5) the methanol permeation problem of methanol fuel cells is solved at high temperatures; (6) there is no need to consider separation and purification devices, and the reforming gas can be matched with online hydrogen production [17], making it possible to produce inexpensive liquid reforming hydrogen (e.g. methanol and acetic acid), and it is easy to store, transport and refill, etc.

As a core component of HT-PEMFC, the proton exchange membrane has an important impact on the lifetime and performance of the fuel cell, and the development of HT-PEM is of very positive significance. However, the technology has some unavoidable challenges: ① The proton conductivity of existing membranes at high temperatures in the temperature range of 100 ~ 200°C is severely reduced, and the perfluorosulphonic acid proton exchange membranes currently in use are heavily dependent on the water content of At high temperatures, the water content in the membrane is low, and the proton carriage mechanism is severely weakened [22]; ② the stability of existing membranes at high temperatures is poor; ③ the performance degradation of fuel cells at high temperatures such as carbon corrosion and platinum dissolution will be exacerbated and durability and lifetime will be reduced [23]; ④ how to solve the compatibility between high-temperature membranes and catalysts [21].

LT-PEMFC systems are already widely used in many areas such as automotive, submarines, portable power supplies, specialist UAV areas and aircraft propulsion. Low operating temperatures offer many advantages, such as lower manufacturing costs, longer service life, high reliability and short start-up times. However, the design of the heat management system of the LT-PEMFC is also a significant challenge due to the operating temperature requirements. The energy-to-weight ratio of the LT-PEMFC is relatively low compared with fuel cell systems operating at higher temperatures. Still, the lower operating temperature and the materials used result in better service life and lower manufacturing costs.

## 3. Aviation PEM fuel cells

### 3.1 Aviation challenges

Civil aviation has always held a relatively large share of transport, especially for medium- and long-haul passenger transport, where the aviation industry holds a significant market share and is growing at a rate of around 3–4% per year. It also brings the problem of contributing to a large amount of greenhouse gas emissions, such as carbon dioxide. According to statistics today, the aviation industry accounts

for 3% of global CO<sub>2</sub> emissions; by 2050, this will be 24% [4]. So how to reduce greenhouse gas emissions and achieve the goal of green flight has become an urgent issue for the aviation industry.

Hydrogen fuel cell systems are widely considered a new type of aviation propulsion system that can replace conventional fuel engines in the future. With its lower noise level, clean, sustainable energy (hydrogen) use and more efficient energy conversion, it is perfect for achieving the goal of truly green flight.

However, there are still many hurdles to overcome before hydrogen fuel cell systems can truly replace conventional fuel engines as the primary propulsion system in large civil aircraft. Firstly, to meet the power requirements of large passenger aircraft, fuel cell systems need to have an output of megawatts or even tens of megawatts. Take the DLR study as an example, a fuel-cell-powered four-seater aircraft (HY4) flown by DLR in 2016. This prototype was equipped with a hybrid power system consisting of an LT-PEMFC and a lithium-ion battery, with the LT-PEMFC acting as the primary output for the main power and the lithium-ion battery as an auxiliary for the aircraft during take-off and climb. The power system has an output of 80 kW [24], and the successful test flight of this aircraft represents the possibility of hydrogen fuel cells as a propulsion system for small manned aircraft. However, for application on large passenger aircraft, a large number of fuel cell units would need to be connected in series to achieve the required power.

To ensure the proper functioning of many fuel cell stacks connected in series, extremely high demands are placed on all system parts. The first is the thermal management of the entire system. As the LT-PEMFC is sensitive to the operating temperature requirements, an efficient and stable thermal management system is necessary. The thermal management of a fuel cell system of this power level is also a severe challenge. Due to the characteristics of the proton exchange membrane used in the LT-PEMFC, a water management system is also required to cope with a large number of cells in the fuel cell system to prevent each fuel cell from being dehydrated and flooded, causing power reduction or even failure, to ensure the regular operation of the whole system.

In aircraft design, weight is always a priority. The overall mass of the aircraft affects the energy consumption; the heavier the mass, the more fuel is required, and the more powerful the propulsion system needs to be to overcome the drag in flight and meet the required lift. This is why the lightweight design of fuel cell systems is also a challenge (**Figure 3**).

There are two ideas for reducing the weight of a fuel cell system. One is to reduce the number of fuel cell stacks, which means increasing the fuel cell unit's efficiency of the fuel cell unit, that is, increasing the power-to-weight ratio. The efficiency of the LT-PEMFC can be effectively improved by developing new types of proton exchange membranes, optimising the design of the flow field inside the fuel cell, etc. The second idea is to simplify and lighten the creation of the system, for example, by developing new fuel cell thermal management systems and using lightweight materials.

For large passenger aircraft, safety always comes first; each new aircraft must undergo rigorous certification before servicing. This requires a higher level of safety redundancy for essential systems. For fuel cell systems, increasing the redundancy of the fuel cell may significantly reduce the specific power of the entire system. A fuel cell system's specific power and lifetime are also considered essential factors for its application in aviation. While the specific power of fuel cells has been increasing over the last decade through the optimisation of components and manufacturing processes, the reliability required in aviation has been significantly less.

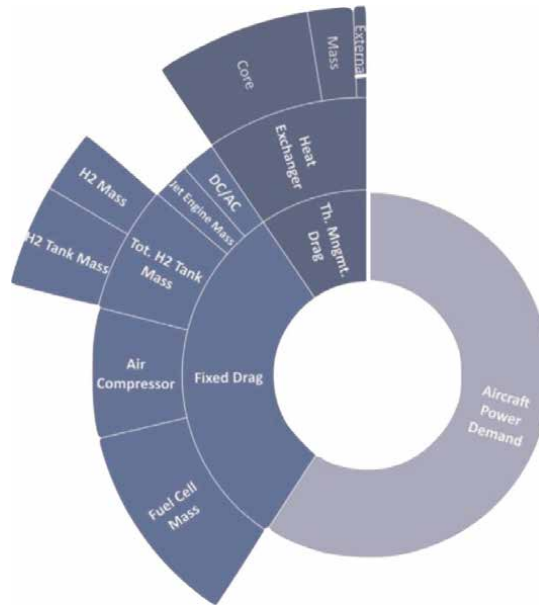


**Figure 3.**  
*The drag power of the hybrid PEMFC-jet.*

In this chapter, the increase in specific power for sizeable civil aircraft fuel cell systems was sought from a different approach rather than focusing on the design of the fuel cell system.

### 3.2 Cooling systems

The cooling of a small LT-PEMFC can rely on air cooling, which is usually sufficient to keep the cell stack at a suitable temperature with the air involved in the reaction. However, when applied to megawatt-class LT-PEMFC systems, huge heat exchangers are required to maintain their operating temperature. This solution is not suitable for practical use. A large heat exchanger increases the air resistance of the aircraft in not only flight but also its weight is enormous, which adds additional drag to the plane. Liquid cooling systems are more widely used in automobiles due to their simple construction and better cooling capacity. But for aerospace applications, where the power of the system has been increased from kW to MW level, phase change cooling (PC) systems seem to have an advantage over liquid-cooled systems. Phase change cooling not only reduces weight but also increases cooling capacity by tens of percentages (**Figure 4**).

Therefore, a heat pump (HP) between the fuel cell system and the heat exchanger is proposed. According to Newton's law of cooling, the heat pump is used to increase the temperature of the coolant by the required heat exchanger capacity (surface area, volume and weight), that is, the flight drag can be effectively reduced. This PCHP (phase change-heat pump) cooling concept was first conceived for LT-PEMFC aeronautical applications in all published literature and the field of hydrogen propulsion in general, referring to Ref. [25].

To study and analyse the above-proposed PCHP cooling system, modelling and analysis were carried out based on a proven aircraft design and a typical flight mission.

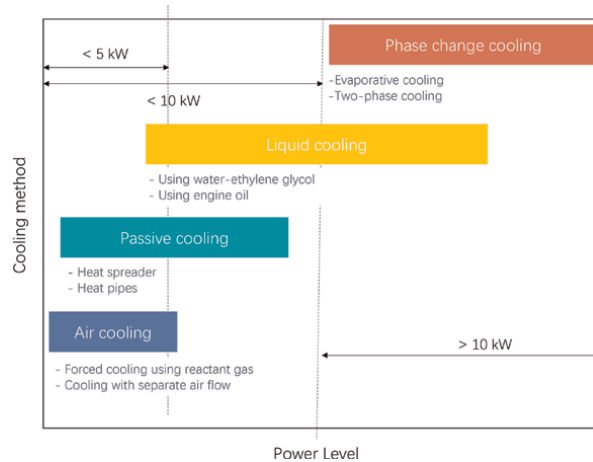


**Figure 4.**  
 Cooling methods for LT-PEMFC vs. power level.

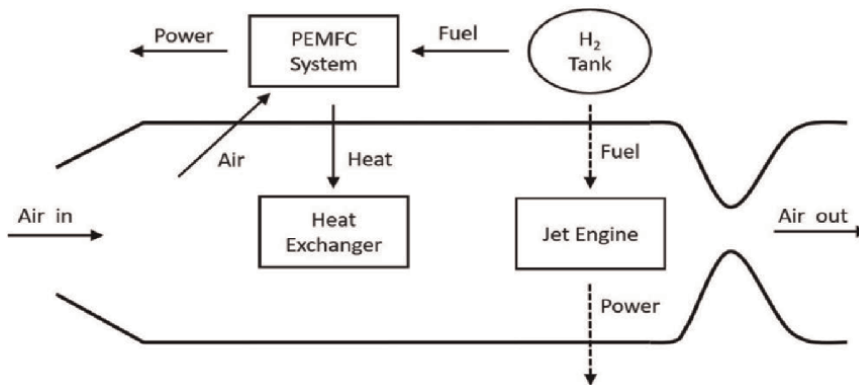


**Figure 5.**  
 Schematic presentation of the hybrid PEMFC-jet engine layout.

A hybrid LT-PEMFC-jet engine layout was chosen and then fine-tuned in size under two different PEMFC cooling schemes. Key performance indicators, including two drag items, are extracted and compared. Finally, they are discussed and summarised.

The Airbus A320–200 jetliner was chosen for this study. The hybrid PEMFC-jet engine system consists of a fuel cell system and a hydrogen internal combustion engine (i.e., a hydrogen-fuelled turbine engine). **Figure 5** shows the entire layout.

To facilitate the study, the fuel cell system in the model consists of a fuel cell stack, a hydrogen tank and a heat exchanger. The hydrogen tank feeds the stored hydrogen to the fuel cell and the jet engine, which provides additional power during take-off by burning the hydrogen directly. The thermal management system and the fuel cell system compressor are not shown as they are included in the ‘PEMFC System’ block. **Figure 6** shows the propulsion power requirements for the different flight phases of a mission, and it can be seen that an enormous amount of power is required during the take-off phase. During the cruise phase, the operating environment is more stable, and propulsion is provided by the fuel cell. For the specific aeroplane, based on data from Kadyk et al [26]., the data also shows us the power requirements of the A320–200 at various stages, as detailed in **Table 1**.

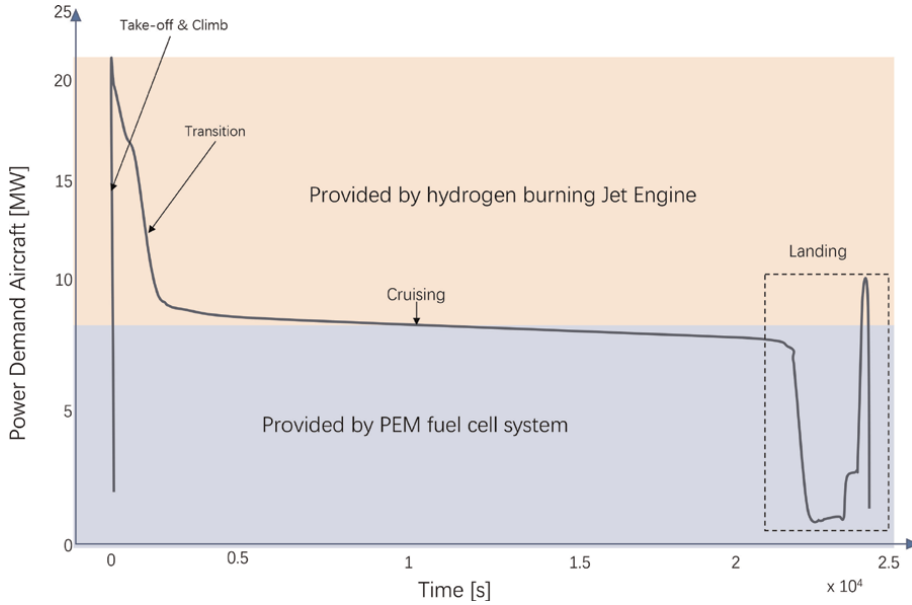


**Figure 6.**  
Analysed flight mission for hybrid PEMFC-jet engine.

Description	Variable	Value	Unit
Average take-off power demand	$P_{TaO,ave}$	20.7256	MW
Maximum take-off power demand	$P_{TaO,max}$	20.8698	MW
Average cruising power demand	$P_{Cru,ave}$	7.7441	MW
Maximum cruising power demand	$P_{Cru,max}$	8.0646	MW
Fuel cell system power supply	$P_{FC}$	9.6775	MW
Jet engine power supply	$P_{JE}$	11.1923	MW
Maximum fuel cell system energy demand	$E_{FC}$		MJ
Average jet engine energy demand	$E_{JE,ave}$	6501	MJ

**Table 1.**  
Power demand of the A320–200 aircraft for take-off and cruising based on data from Kadyk et al. and resulting provided power by the jet engine and the fuel cell system.

### 3.2.1 PEMFC cooling design

A schematic diagram of the PCHP cooling circuit proposed in this work is shown in **Figure 6**. The cooling course (excluding the PEMFC stack) consists of a heat exchanger, a compressor (HP), an expansion valve, ideal piping and a coolant. Water has been chosen as the phase change coolant. For water to evaporate in the operating temperature range of the fuel cell stack, the coolant pressure must be lower than the

ambient pressure (0.2 bar). The low-pressure water (vapour mass of 0.153) evaporates, thus cooling the PEMFC stack and leaving a vapour mass of 0.950. Through the compressor, the pressure of the steam is increased by 5 bar, resulting in a significant temperature increase. Afterwards, the hot and pressurised steam (steam mass of 1.000) is transported to the heat exchanger, which removes heat into the ambient airflow around the aircraft. After passing through the heat exchanger, the steam is transformed into pressurised liquid water (vapour mass of 0.000). The heat exchanger model is implemented using the ‘Condenser Evaporator (2P-MA)’ module in Matlab/Simulink, and the minimum drag is determined using an optimisation algorithm. As the pressure drops through the expansion valve, the water is again mostly evaporated, that is, the vapour mass of the coolant returns to its original 0.153 at a pressure of 0.2 bar. Finally, the under-pressure cold water is piped into the PEMFC stack for a new cooling cycle. For comparison, we have also simulated conventional liquid cooling with the same cooling process as for the PCHP (**Figure 7**).

The reverse Rankine cycle of the coolant in the p-h diagram can be seen in **Figure 6**, where the blue line indicates the coolant cycle, the yellow line shows the isentropic process, and the red line indicates the isothermal process. The numbers 1–4 correspond to the states of the coolant in the PCHP cooling loop depicted in **Figure 8**.

### 3.2.2 PEMFC modelling

The PEMFC is modelled to calculate the heat generated by the PEMFC system during operation and to analyse the cooling system. The following assumptions have been adopted to simulate the PEMFC subsystem of the engine.

1. The operation of each flight phase is assumed to be steady state.
2. All components, except the heat exchanger, were simulated lumped.
3. The properties of hydrogen and air follow the ideal gas law
4. The ambient air properties for the cruise phase (7783 m above sea level) were taken from the International Standard Large Balloon (ISA) model [27].

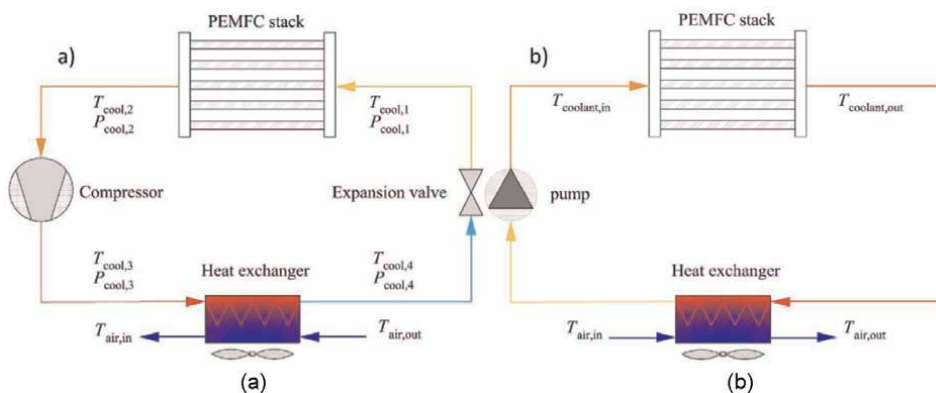


**Figure 7.** a) the PCHP cooling loop proposed in this work for an aviation PEMFC system and b) schematic view of a conventional LC loop for the same PEMFC system.

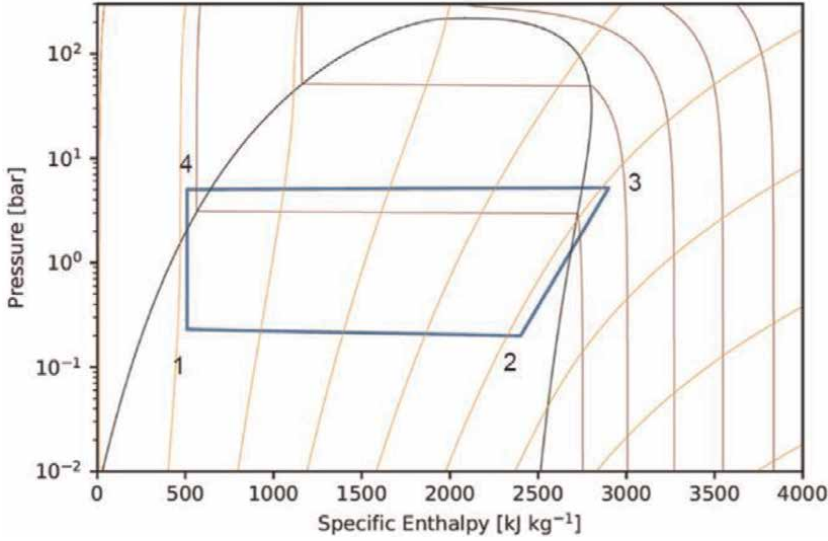


**Figure 8.** Heat pump cycle of the coolant inside the PCHP model. Blue lines: Coolant cycle; yellow lines: Isentropic process; red lines: Isothermal process. The numbers 1–4 correspond to the respective state of the coolant in the cooling loop.

The subsystem-generated waste heat flow is [27],

$$\dot{Q}_{gen} = (V_{th} - V_{out}) \cdot i \cdot A_{cell} \cdot N_{cell} \quad (1)$$

To remove the waste heat flow  $\cdot Q_{gen}$  to the ambient air, the two cooling designs mentioned above use the same aluminium louvre-fin heat exchanger and are of the same size [28].

### 3.2.3 Drag power

The drag generated by the PEMFC subsystem consists mainly of the system mass and aerodynamic friction caused by the heat exchanger, with some drag forces mitigated by the Meredith ramming effect [29]. This is because the air expands within the heat exchanger and leaves the nacelle faster than it entered, generating thrust. The overall drag is expressed as follows:

$$P_{d,tot} = v_{air,0} \times (D_{d,mass} + D_{d,aero}) + P_{comp,r} + P_{misc} - P_{ram} \quad (2)$$

where  $v_{air,0}$  is the free flow velocity of air (m/s);  $D_{d,mass}$  and  $D_{d,aero}$  are the mass and aerodynamic induced drag (N), respectively;  $P_{comp,r}$  is the power consumption of the turbo compressor supplying fresh air from the environment to the fuel cell stack (W);  $P_{ram}$  is the ram thrust caused by the Meredith ramjet effect (W).  $P_{misc}$  is the miscellaneous drag power (W) depending on the other components in each cooling circuit.  $D_{d,mass}$  is determined by the force balance to lift resistance ratio  $L/D$  during the cruise. This ratio is the amount of lift generated divided by the aerodynamic drag due to movement through the air. The expression for the drag caused by mass is  $D_{d,mass} = \frac{m_{sys,tot} \times g}{L/D}$ , where  $g$  is the gravitational constant ( $m/s^2$ );  $L/D$  is the lift-to-drag



ratio; and  $m_{sys,tot}$ , is the sum of all components in the system taken into account, which can be expressed as

$$m_{sys,tot} = m_{HX} + m_{FC} + m_{JE} + m_{Tot,tank}, m_{Tot,tank} = m_{Tank} + m_{H_2} \quad (3)$$

The lift-to-drag ratio of an A320–200 airliner at cruise is [30]

$$L/D = 16.3$$

An analysis comparing the cooling effect and the dragging force of the powertrain of a PEMFC with two cooling systems shows that with a fixed cruise power requirement for the aircraft, all drag power items were found to rise monotonically with increasing current density based on simulations of the model. This is because the current density increase amplifies the heat flow through the system, amplifying the heat exchanger's capacity. This leads to an increase in absolute values for all resistance sources in the interval analysed. At higher current densities, the core drag and the drag caused by the heat exchanger mass rise more rapidly, while the ramjet thrust and external drag follow an almost linear trend. The relationship between the drag source and the size of the heat exchanger can explain this. While the external drag depends on the frontal area of the heat exchanger, the mass and core drag depend on the volume of the heat exchanger, which does not follow a linear trend. The total resistance of the liquid-cooled cooling loop and the phase-change heat pump cooling loop at different current densities is shown in **Figure 8** without accounting for the stack and hydrogen storage mass. It can be seen that the drag resistance first decreases and then increases through increasing current densities, indicating that there is a minimum drag resistance point for which the corresponding current density of the combustion link cell can be identified as the optimum operating point for the fuel cell. It can also be observed that the total drag force of the phase change heat pump cooling system is significantly lower than that of the liquid cooling system for both cold de-circuit designs. For the minimum total drag corresponding to the optimum current density,  $0.5781 A/cm^2$  for the liquid-cooled system and  $0.7313 A/cm^2$  for the phase-change heat pump system, it can be concluded that the phase-change heat pump system is advantageous in reducing the drag force during flight and increasing the efficiency of the fuel cell (**Figure 9**).

The combined performance of the hybrid system with its two different cooling systems is also worth discussing. The first thing to say is the total drag power of the

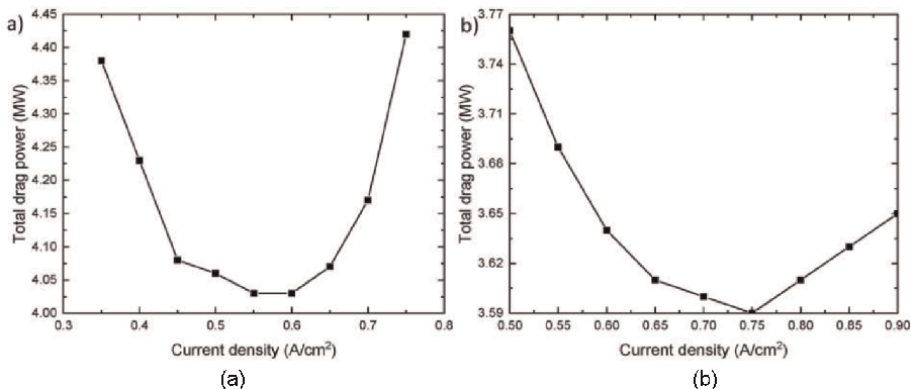


**Figure 9.**  
 a) the total drag of the LC loop. b) the total drag of the PCHP loop vs. stack current density.

two systems: 6.648 MW for the LC system is 1.528 MW more than the PCHP cooling system, representing 15.79% of the aircraft's total propulsion power. As the coolant temperature in the PCHP system is much higher than in the LC system (324.4°C for the PCHP and 56.4°C for the LC), according to Newton's law of cooling and assuming other variables are inconvenient, the PCHP requires about 1/5 the area of the heat exchanger of the LC system. The use of a small-area heat exchanger also allows a further reduction in flight resistance and overall system mass. More drag requires more energy consumption, that is, more fuel needs to be carried to ensure range. At the same time, the current density of the LC system is also relatively low, which exacerbates the gap between the two systems.

Another point worth noting is the effect of the thrust generated by the Meredith Ramjet effect on the overall system for both systems. According to model calculations, the Ramjet effect of the LC cooling system provides an additional 1.773 MW of thrust, approximately three times that of the PCHP system. Still, it only counteracts 53.2% of the drag generated by the LC system, whereas the Ramjet effect in the PCHP cooling circuit counteracts 96.8% of the drag caused by itself. So the drag generated by the PCHP cooling system is entirely negligible, reducing the drag overcome by the propulsion system by 23%, which can also be seen as a 16% increase in airspeed.

### 3.3 Efficiency

From the current research, it is clear that the performance of PEMFC itself still needs to be improved to be used in civil aviation. Previous sections have described the study of a sub-system of the PEMFC system, namely the cooling system. The performance of the entire hybrid PEMFC propulsion system has been optimised by employing a new phase change heat pump performance of the PEMFC [31]. To improve the performance of PEMFC, design optimisation of GDL is often considered an effective approach. Pore-scale simulations are generally regarded as one of the most effective tools for optimising the microscopic performance of porous media, such as GDL [32, 33]. In the last few decades, the rapid development of computer modelling and analysis, X-ray computed tomography and scanning electron microscope has provided a variety of effective modelling methods, simulating and studying GDLs at the microscopic level, such as pore-scale modelling (PSM), which is used below cooling system. This section will discuss how the performance of the PEMFC itself can be further optimised by design (Figure 10).

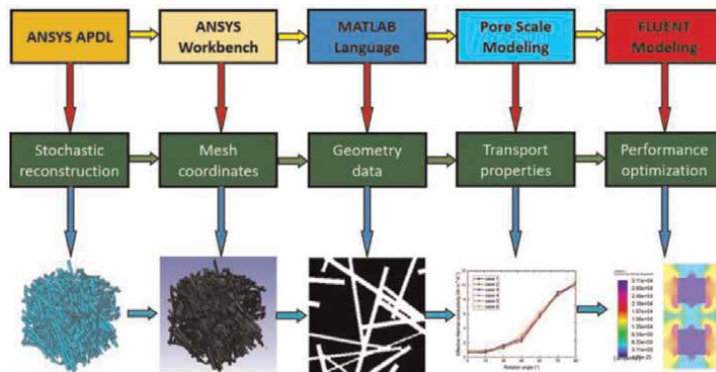


**Figure 10.** Schematic of this multiscale modelling study approach.

The Gas Diffusion Layer (GDL) is a critical component of the PEMFC structure and is responsible for managing water and heat and transporting substances in the PEMFC [34, 35]. The GDL transports the reactants to the catalyst layer (CL) and transports the products from the CL efficiently and uniformly, a link that impacts the performance of the PEMFC.

To design a new GDL, a 3D GDL model with a specific structure is first generated by the stochastic reconstruction method of the ANSYS Para-metric Design Language (APDL). The stochastic reconstruction method utilises a stochastic algorithm which allows the fibres to be placed randomly in a specified space. To facilitate the study, the following restrictions are imposed on the model: the generated GDL consists only of solid carbon fibres and pore scale, all carbon fibres on the same diameter and is entirely allocated on every single x-y plane, allowing for stacking between fibres. As a result, a numerical GDL is generated with only solid carbon fibres on the same diameter and is entirely allocated on every single x-y plane, allowing for the stacking of fibres. As a result, a numerical GDL is reconstructed, with a domain of size  $304 \times 304 \times 304 \mu\text{m}^3$  and a resolution of which the porosity is 0.78 and the fibre diameter is  $8 \mu\text{m}$ . **Figure 11 b)** analyses the pore size distribution to validate the reconstructed geometry. It demonstrates that the structure is ready for the GDL study.

ANSYS Workbench then carried out pre-processing to obtain the mesh coordinates. To improve its electrical and hydrothermal properties, the reconstructed GDL was rotated by different angles to form a new GDL. This step was transformed and tilted using MATLAB scripts and matrix transformation functions to obtain matrices with different degrees of GDL phase data. PSM, including gas diffusivity and electrical and thermal conductivities, extracted the effective transport properties of these angled GDLs. It should be noted that anisotropy is evident in common GDL materials. Calculating fluxes in the in-plane direction (x and y) and across the plane direction (z) is necessary. Finally, these properties were applied to a CFD model to investigate the performance of the PEMFC using this new design.

For ease of calculation, the simulation of the 3D macroscale model covers only one channel of the PEMFC, as shown in **Figure 12**. It consists of seven components: the anode current collector (ACC), the cathode current collector (CCC), the anode catalyst layer (ACL), the cathode catalyst layer (CCL), the anode gas diffusion layer (AGDL), the cathode gas diffusion layer (CGDL) and the membrane. Thermal and electrical conductivities at different GDL fibre angles were used in this model. Based on our PSM results, the effect of compression on the GDL has been considered.

In this macro model, the following assumptions are taken.

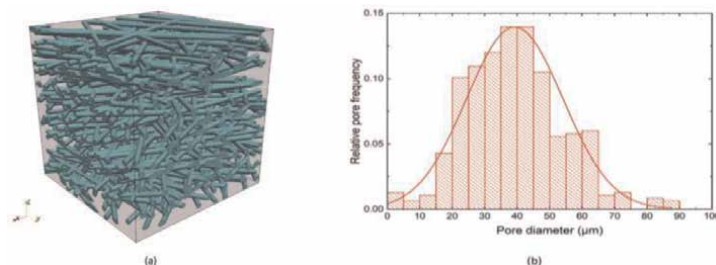


**Figure 11.**  
*Stochastic reconstruction of the GDL.*

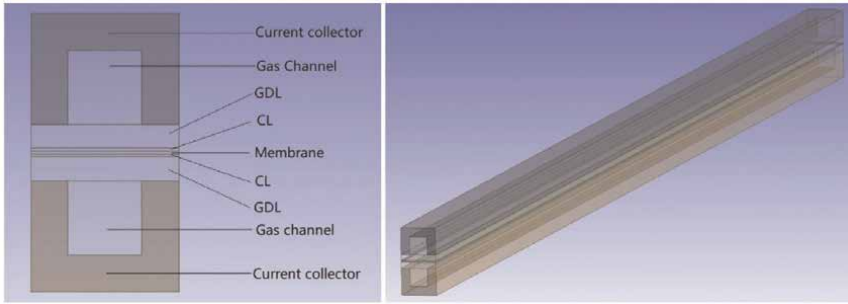


**Figure 12.** Schematics of the PEMFC model, 2-D view (left) and 3-D view (right).

- a. The fuel cell operates under steady-state conditions, and gravitational effects are neglected.
- b. The properties of the GDL are considered to be anisotropic, and the other components of the fuel cell are isotropic.
- c. Thermal and electrical contact resistances are neglected.
- d. The gases in this model are considered ideal.
- e. The membrane is impermeable to all gases.

The conservation of mass governs this macroscopic PEMFC model, conservation of momentum, conservation of energy and electrochemical reaction equations [36–38].

With the help of the constructed micro and macro models, the properties of GDL, such as gas diffusivity, and electrical and thermal conductivity, are analysed.

The GDL was set at 15-degree intervals around the y-axis from 0 to 90 degrees, as shown in **Figure 13** and then rotated around the z-axis from 0 to 90 degrees. It can be observed that the porosities of the GDL appear to become more uniform as the angle increases. By calculating the effective gas diffusivity (EGD) using PSM, it was found that the effective gas diffusivity increased with increasing rotation angle.

To understand this phenomenon, relative gas diffusivity (RED) was introduced. As shown in **Figure 14a**, the RED increases with increasing angle. According to the

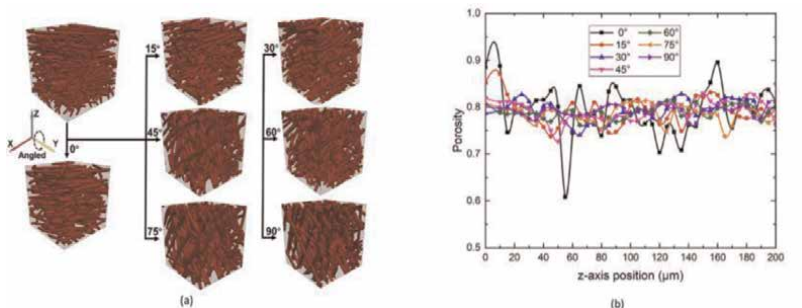


**Figure 13.** GDL angling, a) schematics of the angling around the y-axis and b) porosity distributions through the z-axis direction of these angled GDLs.

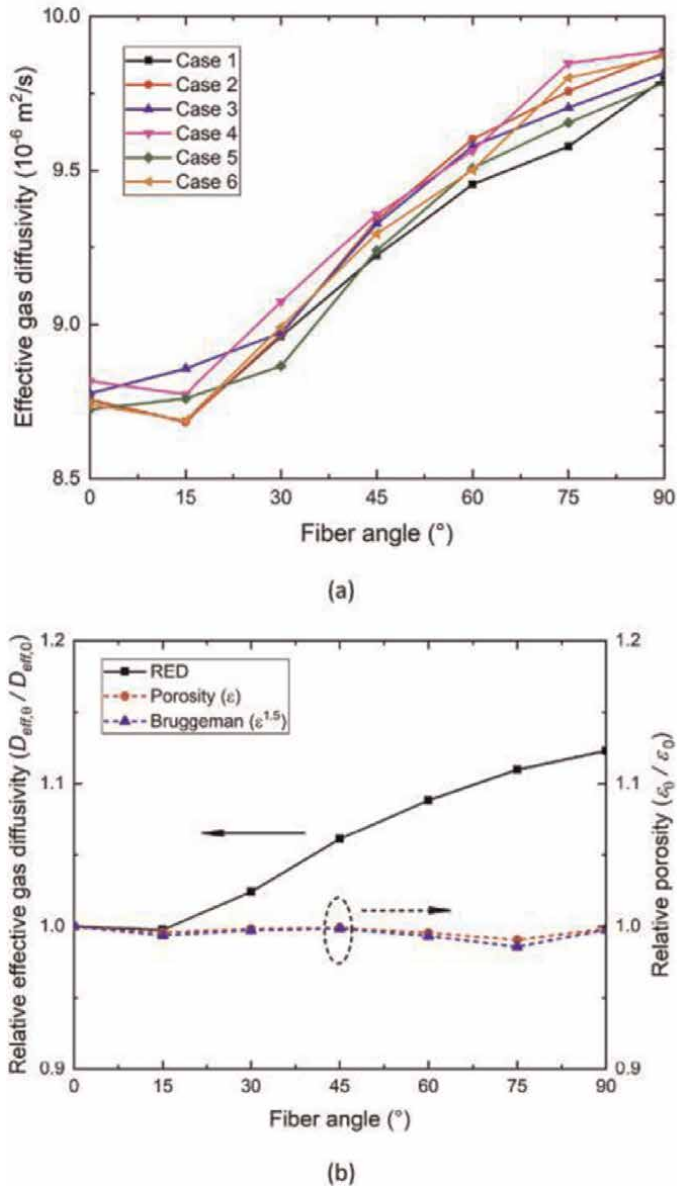


**Figure 14.** Effects of the fibre angle on the EGD, (a) the EGD with the angle, (b) the RGD and relative porosity with the angle, including the calculation results and Bruggeman function.

Bruggeman function, it can be concluded that EGD is correlated with porosities. This also shows that porosities are one of the determinants of EGD. However, we can also see from **Figure 14b** that the relative porosities are almost unity, which indicates that porosities' effect on EGD can be neglected. Research reveals that it is not porosity but tortuosity that causes EGD to increase with angle [39, 40]. Tortuosity is inversely proportional to EGD, with tortuosity decreasing as the angle increases, which is reflected in EGD increasing with the angle.

For carbon fibres, effective electrical conductivity (EEC) and effective thermal conductivity (ETC) increase with the angle but show an S-shaped curve as more electrons/heat is conducted through the fibres and less through the contact points between the fibres. This would result in less resistance to electrical/heat conduction through the planar direction [41, 42]. The difference between REEC and RETC is illustrated in **Figure 15** mainly because heat is also conducted through air, while electricity is only conducted through carbon fibres [43].

From the macroscopic model, the fuel cell performance has been dramatically improved by the optimised design of the GDL. The benefits of the new GDL design translate into performance gains of up to approximately 80% for the macroscopic PEMFC due to the significant improvements in EEC and ETC. In addition, the increase in ETC leads to a reduction in membrane temperature, leading to a higher membrane water content. The result is an increase in membrane proton conductivity, which increasingly reduces the ohmic overpotential and dramatically improves the fuel cell performance.

### **3.4 Hydrogen storage**

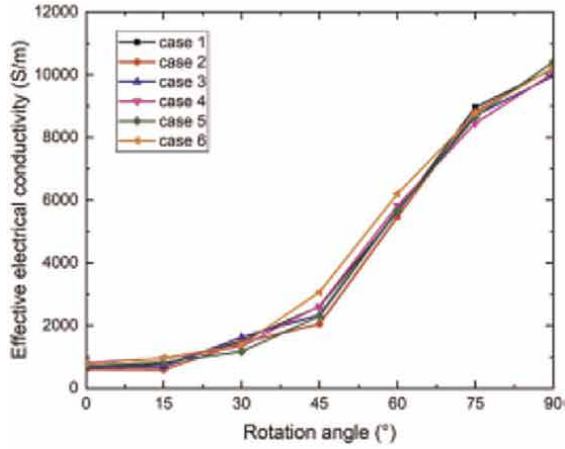
As the bridge between the production and utilisation of hydrogen, hydrogen storage technology runs through the hydrogen end of the industry chain to the fuel cell end. It is an important link in controlling the cost of hydrogen.

How hydrogen is stored is of great concern. Hydrogen has a high energy density, three times that of petrol; it is light, weighing only 1 kg for  $11.2m^3$ ; it is very easy to dissipate because it is far less dense than air; and since hydrogen is a liquid with a density of  $70.78kg/m^3$  at  $-253^\circ C$ , it is nearly 850 times denser than hydrogen under standard conditions (approx.  $0.08342kg/m^3$ ). Therefore, cryogenic liquid hydrogen storage is a highly desirable form of hydrogen storage in terms of energy storage density alone. However, there are still some problems with low-temperature liquid hydrogen storage technology. Firstly, the process of hydrogen liquefaction consumes much energy, with the actual energy consumption being equivalent to 30% of the total hydrogen energy; secondly, liquid hydrogen storage tanks require high selection criteria for insulation materials and tank design due to issues such as sealing, insulation and safety, leading to increased manufacturing difficulties and high costs.

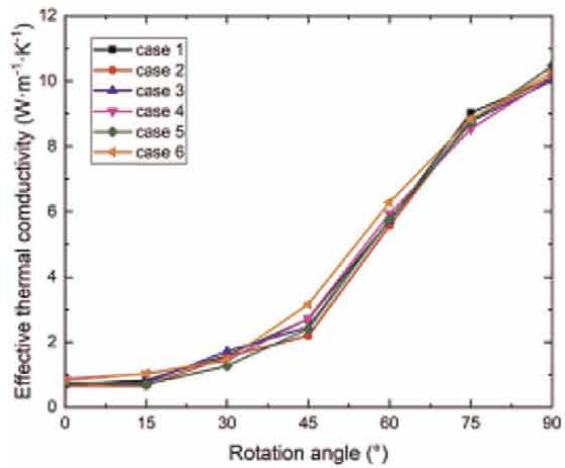
The abovementioned problems limit the use of hydrogen as a fuel in aviation. A new hydrogen storage tank concept has been proposed to solve this problem, using cryogenic liquid nitrogen as an insulating layer. The structure is shown in **Figure 16**. This is a multi-layer isolation structure with a chamber between the tank walls that can be filled with cryogenic liquid nitrogen, which is used to maintain the temperature of the liquid hydrogen inside the tank. The liquid nitrogen can be replenished simultaneously as the fuel is refuelled.

To better analyse this concept and explore its actual performance, a modelling analysis of the structure of the hydrogen storage tank was carried out. It is first assumed that this tank is designed to meet the following mission requirements. A regional aircraft capable of carrying 32 passengers, with a required range of 2100 km, an altitude of 9144 m, a cruise speed of Mach 0.65 and a fuel load (liquid hydrogen) of 1150 kg. To compare with the original liquid hydrogen storage equipment, two more advanced types of hydrogen storage tanks (Polyurethane (PU) foam and vacuum-based multilayer insulation (MLI)) were also analysed.

The analysis of the thermodynamic properties, insulation capacity and adaptability to different environmental conditions of the three tanks leads to the conclusion that



(a)



(b)

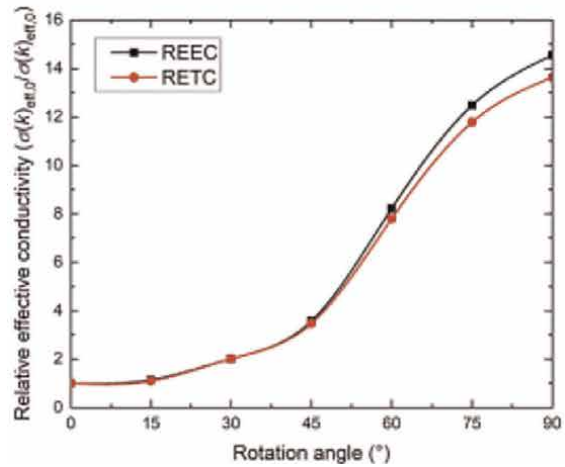


**Figure 15.** Effects of the fibre angle on (a) the EEC, (b) the ETC and (c) the REEC and RETC.



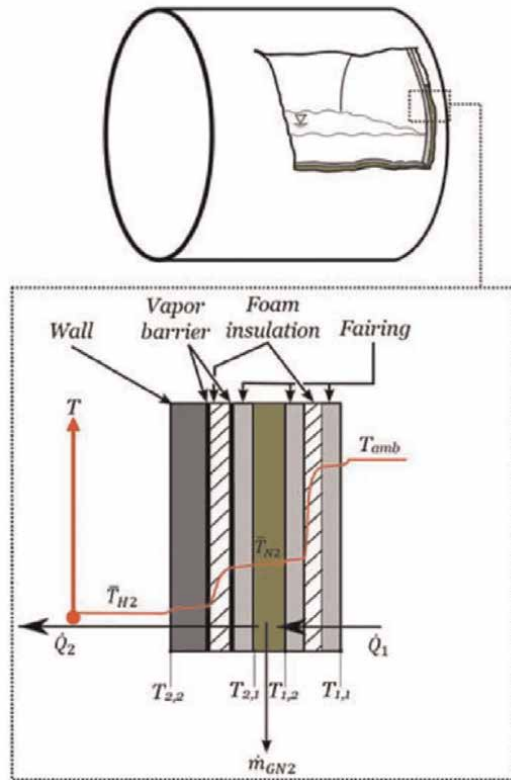


**Figure 16.**  
Schematic description of the new concept of the hydrogen storage tank.

the novel concept hydrogen storage tank can significantly limit the tank's volume by introducing liquid nitrogen to limit the heat flux into the tank. The volume savings compared with foam materials increase with the reduction of the liquid hydrogen payload. For small tanks, the volume savings compared with pure foam insulation, as well as the increased adaptability and robustness, come at the cost of the tank weight, as additional structural walls are necessary. MLI is the best performer of all concepts in tank volume because it has the lowest insulation thickness. For larger tanks, however, the MLI has a comparative advantage over the novel concept in weight reduction. In the 12-hour overnight stop design, the MLI outperforms the other two concepts. But the novel concept still fulfils the challenge of the 12-hour stop. The novel concept is expected to be a reliable hydrogen storage system in the future because it does not need to maintain vacuum conditions and its reliability in the face of active thermal system failure.

### 3.5 Reliability

Safety is the most critical factor for a civil airliner; therefore, the safety requirements of such aeroplanes are extremely stringent according to national regulations. However, higher safety redundancy means lower specific power for the fuel cell. The increase in specific power for large civil aircraft fuel cell systems is sought from different approaches rather than focusing on the design of the fuel cell system. Having



quantified the extent to which aviation safety specifications affect the specific power of fuel cell systems, strategies to reduce these effects need to be investigated.

The safety certification guidelines for aircraft guide the design of fuel cell systems. To meet the requirements of safety certification guidelines, it is necessary to design the fuel cell system with sufficient redundancy. However, the more redundancy there is in a system, the heavier it becomes, thus reducing the specific power of the fuel cell system and payload. The theoretical redundancy ( $DOR_{theo}$ ) can be calculated using the following formula.

$$DOR_{theo} = \log_{(1-w)}(p) \quad (4)$$

As the DOR follows a logarithmic function, a considerable increase in reliability is required to reduce the DOR significantly. The relationship between redundancy and failure rate is given in **Figure 17**. It can be seen that the sensitivity of DOR and the sensitivity of different powers to system reliability increase as system reliability increases.

Subsystem redundancy analysis of fuel cells helps reduce the overall system's mass, as less redundancy is required for reliable components than for the system as a whole. Further improvements in fault-tolerant systems are a good direction, such as the new PEMFC stacks, which can bypass faulty cells [44].

### 3.5.1 Time constant determined extended operations (TCD-ETOPS)

TCD-ETOPS is a newly introduced concept based on ETOPS (Extended Operations), which allows the aircraft to maintain a greater distance from diversionary airports, allowing shorter flight paths and operations over water and in remote areas [45]. And the purpose of TEC-ETOPS is to reduce the impact of safety certification on

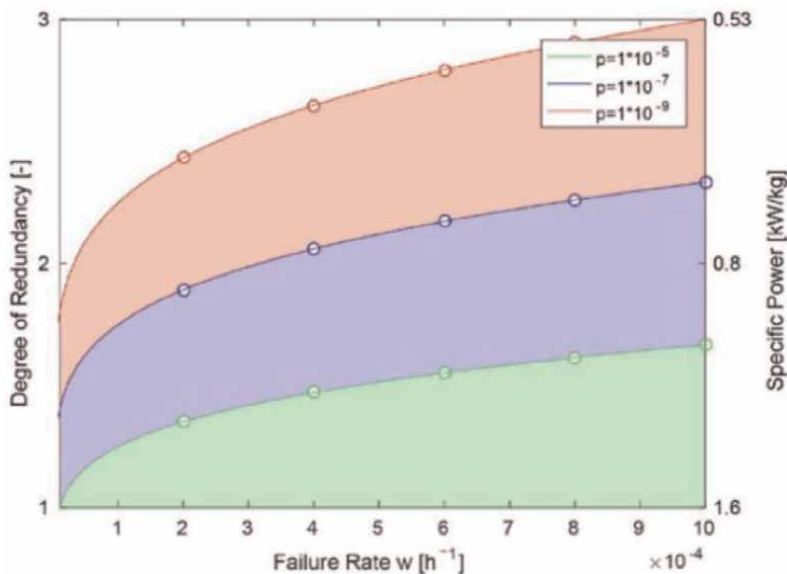


**Figure 17.** Degree of redundancy as a function of failure rate. Area colours show different failure modes. Green: minor, blue: major, red: hazardous, white: catastrophic.

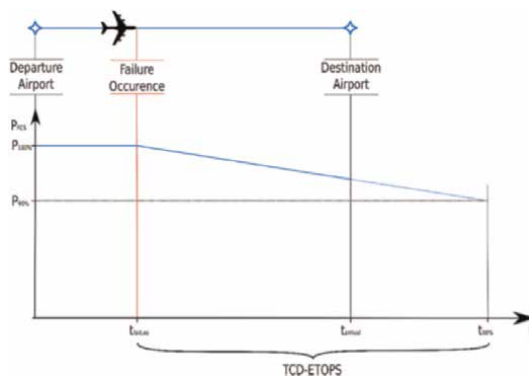


**Figure 18.** Visualisation of the time constant determined extended operations (TCD-ETOPS). The failure condition is met at 10% initial power loss.

the specific power of the system. The time constant for a given degradation mechanism represents the time scale of power loss of the FC. If the diversionary airport is within the TEC-ETOPS range, the aircraft can continue flying and landing in the event of a subsystem failure. Suppose the time scale of degradation allows the aircraft to reach the destination airport without further deterioration of the failure. In this case, a greater incidence of failure can be allowed with a guarantee of safety; therefore, the system's redundancy can be reduced.

For example, as shown in **Figure 18**, the range of the aircraft's TCD-ETOPS after a failure encompasses the time the plane arrives at the destination airport. This failure has a minimal impact on the aircraft's operations, and then there is a possibility that the failure of this subsystem can be degraded to a lower failure level.

The PEMFC system can fail to power an aircraft due to several failure conditions, the 10 most serious being: overheating, leakage, fracture, extruded, stress corrosion cracking, erosion, deposition, cavitation, inadequate structural support and failure to perform its function [46]. But some of the degradations that occur are also reversible; for example, the loss of voltage due to low humidity in the ground is reversible to some extent [47], while the supply of pure hydrogen to the anode after carbon monoxide poisoning of the membrane restores the total voltage [48]. In this way, the failed FCs are restored after TCD-ETOPS, then repair or replacement of the FCs can be postponed or avoided, and if in flight, the range of TCD-ETOPS in flight can also be extended.

By proposing the TDC- ETOPS concept, the impact on the specific power of the fuel cell due to excessive redundancy requirements can be compensated. By analysing the fuel cell system at the component level, there is also the prospect of reducing the system's mass. In future research, it is also necessary to address the different failure modes of PEMFCs and the degradation relationships caused by failures, thus being a more detailed fuel cell system design.

#### 4. Summary and outlook

As early as the 1960s, fuel cells were used in the NASA Gemini spacecraft, followed by the launch of fuel cell concept models by many internationally renowned car companies. In the twenty-first century, as the development of hydrogen energy

technology has gradually matured, the world's major developed countries have attached great importance to the development of the hydrogen energy industry, and hydrogen energy has become an important strategic choice to accelerate energy transformation and upgrade and cultivate new economic growth points.

Fuel cells have the following advantages.

1. High efficiency. Since the chemical energy of the fuel is directly converted into electrical energy without thermal energy conversion in the middle, the conversion efficiency is not limited by the thermodynamic Carnot cycle; since there is no mechanical energy conversion, mechanical transmission losses can be dispensed with, plus the conversion efficiency does not vary according to the size of power generation, so the fuel cell has a high conversion efficiency.
2. Low noise and low pollution. In converting chemical energy into electrical energy, the fuel cell has no mechanical moving parts, only a part of the control system has small moving parts, so it is low noise. In addition, the fuel cell is also a low-pollution energy source. Take phosphoric-acid-type fuel cells as an example; the sulphur oxides and nitrogen compounds emitted by them are two orders of magnitude lower than the standard set by the United States.
3. High adaptability. Fuel cells can use a variety of hydrogen-containing fuels, such as methane, methanol, ethanol, biogas, LPG, natural gas and synthetic gas, and the oxidiser is inexhaustible air. Fuel cells can be made into standard modules of specific power (e.g. 40 kW) and assembled into different power and types according to the user's needs and installed in the most convenient place for the user. They can also be installed as large power stations if required and used in parallel with the conventional power supply system, which will help regulate the electrical load.
4. Short construction cycle and easy maintenance. After the fuel cell has been formed for industrial production, the various standard components of the power generation unit can be produced continuously at the factory. It is easy to transport and can also be assembled on-site at the power station. Some estimate that the maintenance of a 40 kW phosphate-type fuel cell is only 25% of that of a diesel generator of the same power.

Although the fuel cell presents many attractive advantages, it also has severe shortcomings. The main bottleneck for fuel cell applications is the high cost. Due to cost constraints, fuel cell technology is currently only economically competitive in a few specific applications (e.g. on space vehicles).

Power density is another significant limitation. Power density represents the power produced per unit volume (volumetric power density) or per unit mass (mass power density) of a fuel cell.

Although the power density of fuel cells has increased significantly over the last few decades, it needs to be increased further if they are to be competitive in portable electronics and the automotive sector. Internal combustion engines and ordinary batteries often outperform fuel cells in terms of volumetric power density, while they are very close in terms of mass power density.

The availability and storage of fuel pose an even more profound challenge. Fuel cells work best when fuelled by hydrogen, but hydrogen is not readily available, has a

low bulk energy density and is challenging to store. Other alternative fuels are difficult to use directly and often require reforming. All of these issues reduce the performance of the fuel cell and increase the requirement for auxiliary equipment. Thus, although gasoline is an attractive fuel from an energy density point of view, it is not suitable for fuel cell use.

For the time being, the hydrogen energy sector is still in its early stages of development and is an integral part of the zero-carbon, low-carbon era. But hydrogen has strengths and weaknesses in equal measure, so it needs to be used for its strengths and avoided for its shortcomings.

## **Author details**

Xin Gao<sup>1,2\*</sup> and Chengwei Zhao<sup>2</sup>


1 “Fuel Cells for Aviation” of Excellence Cluster SE2A, Technische Universität Braunschweig, Braunschweig, Germany

2 Institut für Energie- und Systemverfahrenstechnik (InES), Institute of Energy and Process Systems Engineering, Technische Universität Braunschweig, Braunschweig, Germany

\*Address all correspondence to: [xin.gao@tu-braunschweig.de](mailto:xin.gao@tu-braunschweig.de)

## **IntechOpen**

---

© 2023 The Author(s). Licensee IntechOpen. This chapter is distributed under the terms of the Creative Commons Attribution License (<http://creativecommons.org/licenses/by/3.0>), which permits unrestricted use, distribution, and reproduction in any medium, provided the original work is properly cited. 

## References

- [1] Sharaf OZ, Orhan MF. An overview of fuel cell technology: Fundamentals and applications. *Renewable and Sustainable Energy Reviews*. 2014;**32**: 810-853
- [2] European Commission, Directorate-General for Mobility and Transport, Directorate-General for Research and Innovation, Flightpath 2050: Europe's Vision for Aviation: Maintaining Global Leadership and Serving Society's Needs. Publications Office; 2011. DOI: 10.2777/50266
- [3] CO2 emissions from Commercial Aviation. International Council on ... (no date). 2018. Available from: [https://theicct.org/sites/default/files/publications/ICCT\\_CO2-commercl-aviation-2018\\_20190918.pdf](https://theicct.org/sites/default/files/publications/ICCT_CO2-commercl-aviation-2018_20190918.pdf). [Accessed: November 16, 2022]
- [4] Noland JK. Hydrogen electric airplanes: A disruptive technological path to clean up the aviation sector. *IEEE Electrical Insulation Magazine*. 2021; **9**(1):92-e102. DOI: 10.1109/MELE.2020.3047173
- [5] Castro AL, Lacava PT, Moura CHB. Feasibility of using fuel cells in a small aircraft. In: *AIAA Aviation 2021 Forum*. Reston, Virginia: American Institute of Aeronautics and Astronautics; 2021
- [6] Wang B et al. Current technologies and challenges of applying fuel cell hybrid propulsion systems in unmanned aerial vehicles. *Progress in Aerospace Sciences*. 2020;**116**:100620. DOI: 10.1016/j.paerosci.2020.100620
- [7] Huang Y, Xiao X, Kang H, Lv J, Zeng R, Shen J. Thermal management of polymer electrolyte membrane fuel cells: A critical review of heat transfer mechanisms, cooling approaches, and advanced cooling techniques analysis. *Energy Conversion and Management*. 2022;**254**:115221. DOI: 10.1016/j.enconman.2022.115221
- [8] Parent KE. Fuel Cells: Energy from Gases Instead of Gasoline [Internet]. acs.org. Available from: <https://www.acs.org/content/dam/acsorg/greenchemistry/education/resources/fuel-cells-energy-from-gases-instead-of-gasoline.pdf>. [Accessed: Nov 2022]
- [9] Kurzweil P. Renaissance Der Brennstoffzelle. In: *Brennstoffzellentechnik Grundlagen, Komponenten, Systeme, Anwendungen*. Wiesbaden, Germany: Springer Vieweg; 2013. pp. 8-9. DOI: 10.1007/978-3-658-00085-1
- [10] Wee J-H. Which type of fuel cell is more competitive for portable application: Direct methanol fuel cells or direct borohydride fuel cells? *Journal of Power Sources*. 2006;**161**(1):1-10. DOI: 10.1016/j.jpowsour.2006.07.032
- [11] [https://en.wikipedia.org/wiki/Proton-exchange\\_membrane\\_fuel\\_cell#History](https://en.wikipedia.org/wiki/Proton-exchange_membrane_fuel_cell#History)
- [12] Rathke P, Kallo J, Schirmer J, Stephan T, Waiblinger W, Weiss-Ungethüm J. Antares DLR-H2 e flying test bed for aircraft fuel cell systems development. *ECS Transactions*. 2013; **51**(1):229-e41. DOI: 10.1149/05101.0229ecst
- [13] DLR - zero-emission air transport [Internet]. DLRARTICLE DLR Portal. Available from: [https://www.dlr.de/content/en/articles/news/2016/20160929\\_zero-emission-air-transport-first-flight-of-four-seat-passenger-airc](https://www.dlr.de/content/en/articles/news/2016/20160929_zero-emission-air-transport-first-flight-of-four-seat-passenger-airc)

raft-hy4\_19469.html. [Accessed: Nov 2022]

[14] Hydrogeit. Hy4 gets permit to fly [Internet]. H2. 2021. Available from: <https://h2-international.com/2021/02/12/hy4-gets-permit-to-fly/>. [Accessed: Oct 2022]

[15] Kandlikar S, Garofalo M, Lu Z. Water management in a pemfc: Water transport mechanism and material degradation in gas diffusion layers. *Fuel Cells*. 2011;**11**:814-823

[16] Chen J, Matsuura T, Hori M. Novel gas diffusion layer with water management function for pemfc. *Journal of Power Sources*. 2004;**131**:155-161

[17] Wang B, Deng H, Jiao K. Purge strategy optimisation of proton exchange membrane fuel cell with anode recirculation. *Applied Energy*. 2018;**225**: 1-13

[18] Halseid R, Vie PJ, Tunold R. Effect of ammonia on the performance of polymer electrolyte membrane fuel cells. *Journal of Power Sources*. 2006;**154**:343-350

[19] Imamura D, Ebata D, Hshimasa Y, Akai M, et al. Impact of Hydrogen Fuel Impurities on PEMFC Performance. *SAE Technical Paper 2007-01-2010*. 2007. DOI: 10.4271/2007-01-2010

[20] Wang H, Turner J. Reviewing metallic pemfc bipolar plates. *Fuel Cells*. 2010;**10**:510-519

[21] Haider R et al. High temperature proton exchange membrane fuel cells: Progress in advanced materials and key technologies. *Chemical Society Reviews*. 2021;**50**(2):1138-1187. DOI: 10.1039/d0cs00296h

[22] Araya SS, Zhou F, Liso V, Sahlin SL, Vang JR, Thomas S, et al. A

comprehensive review of pbi-based high temperature pem fuel cells. *International Journal of Hydrogen Energy*. 2016;**41**: 21310-21344. [Accessed: Nov 2022]

[23] Hartnig C, Schmidt TJ. On a new degradation mode for high-temperature polymer electrolyte fuel cells: How bipolar plate degradation affects cell performance. *Electrochimica Acta*. 2011;**56**:4237-4242

[24] Deutsches Zentrum für Luft- und Raumfahrt. Emissionsfreier Antrieb für die Luftfahrt: Erstflug des viersitzigen Passagier- flugzeugs HY4. 2016. Available from: [https://www.dlr.de/content/de/artikel/news/2016/20160929\\_emissionsfreier-antrieb-fuer-die-luftfahrt-erstflug-des-viersitzigen-passagierflugzeugs-hy4\\_19469#/gallery/24480](https://www.dlr.de/content/de/artikel/news/2016/20160929_emissionsfreier-antrieb-fuer-die-luftfahrt-erstflug-des-viersitzigen-passagierflugzeugs-hy4_19469#/gallery/24480). [Accessed: November 26, 2020]

[25] Srinath AN, Pena Lopez A, Miran Fashandi SA, Lechat S, Di Legge G, Nabavi SA, et al. Thermal management system architecture for hydrogen-powered propulsion technologies: Practices, thematic clusters, system architectures, future challenges, and opportunities. *Energies*. 2022;**15**(1):304. DOI: 10.3390/en15010304

[26] Kadyk T, Schenkendorf R, Hawner S, Yildiz B, Roemer U. Design of fuel cell systems for aviation: Representative mission profiles and sensitivity analyses. *Front Energy Res*. 2019;**7**:35. DOI: 10.3389/fenrg.2019.00035

[27] NASA. U.S. Standard Atmosphere. Available from: <https://ntrs.nasa.gov/api/citations/19770009539/downloads/19770009539.pdf>. [Accessed: May 31, 2022]

[28] Kozulovic D. Heat release of fuel cell powered aircraft. In: *Proceedings of Global Power and Propulsion Society*. 2020. DOI: 10.33737/gpps20-tc-99

- [29] Piancastelli L, Frizziero L, Donnici G. The Meredith ramjet: An efficient way to recover the heat wasted in piston engine cooling. *Journal of Engineering and Applied Science*. 2015; **10**(12):5327-5333
- [30] Martinez-Val R, Perez E, Palacin J. Historical perspective of air transport productivity and efficiency. In: 43rd AIAA Aerospace Sciences Meeting and Exhibit. 2005. DOI: 10.2514/6.2005-121
- [31] Chen L, Kang Q, Tao W. Pore-scale study of reactive transport processes in catalyst layer agglomerates of proton exchange membrane fuel cells. *Electrochimica Acta*. 2019; **306**:454e65. DOI: 10.1016/j.electacta.2019.03.158
- [32] Ryan EM, Mukherjee PP. Mesoscale modelling in electrochemical devices: a critical perspective. *Progress in Energy and Combustion Science*. 2019; **71**:118-e42. DOI: 10.1016/j.peccs.2018.11.002
- [33] Chen Q, Niu Z, Li H, Jiao K, Wang Y. Recent progress of gas diffusion layer in proton exchange membrane fuel cell: Two-phase flow and material properties. *International Journal of Hydrogen Energy*. 2021; **46**:8640-8e71. DOI: 10.1016/j.ijhydene.2020.12.076
- [34] Sui PC, Djilali N. Analysis of coupled electron and mass transport in the gas diffusion layer of a PEM fuel cell. *Journal of Power Sources*. 2006; **161**:294-e300. DOI: 10.1016/j.jpowsour.2006.03.079
- [35] Bazylak A. Liquid water visualisation in PEM fuel cells: A review. *International Journal of Hydrogen Energy*. 2009; **34**:3845e57. DOI: 10.1016/j.ijhydene.2009.02.084
- [36] Um S, Wang C-Y, Chen KS. Computational fluid dynamics modelling of proton exchange membrane fuel cells. *Journal of the Electrochemical Society*. 2000; **147**:4485. DOI: 10.1149/1.1394090
- [37] Shen J, Tu Z, Chan SH. Performance enhancement in a proton exchange membrane fuel cell with a novel 3D flow field. *Applied Thermal Engineering*. 2020; **164**:114464. DOI: 10.1016/j.applthermaleng.2019.114464
- [38] Kulikovskiy AA, Divisek J, Kornyshev AA. Modeling the cathode compartment of polymer electrolyte fuel cells: Dead and active reaction zones. *Journal of the Electrochemical Society*. 1999; **146**:3981-3e91. DOI: 10.1149/1.1392580
- [39] Wu W, Jiang F. Microstructure reconstruction and characterization of PEMFC electrodes. *International Journal of Hydrogen Energy*. 2014; **39**:15894-1e906. DOI: 10.1016/J.IJHYDENE.2014.03.074
- [40] Nabovati A, Hinebaugh J, Bazylak A, Amon CH. Effect of porosity heterogeneity on the permeability and tortuosity of gas diffusion layers in polymer electrolyte membrane fuel cells. *Journal of Power Sources*. 2014; **248**:83-e90. DOI: 10.1016/J.JPOWSOUR.2013.09.061
- [41] Zamel N, Li X, Shen J. Numerical estimation of the effective electrical conductivity in carbon paper diffusion media. *Applied Energy*. 2012; **93**:39-e44. DOI: 10.1016/J.APENERGY.2011.08.037
- [42] Yablecki J, Bazylak A. Determining the effective thermal conductivity of compressed PEMFC GDLs through thermal resistance modelling. *Journal of Power Sources*. 2012; **217**:470-4e8. DOI: 10.1016/j.jpowsour.2012.06.011
- [43] Lange KJ, Sui PC, Djilali N. Pore scale modeling of a proton exchange membrane fuel cell catalyst layer: Effects

of water vapor and temperature. *Journal of Power Sources*. 2011;**196**:3195-e203. DOI: 10.1016/j.jpowsour.2010.11.118

[44] Scott P, Chen Y, Calay R, Bhinder F. Experimental investigation into a novel modular PEMFC fuel cell stack. *Fuel Cells*. 2015;**15**:306-321. DOI: 10.1002/fuce.201200212

[45] Airbus: Getting to Grips with ETOPS: Flight Operations & Line Assistance. 1998. Available from: <https://www.737ng.co.uk/AIRBUS%20ETOPS%20Guide.pdf>. [Accessed: November 26, 2020]

[46] Bahrebar S, Blaabjerg F, Wang H, Vafamand N, Khoo-Ban M-H, Rastayesh S, et al. A novel type-2 fuzzy logic for improved risk analysis of proton exchange membrane fuel cells in marine power systems application. *Energies*. 2018;**11**:721. DOI: 10.3390/en11040721

[47] Knights SD, Colbow KM, St-Pierre J, Wilkinson DP. Aging mechanisms and lifetime of PEFC and DMFC. *Journal of Power Sources*. 2004;**127**:127-134. DOI: 10.1016/j.jpowsour.2003.09.033

[48] Le Canut J-M, Abouatallah RM, Harrington DA. Detection of membrane drying, fuel cell flooding, and anode catalyst poisoning on pemfc stacks by electrochemical impedance spectroscopy. *Journal of Power Sources*. 2006;**153**:A857. DOI: 10.1149/1.2179200



## Chapter 5

# Cyclic Oxidation of Diffusion Aluminide Coatings

*Marta Kianicová*

### Abstract

The diffusion aluminide coatings are used for high-temperature applications. Structural materials of particular components degrade during service due to fatigue, creep, oxidation, corrosion and erosion. The requirements of higher efficiency of modern industrial applications increase the development of new structural materials, technologies and protective coatings. Properties of many structural materials such ultimate tensile strength, creep strength and fatigue are generally optimized for maximum high-carrying loading with less emphasis on environmental resistance. For these applications, the performance characteristics are limited by the operating conditions, which can be tolerated by the used materials. The main structural materials for high mechanical and thermal loading are superalloys protected against aggressive environment by coatings. Cyclic oxidation is the superposition of thermal cycles in an oxidation environment. The main goal of the experimental work was to compare the cyclic oxidation of protective Al and AlSi coatings deposited on both Inconel 713 LC and MAR-M247 superalloys. The resulting graph revealed that samples from IN 713 LC without coating show good resistance and their mass change is maintained above zero limit. Samples from MAR 247 LC with both Al and AlSi coatings appear to be the most acceptable selection of combination relating to superalloys/coating.

**Keywords:** cyclic oxidation, superalloys, diffusion aluminide coating, CVD deposition

### 1. Introduction

Increasing the technical level, utility values, quality and reliability of engineering components belong to the main directions of economic development. The surface treatment also plays a significant role in the final quality of the structural unit. An inappropriate choice of surface treatment, non-compliance with the technological procedure or just an unaesthetic appearance can devalue an otherwise excellent technical work.

Surface engineering includes those processes that make it possible to modify the surfaces of structural components with the aim of improving primarily their mechanical and utility properties and, last but not least, their esthetic appearance, or

to reduce the economic costs of production. It is therefore a modification of the surface of the component, which does not affect the bulk properties. The main goal is to increase the service life of components and the operational reliability of equipment. It is often aimed at increasing corrosion resistance, surface sliding wear resistance, providing a diffusion barrier, thermal insulation, etc. while reducing production costs, especially energy savings with an impact on minimizing environmental pollution.

There are several ways to treat metal surfaces, which can be divided into three main categories:

1. **Strengthening by phase transformation** is the treatment of the surface without changing the chemical composition of the substrate, while the structure of the surface is changed by thermal or mechanical treatment. The most common request is to increase the hardness while maintaining the toughness of the bulk material.
2. **Modification of surface layers by changing its chemical composition** through diffusion processes at elevated temperatures without affecting the properties of the substrate.
3. **Surface treatment by coating deposition.** This group includes a wide group of coating processes, where the properties and chemical composition of the substrate differ significantly from the substrate. Unlike previous surface treatment methods, the coating/substrate interface is clearly distinguishable in this method. The most important aspect is the thickness of the coating, its porosity and adhesion.

## **1.1 Modifying the surface without altering chemical constitution.**

### **A. Heat treatment**

Heat treatment is the practical application of physical metallurgy with the aim of modifying the material structure to obtain desired properties. Strengthening by phase transformation essentially belongs to thermal technology processing. Surface hardening is a common method of changing the mechanical properties of surface layers especially for steels. The purpose of this treatment is to increase hardness and wear resistance component surface. The conditions of transformation or breakdown of austenite are decisive depending on temperature, time and rate of cooling. To austenitize the surface layer, it is necessary to perform heating at a higher rate than the heat is dissipated into the part. Phase diagrams are used to understand the heat treatment process. For example, an Isothermal diagram (IT) describes the formation of austenite, Time Temperature Transformation (TTT) diagram describes the decomposition of austenite, Continuous Cooling and Continuous Heating diagrams are commonly referenced to as CCT and CHT diagrams, which are also used to understand the effects of heating and cooling of steel during heat-treatment process [1]. In practice, heating is commonly used by flame or electrical induction. Recently, they have been focusing on themselves for changes induced by laser irradiation or electron

beam techniques [2–6]. Surface heat treatments by laser are manufacturing technologies that are gaining industrial interests in the last years.

Laser radiation makes it possible to concentrate the power density up to  $10^{16} \text{ W.m}^{-2}$  and deliver considerable amount of energy to the treated surface contactlessly and quickly. To the characteristic energy parameters of radiation, pulse length or speed of movement have a great influence on the temperature field temperature source (for a continuous laser), temperature-physical characteristics and geometric dimensions processed body. Depending on the power density and duration of action, either only heating and cooling in the solid phase takes place in the surface layer, or there is melting of the surface and the possibility of forming an amorphous state during particularly rapid cooling. Rapid temperature and structural changes cause thermal stresses, which can also result in the formation of cracks. Lasers are particularly suitable for curing relatively small or inaccessible surfaces. Laser is considered a useful technique since it offers control over case depth, uniform microstructure, uniform hardness, and minimum material distortion. Laser transformation hardening of steels is a diffusion-less transformation process and eliminates the formation of pearlite phases [7].

In addition, the interestingness of this process lies in the possibility of direct integration of a very flexible laser heat source without the use of a quenching medium, as well as in the possibility of producing various microstructures with a hard surface and residual compressive stresses. Electron beam techniques have lower investment and operating costs.

## B. Mechanical treatment

**Cold working** the surface by shot peening or other specialized surface treatments were designed to enhance the surface integrity and service life of structural components. Most of these mechanisms are very sensitive to microstructure. Surface treatments like Ultra Sonic Peening, Laser Shock Peening, and Shot Peening are used to enhance the surface microstructural properties that help in improving the service life. These applications lead to deformed surface layers and increase the stored energy, form compressive residual stresses due to higher density of defects in the crystal structure, increase the hardness, fatigue life and stress corrosion resistance. Residual compressive stresses and increased surface hardness are the key outcomes of shot peening [8–10]. The simulation methodology and numerical prediction are used to optimize microstructure and shot peening parameters to reduce the relaxation of compressive residual stresses during service life [11].

## C. Thermomechanical treatment

This process consists of a combination of heat treatment and plastic deformation. Thermomechanical processing is based on a combination of several operations such as deformation, heating and cooling performed in different cycles, which further determine their classification. A high density of structural imperfections such as dislocations, vacancies or layer defects and their

distribution due to deformation mechanisms affect the processes of structural changes and thus the resulting properties and integrity of the surface of the components. However, structural changes generate new ones and redistribute the original ones. Thus, the mechanism and kinetics of these structural changes depend on the nature and density of imperfections and consequently affect the number and distribution of such imperfections. Thermomechanical treatment is although used to improve the mechanical properties of alloys by introducing twins and nano-precipitation phase in the lamellar structure of the homogenized alloys [12]. Multi-stage thermomechanical processing with the stepwise temperature reduction can improve not only the mechanical but also the electrical properties of the alloy [13].

## 1.2 Altering the chemistry of surface regions of the substrate

- i. **Thermochemical diffusion treatments** are widely applied to transport reactive interstitial elements (carbon, nitrogen, boron or their combinations) from a medium (gas, plasma etc.) to the surface of structures. Reaction of these elements with solid under higher temperatures lead to the phase transformation and forming of separate layers at the surface [14]. Thermomechanical processes such carburizing, nitriding, boriding or carbonitriding are different from processes chromizing, aluminizing and siliconizing in which the elements Cr, Al or Si are represented as a substitute in a solid solution. Diffusion of interstitial elements into steels can take place at low (ferritic range) or high temperatures (austenitic range). This processes are also used for decreasing friction coefficients and improving wear resistance of structures [15].
- ii. **Ferritic processes** include convenient gas nitriding to enhance the surface hardness of structures by uniform nitride layer [16]. Plasma nitriding diffusion technique improve tribological properties of steel surfaces depending on processing parameters and demanded layer characteristics [17]. Low thermal ferritic nitrocarburizing include various treatment media such salth bath, endothermic ammonia gas mixtures, and methane or propane/ ammonia/oxygen mixtures. Nitrocarburized layers consist of an inner diffusion layer and outermost thin compound layer, which is detrimental due to its brittle nature. Transition layer can be formed between the above two layers in some cases [18].
- iii. **Austenitic treatments** broadly include carburizing process, which requires a high temperature and carbon donor. Various agents fulfill the function carbon donor for the different carburizing processes (powder, salt bath or gas atmospheric and low pressure carburizing). Carbonitriding and boronizing belong to the austenitic treatment and they are performed at elevated temperatures (near 900°C). Laser-beam carburizing process is used to enhance fatigue wear resistance of surface steel structures. In this process, the surface of the material is coated with graphite prior to laser irradiation. Carburizing can be achieved by two mechanisms: (a) the surface alloying mechanism, which incorporates melting of the substrate and dissolution of the graphite in the liquid phase; and (b) the solid-state diffusion mechanism, which incorporates austenitization of the substrate and carbon diffusion in austenite [19].

- iv. **Electroplating** is the process using electrodeposition of metals onto surface from an anode (part containing desired metal) to a cathode (part to be plated). The anode and the cathode are placed into electrolyte chemical bath and exposed to the electrical charge. This process has high productivity, simplicity of equipment and low operating costs. More metals (Cd, Cr, Cu, Au, Fe, Ni, Ag, Ti, Zn) and their combination can be used for electroplating. Plastic parts manufactured by 3D printing can be also electroplated [20, 21]. This combination offers unique tensile strength options for finished designs.
  
- v. **Oxide coatings** have been developed for large variety of properties such as high chemical stability, crystal structures, compositions, physical, mechanical, optical or electrical properties with various thickness, porosity etc. In general, they are brittle at room temperature. They are largely used as insulating coatings. Thin layer of oxide coatings deposited on the surface serve as physical barrier between substrate and environment. Metals, nonmetals and ceramics can be used as protective coatings and various method has been applied to form functional coatings.  
  
Nowadays, the structural materials made for marine, aerospace engineering, transport vehicles must be protected against corrosion, abrasion, or high temperature oxidation and dense and adhesive oxide coatings improve the resistant of substrates against these degradation modes and enhance the surface chemical and mechanical properties [22]. Nanocoatings developed in thin layer having scale 1–100 nanometers thickness offer much better processing properties than conventional coatings. They provide effective solution against chemical or mechanical effects. Nanocoatings are not protective layers but their particles bind themselves both physically and chemically to the substrate surface and give it very good protection. Nanocoatings have huge application in different industries except for automobile, marine or aircraft industries, also in defense, electronic or medical industries [23, 24].
  
- vi. **Sulfur treatments** are used due to their good lubricating properties. Laser cladding and low temperature ion sulfurizing technology (300°C) are processes for deposition of sulfur layers with wear resistance and self-lubrication performance. The resulting product FeS layer have excellent anti-friction properties [25].
  
- vii. **Phosphating** is one of the most treatment technology in electrical or automotive industries because low production cost and simplicity. Processes include zinc, calcium, manganese or magnesium phosphate coatings especially with excellent lubricity. Chemicals involved in oxidizing accelerators such as nitrates, nitrites, chlorates, hydrogen peroxide, etc. and heavy metal ion accelerators, which are usually toxic to humans and lead to the environmental problems. Therefore, the main goal is to investigate ECO-friendly accelerators for phosphating process [26, 27].
  
- viii. **Ion Implantation** is the most common application in the semiconductor industry. Various ions can be implanted onto steel structures with the aim to control crack propagation and corrosion. The technology by which ions of gaseous or metallic elements are accelerated in an electrical field and

impacted into a solid. Ions impinging on the component cause many chemical and physical changes of materials transferring energy and momentum to electrons causing a structural change. The ion energy and the target composition determine the depth of ion penetration. Some studies reported that some of ions have antimicrobial effect and its nanoparticles act as antimicrobials [28].

### **1.3 Surface treatment by coating deposition**

The current age is the age of surface treatment technologies that allow countless possibilities of obtaining coatings with multiple properties. State-of-the-art manufacturing techniques are used in diverse areas, such as optical memories and filters, fiber lasers, LED displays, various implants or environmental devices.

- i. **Weld cladding** is technique to achieve enhanced mechanical and tribological properties of several engineering components such as high strength and corrosion resistance. It is technique that allows to create relatively thick coating on substrate material (from 1 mm to several cm) using TIG welding, plasma transferred arc cladding or laser beam cladding [29].
- ii. **Laser surface alloying** have been used for improve mechanical properties and promote functional applications and of surfaces of advanced structural applications [30]. This technique makes it possible to obtain novel multiphase coatings to improve mechanical, wear properties and refine the microstructure [31].
- iii. **Thermal spraying** is an important surface modification method and plays crucial role in industrial production for depositing of metals, alloys, metal oxides, various ceramic and composite materials or polymers on a variety of substrates to form functional surfaces. Key functions include restoration, corrosion and erosion protection, heat insulation or conduction, electrical insulation or conduction etc. Thermal spraying can be formed either by deposition of ductile solid metals (referred as cold spaying) or by deposition through molten or semi-molten particles (flame spraying, high-velocity oxygen or air fuel, plasma spraying, wire arc spraying). Among advantages of these processes belong high deposition rate, low processing cost, wide thickness range and minimal degradation of substrates. However, this technology is a line-of-sight process and coatings have lower bond strength, are porous and have anisotropic properties. Porosity is sometimes beneficial in case the coating must have low thermal conductivity [32]. Liquid thermal spraying provides a novel method for preparation of micro-nano structured coating, which significantly reduces manufacturing cost. In this method suspended droplets in the plasma are first atomized and vaporized, then partially sintered and melted before hitting the substrate surface to form a coating [33].
- iv. **Galvanizing** is the process of forming coating with zinc which provides corrosion protection of steels. Galvanized coatings are widely used for steel reinforcement in concrete to increase the long-term service life of concrete

structures. It has been shown that galvanized bar slows down cracking during service and concrete spalling is less likely or delayed [34].

- v. **Chemical Vapor Deposition (CVD)** is based on the dissociation of metal compound vapors at elevated temperatures to produce thin, diffusion-bonded, adherent coatings of metal carbides, nitrides, carbo nitrides and oxides; typically TiN, TiC, Ti(CN) and Al<sub>2</sub>O<sub>3</sub>. CVD coatings are used on carbide tool tips (indexable inserts) and on selected tribological items. Plasma assisted chemical vapor deposition (PACVD) uses electrical discharge to produce plasma and this method permit forming of thin solid film on the substrate. Recent studies have reported higher effectiveness of process and better properties of uniform coating using hollow cathode [35].
- vi. **Physical Vapor Deposition (PVD)** is a process based on physical principles. The essence of the method is thermal evaporation of the material from the target, or ion sputtering on the surface of the substrate, where a thin, highly adhesive layer is subsequently formed. PVD processes take place at relatively low temperatures of (150-500) °C in the presence of an inert gas or a vacuum, in which no toxic substances are released. Therefore, this method is ecological and characterized by high purity of the process. In most cases, the grain sizes in PVD coatings are below 100 nm and are therefore classified as nanostructured materials. The properties of PVD coatings are mainly influenced by their chemical composition, structure (size and shape of grains, number and distribution of defects, density of the coating) and also residual stresses, which depend on the application method and parameters. PVD processes generate compressive stresses in the coatings, and the coatings exhibit high modulus of elasticity, hardness and low coefficient of friction. The PVD coating process includes various techniques such as arc evaporation, magnetron sputtering and ion plating, which make it possible possible to apply thin layers of precisely determined thicknesses to the base material [36].
- vii. **Painting** is the technology of applying a thin organic coating to the surface of a material for the purpose of corrosion protection of substrates or improving the esthetic appearance. Compared to other processes for protection or decoration, the technology offers a number of advantages such as lower costs, a wide range of coatings with requirements for color, gloss and surface structure, resistance of the coating to various corrosion agents and their combinations, good dielectric properties, if necessary also ensuring suitable conductivity for grounding induced or static electricity. The organic coatings have been developed to meet the latest environmental regulations.

The preceding brief review shows an extraordinary extend and variability of methods utilized in the surface engineering. Hereafter, we will focus on some important kinds of coatings on metallic surfaces and the processes of their degradation in service. Metals as the primary construction materials used in industry are exposed to oxidation and to active chemical environment. To ensure the quality and protection of metal products, different kinds of metal coatings are employed in the industry. There are two basic determinants of metal coatings.

The first class of coatings serves as a protection against the aggressive environment, i.e., they increase the resistance to thermal oxidation, corrosion and erosion.

The second class represents layers obtaining by surface hardening which increases surface strength for load carrying, surface hardness of a substrate material and introduce compressive residual stresses.

Thus, with respect to their function, the coatings can be divided into two main classes:

- i. surface protection and.
- ii. surface hardening.

Diffusion aluminide coatings (DACs), overlay coatings and thermal barrier coatings (TBCs) are typical representatives of the first class. They improve the resistance to high temperature creep, fatigue, thermal oxidation, corrosion and erosion. Nickel and cobalt based superalloys are mostly utilized as substrate materials for turbine blades, blade rings, stator/rotor discs, etc. From the point of view of corrosive and oxidizing effects, to the monolayer protective coatings belong DAC and overlay coatings. DAC are based on the intermetallic compound  $\beta$ -NiAl that forms under the influence of the substrate (usually Ni superalloys). The technological procedures lie in various methods of deposition of an equally balanced suspension of aluminum- and silicon powders on the substrate surface together with activators (e.g.,  $\text{NH}_4\text{Cl}$ ) and organic binders (e.g. coloxylin). Diffusive tempering is applied at about  $1000^\circ\text{C}$  in an inert argon atmosphere or vacuum with the dwell time of several hours and subsequent slow cooling in the retort. As shown in **Figure 1**, the resulting microstructure of the layer consists of two sublayers – the outer layer (OL) and the diffusion zone (DZ). The microstructure of OL is composed of the  $\beta$ -NiAl phase with small number of complex phases and carbides Al-Cr-Ni, Mo-Cr-Nb. The DZ is formed by  $\beta$ -NiAl with

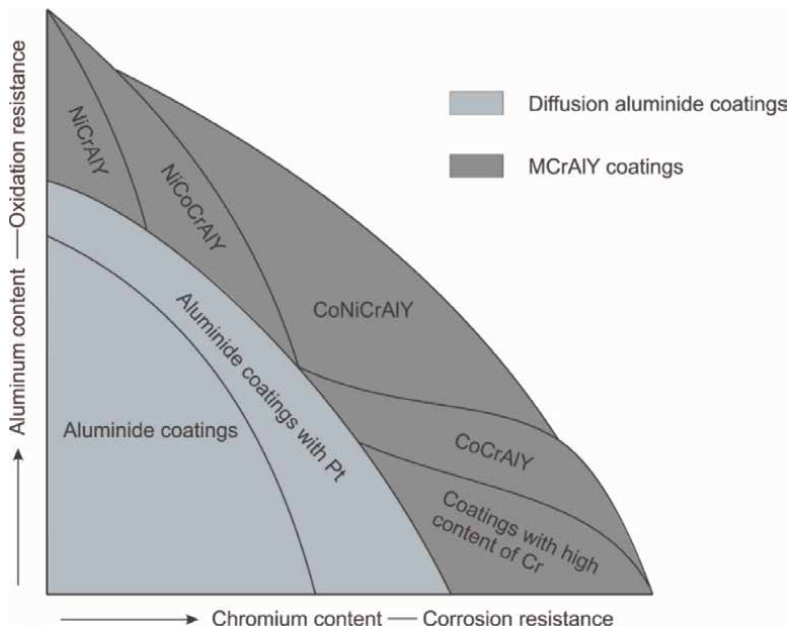


**Figure 1.** Corrosion and oxidation resistance of metallic coatings on superalloys.



many Cr-Mo, Mo-Cr-Nb rich particles. DACs are an integral part of the substrate material with just a slightly higher hardness. Their primary role is to protect the surface from high-temperature oxidation, corrosion and erosion but they should not reduce the resistance to creep, cyclic creep and thermo-mechanical fatigue [37]. On the other hand, the composition of the overlay coatings (known as MCrAlX) remains independent of the substrate alloy.

The most popular representatives of the second class are carburized or nitrided surface layers (CNSLs) produced by gas diffusion or plasma deposition processes - the case hardening. This process increases the surface hardness of a substrate material and introduces compressive residual stresses which results in a higher resistance to fatigue and wear of low-carbon steels, the materials mostly used in various dynamically loaded components as gears and shafts at room temperature. All the above mentioned components are subjected to cyclic loading in bending (tension) or, most frequently, to a combined bending (tension)/torsion loading.

## 2. Diffusion aluminide coatings

The diffusion aluminide coatings belong to the wide category of coatings used for high-temperature applications. Structural materials of particular components degrade during service due to fatigue, creep, oxidation, corrosion and erosion. With requirements of higher efficiency of modern industrial applications increase the development of new structural materials, technologies and protective coatings. Properties of many structural materials such as ultimate tensile strength, creep strength and fatigue are generally optimized for maximum high-carrying loading with less emphasis on environmental resistance. For these applications, the performance characteristics are limited by the operating conditions which can be tolerated by the used materials. The main structural materials for high mechanical and thermal loading are nickel and cobalt-base superalloys protected against aggressive environment by coatings [38–39]. The coating systems currently in use particularly in gas turbine blade applications can be divided into three generic groups [40]:

1. Diffusion aluminide coatings (DACs) are based on the intermetallic compound  $\beta$ -NiAl that forms under the influence of the substrate (usually Ni superalloys). Application processes include pack cementation and gas-phase processes such as chemical vapor deposition.
2. The properties of MCrAlX substrate/coating system (where M represents elements of Ni, Co, Fe or their combination; X represents minor elements such as Y, Ce, Si, Ta, Hf, etc.) can be controlled and balanced for a specific application. In **Figure 1** it is demonstrated how the applied coating can be selected on basis of the corrosion and oxidation performance.
3. Thermal Barrier Coatings (TBCs) is a complex system, which consist of three different layers: ceramic top layer (typically of YSZ), thermally grown oxide (TGO formed at TBC/BC interface), metallic bond coat (BC) and substrate.

The coatings deposited on rotor turbine blades provide an optimal protect in the range of specified lifetime against destructive effects of high-temperature corrosion, oxidation and erosion provided the following requirements are satisfied [41]:

- High oxidation and corrosion resistance.

The coating must be thermodynamically stable and creates protective thin oxide film of uniform thickness. Slow growth rate of protective and adherent scale is desirable. In accordance with these requirements the coating should contain higher content of element (Al, Cr) to able to form protective scales.

- Interface stability. Low diffusion rate across the interface coating/substrate at use temperatures, minimized brittle phase formation and no undesired changes within coating are required.
- Good adhesion. Good adherence of coating to substrate; optimized properties of coating surface before deposition (rough or smooth); matched coating/substrate properties to reduce thermal stresses; minimized growth of residual stresses during coating deposition.
- Mechanical strength. Coating must withstand service-related stresses (creep, fatigue and stresses generated by impact of others particles). Suitable combination of strength and toughness is demanded and similar match of both thermal expansion coefficients for minimization of thermal stresses and thermal fatigue.

Diffusion aluminide coatings have been designed to protect nickel-base superalloys at elevated temperatures and they are based on simple aluminide or modified aluminide compounds. DACs and modified DACs involve the surface layers of substrate alloy which is enriched with aluminum, chromium, silicon, platinum, zirconium, palladium, yttrium or hafnium to form protected oxides through diffusion and/or enhance TGO adherence [42]. Their thickness is in the range of (10–100)  $\mu\text{m}$ . These elements react with the main constituents of substrate and form intermetallic compounds (aluminides) with significant part of element comprising protected oxide. For nickel-base superalloys NiAl (Figure 2) is the main aluminide compound of coating which produces corrosion and oxidation resistant thermally grown oxide.

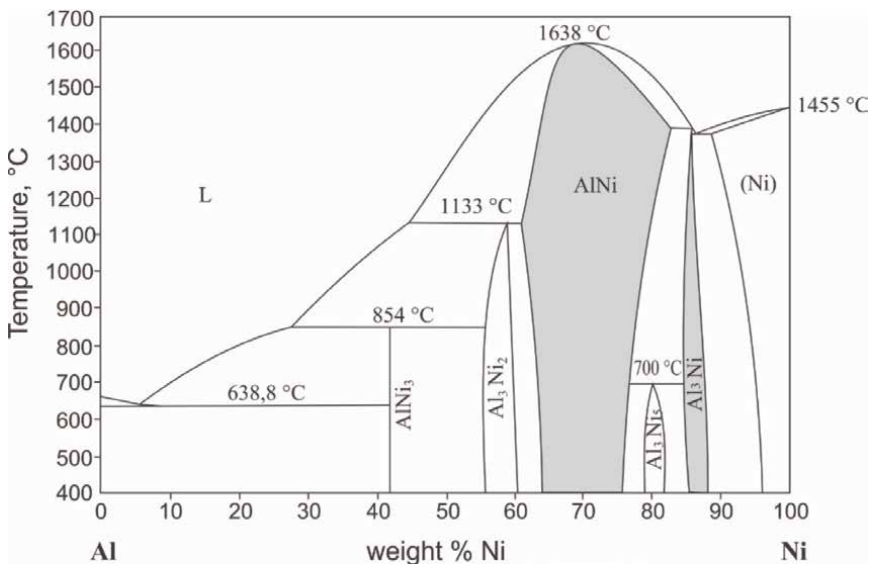


**Figure 2.**  
*Binary phase diagram Al-Ni.*

The selection of the appropriate coating composition depends on requirements of the corrosion/oxidation resistance and the environment. The main alloying elements in metallic coatings are briefly described below [43, 44]:

**Nickel** is the base element in DACs in Ni base substrates because it depresses chemical activity of Al and minimizes the interdiffusion between coating and substrate.

Aluminum form on the top of coating oxide  $Al_2O_3$  which protects against oxidation up to 1200°C.

**Chromium** reduces critical level of Al needed to form alumina and chromium oxides protect coating against hot corrosion and oxidation up to 900°C.

**Silicon** is effective against low temperature hot corrosion and promotes formation of  $Al_2O_3$ .

**Platinum** increases TGO adherence as well as reduces oxidation kinetics. The presence of Pt in a solid solution, or as two-phase coating, provide resistance to I. type of hot corrosion; if a continuous  $PtAl_2$  phase is present, coating is resisting against II. type of hot corrosion.

**Zirconium** has beneficial effect on the adhesion of TGO, it hinders the outward diffusion of Al cations.

**Palladium** provides excellent high temperature oxidation resistance and scale adhesion by reducing or preventing void growth, mitigating the detrimental effects of sulfur and accelerating alumina scale healing after spallation. Pd replaces Pt in aluminide coatings due to high costs of Pt.

**Yttrium** is a typical oxygen-active element which has beneficial effect on corrosion behavior of coatings.

**Hafnium** additions to aluminides markedly improve the adhesion of thermally grown oxides thereby improving the high-temperature oxidation performance.

DACs are the most spread types of coatings for turbines blades. Their disadvantage is strong dependence on substrate composition. For the application in aerospace industry is very important to find the critical ductile-to-brittle transition temperature (DBTT) which limits the utilization. Material undergoes under DBTT to failure by brittle fracture. The DBTT of diffusion aluminide coatings on superalloys varies between (700 up to 900) °C [45]. Some of the factors influencing the DBTT are coating process, composition, microstructure and phase distribution. With decreasing content of Al, thickness and roughness of coating DBTT decreases. DBTT of NiAl phase is reduced by more than 100°C when Al content is lowered from 32 to 25 wt. %.

## 2.1 Technologies of deposition

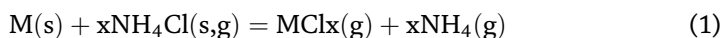
Results of many examinations have confirmed that aluminide coatings are characterized with very good corrosion and oxidation resistance at high-temperatures. They have homogeneous microstructure with good thermomechanical properties. In order to protect critical internal surfaces from oxidation and hot corrosion, the state of the art involves the use of diffusion coatings, formed by pack cementation, chemical vapor deposition (CVD), above-the-pack diffusion processes and/or by slurry cementation.

### 2.1.1 Pack cementation

Halide-activated pack cementation is a CVD process in which “pack” is made up of a mixture of a pure metal or alloy source, a halide salt activator and an inert filler material, usually  $Al_2O_3$ .

A filler allows the active pack constituents (the master alloy and activator salt) to be well distributed. This allows the halide vapors to easily reach the substrate surface, resulting in an overall uniform coating. The substrate to be coated is either buried inside the pack (the ‘in-pack process’) or suspended outside the pack (the ‘out-of-pack’ process). A controllable atmosphere, usually Ar or H<sub>2</sub>/Ar, surrounds the pack as it is heated at a definite process temperature ranging from 700 to 1050°C. The metallic powder reacts with the halide salt activator to form volatile metal halide species of significant partial pressures. In the case of Pt-modified aluminide coatings, components are electroplated with a thin Pt layer prior to the aluminization.

Suppose NH<sub>4</sub>Cl is used as the activator, the reaction will be given below [46]:



where M is the element to be coated.

For aluminizing process Al, AlCl, AlCl<sub>2</sub> and AlCl<sub>3</sub> vapor substances can be formed and for chromizing Cr, CrCl<sub>2</sub>, CrCl<sub>3</sub> and CrCl<sub>4</sub>.

Partial pressure gradients support vapor transport to the metal surface where desired coating specified phase, microstructure and composition forms via dissociation or disproportionation of the halide molecules and reaction with substrate.

On this basis, the pack cementation can be described as follows [46]:

- i. the reaction and a thermodynamic equilibrium between the activator and the powder, which determines the vapor pressures of the active gaseous substances in the pack;
- ii. the movement of these gases through the porous pack;
- iii. diffusion of the metal halides to the alloy matrix surface;
- iv. reactions on the surface to deposit the coating elements and form the products with vapor substances; and.
- v. solid-state diffusion of the coating elements into the matrix to form the protective surface layer.

Illustration of these events are schematically visible in the **Figure 3**. All of these events dictate the nature of the final microstructure and thickness of the surface layer.

There are several pack cementation processes, i.e. pack aluminizing, chromizing, siliconizing, or co-deposition needed for suitable surface layers. Aluminized coatings and chromized coatings are two traditional diffusion coatings that have been extensively used for almost a century.

Halide-activated pack cementation is a simple and inexpensive process useful for different structure geometries and sizes. It has great potential for using by innovative ways.

### *2.1.2 Chemical vapor deposition*

In the CVD method two basic processes, i.e. the low-activity and high-activity process of aluminizing are distinguished. During the aluminide coating deposition process at high temperature, about 1050°C, low aluminum content NiAl phases are

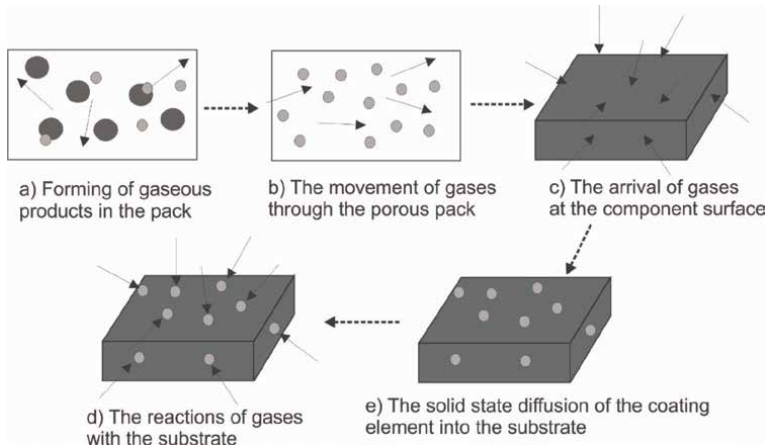


**Figure 3.**  
*Illustration of steps occurring in the pack cementation process.*

created (low activity process), whereas at about 700°C, NiAl phases containing more aluminum are formed (high activity process).

In “low-temperature high activity” (LTHA) process the coating grows by the inward diffusion of Al and Ni<sub>2</sub>Al<sub>3</sub> ( $\delta$ -phase) forms at the matrix surface. Al further diffuses inward and the initial surface of the substrate remains at the outermost surface upon aluminizing. Alloying elements that diffuse more slowly and carbides in the substrate remain in  $\delta$ -phase. Ni<sub>2</sub>Al<sub>3</sub> is a brittle phase and further vacuum annealing is necessary to transform it into desired thermodynamically stable NiAl ( $\beta$ -phase). A disadvantage of coatings obtained by LTHA process an overall thickness of structures, in some cases is not possible to use LTHA technology.

In “high-temperature low activity” (HTLA) process, thermodynamic activity of Al is lower and the coating grows by the outward diffusion of Ni, which leads to direct formation of additive  $\beta$ -NiAl phase above the initial surface. Interdiffusion zone forms in the substrate due to depletion of Ni and slowly diffusing elements.

Mixed coating growth mechanisms are also known and involve the diffusion of both Al and Ni [47]. This is schematically illustrated below (**Figure 4**).

An effective role of diffusion barrier between the coating and superalloy would slow the loss of Al to the substrate and limit or delay diffusion of refractory elements into the coating. Microstructure of superalloys IN 713 LC after aluminizing and heat treatment is visible in the **Figure 5**.

The CVD method gives the possibility of control of the AlX<sub>n</sub> concentration and the temperatures of the processes and through this control of aluminizing process. The HTLA CVD aluminizing process indicate superior oxidation resistance compared with the LTHA process because clean  $\beta$ -NiAl phase is free of precipitates and carbides.

### 2.1.3 “Out of pack” or “over-pack” method

This method operates in a manner very similar to pack cementation; except the parts to be coated are suspended either above the pack or downstream from the pack (vapor generating) retort. The technology is based on placing the parts to be coated in a retort or vacuum furnace oven without coming into direct contact with the granulated mixture. The transfer of gases, which ensure the formation of the coating, is

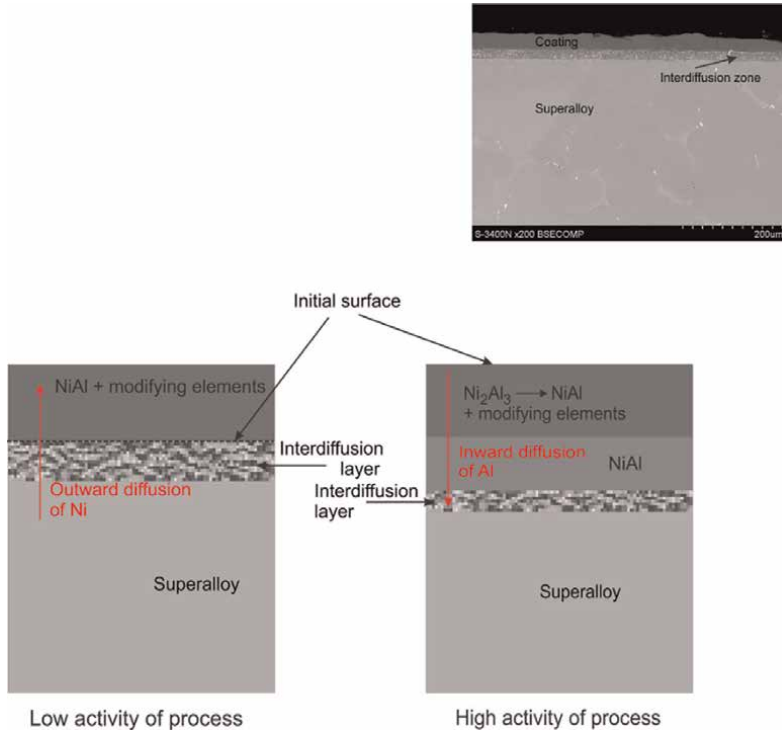


**Figure 4.** Schematically illustrated microstructures in the low and high activity processes after heat treatment.

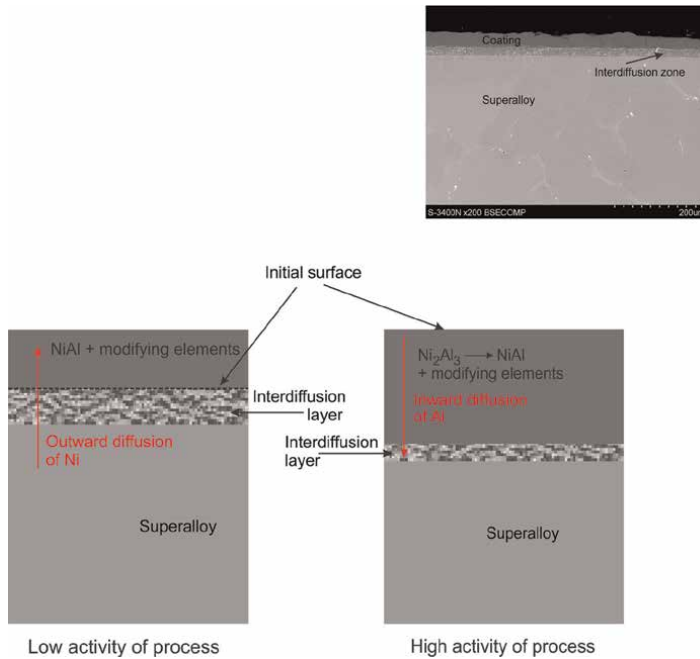


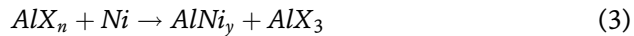
**Figure 5.** Microstructure of coating on superalloy IN 713 LC after high activity CVD aluminizing and heat treatment.

made possible by a neutral gas, guided by the container. Currently, several variations of the applied methods are already known (e.g. SNECMA). This process relates to the deposition of an aluminum coating on a metal part, especially on a hollow metal part comprising an internal liner [48].

The key step of the “out of pack” method is the formation of  $Al(Cl, F, Br)_n$  ( $n < 3$ ) halides at temperatures above  $800^\circ C$  which react with the surface of superalloy by the following reaction [49]:

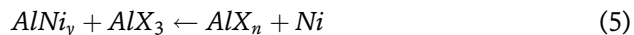


The  $AlX_3$  compound is called “activator”. At the temperature  $900-1150^\circ C$  halides in the gaseous phase are reacting with substrate according to the reaction:



where:  $1/3 < n < 3$ .

Activator is one of reaction products, is penetrating into the source of aluminum and is supporting the process according to the scheme:



All reactions are in the equilibrium and they are leading for creating the intermetallic phase  $AlNi_y$ .

CVD and “out-of-pack” methods are the same from the view of chemical reactions. The difference between both methods results from the fact, that reaction:  $Al + AlX_3 \rightarrow AlX_n$  is occurring in the special generator (external) where from products are transported in the gaseous phase to the retort in which coated elements are.

#### 2.1.4 Slurry process

Slurry aluminide coatings belong to the high temperature diffusion processes. They have been well known for a number of years and are widely used to protect metallic surfaces from oxidation and hot corrosion. Composition and microstructure of coatings formed by slurry-aluminizing process are similar to those obtained by pack cementation. Coatings made by slurry-aluminizing have high quality and the technology is characterized by smallest consuming applied materials. This allows to obtain coatings of the lowest cost and slurry method is one of the cheapest available methods of manufacture of aluminide coatings. Because of the environmental constraints of pack cementation and of out-of-pack processes related to the use of halides and other hazardous chemicals, significant efforts led to the use of water-based technologies [50, 51]. The suspension designed for deposition process can be easily modified and may be stored for a long time. In the deposition process an aluminum-containing slurry is being applied onto the component to be coated, and during heat treatment the slurry react with the substrate forming an aluminide. Slurry is composed from a powder mixture of aluminum or an aluminum alloy plus an activator along with a binder either by spraying or brushing, which is then submitted to diffusion heat treatment at temperatures usually in the  $1000-1200^\circ C$  range. From the point of view of the coating microstructure properties, this method can form precipitates that

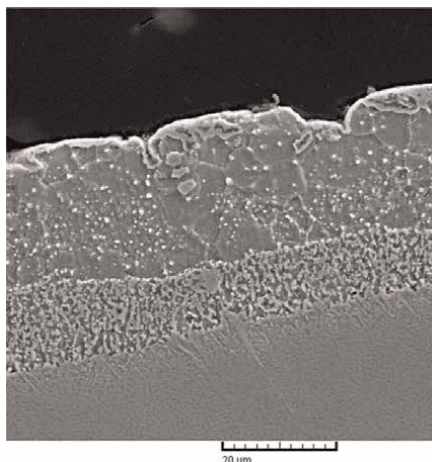


**Figure 6.**  
*Microstructure of Al-Si coating on nickel-based superalloy JS6K.*

inhibit the adhesion of the coating. Another problem lies on inaccessibility of some area as cooling internal passages of turbine blades. Modified aluminide coatings have been industrially developed to overcome the composition limitation that conventional slurries have. Al-Si eutectic slurries are commercially often used for elements working in hot-corrosion environments. No other components have been successfully diffused simultaneously by the slurry route. The microstructure of AlSi layer is shown in the **Figure 6** and it is composed of two sublayers. The outer Al-sublayer is created by NiAl with content of Al < 50 at. % and lower amount of phases containing refractory elements. The inner Si-sublayer creates Ni-Al matrix and higher amounts of phases of elements as Si, Cr, Mo, Ti, W and Co. The thickness of the layer varies in the range of 20–50  $\mu\text{m}$ . Al-sublayer is formed by inward diffusion of aluminum what is typical for high-activity coatings. The inner Si-layer can forms during aluminizing process or operation in the high temperature environment needle-like precipitates in a  $\beta$ -NiAl matrix, which are oriented perpendicular to the interface substrate/diffusion zone (**Figure 7**) where is although visible coating degradation.

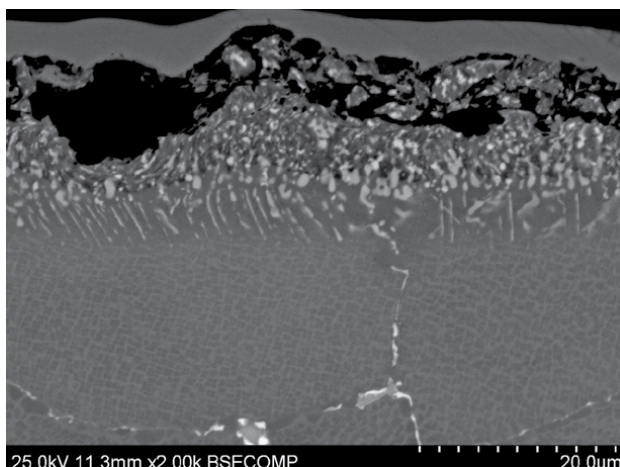


**Figure 7.**  
*Microstructure of Al-Si coating on JS6K superalloy after operation in the high temperature environment.*



## 2.2 Oxidation resistance of DACs

Protective coatings used on turbine blades were developed to serve as physical barriers between aggressive environment and the substrate. In addition, TBCs are used as thermal barriers, retard creep degradation and reduce the severity of thermal gradients. Up to now, however, no coating that would fully survive the aggressive turbine environment has been found.

The coating degrades during service at two fronts: at the coating/gas-path interface when service temperatures are below the melting point of the coating and at the coating/substrate interface at higher temperatures when diffusion mechanisms play the main role in degradation of the system substrate/coating.

The most serious degradation modes are as follows [38]:

- High-temperature oxidation.
- Hot corrosion.
- Damage by thermal and thermo-mechanical fatigue.
- Mechanical damage by erosion.
- Creep degradation during overheating.

Inter-diffusion of elements at the interface with the substrate that results in a creation of undesirable phases is, sometimes, also mentioned as an independent degradation mode.

DACs coatings have been designed to withstand three types of environmental attack: high temperature oxidation, high-temperature hot corrosion (type I) and low-temperature hot corrosion (type II). Oxidation is a special form of corrosion degradation mode which occurs when metals and alloys are exposed to the oxygen environment. However, it should be paid regard to that the oxidation of the DACs at the coating/gas-path interface results in the formation of a protective oxide scale and in respect thereof high-temperature oxidation is not explicitly a degradation mode. If the formed oxide scale is thin, slow-growing, and adherent, it protects the substrate from further oxidation and form barrier to further oxidation. If it be to the contrary oxide scales spall and substrate is exposed to the oxygen environment and suffers from consumption of metals. "Pilling–Bedworth ratio" (PBR) is an important parameter for prediction of the oxide protection properties. It was found out that if the volume of oxide is less than the volume of metal consumed in the reaction, then it is likely that a porous oxide layer will result. This criterion is effective for most metals and alloys of practical importance and by PBR we can assume if the oxide is protective or not. Based on this theory PBR for oxidation of alloys can be expressed as [52]:

$$PBR_{\text{alloy}} = \frac{\text{Volume of a mole of } B_xO_y}{\text{Volume of } x \text{ moles of } B \text{ in the alloy}} \quad (6)$$

It is believed that if  $PBR > 1$  compressive stresses are developed in the oxide scales while tensile stresses occur when  $PBR < 1$ . The larger the difference of PBR from 1, the larger stresses. Although it is well known that direct relation between PBR value and the level of stresses does not hold because mechanisms for growth stresses

and their relaxation are complicated. PBR calculated for aluminum gave value 1.29. However, in the practice alloys are widely used for high temperature applications and values of PBR are different from those of metals. Authors in [52] calculated PBR for  $\text{Ni}_3\text{Al}$ ,  $\text{NiAl}$  and  $\text{NiAl}_3$  and their results indicated that the PBR for oxidation of Ni-Al alloys are larger in regard of PBR for Al metal. PBR for  $\text{Ni}_3\text{Al}$  was calculated from 1.71 to 1.88; for  $\text{NiAl}$  was in the range from 1.64 to 1.78 and PBR for  $\text{NiAl}_3$  from 1.48 to 1.57.

### *2.2.1 Cyclic oxidation*

Cyclic oxidation is the superposition of thermal cycles in an oxidation environment. Alloys used at high temperatures are subjected to the operative cycles which vary widely depending of operating conditions.

More or less rapid temperature changes in oxidizing atmosphere result in thermo-mechanical stresses in the oxide scales which fail due to spallation. Turbine blades of aircraft engines are a typical example for working in such conditions. Turbine blades of aircraft engines are a typical example for working in these conditions.

The main parameters that determine the operating conditions of aircraft turbine blades are the gas temperature at the turbine inlet, pressure, velocity and composition of the gas flow. The gas temperature is the most important parameter determining the specific thrust and performance of an aircraft engine. The thermal composition of the gas flow at the turbine inlet is inhomogeneous; is caused by factors that determine the dynamics of the gas flow, such as the construction of the combustion chamber, the layout of the burners, or the combustion process. The stator disks and blades of the high-pressure turbine are the hottest part of the turbine, their temperature is (200-300) °C lower than the temperature of the gases, while the difference in temperature fields is based on the height of the blades and their circumference. The temperature field in the rotor part is more homogeneous and results from the high rotational speed of the impeller.

The critical elements of an aircraft turbine are the rotor blades. They determine the maximum permissible gas temperature and the lifetime of the entire engine. They are loaded with centrifugal and dynamic forces, which cause them to be strained by tension, bending and twisting. Tensile stresses are usually higher than (200-250) MPa and are different on the convex and concave sides, being the highest near the root of the blade. High temperatures and voltages, unstable load conditions and the possibility of resonant vibrations make vanes among the most complicated parts of the engine. The highest temperature load is in the upper third of the blade, where the centrifugal force is the lowest. The temperature of the gas stream can increase by up to 500°C in just a few seconds in aircraft turbines during transients or sudden regime changes. Static stresses and high temperature of the blades lead to their deformation as a result of creep. The combination of the effects of high temperature, dynamic forces, and thermal stresses causes blade failure due to thermal fatigue.

The surface of the blades is exposed to the effects of combustion products, which cause their degradation by oxidation, corrosion and damage by solid particles carried by the gas flow. The fuel combustion process takes place at the temperature of (2000–2200) °C. Hydrocarbon combustion is the process of its oxidation by oxygen from the air, the main products of combustion are  $\text{CO}_2$  and water vapor. The gas flow at the entrance to the turbine contains, in addition to the main ones, also secondary products of combustion, such as certain amounts of  $\text{CO}$ ,  $\text{H}_2$ ,  $\text{CH}_4$ , solid particles of carbon and sulfur compounds and other elements entering the chamber from fuel or air. The

difference in the sample of combustion products depends on the chemical composition of the fuel and on the environment (overseas, industrial, desert).

Cyclic oxidation tests are used to monitor scale adherence and the ability of scale to successfully regenerate after repetitive scale failure. The performance of materials is generally monitored by gravimetric method although others methods have been used [53]. Experimental techniques are needed to obtain both, data on the kinetics of the oxidation reactions and characterization of the scales formed during oxidation.

The most important method used to study oxidation kinetics and oxidation rate is the gravimetric method. The principle of this method is to examine weight change due to oxidation as a function of time. Heating and cooling can be quite rapid and short cycles can be used. A simple gravimetric technique involves the exposition of the sample with known area in a furnace followed by measuring the weight change at definite intervals of time, using a sensitive balance. In this method the experiment have to be interrupted every time the weight change is measured. The sample is frequently heated and cooled what causes changes in the scale behavior such as onset of scale failure, buckling, spallation and finally mass loss. **Figure 8** represents typical mass changes during thermal cycling for three types of coatings. Non-protective behavior and negative weight change during thermal cycling represents gross scale spallation occurring from the onset of the cycling test. Protective behavior of a scale for a definite time is characteristic for materials that have a limited reserve of elements (Cr, Al or Si) to form stable oxides. After certain number of cycles scale composition changes to less protective spinels which spall rapidly and mass loss is recorded. Spallation is the loss of protective oxides at the coating/oxide interface. Strains induced by stresses during repeated thermal cycling due to thermal mismatch between oxide and metal, result in crack initiation and eventual spalling of the scales. In the case that the scale is too thin to sustain a temperature gradient, not thermal shock to the oxide. If the oxide thickens sufficiently, the strain energy stored in the oxide becomes greater than that for fracture of interface, the scale spalls [54].

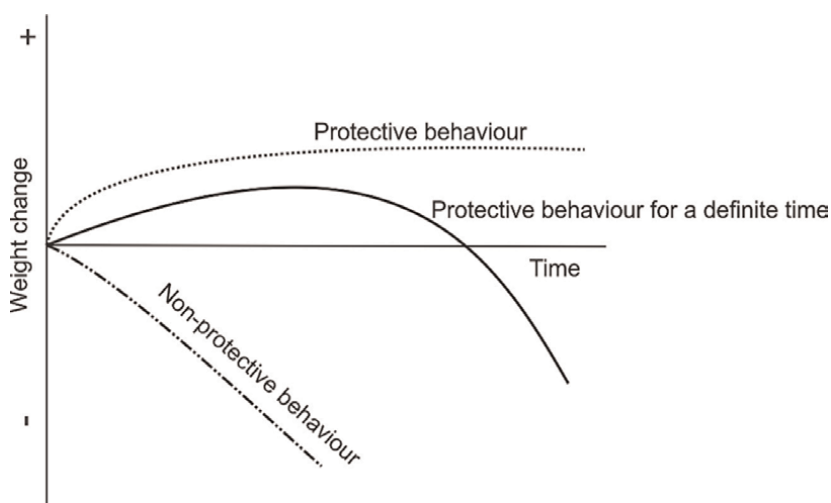


**Figure 8.**  
*Schematic diagram of typical mass changes of coatings.*

2.2.2 Experimental work to study of DACs oxidation behavior

The main goal of the experimental work was to compare the cyclic oxidation of protective aluminide coatings deposited on two types of nickel superalloys, Inconel 713 LC and MAR-M247 (Table 1). All samples with and without aluminide coatings were exposed to cyclic oxidation. Two type of superalloys were deposited by aluminide coating and Si modified aluminide coating using CVD out-of-pack process.

Experimental samples casted from IN 713LC and MAR 247 LC for cyclic oxidation test had cylindrical shape with dimensions of 14 × 5 mm. Their microstructure was consisted of the  $\gamma$  matrix strengthened by  $\gamma'$  phase with the shape of cuboidal particles of Ni<sub>3</sub>(Al, Ti) as coherent precipitates and complex carbides. Three types of samples for two kinds of superalloys were used for cyclic oxidation tests [39]:

- samples of IN 713 LC and MAR 247 LC without coating,
- samples of IN 713 LC and MAR 247 LC with aluminide coating and,
- samples of IN 713 LC and MAR 247 LC with Si modified aluminide coating.

Aluminide coatings were applied by the “out-of-pack” method and Si modified aluminide coatings were made by the method of “pack-cementation”.

Disc samples in ceramic bowl (Figures 9 and 10) were placed into induction furnace with the temperature 1100°C. After 23 h, the tested samples were taken from furnace and they were immediately exposed to the cooling process in the air at room

	Cr	Al	Mo	W	Nb	Ti	Ta	Zr	Hf	C	B	Co
IN 713 LC	11.85	5.8	4.54		2.27	0.72		0.11		0.04	0.015	
MAR 247 LC	8.4	5.5	0.7	10.0		1.0	3.0	0.05	1.5	0.15	0.015	10.0

**Table 1.** Chemical composition of tested superalloy (wt. %, bal. Ni).

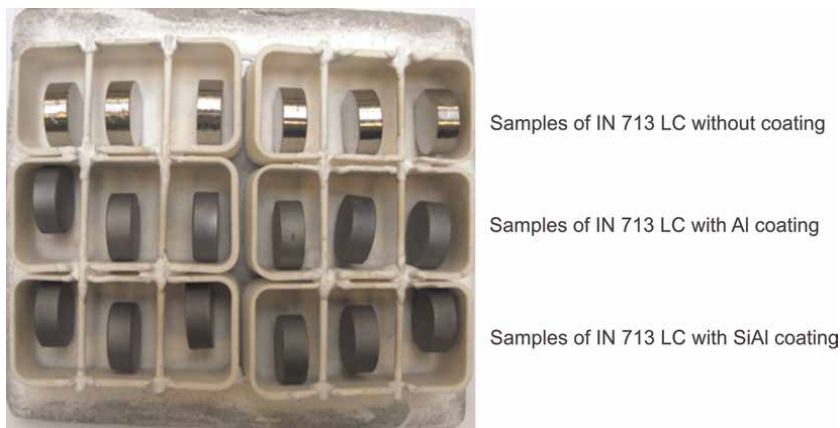


**Figure 9.** Samples of IN 713 LC with and without coatings before testing.

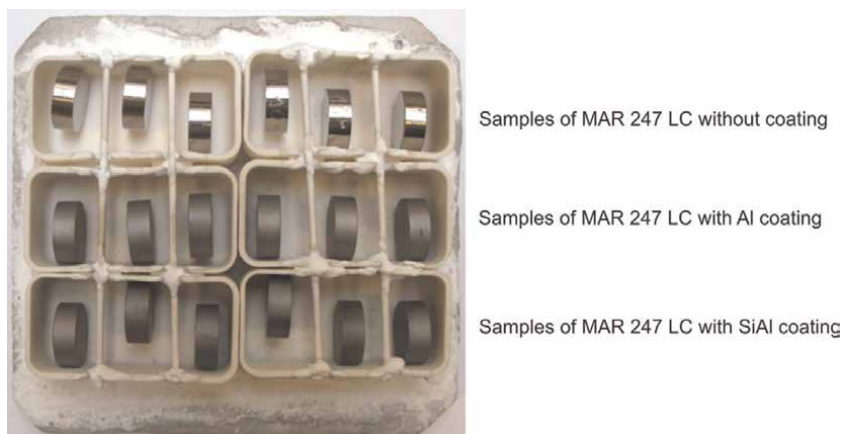


**Figure 10.**  
*Samples of MAR 247 LC with and without coatings before testing.*

temperature for 1 h and then the mass changes were measured. This description represented one oxidation cycle. Mass changes of samples were written down after each second cycle and the photos were done.

Gravimetric weight changes of cyclically tested superalloys with coatings followed weight changes during oxide formation and the results were used to compare the resistance of superalloy/coating systems to cyclic oxidic loading in a high temperature environment as well as to choose the most suitable combination for application in practice [39].

Macroscopic views of all samples after 3rd, 10th and 20th cycles are visible in the **Figures 11–13**. As for uncoated superalloy MAR 247 LC test of cyclic oxidation was interrupted after 13th cycle due to continuing decrease of weight.

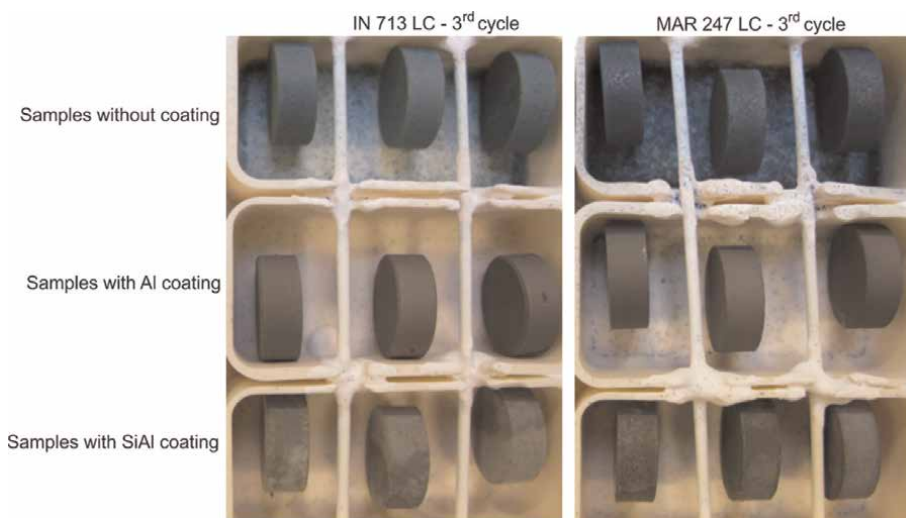


**Figure 11.**  
*Overall view on all samples after 3rd cycle of testing.*

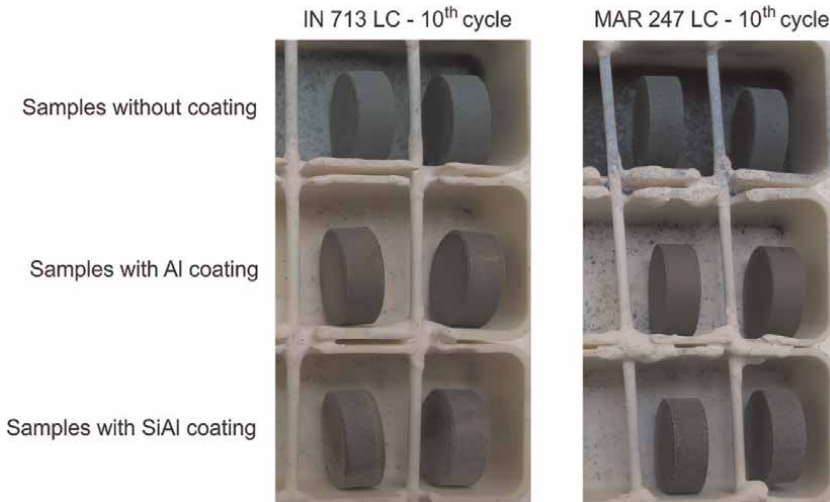


**Figure 12.**  
*Overall view on all samples after 10th cycle of testing.*

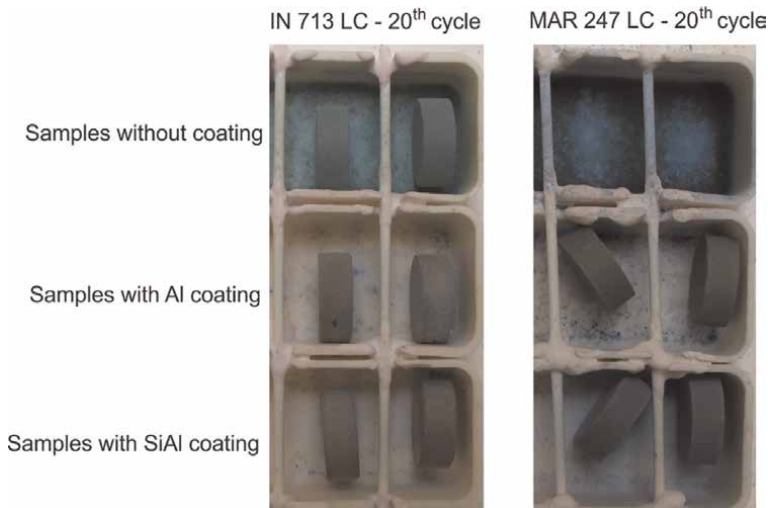


**Figure 13.**  
*Overall view on all samples after 20th cycle of testing.*

The resulting graph of samples made from IN 713 LC with and without coatings is shown in **Figure 14**. From this picture, it is clear that IN 713 LC with unmodified aluminide coating had lower life-time than without coating and it is very surprising finding. Weight changes after each oxidation cycle for MAR 247 LC samples with and without coatings are visible in the **Figure 15**. We can see that life time of MAR 247 LC without coating is very low and structural components made from this type of superalloy without coating could not be used for practice application in the oxidation environment. On the basis of results in the **Figure 15** we can see that life time of samples from MAR 247 LC superalloy with aluminide Al and AlSi coatings is practically the same.

The resulting graph of all tested samples is shown in **Figure 16**. This picture revealed that samples from IN 713 LC without coating after 24-h cycles in environment of 1100°C

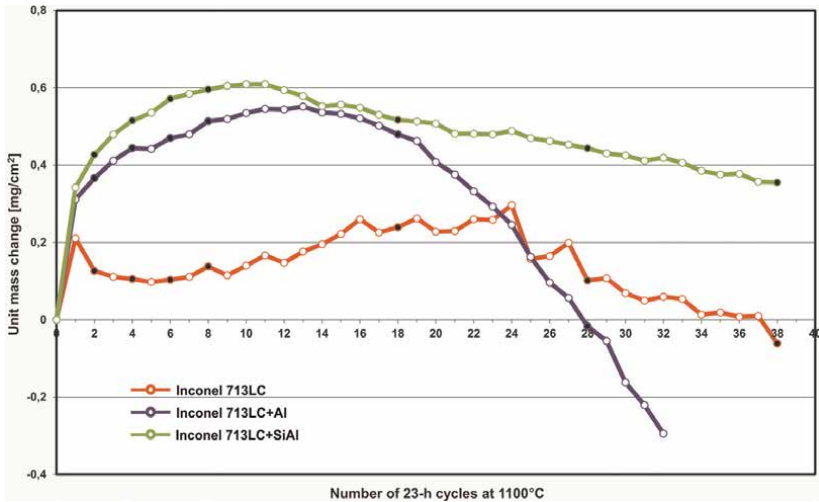


**Figure 14.** Mass change data for IN 713 LC with and without coatings achieved from thermogravimetric analyses.

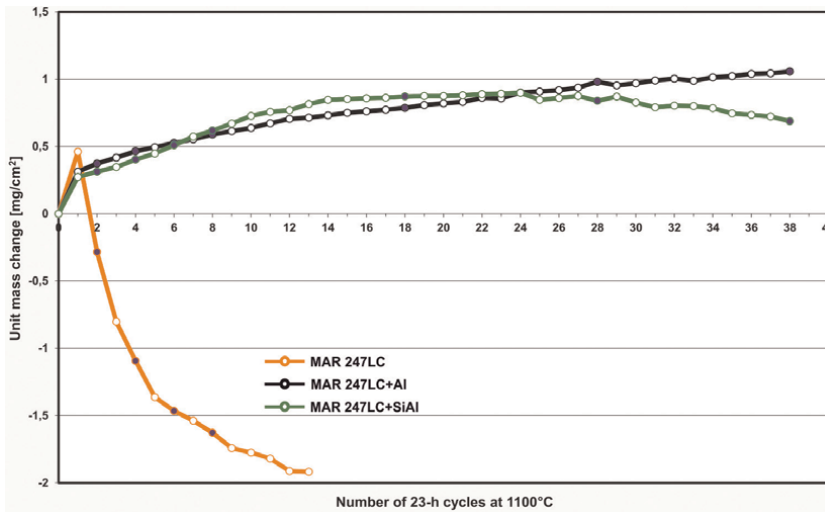


**Figure 15.** Mass change data for MAR 247 LC with and without coatings achieved from thermogravimetric analyses.

show good resistance and their mass change maintain above zero limit. Samples from MAR 247 LC superalloy with both aluminide Al and AlSi coatings appear to be the most acceptable selection of combination relating to superalloys/coating.

### 2.2.3 Microstructural research of DACs in the oxidation environment

#### 2.2.3.1 Microstructural examination of IN 713 LC without coating

Microstructure of IN 713 LC before cyclic oxidation test (**Figure 17**) consisted of the  $\gamma$ -solid solution strengthened by  $\gamma'$  phase with the shape of cuboidal particles of



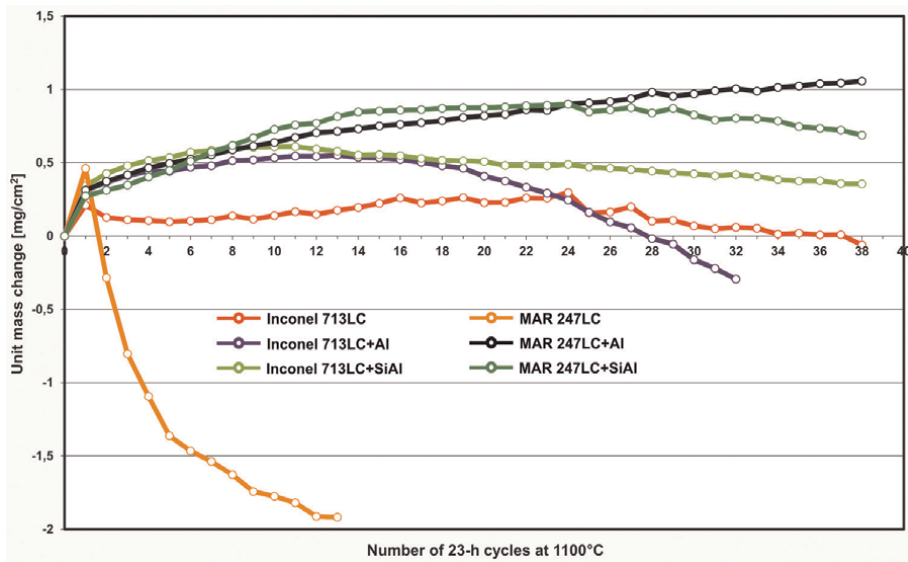


**Figure 16.**  
Weight changes after each oxidation cycle for all tested samples.

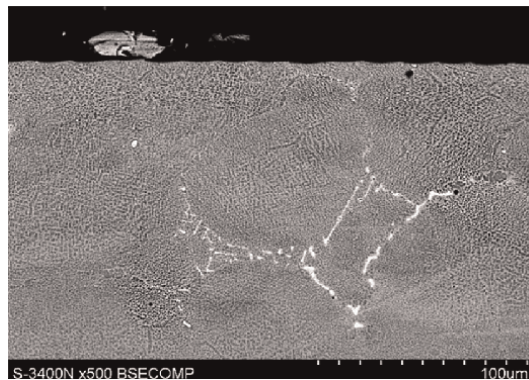


**Figure 17.**  
Microstructure of IN 713 LC without coating before testing.

Ni<sub>3</sub>(Al, Ti) as coherent precipitates (dark particles in **Figure 18**) and complex carbides (bright particles in **Figure 17**).

After 8 cycles of cyclic oxidation testing the microstructure of IN 713 LC without protective coating degraded as we can see in **Figure 19**. It was found that  $\gamma'$  particles near the surface region dissolved to the solid solution and below is the area of larger  $\gamma'$  coarsened ones. The thickness of oxide scales and area of dissolved precipitates under the surface reached on average 5.3  $\mu\text{m}$  and 32.6  $\mu\text{m}$ , respectively.

From **Figures 19** and **20** is clear that degradation of uncoated samples from 8 to 18 cycles continued in the sense of formed the thicker area of oxide scale (9.9  $\mu\text{m}$ ) and dissolved precipitates (46.4  $\mu\text{m}$ ). Mechanical properties of investigated alloy mainly depend on morphology, size and volume fraction of gamma prime strengthening particles. Increasing of cycle number resulted in decreasing of the  $\gamma'$  phase volume fraction what is not acceptable considering strength of the alloy.



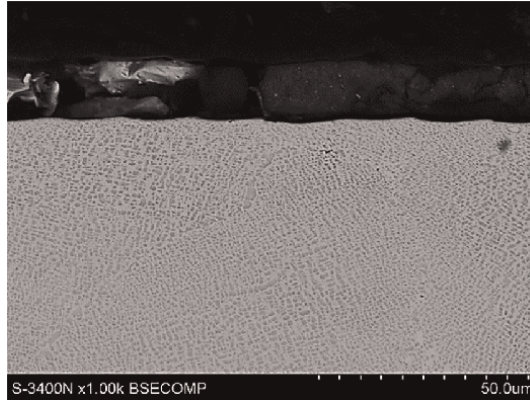


**Figure 18.**  
 *$\gamma$ -solid solution of IN 713 LC with  $\gamma'$  phase.*

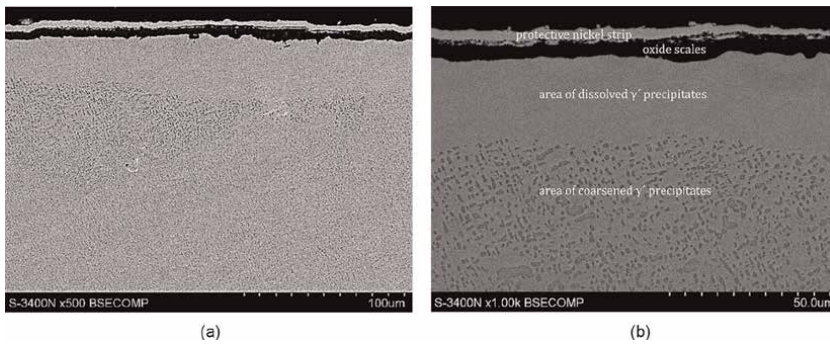


**Figure 19.**  
*(a) Microstructure of IN 713 LC (b) Detail focused on the after 8 cycles of testing microstructure near surface region.*

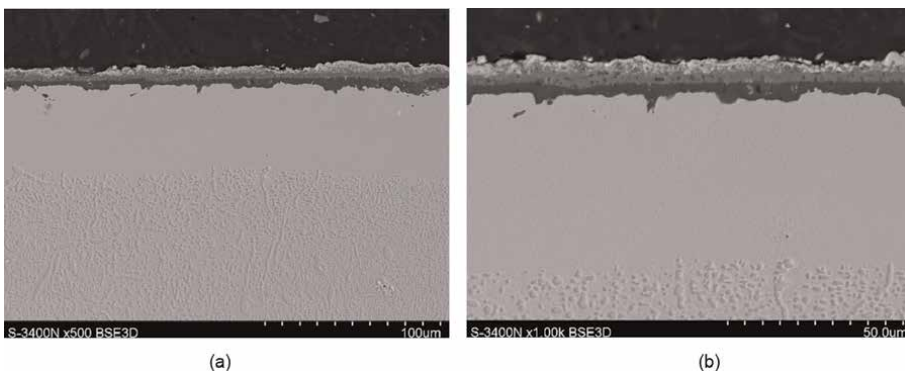


**Figure 20.**  
*(a) Microstructure of IN 713 LC (b) Microstructural appearance of after 18 cycles of testing the region under oxide surface.*

Growth of oxide scale and area of dissolved precipitates continued with increase in test cycles. After 28 cycles of cyclic oxidation was observed growth of oxide scale deeper into superalloy and the oxide thickness reached 12.9  $\mu\text{m}$ . The thickness of

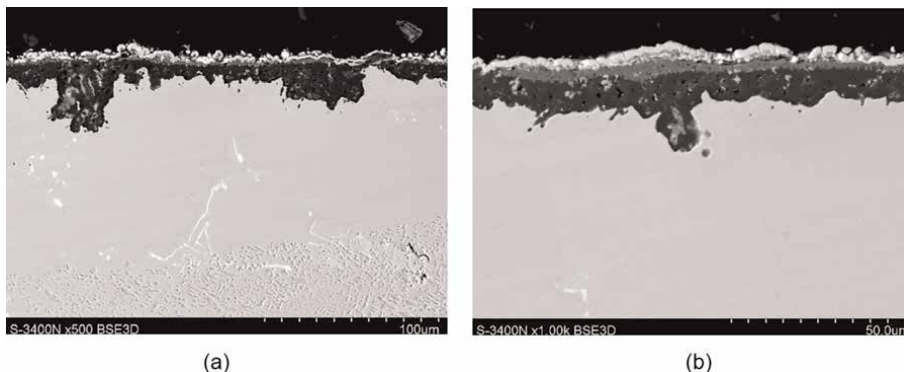


**Figure 21.**  
 (a) Microstructure of IN 713 LC (b) Oxide scales after 28 cycles after 28 cycles of testing of testing.

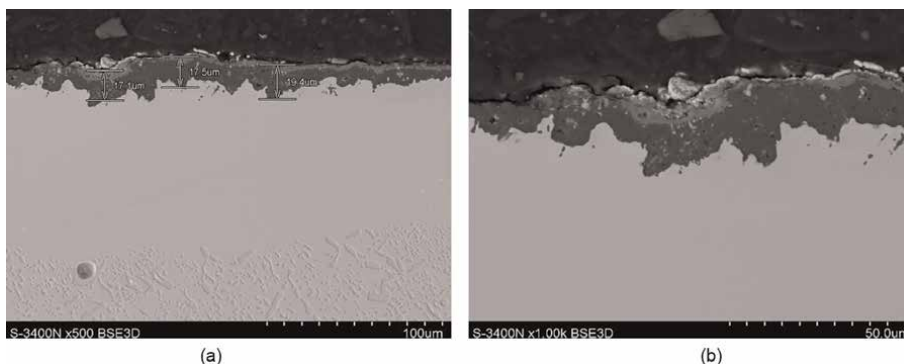


**Figure 22.**  
 (a) Microstructure of IN 713 LC (b) Oxide scales under surface of after 38 cycles of testing alloy after 38 cycles of testing.

dissolved precipitates was 73.4  $\mu\text{m}$  (see **Figure 21a** and **b**). 38 test cycles caused growth of oxide scales up to 17.8  $\mu\text{m}$  and area of dissolved precipitates to 100.1  $\mu\text{m}$  (**Figure 22a** and **b**).

Chemical contents of the  $\gamma$ -solid solutions of elements in nickel (dissolved precipitates areas) in all samples after cyclic oxidation tests were roughly identical. Contents of Al were from 7.5 at. % to 8.5 at. % in the samples after 8, 18, 28 and 38 cycles; Ni ranged between 73.1 at. % and 73.4 at. %; Cr was from 15.1 at. % to 15.3 at. %. Below this zones were areas of coarse precipitates which contained a bit higher amount of Al (9.1 at. % – 9.8 at. %), a lower content of Cr (12.8 at. % – 13.4 at. %) and an identical content of Ni. Cross sections of oxide scales of all samples after testing (**Figure 23**) revealed two zones; inner oxide layer and outer oxide layer. It was found that the outer oxide zones were composed of lower contents of Al (about 59 at. %) compared to the inner zone (about 96 at. % Al), higher contents of Cr (about 4.9 at. %) with respect to that in the inner ones (about 0.6 at. %) and a considerably higher content of Ni in the outer layers (about 32 at. %) compared to that in the inner layers (about 2.5 at. %). From these examinations results that the degradation of uncoated samples from IN 713 LC superalloy started with a creation of oxide scales on the surface by exhausting of aluminum and chromium from the alloy inside and formation of an area of dissolved  $\gamma'$  precipitates.

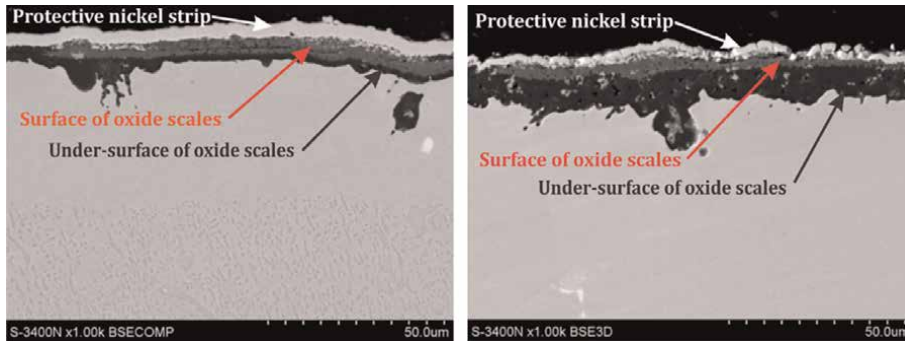


**Figure 23.**  
 (a) Oxide scales after 8 cycles (b) Oxide scales after 18 cycles.

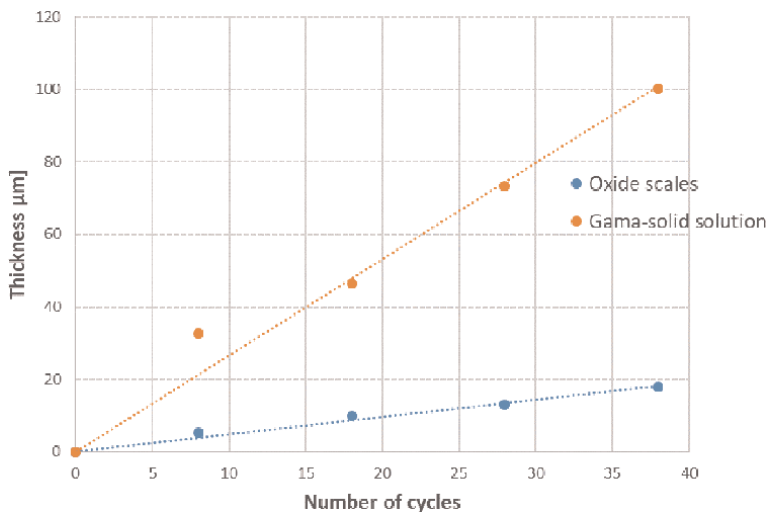


**Figure 24.**  
 Thicknesses of oxides and gama-solid solution after 8, 18, 28 and 38 cycles of testing.

Next cyclic oxidation cycles resulted in linearly increasing thicknesses of oxide scales and area of dissolved precipitates, i.e., solid solution  $\gamma$  without strengthening  $\gamma'$ -phase. The  $\gamma$ -solid solution grown about 5 times faster than oxide scales (Figure 24). The continuously growth of oxides and their mass gain on the surface of samples without coating has shown that although the oxides underwent spallation processes during each cooling cycle of testing, the surface of alloy was doped by aluminum from the bulk after each cycle (see Figure 14), whereas strength and creep properties of the alloy decreased. Decreasing mass gain started from the 29th cycle when the forming of oxides continued mainly in the inside of the alloy whereas the surface was subjected to the spalling process. X-ray diffraction analysis of phase of the sample after 38 cycles of cyclic oxidation revealed a presence of protective oxide phases on the base of Al and Ti in the mixture with  $\text{NiAl}_2\text{O}_4$  spinel phase (Figure 25).  $\text{NiAl}_2\text{O}_4$  could be formed in the process of cyclic oxidation by the reaction of NiO and  $\text{Al}_2\text{O}_3$ .

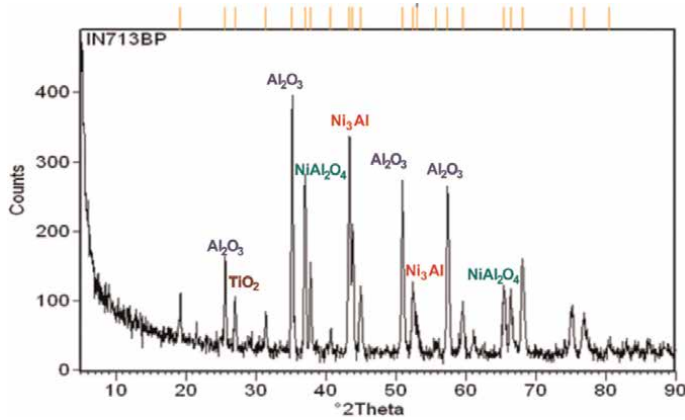


**Figure 25.**  
X-ray analysis of phases on the surface of sample after 38 cycles of cyclic oxidation.

### 2.2.3.2 Microstructural examination of IN 713 LC with Al coating

**Figure 26a** and **b** represent the microstructure of superalloy IN 713 LC with Al coating deposited by the “out-of-pack” method before the cyclic oxidation test. The upper layer of the coating was composed from the NiAl solid solution and the inner one contained Ni<sub>3</sub>Al solid solution with particles of Cr, Nb, Ti and Mo. The thicknesses of upper and inner sublayers were 32.8 μm and 17.7 μm, respectively. **Figures 27–30** show changes of microstructures of samples after 8, 18 and 28 cycle, respectively. They revealed that the degradation of the protective coating continued very fast and a zero gain was reached after 28 cycles of testing (see **Figure 14**). This mass change of 0 mg/cm<sup>2</sup> compared to the original state of sample indicated that the reserve of aluminum was exhausted and the protected function of the coating was stopped. The oxide thicknesses on the sample surfaces after 8, 18 and 28 cycles were 6.68, 4.97 and 4.68 μm, respectively.

The oxidation behavior at the beginning of the test was controlled by the formation of a fast-growing layer of a mixed oxide. At cyclic oxidation times longer than

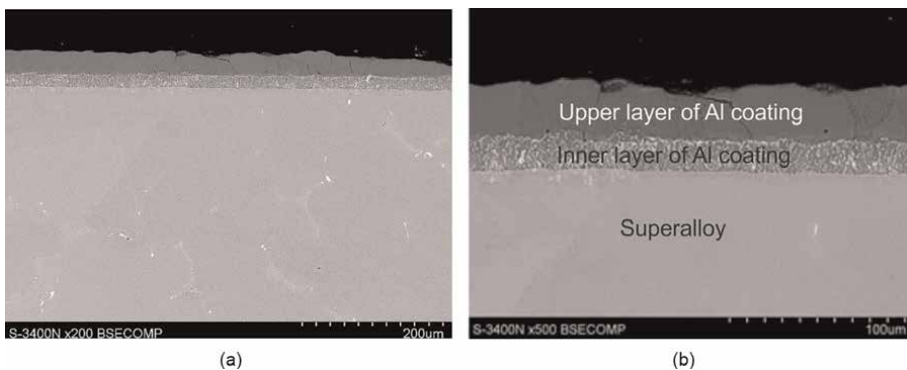


**Figure 26.**  
(a) Microstructure of IN 713 LC with Al coating before testing (b) Detail on the coating before testing.

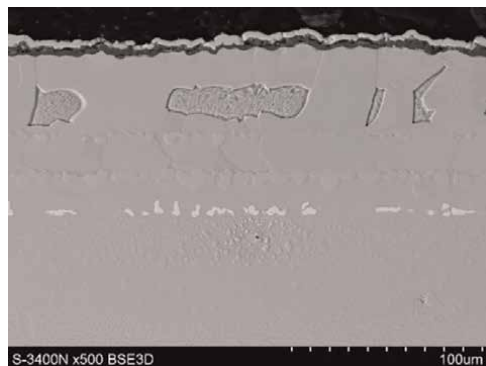


**Figure 27.**  
*Microstructure of IN 713 LC with Al coating after 8 cycles of testing.*

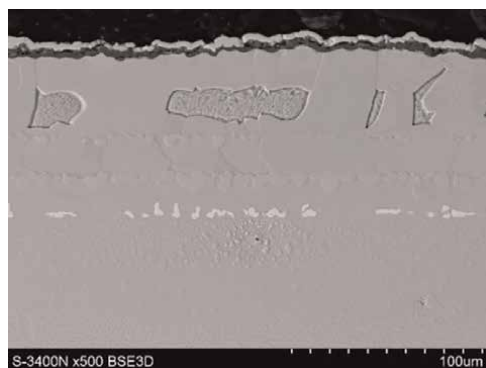


**Figure 28.**  
*Microstructure of IN 713 LC with Al coating after 18 cycles of testing.*

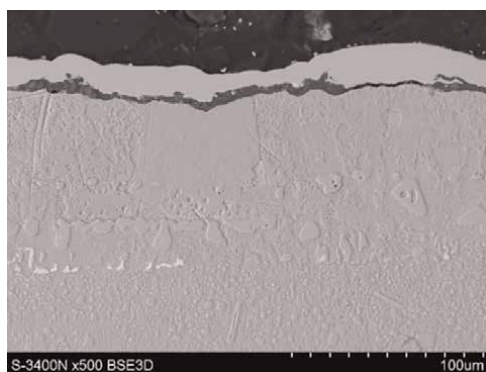


**Figure 29.**  
*Microstructure of IN 713 LC with Al coating after 28 cycles of testing.*

12 cycles this rather thick layer started to spall off. In accordance with the unit mass change (**Figure 14**) up to 12th cycle the protective oxide scales formed on the surface of samples prevailed over the effects of spallation and starting from the 13th cycle the

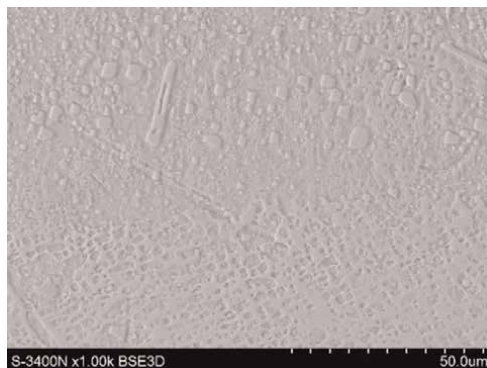


**Figure 30.**  
*Intermediate zone between the inner layer of coating and the superalloy of sample after 28 cycles of testing.*

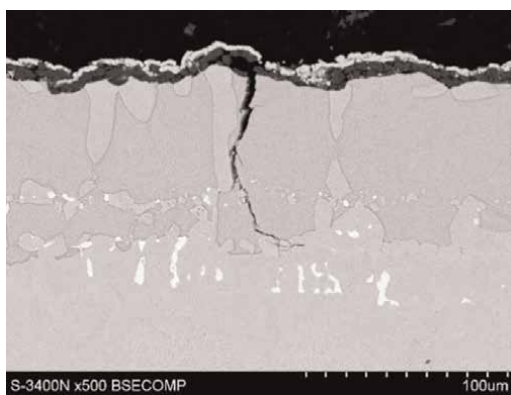


**Figure 31.**  
*Crack in the Al coating after 8 cycles of testing.*

spalling processes become dominating. Both the weight gain in **Figure 14** and the measured oxide layer thickness demonstrate this behavior. A crack in the coating of sample after 8 cycles was found as a result of thermal stresses (**Figure 31**). A major problem of such coatings is that the coefficient of thermal expansion of the alumina layer differs from the coefficient of expansion of the base material.

During thermal cycling, stresses arise between the aluminum oxide top layer and the coating material. The resulting oxide layer is relatively brittle and tends to crack and peel off, exposing the fresh surface to a damaging atmosphere. This repeating process consumes the aluminum in the coating. When the aluminum level in the coating drops below a certain point, the coating becomes ineffective as an alumina generator and the protective benefits of the coating material are lost.

Process of spalling can be examined by the view on the surfaces of samples after 8, 18 and 28 cycles (**Figure 32a–d**).

Dark areas in **Figure 32b–d** responded to protective alumina scales and white places to the  $\text{Ni}_3\text{Al}$  phase with an amount of Cr, Nb, Ti and Mo. This is in accordance with EDS analyses of elements from surfaces and cross sections of each of samples. An example of this examination from the sample after 18 cycles we can see in **Figure 33** where phase 1 corresponds to the oxides and phase 2 to the solid solution  $\text{Ni}_3\text{Al}$ .



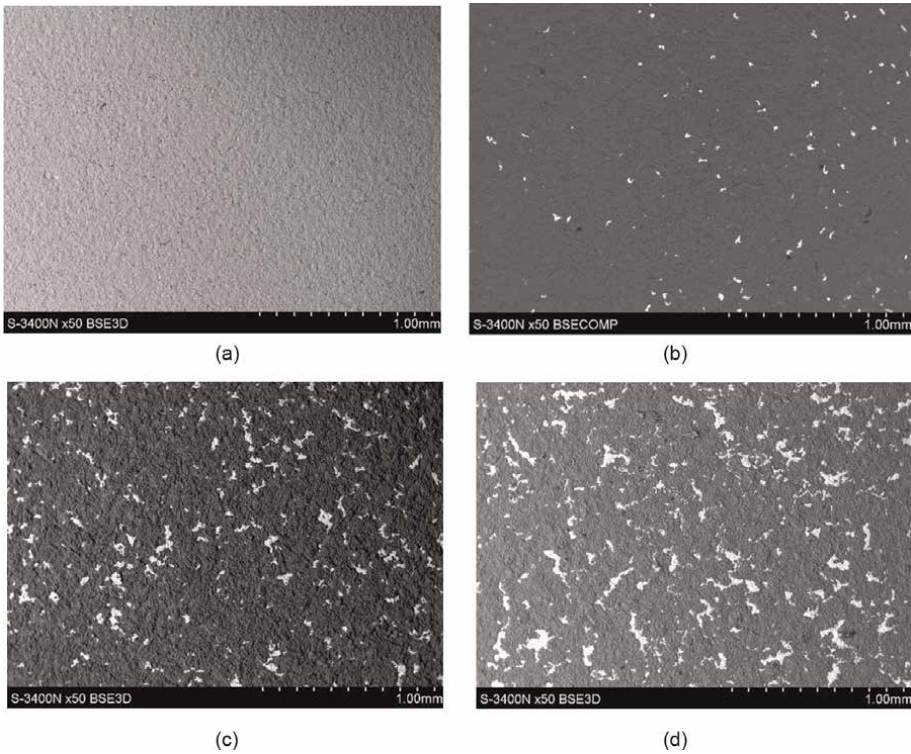


**Figure 32.**  
 (a) The surface of IN 713 LC with Al coating before testing (b) The surface of IN 713 LC with Al coating after 8 cycles of testing (c) The surface of IN 713 LC with Al coating after 18 cycles of testing and (d) The surface of IN 713 LC with Al coating after 28 cycles of testing.

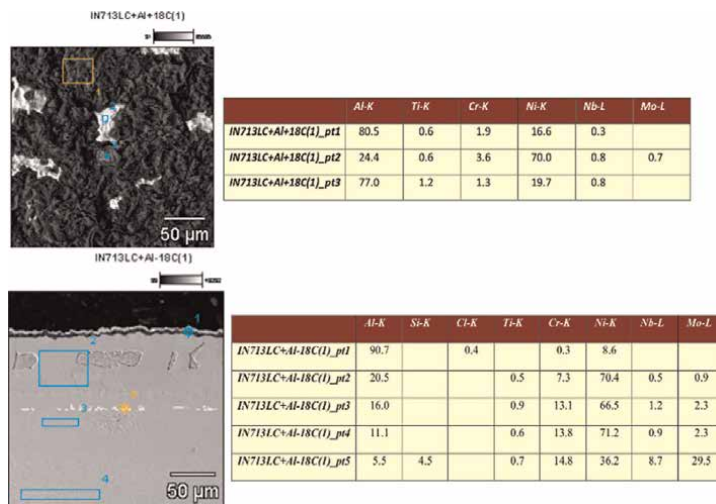


**Figure 33.**  
 EDS analyses of phases from surface and cross section of samples after 18 cycles of testing.

### 2.2.3.3 Microstructural examination of IN 713 LC with AlSi coating

Si modified aluminide coatings were made on the surface of IN 713 LC samples by the method of “pack-cementation”. Silicon was added to the aluminide coatings to improve their oxidation resistance and the oxide scale adherence and, as a consequence, the oxidation rate was lower. After the pack cementation process some of Ni atoms were replaced by Si in the solid solution of aluminide phase. This resulted from the X-ray diffraction phase analysis (**Figure 34**) since no Si-containing phases were found. During pack aluminizing, the superalloy samples to be coated were placed in an air-tight retort containing a mixture powder of aluminum and silicon activated with ammonium chloride and an inert  $\text{Al}_2\text{O}_3$  filler which prevented the sources from sintering. The box was then inserted into a furnace and heated in a protective atmosphere. The pack cementation process is essentially an in situ chemical vapor deposition (CVD) coating process. The coating achieved by this method and subsequent heat treatment was composed from outer and small inner sublayers (**Figures 35 and 36**). According to the results of the EDS analyses, the element distribution of outer and inner coating layers and the substrate is

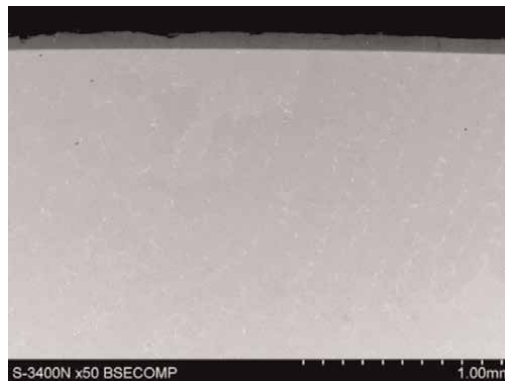


**Figure 34.**  
*The X-ray diffraction phase analysis from the surface of the sample IN 713 LC with the AlSi coating.*

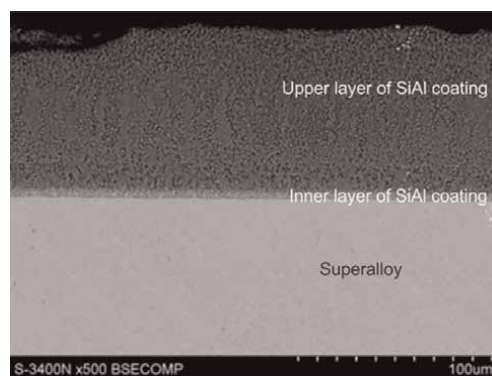


**Figure 35.**  
*The cross section of sample IN 713 LC with AlSi coating before cycling oxidation test.*



	Al-K	Si-K	Ti-K	Cr-K	Fe-K	Ni-K	Nb-L	Mo-L
Outer layer	50.1	1.9	0.3	8.0	0.5	37.8		1.3
Inner layer	31.4		1.4	17.6	0.2	45.0	1.2	3.1
Substrate IN 713 LC	11.9		0.7	12.9		72.7		1.8

**Table 2.**  
 Element distribution in the IN 713 LC superalloy with the AlSi coating in at. %.

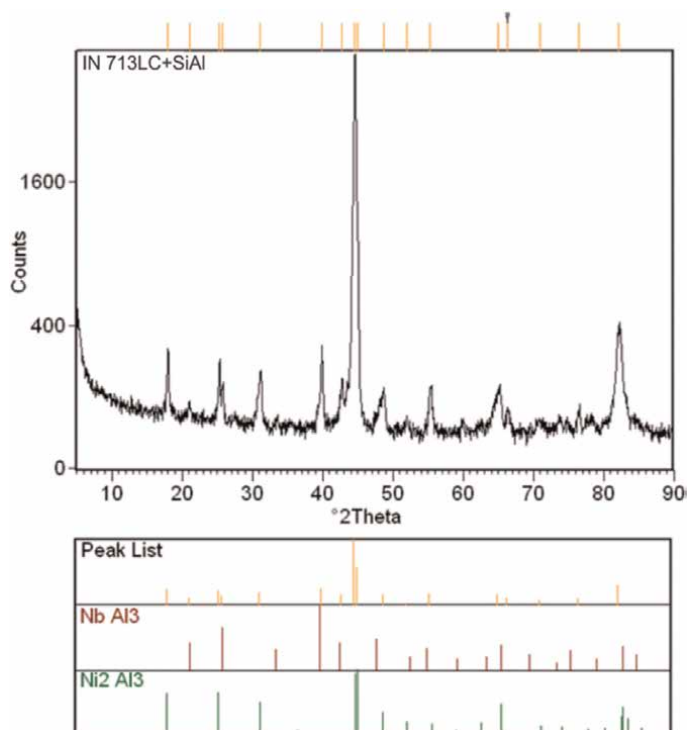


**Figure 36.**  
 Individual parts of AlSi coating on superalloy.

displayed in **Table 2**. The element distribution confirmed that the outer layer contained a large amount of small precipitates containing atoms with higher atomic numbers such as Cr, Ti and Mo which are present in the substrate. This is a typical feature for inward diffusion of Al and Si. The small diffusion underneath suggests a limited degree of the outward diffusion of Ni. The total thickness of the coating including the diffusion zone was approximately 77  $\mu\text{m}$ . The X-ray diffraction phase analysis by JEOL JDX-7S from the sample surface revealed that the matrix of the coating was the  $\text{Ni}_2\text{Al}_3$  phase in which particles of niobium aluminide were present (**Figure 34**).

Microstructures of IN 713 LC samples with AlSi coating after testing of cyclic oxidation are visible in **Figures 37–41**. Specimens after 8 cycles of testing changed

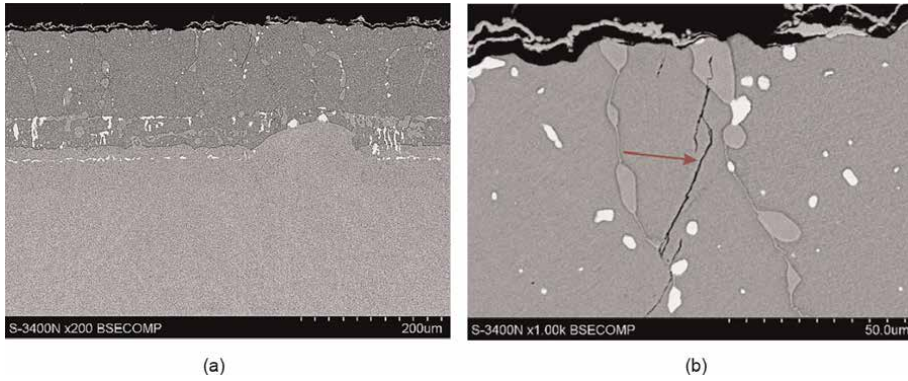


**Figure 37.**  
*(a) Microstructure after 8 cycles (b) Crack in the coating after 8 cycles.*

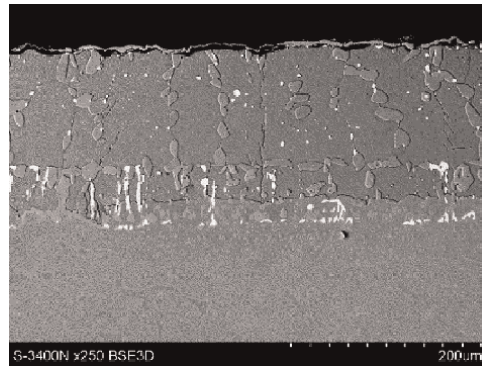


**Figure 38.**  
*Microstructure after 18 cycles.*

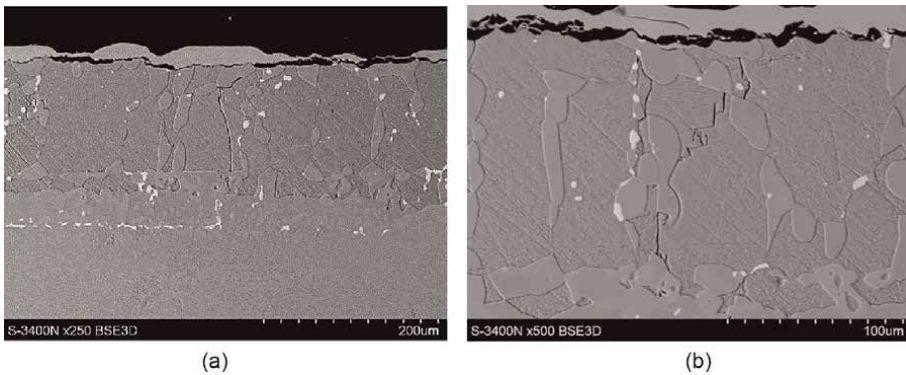


**Figure 39.**  
*(a) Microstructure after 28 cycles (b) Cracks after 28 cycles.*

their microstructural view. The white particles visible in **Figure 37a** are composed from elements as Si, Cr, Ti, Nb and Mo as found on the basis of the EDX analyses. The content of Al in the coating was about 50 at. % and after 8 cycles decreased to 29 at. %



**Figure 40.**  
*Microstructure after 38 cycles.*

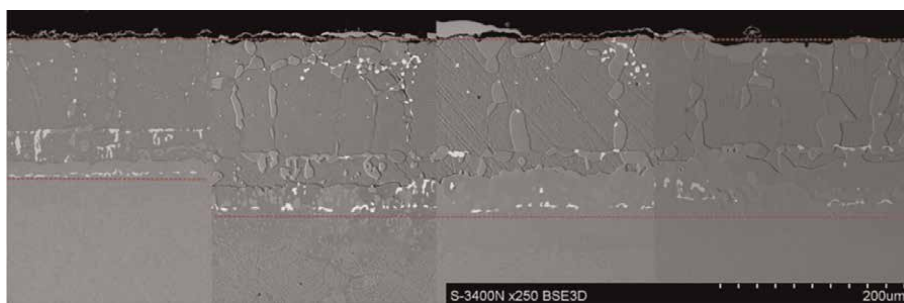


**Figure 41.**  
*View on the thicknesses of coatings after 8, 18, 28 and 38 cycles of testing.*

and then remained constant up to 38 cycles. The content of Ni exhibited an opposite behavior and increased from the original 38 at. % to 64 at. % after 8 cycles and then remained constant up to 38 cycles.

The content of particles based on Si, Ti, Cr, Nb and Mo maintained practically identical during all the testing cycles. As one can see from **Figure 41**, the coating thickness grew larger after 8 cycles of testing and then remained practically unaffected up to 38 cycles.

There were practically no changes in the thickness of surface oxide scales during the cycling. **Figure 42a–h** represent surfaces of coatings before and after 8, 18, 28 and 38 cycles of testing. Contents of Al and Ni before testing changed from about 51 at. % and 40 at. % to 92,5 at. % and 5,8 at. % after testing, respectively. Alumina phase on the surface was subjected to the processes of buckling and scaling off and white particles were exposed. A large amount of small cracks on the top of coating (**Figure 42c, e, g**) represents an evidence of such a mechanism. Since the concentration of white phases during the cycling did not change too much it means that new alumina phases were created simultaneously with the scales. This behavior along with the small mass gain to the 11th cycle of testing and a very small weight loss up to the end of the cycling (**Figure 14**) confirm a good resistance of IN 713 LC with AlSi coating to the thermal cycling.

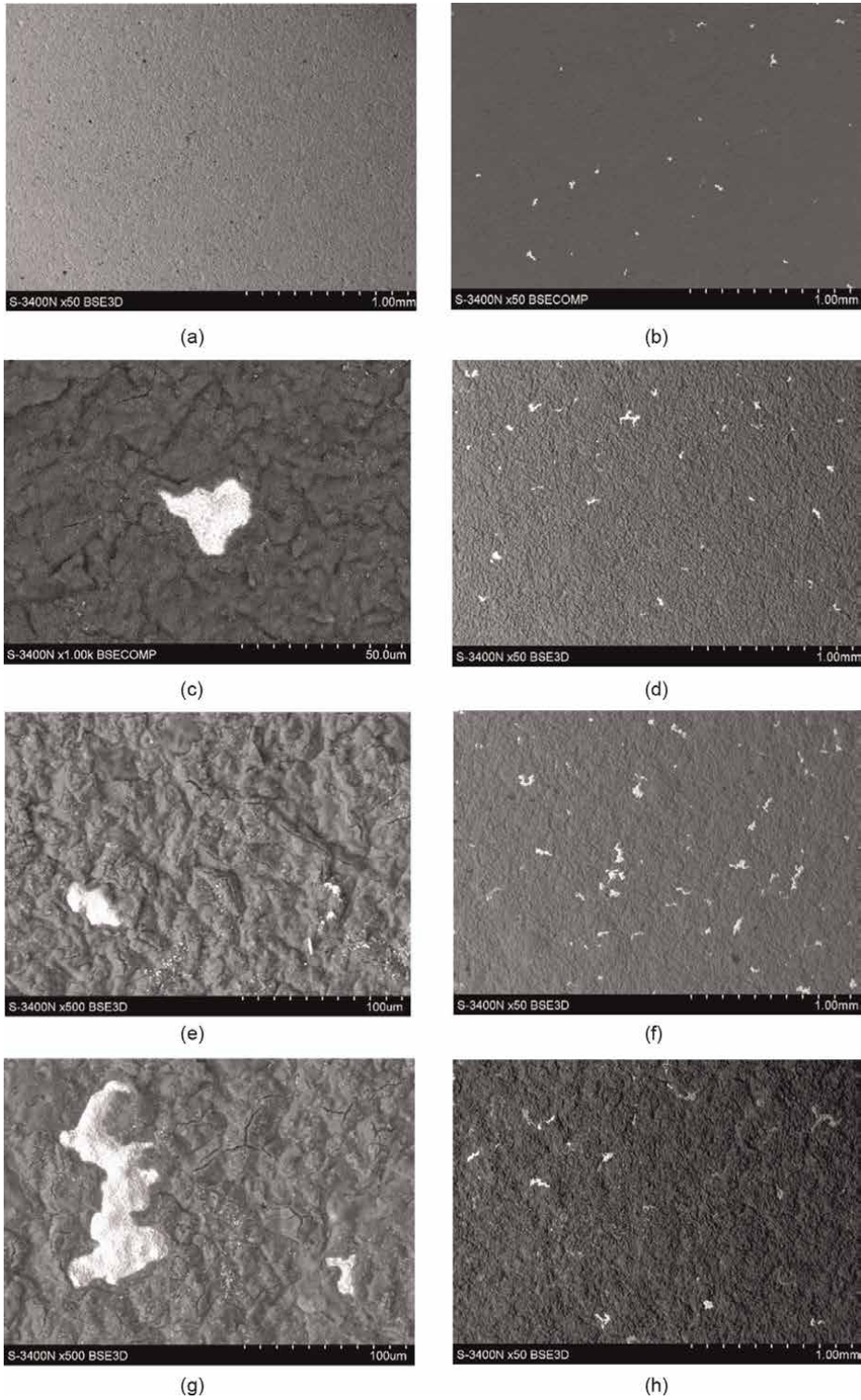


**Figure 42.** Surfaces of Inconel 713LC samples before cyclic oxidation and after 8, 18, 28 and 38 cycles of testing.

- a. Surface of IN 713 LC with AlSi – 0 cycles
- b. Sample after 8 cycles.
- c. Detail of the sample after 8 cycles
- d. Sample after 18 cycles.
- e. Detail of the sample after 18 cycles
- f. Sample after 28 cycles.
- g. Detail of the sample after 28 cycles
- h. Sample after 38 cycles.

#### 2.2.3.4 Microstructural examination of MAR 247 LC without coating

MAR 247 LC belongs to widely used high temperature nickel-base superalloy. It is a cast polycrystalline material used especially for turbine blades and discs. The chemical composition (**Table 1**) of the alloy has, in comparison with IN 713 LC, a larger content of heavy elements as tungsten and tantalum which act as the most efficient matrix hardeners and promote creep strength. Cobalt in MAR 247 LC has only a small direct influence on strengthening but it affects the solubility of elements in the matrix solid solution and often raises the temperature of solidus which can lead to the larger amount of precipitates at low to medium temperatures [28]. Carbon is present at higher concentration (0.15 wt.%) than in the IN 713 LC (0.04 wt.%) and it combines with reactive elements such as titanium, tantalum, hafnium and tungsten to form MC carbides. During processing or service these carbides can decompose to other forms as  $M_{23}C_6$  and  $M_6C$  which are rich in chromium, molybdenum and tungsten. Excessive amount of tungsten together with molybdenum and chromium leads to the formation of so-called topologically close-packed (TCP) phases. Various semi-empirical models are used for balancing composition of superalloys to avoid forming of these undesirable phases. The material before testing and without coating was subjected to a hot isostatic pressing and, subsequently, it was heat treated by two steps to reach the microstructure shown in **Figure 43a**. This initial microstructure of the MAR 247 LC alloy consisted of  $\gamma$  Ni-rich solid solution containing a dispersion of  $\gamma'$  precipitates, carbide particles, and  $\gamma/\gamma'$  eutectics as depicted in **Figure 43b**.

As one could see in **Figure 15**, the superalloy MAR 247 LC without coating revealed a very poor resistance to thermal cycling. Mass loss started immediately after the 1st cycle and continued during subsequent 12 cycles when test was stopped. Microstructures of this alloy after 8 cycles of testing well reflect that behavior – see **Figures 44** and **45**.

Precipitation-hardenable superalloys usually have a good oxidation resistance in oxidizing atmospheres within their normal range of service temperatures. Exposure to high-temperature environments can cause changes in the alloy composition near the surface. **Figure 45** shows the changes in the subsurface microstructure formed under a high temperature environment. As we can see in **Figure 45**, the surface of the alloy is covered by oxidation scales based on



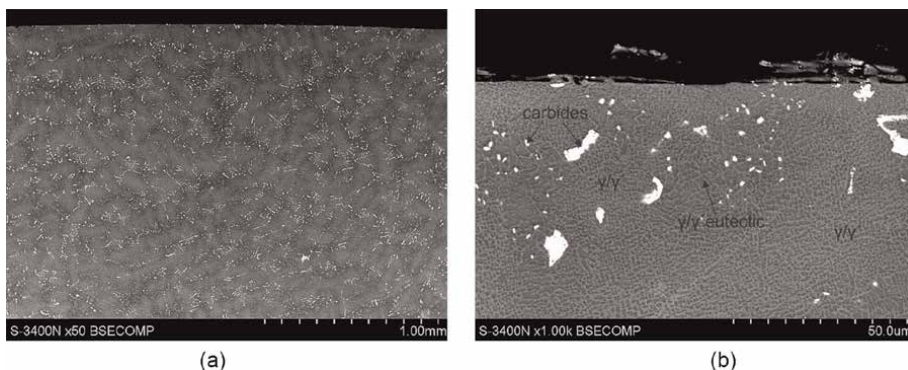


**Figure 43.**  
 (a) View on the microstructure of MAR 247 LC without coating before testing (b) Phases in the microstructure of the MAR 247 LC alloy.

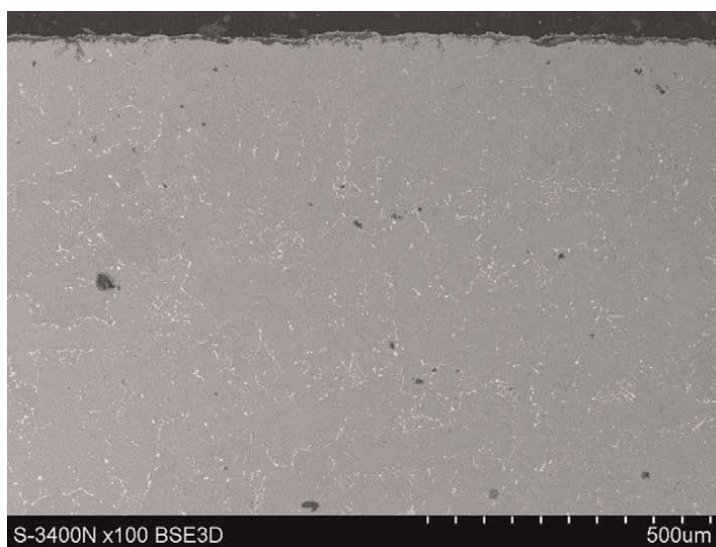


**Figure 44.**  
 View on the structure of MAR 247 LC after 8 cycles.

aluminum (area 5 in **Figure 45**) but an internal oxidation is also visible. Preferential oxygen attacks on carbide phases were observed. Since certain elements as aluminum or chromium are consumed by the scale layer, the bulk composition can become depleted. Subsurface zone (area 2 in **Figure 45**) is composed from a solid solution of elements in nickel with small amounts of aluminum and without  $\gamma'$  coherent precipitates. Chemical content of phases highlighted in the **Figure 45** is in **Table 3**.

A comparison of both surfaces, i.e. before and after cycling oxidation, is presented in **Figures 46–48**. The EDX analyses confirmed that the chemical composition of the alloy on the sample surface (**Figure 46**) without cycling is identical with that declared in **Table 1**. The specimen surface after 8 cycles is covered by oxidation scales as can be seen in **Figures 47 and 48**. The surface is mainly rich in aluminum, chromium and hafnium. Tungsten and tantalum are present in carbides

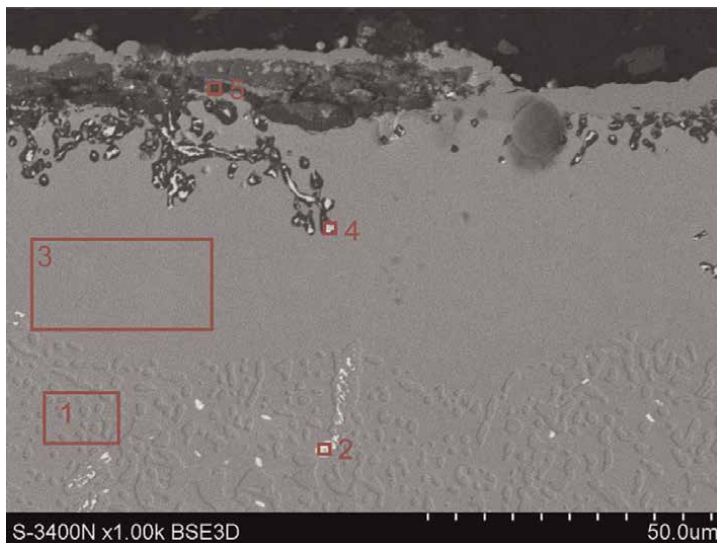


**Figure 45.**  
 Subsurface zone of the sample after 8 cycles.

MAR 247 LC	Al-K	Ti-K	Cr-K	Co-K	Ni-K	Zr-L	Mo-L	Hf-L	Ta-L	W-M
Area 1	7.5	1.3	9.7	10.7	66.6	0.2				4.0
Area 2		8.5	1.8	3.3	16.9			41.7	27.8	
Area 3	5.4	0.9	11.8	11.8	65.2	0.1	0.5			4.3
Area 4	51.0		0.7	1.6	7.6			39.1		
Area 5	95.8				4.2					

**Table 3.**  
 Element distribution in MAR 247 LC without coating after 8 cycles of testing in at. %.

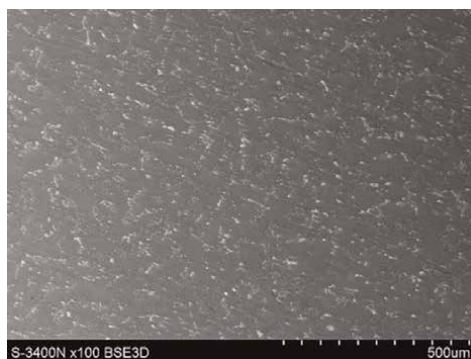


**Figure 46.**  
 Surface of MAR 247 LC.

(white particles in **Figures 47 and 48**). The detail depicted in **Figure 48** shows an attack of carbides along grain boundaries even more clearly than one could see from **Figure 45**.

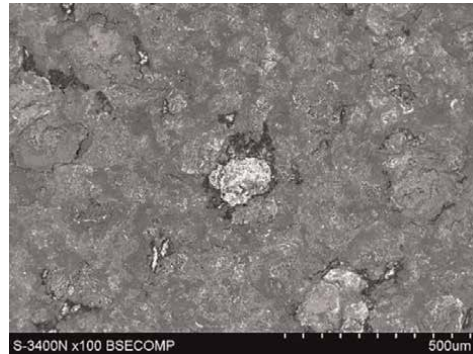


**Figure 47.**  
*Surface of MAR 247 LC without coating without coating before testing after 8 cycles of testing.*

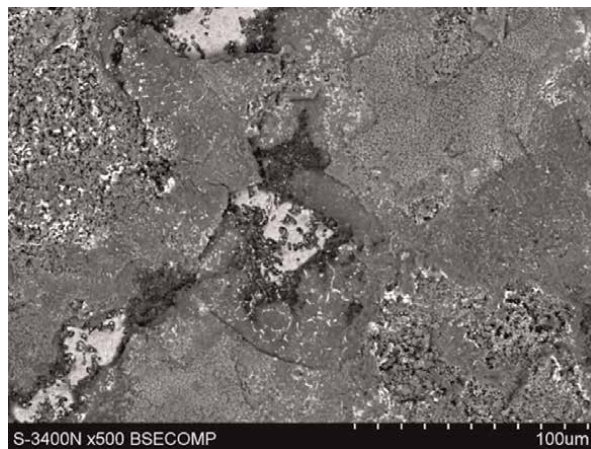


**Figure 48.**  
*Oxide scales on the surface of MAR 247 LC without coating after 8 cycles of testing.*

#### 2.2.3.5 Microstructural examination of MAR 247 LC with Al coating

**Figures 49** and **50** show cross-sectional images of the sample MAR 247 LC with Al coating before testing of cycle oxidation at 1100°C in the air environment. The two-layered coating (**Figure 50**) includes the upper NiAl layer which serves as aluminum reservoir and the inner diffusion layer of solid solution of Ni with a smaller content of Al and carbide particles on the basis of Cr, W, Hf and Mo. The chemical content of elements in the highlighted areas (1-4) in **Figure 50** achieved from the EDX analysis is in **Table 4**. The average thicknesses of upper and inner parts are 24.9 μm and 18.2 μm, respectively.

The view on the microstructure of the specimen after 8 cycles of testing at 1100°C in the air for 8x23 hours is in **Figure 51**. The surface is covered by an oxide film and, with respect to this diffusion process, the upper part of the coating is depleted of aluminum. The content of aluminum in the matrix of upper layer dropped from 49.5 at. % before testing to 27.4 at. % after 8 cycles of oxidation. In this zone one can observe grains with a higher concentration of nickel (65 at. %) than in the matrix (in **Figures 51–53** described as “Grains of Ni”). These grains are bigger in samples after 18



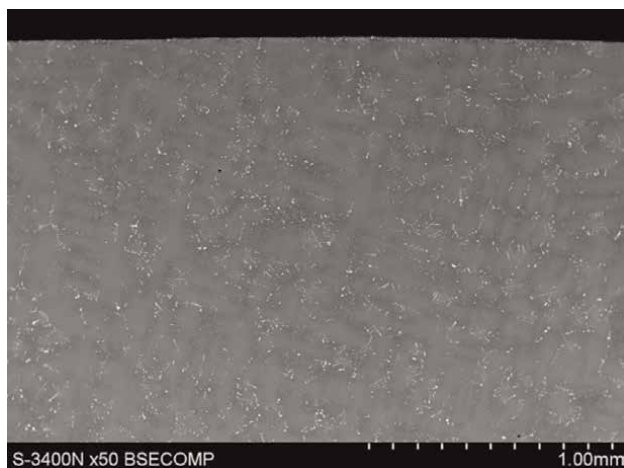


**Figure 49.**  
 SEM micrograph of the microstructure of the sample MAR 247 LC with Al coating before testing at low magnification.

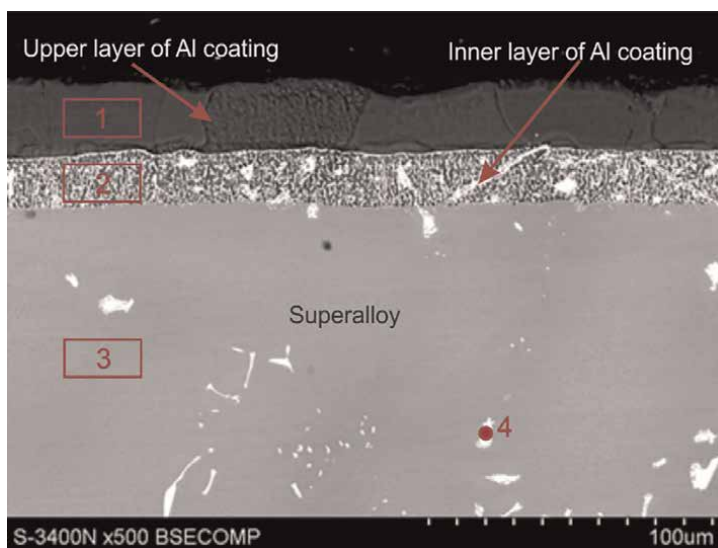


**Figure 50.**  
 Cross-section of sample MAR 247 LC with Al coating before cycle oxidation testing at 1100°C.

MAR 247 LC	Al-K	Ti-K	Cr-K	Fe-K	Co-K	Ni-L	Mo-L	Hf-L	Ta-L	W-M
Area 1	49.5		2.0	0.3	5.3	43.0				
Area 2	25.9	1.9	11.9	0.3	10.0	43.8	0.6	1.1		4.6
Area 3	10.5	1.0	10.4	0.3	10.6	61.9			0.9	4.6
Area 4		28.0	2.7		2.2	9.8	1.6	8.6	34.4	12.6

**Table 4.**  
 Element distribution in MAR 247 LC with Al coating before testing in at. %.

and 28 cycles of oxidation. The microstructure view on the sample after 38 cycles (**Figure 54**) is different from the previous ones.

Coating upper layer of the sample after 38 cycles has two phases as in previous samples (**Figures 51–53**) but proportion of these phases is changed. Grains of Ni are extended to a large extent that they can be assumed as matrix of the sample after 38 cycles and second dark phases mean unchanged grains of the upper layer matrix of samples after 8, 18 and 28 cycles.

Moreover, needles of topologically close packed phases (TCP) were observed. Presence of refractory elements in the superalloys provide strength benefits from solid solution hardening but a tendency for an alloy instability due to a formation of TCP phases (or secondary reaction zone phenomena) is high. The formation of these phases has a detrimental effect because of their brittle nature and depletion of Ni-rich matrix from strengthening elements [29]. The thickness of coating after 8 cycles rose up twice in comparison with original state and then it kept changeless up to the end of thermal cycling.

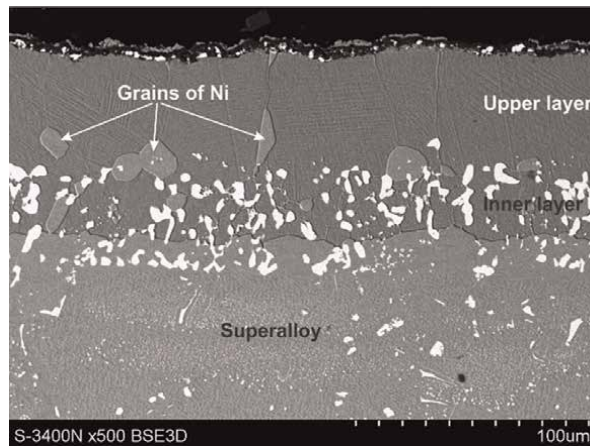


**Figure 51.**  
*Microstructure of MAR 247 LC.*

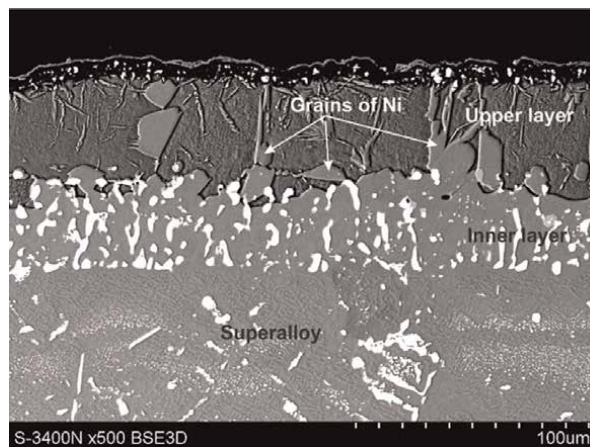


**Figure 52.**  
*Microstructure of MAR 247 LC with Al coating after 8 cycles with Al coating after 18 cycles.*

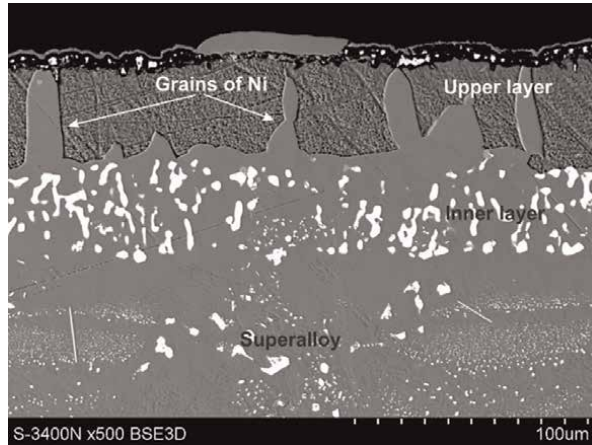


**Figure 53.**  
*Microstructure of MAR 247 LC.*

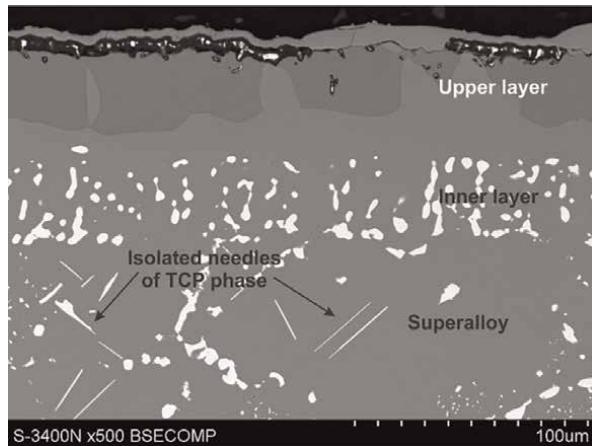


**Figure 54.**  
*Microstructure of MAR 247 LC with Al coating after 28 cycles with Al coating after 38 cycles.*

Appearance of the sample surface after 8 cycles of oxidation is in **Figure 55** where a spallation of small oxide segments can be seen. Similar images were observed on samples after 18, 28 and 38 cycles (**Figure 56**).

The spallation started already at very early stages of oxidation. Stress generation within the oxide during its growth and its release due to cracking in the scale or creep of the substrate metal led to the spallation process and exposure of the substrate. In spite of the loss of protective scales during the exposure by a substantial number of 38 cycles some new scales were reformed. On the basis of data achieved from the thermogravimetric analyses (**Figure 15**) the MAR 247 LC with Al coating after 38 cycles of cyclic oxidation can be still considered to be a good protective system.

#### 2.2.3.6 Microstructural examination of MAR 247 LC with AlSi coating

Pack powder mixture for codepositing Al and Si on MAR 247 LC superalloys by the pack cementation process was used to form AlSi diffusion coating. Silicon (similarly to

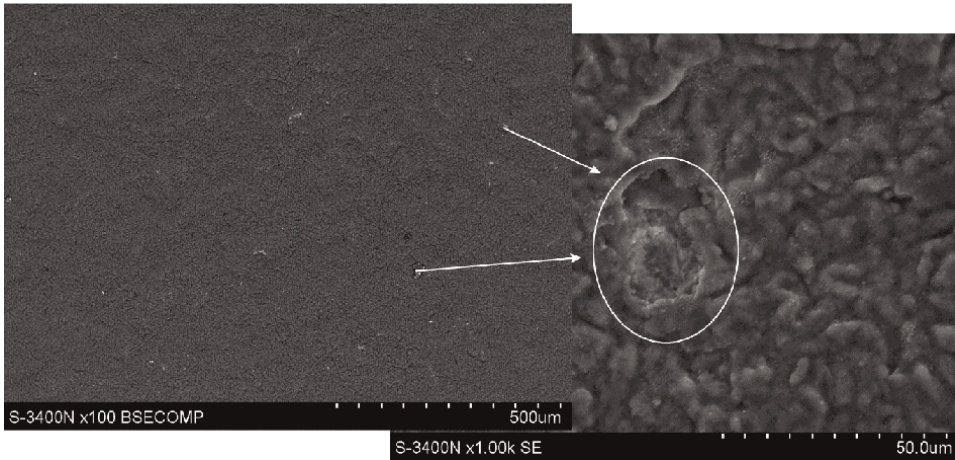


**Figure 55.**  
*General view on the surface of sample after 8 cycles of oxidation and detail from spalled area.*

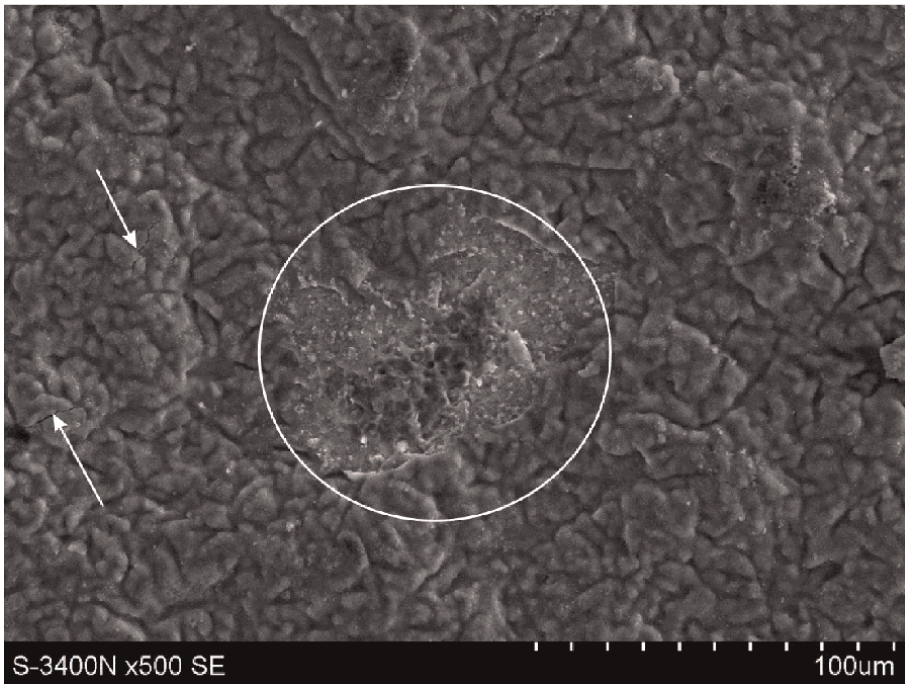


**Figure 56.**  
*Spalled area and cracks on the oxide surface of sample after 38 cycles.*

chromium) was added to the aluminide coating to enhance the resistance against oxidation and sulfur-carrying gases i.e. hot corrosion. However, application of Si is limited to small amounts because silicon bears the risk of forming low-melting phases in nickel-base superalloys [23]. Overall microstructure view on the sample MAR 247 LC with AlSi coating is visible in **Figure 57** where coating is two-layered. The upper





**Figure 57.**  
 General cross-section view on the sample MAR 247 LC with AlSi coating before testing.

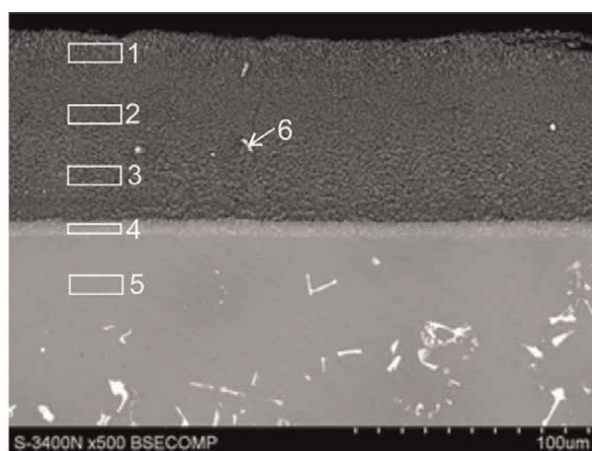


**Figure 58.**  
 The coating at higher magnification.

MAR-247 + AlSi	Al-K	Si-K	Ti-K	Cr-K	Co-K	Ni-K	Mo-L	Hf-L	Ta-L	W-L
Area 1	44.7	4.2	0.4	7.6	5.9	34.8	0.2			2.3
Area 2	47.2	0.6	0.6	6.7	5.8	36.6	0.3			2.3
Area 3	45.2	0.0	0.2	4.9	6.4	41.2	0.2			1.9
Area 4	29.2		1.7	16.5	9.2	37.1	0.7			5.2
Area 5	10.9		1.1	10.4	10.5	61.3			0.7	4.3
Area 6	11.0	9.3	20.6	3.5	2.7	13.4	1.0	4.6	22.6	11.2

**Table 5.**  
 Element distribution in MAR 247 LC with AlSi coating before testing in at. %.

part has average thickness of 94.4  $\mu\text{m}$  and the inner diffusion part is much smaller. Detailed chemical compositions achieved by EDX analyses of individual marked zones (see **Figure 58**) is in **Table 5**.

Silicon is the most placed in region 1 and it has thickness about 12.5  $\mu\text{m}$ . Lower regions 2 and 3 have hardly any silicon and chemical content of others elements is similar to the region 1. The upper part of this coating has a few of precipitates based on Si and refractory elements (point 6 in **Figure 58**). Thin diffusion coating part (area 4 in **Figure 58**) is formed from NiAl solid solution with precipitates on the base of refractory elements and its chemical content is very similar to the diffusion zone of Mar 247 LC with Al coating (see **Table 4**). EDX analyses show that representation of silicon gradually falls from the surface to the diffusion zone of the coating. Under this coating, we can observe dendritic microstructure of the superalloy. Ni-rich  $\gamma$  matrix with  $\gamma'$  semi-coherent precipitates contains MC carbides characterized by different shapes (from discrete blocky precipitates of a diversified shape and size to the shape known as Chinese script) and borides (**Figure 57**). MC carbides precipitated in the final stage of solidification via eutectic reaction with  $\gamma$ -matrix in the interdendritic areas. The secondary  $\text{M}_{23}\text{C}_6$  carbides are very fine and exist at the grain boundaries.

Testing of samples on cyclic oxidation at the temperature 1100°C in the air environment showed that this system MAR 247 LC superalloy/AlSi coating had excellent resistance to cyclic oxidation. The amount of aluminum in the upper part of coating decreased after first cycles on the average from 47 at. % to 26 at. % and then up to 38 cycles of testing remained at the same value. This means that aluminum reservoir is sufficient to form protective oxides on the surface and the oxidation rate is slow. From the point of view of engineering design, kinetics of oxidation is very important because it gives an estimate of design life of system superalloy/coating. The microstructures of samples after 8, 18, 28 and 38 cycles are visible in **Figures 59–62**. The thickness of the coating of sample after 8 cycles rose sharply 3.3 times and then the thicknesses of all tested samples remained the same. Topologically close packed phases emerged after 8 cycles of testing, their amounts gradually increased to 38 cycles. This behavior was although observed in samples of MAR M247 LC with Al coating. From the point of view of other phases, the microstructure remained without significant changes up to 38 cycles of testing of the cycle oxidation. Chemical contents of phases found in MAR 247 LC with AlSi coating after 38 cycles were similar to the phases in MAR 247 LC with Al coating.

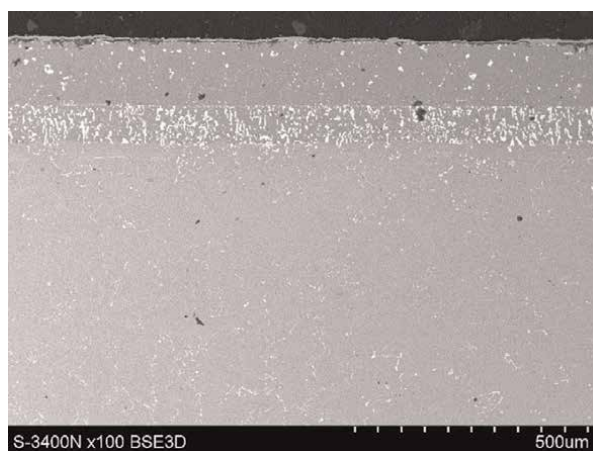


**Figure 59.**  
*Microstructure of MAR 247 LC.*

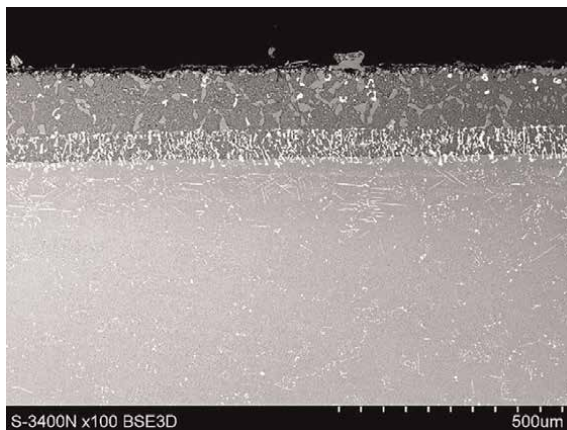


**Figure 60.**  
*Microstructure of MAR 247 LC with AlSi coating after 8 cycles with AlSi coating after 18 cycles.*

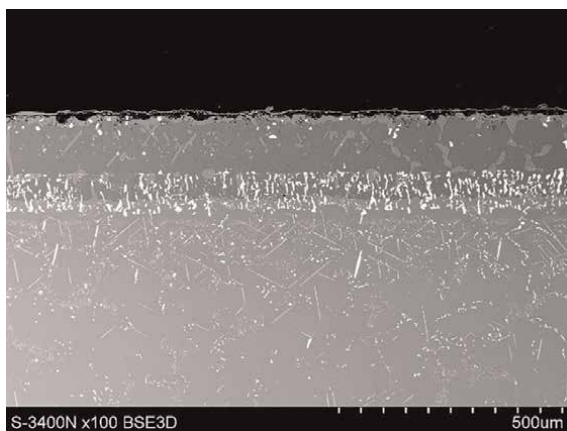


**Figure 61.**  
*Microstructure of MAR 247 LC.*

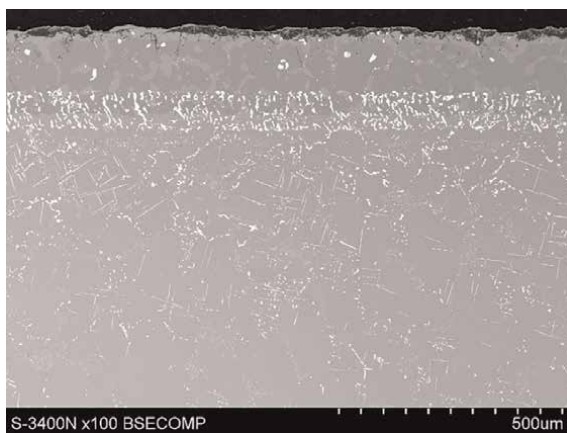


**Figure 62.**  
*Microstructure of MAR 247 LC with AlSi coating after 28 cycles with AlSi coating after 38 cycles.*

Surfaces of MAR 247 LC with AlSi coating samples after 8, 18, 28 and 38 cycles of testing represent **Figures 63–69**. We can observe that protective alumina oxide after 8 cycles spalled out and the layer composed from solid solution of Al in Ni and precipitates based on refractory elements revealed (**Figure 64**). Some of these spalled

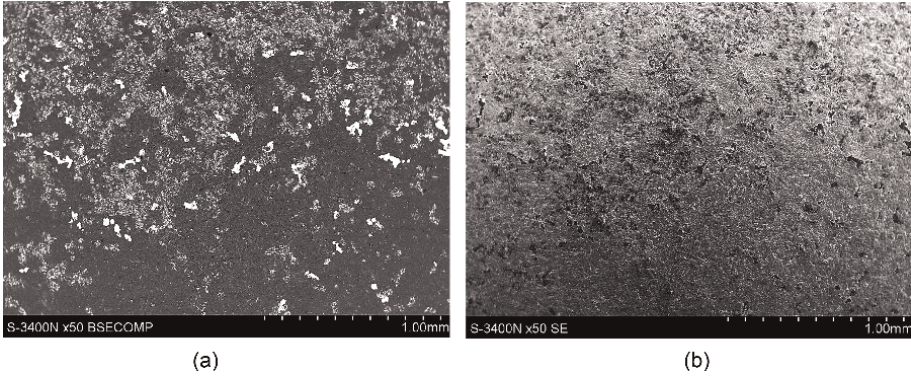


**Figure 63.**  
*Surface of MAR 247 LC with AlSi coating after 8 cycles (left BSE image, right SE image).*

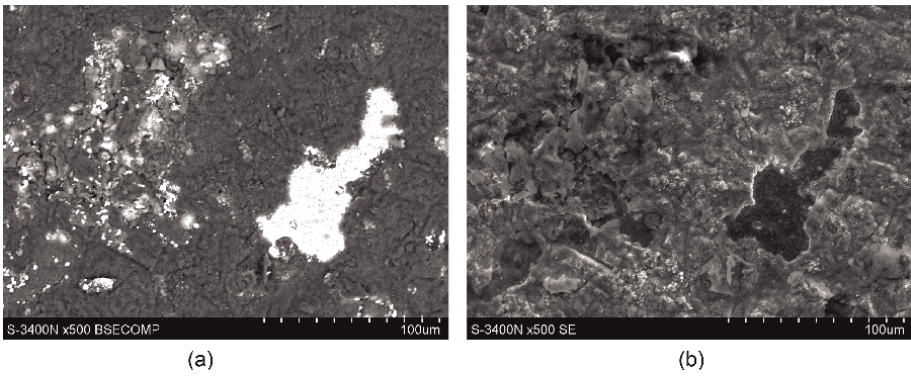


**Figure 64.**  
*Detail from the surface displayed in Figure 63 (left BSE image, right SE image).*

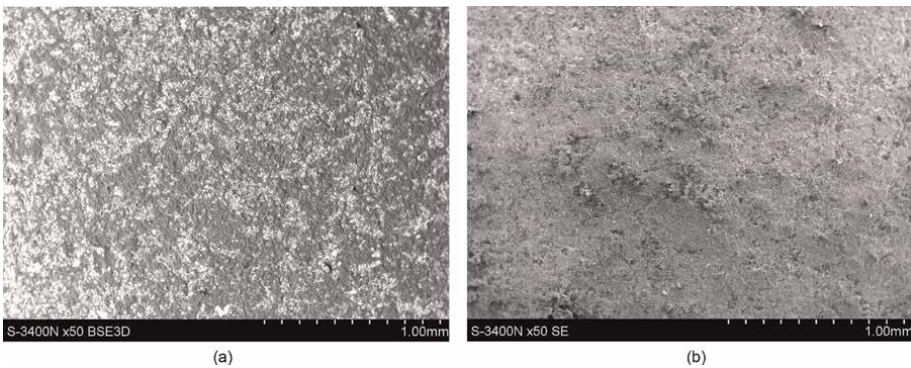


**Figure 65.**  
*Surface of MAR 247 LC with AlSi coating after 18 cycles (left BSE image, right SE image).*



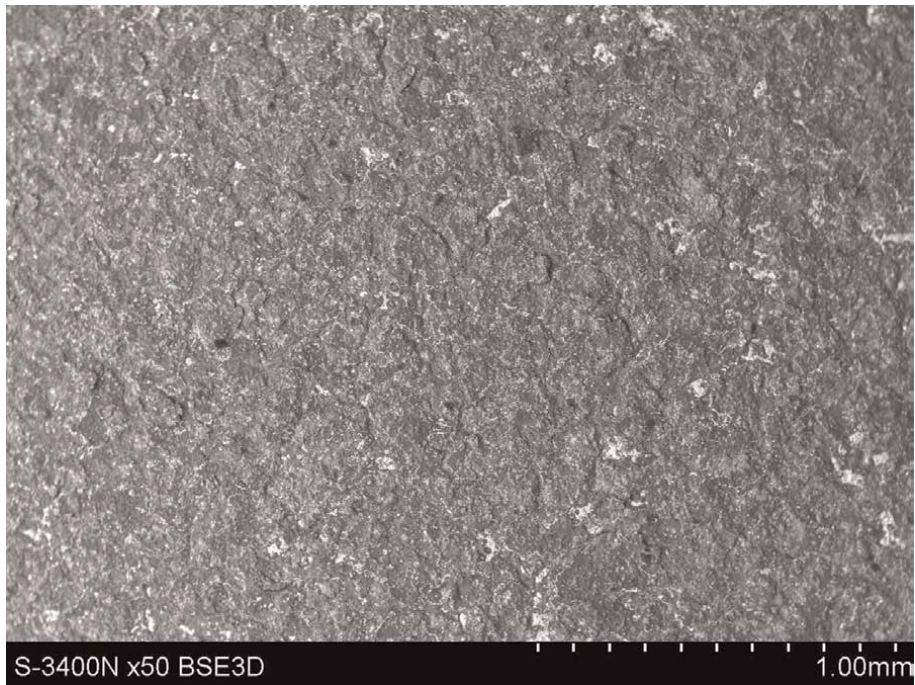


**Figure 66.**  
*Surface of MAR 247 LC with AlSi coating after 28 cycles.*

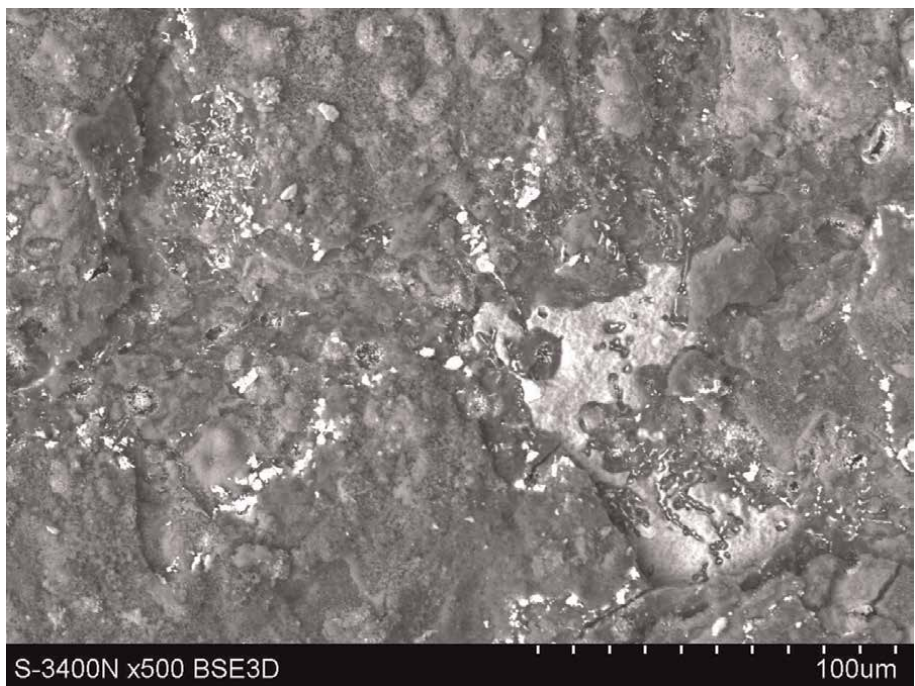


**Figure 67.**  
*Part of the surface displayed in **Figure 66** in higher resolution.*

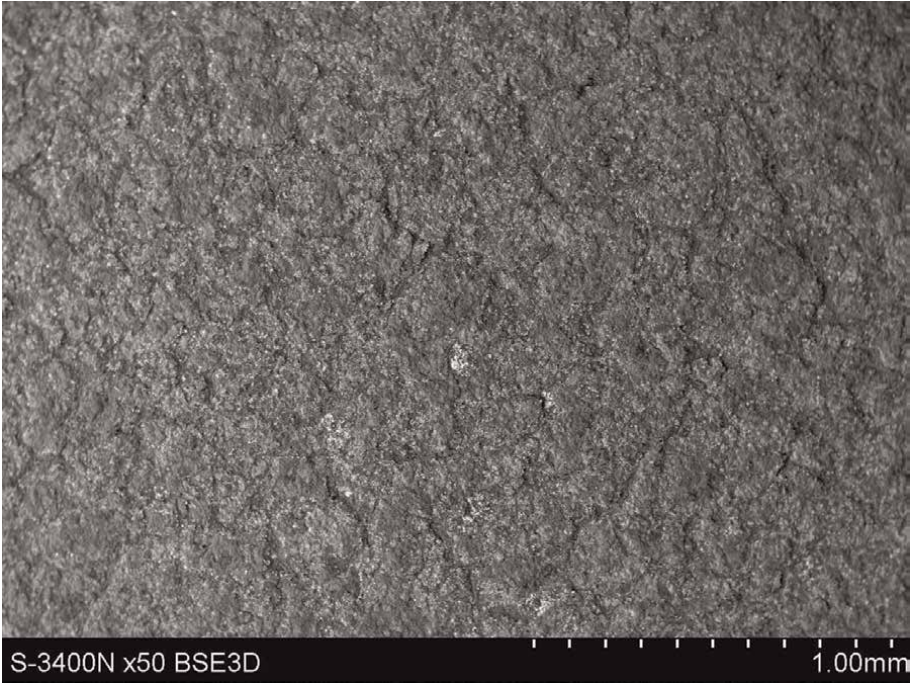


**Figure 68.**  
*Surface of MAR 247 LC with AlSi coating after 38 cycles.*

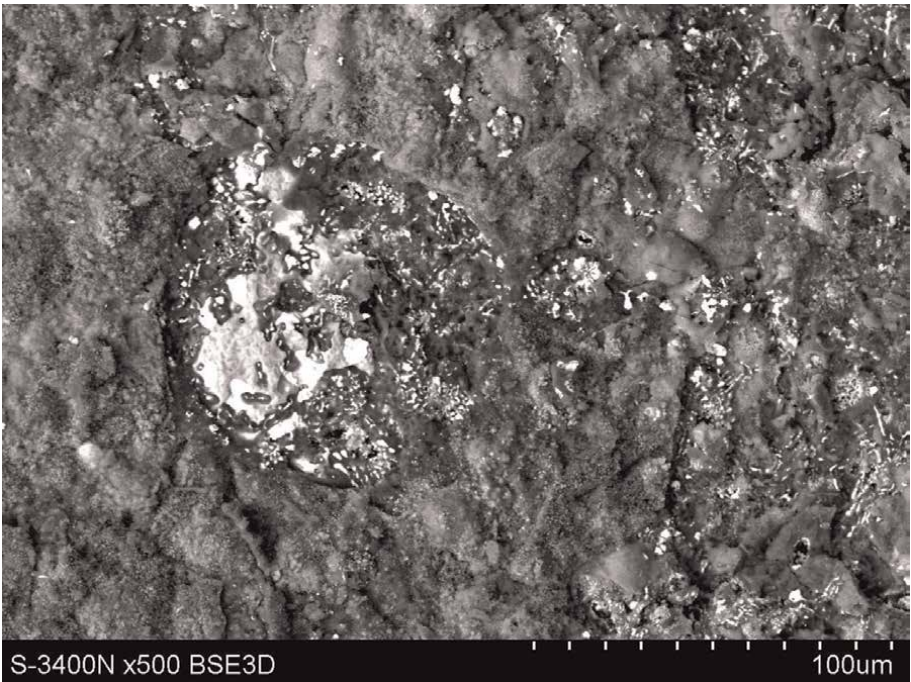


**Figure 69.**  
*Part of the surface displayed in Figure 68 in higher resolution.*

parts had a bigger size (the white particle in **Figure 64**). Next cyclic oxidation caused new alumina scales formation and white particles seen in **Figure 65** were smaller. Creation of protective alumina scales continued (see **Figure 66**) and after 38 cycles of testing protective oxides (**Figure 68**) covered almost all the surface of coated superalloy.


## Author details

Marta Kianicová  
Alexander Dubcek University in Trencin, Trencin, Slovakia

\*Address all correspondence to: [marta.kianicova@tnuni.sk](mailto:marta.kianicova@tnuni.sk)

## IntechOpen

---

© 2022 The Author(s). Licensee IntechOpen. This chapter is distributed under the terms of the Creative Commons Attribution License (<http://creativecommons.org/licenses/by/3.0>), which permits unrestricted use, distribution, and reproduction in any medium, provided the original work is properly cited. 

## References

- [1] Singh R. Applied Welding Engineering. In: Processes, Codes and Standards. 3rd ed. BH Amsterdam: Elsevier Inc.; 2020. p. 442. DOI: 10.1016/C2019-0-03490-5
- [2] Xiongfeng H, Siyu J, Fuqiang L, Li J, Xiaoqiang L, Shengguan Q. Investigation on the parameters optimization and sliding wear behaviors under starved lubrication of discrete laser surface hardened 25CrNi2MoV steel. *Tribology International*. 2021;**163**:163. DOI: 10.1016/j.triboint.2021.107176
- [3] Zhang B, Chen J, Wang P, Sun B, Cao Y. Enhanced strength-ductility of CoCrFeMnNi high-entropy alloy with inverse gradient-grained structure prepared by laser surface heat-treatment technique. *Journal of Materials Science & Technology*. 2022;**111**:111-119. DOI: 10.1016/j.jmst.2021.09.043
- [4] Laketić B, Rakin M, Momčilović M, Ciganović J, Veljović D, Cvijović-Alagić I. Influence of laser irradiation parameters on the ultrafine-grained Ti-45Nb alloy surface characteristics. *Surface and Coatings Technology*. 2021;**418**:14. DOI: 10.1016/j.surfcoat.2021.127255
- [5] Guo Y, Jia J, Kong B, Peng H, Zhang H. Heat treatment induced phase transition and microstructural evolution in electron beam surface melted Nb-Si based alloys. *Applied Surface Science*. 2017;**423**:417-420. DOI: 10.1016/j.apsusc.2017.05.248
- [6] Vazquez-Martinez J, Del Sol II, Arrien EU, Batista M, Salguero J. Laser surface texturing as a finishing process for aerospace alloys. In: *Handbooks in Advanced Machining and Finishing*. 1st ed. BH Amsterdam: Elsevier Inc.; 2021. DOI: 10.1016/B978-0-12-817452-4.00010-5
- [7] Muthukumaran G, Dinesh BP. Metallurgical characterization of laser hardened, mechanically textured 2.5 Ni-Cr-Mo low alloy steel and optimization using RSM. *Optics & Laser Technology*. 2021;**141**. DOI: 10.1016/j.optlastec.2021.107126
- [8] Zaleski B. A study on the properties of surface – active fluids sused in burnishing and shot peening processes. *Advances in Science and Technology Research Journal*. 2016;**10**:235-239. DOI: 10.12913/22998624/64012
- [9] Maleki E, Unal O, Guagliano M, Bagherifard S. The effects of shot peening, laser shock peening and ultrasonic nanocrystal surface modification on the fatigue strength of Inconel 718. *Materials Science and Engineering: A*. 2021;**810**:11. DOI: 10.1016/j.msea.2021.141029
- [10] Maleki E, Farrahi GH, Kashyzadeh KR, Unal O, Gugaliano M, Bagherifard S. Effects of conventional and severe shot peening on residual stress and fatigue strength of steel AISI 1060 and residual stress relaxation due to fatigue loading: experimental and numerical simulation. *Metals and Materials International*. 2021;**27**: 2575-2591. DOI: 10.1007/s12540-020-00890-8
- [11] Agaram S, Srinivasan SM, Kanjarla AK. Crystal plasticity modelling of stability of residual stresses induced by shot peening. *International Journal of Mechanical Sciences*. 2022;**230**:13. DOI: 10.1016/j.ijmecsci.2022.107526
- [12] Fu P, Su H, Li Z, Dai P, Tang Q. Enhancing mechanical properties of dual-phase Al0.5CoCrFeNiSi0.25 high entropy alloy via thermomechanical treatment. *Journal of Alloys and*



Compounds. 2022;**921**:11. DOI: 10.1016/j.jallcom

[13] Wang X, Xiao Z, Qiu W, Li Z, Liu F. The evolution of microstructure and properties of a Cu–Ti–Cr–Mg–Si alloy with high strength during the multi-stage thermomechanical treatment. *Materials Science and Engineering: A*. 2021;**803**:9. DOI: 10.1016/j.msea.2020.140510

[14] Mittemeijer EJ, Somers MAJ. Kinetics of thermochemical surface treatments. *Thermochemical Surface Engineering of Steels*. Elsevier Inc.; 2015. 113-140 p. DOI: 10.1533/9780857096524.1.113

[15] Yao J et al. On the growth of functionally graded self-lubricating layer during a plasma-assisted thermochemical treatment of M50NiL steel. *Applied Surface Science*. 2022;**584**:10. DOI: 10.1016/j.apsusc.2022.152517

[16] Prasad MA, Dharmalingam G, Salunkhe S. Microstructural evaluation of gas nitrided AISI 316 LN austenitic stainless steel. *Journal of the Energy Institute*. 2022;**104**:112-123. DOI: 10.1016/j.joei.2022.07.015

[17] Naeem N et al. Improved wear resistance of AISI-1045 steel by hybrid treatment of plasma nitriding and post-oxidation. *Tribology International*. 2022;**175**:11. DOI: 10.1016/j.triboint.2022.107869

[18] Chen W et al. The thermal process for hardening the nitrocarburized layers of a low-carbon steel. *Scripta Materialia*. 2022;**210**:4. DOI: 10.1016/j.scriptamat.2021.114467

[19] Katsamas AI, Haidemenopoulos GN. Laser-beam carburizing of low-alloy steels. *Surface and Coatings Technology*.

2001;**139**:183-191. DOI: 10.1016/S0257-8972(00)01061-6

[20] Kucherov FA, Romashov LV, Anamikov VP. Development of 3D+G printing for the design of customizable flow reactors. *Chemical Engineering Journal*. 2022;**430**:9. DOI: 10.1016/j.cej.2021.132670

[21] Kalkal A et al. Recent advances in 3D printing technologies for wearable (bio) sensors. *Additive Manufacturing*. 2021;**46**:20. DOI: 10.1016/j.addma.2021.102088

[22] Wang W, Cui W, Xiao Z, Qin G. The improved corrosion and wear properties of Ti-Zr based alloys with oxide coating in simulated seawater environment. *Surface and Coatings Technology*. 2022;**439**:11. DOI: 10.1016/j.surfcoat.2022.128415

[23] Welegergs GC, Akoba R, Sacky J, Nuru ZY. Structural and optical properties of copper oxide (CuO) nanocoatings as selective solar absorber. *Materials Today: Proceedings*. 2021;**36**:509-513. DOI: 10.1016/j.matpr.2020.05.298

[24] Dai D, Zhou D, He L, Wang C, Zhang C. Graphene oxide nanocoating for enhanced corrosion resistance, wear resistance and antibacterial activity of nickel-titanium shape memory alloy. *Surface and Coatings Technology*. 2022;**431**:13. DOI: 10.1016/j.surfcoat.2021.128012

[25] Li M, Han B, Song L, He Q. Enhanced surface layers by laser cladding and ion sulfurization processing towards improved wear-resistance and self-lubrication performances. *Applied Surface Science*. 2020;**503**:11. DOI: 10.1016/j.apsusc.2019.144226

[26] He X, Wu J, Chen Y, Zhang L, Sheng X. A trace amount of

MXene@PDA nanosheets for low-temperature zinc phosphating coatings with superb corrosion resistance. *Applied Surface Science*. 2022;**603**:11. DOI: 10.1016/j.apsusc.2022.154455

[27] Tian Y et al. Accelerated formation of zinc phosphate coatings with enhanced corrosion resistance on carbon steel by introducing a-zirconium phosphate. *Journal of Alloys and Compounds*. 2020;**831**:9. DOI: 10.1016/j.jallcom.2020.154906

[28] Vazirgiantzikis I, George SL, Pichon L. Surface characterisation and silver release from Ti-6Al-4V and anodic TiO<sub>2</sub> after surface modification by ion implantation. *Surface and Coatings Technology*. 2022;**433**:10. DOI: 10.1016/j.surfcoat.2021.128115

[29] Ranjan R, Das AK. Protection from corrosion and wear by different weld cladding techniques: A review. *Materials Today: Proceedings*. 2022;**57**(3):1687-1693 DOI: 10.1016/j.matpr.2021.12.329

[30] Qian Y et al. Microstructure and mechanical properties of SiC particle reinforced Zr-based metallic glass surface composite layers produced by laser alloying. *Surface and Coatings Technology*. 2022;**446**:10. DOI: 10.1016/j.surfcoat.2021.128784

[31] Monisha K et al. Titanium boride and titanium silicide phase formation by high power diode laser alloying of B<sub>4</sub>C and SiC particles with Ti: Microstructure, hardness and wear studies. *Materials Today. Communications*. 2022;**31**:19. DOI: 10.1016/j.mtcomm.2022.103741

[32] Yang GJ, Suo XK, Li GR. *Advanced Nanomaterials and Coatings by Thermal Spray*. 1st ed. BH Amsterdam: Elsevier Inc.; 2019:328. DOI: 10.1016/C2017-0-00237-9

[33] Hu H et al. Wear-resistant ceramic coatings deposited by liquid thermal spraying. *Ceramics International*. 2022;**48**(22):33245-33255. DOI: 10.1016/j.ceramint.2022.07.267

[34] Poursaei A, editor. *Corrosion of Steel in Concrete Structures*. 1st ed. Cambridge UK: Elsevier Inc.; 2016. p. 285. DOI: 10.1016/C2014-0-01384-6

[35] Wei X et al. Deposition of DLC films on the inner wall of U-type pipes by hollow cathode PECVD. *Diamond & Related Materials*. 2021;**114**:11. DOI: 10.1016/j.diamond.2021.108308

[36] Biava G et al. Evaluation of high temperature corrosion resistance of CrN, AlCrN, and TiAlN arc evaporation PVD coatings deposited on Waspaloy. *Surface and Coatings Technology*. 2022;**348**:15. DOI: 10.1016/j.surfcoat.2022.128398

[37] Agüero A, Østergård MJL, Hansson AN, Gutierrez M. Thermal cyclic resistance and long term inter-diffusion properties of slurry aluminide coatings modified with Si. *Results in Surfaces and Interfaces*. 2022;**6**:16. DOI: 10.1016/j.rsurfi.2022.100042

[38] Pokluda J, Kianicová M. Gas turbines. In: Injeti G, editor. *Damage and Performance Assessment of Protective Coatings on Turbine Blades*. Rijeka Croatia: IntechOpen; 2010. DOI: 10.5772/45608

[39] Kianicová M, Kafrík J, Trnák J. Degradation of aluminide coatings deposited on nickel superalloys. *Procedia Engineering*. 2016;**136**:346-352. DOI: 10.1016/j.proeng.2016.01.221

[40] Fu C, Wang C, Ren ZM, Cao GH. Comparison of microstructure and oxidation behavior between Pt-free and Pt-modified -Ni Si coatings on Ni-based

- superalloys. *Corrosion Science*. 2015;**98**: 211-222. DOI: 10.3323/jcorr1991.50.582
- [41] Takahasi RJ, Assis JMK, Neto FP, Reis DAP. Thermal conductivity study of ZrO<sub>2</sub>-YO<sub>1.5</sub>-NbO<sub>2.5</sub>.TBC. *Journal of Materials Research and Technology*. 2022;**19**:4932-4938. DOI: 10.1016/j.jmrt.2022.07.037
- [42] Liew W et al. Thermal stability, mechanical properties, and tribological performance of TiAlXN coatings: Understanding the effects of alloying additions. *Journal of Materials Research and Technology*. 2022;**17**:961-1012. DOI: 10.1016/j.jmrt.2022.01.005
- [43] Pakseresht A, Sharifahmadian O. *Handbook of Research on Tribology in Coatings and Surface Treatment*. 1st ed. Hersey, Pennsylvania, USA: IGI Global; 2022. p. 470. DOI: 10.4018/978-1-7998-9683-8
- [44] Zare Mohazabie MS, Nogorani FS. The addition of zirconium to aluminide coatings: The effect of the aluminide growth mode. *Surface and Coatings Technology*. 2019;**378**:8. DOI: 10.1016/j.surfcoat.2019.125066
- [45] Rahmani KH, Nategh S. Isothermal LCF behavior in aluminide diffusion coated René 80 near the DBTT. *Materials & Design*. 2009;**30**:1183-1192. DOI: 10.1016/j.matdes.2008.06.064
- [46] Peng X. 3-Metallic coatings for high-temperature oxidation resistance. In: Xu H, Guo H, editors. *Thermal Barrier Coatings. A volume in Woodhead Publishing Series in Metals and Surface Engineering*. 2011. p. 339. DOI: 10.1533/9780857090829.1.53
- [47] Bozza F et al. Diffusion mechanisms and microstructure development in pack aluminizing of Ni-based alloys. *Surface and Coatings Technology*. 2014;**239**:147-159. DOI: 10.1016/j.surfcoat.2013.11.034
- [48] Patent US8137749B2, SNECMA, 2012, Method of aluminization in the vapour phase on hollow metal parts of a turbomachine
- [49] Squillace A, Bonetti R, Archer NJ, Yeatman JA. The control of composition and structure of aluminide layers formed by vapour aluminizing. *Surface and Coatings Technology*. 1999;**120-121**: 118-123. DOI: 10.1016/S0257-8972(99)00347-3
- [50] Grégoire B, Bonnet G, Pedraza F. Development of a new slurry coating design for the surface protection of gas turbine components. *Surface and Coatings Technology*. 2019;**374**:521-530. DOI: 10.1016/j.surfcoat.2019.06.020
- [51] Grégoire B, Oskay C, Meisner T, Galetz M. Corrosion performance of slurry aluminide coatings in molten NaCl-KCl. *Solar Energy Materials and Solar Cells*. 2021;**223**:20. DOI: 10.1016/j.solmat.2021.110974
- [52] Xu C, Gao W. Pilling-Bedworth ratio for oxidation of alloys. *Materials Research Innovations*. 2000;**3**:231-235. DOI: 10.1007/s100190050008
- [53] Li Y, Li Z, Liu L, Cai N. Measuring the fast oxidation kinetics of a manganese oxygen carrier using microfluidized bed thermogravimetric analysis. *Chemical Engineering Journal*. 2020;**385**:12. DOI: 10.1016/j.cej.2019.123970
- [54] Young DJ. In: Young DJ, editor. *High Temperature Oxidation and Corrosion of Metals*. BH Amsterdam: Elsevier Inc.; 2016. p. 733. DOI: 10.1016/C2014-0-00259-6





# Perspective Chapter: Effect of Laser Key Parameters on the Ignition of Boron Potassium Nitrate with a Changing Working Distance

*Ghedjatti Ilyes, Yuan Shiwei and Wang Haixing*

## Abstract

The need to realize more effective ignition systems and exploit their full potential in aerospace propulsion applications has led to significant developments in laser and power systems. This work aims to investigate experimentally and describe mathematically the effectiveness of laser systems based on varying key parameters and their related effects on the sensitivity, ignition threshold, and combustion performance of boron potassium nitrate, then to define the key variables with the most significant influence on the overall system. Understanding the physics and chemistry behind the combined system of laser power source and optics system, and the considered medium as well as the interaction in between, led to a better apprehension of how an optimal and viable solution can be achieved in terms of ignition delays, burning times, and combustion temperatures, considering laser wavelength, power and energy densities, and the focal length displacement over a changing working distance. This is of paramount importance when operating amid difficult conditions in aerospace propulsion applications or during outer space missions, particularly those involving manned missions, not only in terms of performance and efficiency but also safety, engineering, and economic feasibility.

**Keywords:** output power, power density, energy density, Rayleigh range, beam parameter product, beam quality factor, laser brightness, beam diameter, focusability, spot size, working distance, pulse duration, threshold ignition energy, absorbed intensity, thermal penetration depth, ignition time

## 1. Introduction

In contrary to electricity, the only form of energy that is not mass bound is electromagnetic energy; and light being highly focusable in space and time, is part of the spectrum of this electromagnetic form of energy. Laser initiation offers several advantages over bridge wire initiation [1], such as low initiation energy quantities

requirements, multipoint initiation, and multi-times reuse, are easily achieved; it can also be made fully electronic, with lower cost, size, and weight compared to bridge wire. Ease of manufacturing, simpler safety, and arming systems, whilst common failure mechanisms are minimized or removed. It can prevent the occurrence of accidental firings, caused by electromagnetic fields, electrostatic discharge, or stray electrical energy.

The most relevant areas related to laser initiation of pyrotechnics and worth being investigated are sensitivity of pyrotechnics and practical designs for laser systems. Laser initiation aims at safely delivering stimuli for the generation of heat and thus ignition. These are also characterized by different parameters that can be varied or controlled depending upon the type of the targeted energetic material and ignition conditions. For this purpose, lasers must be compact and cost-effective, with the ability to meet the ignition energy requirements, while minimizing the need for chemical modification of the energetic material.

This work aims to mathematically describe and experimentally investigate the effectiveness of a laser system based on varying the laser key parameters, as well as their related effects on the sensitivity, ignition threshold, and combustion performance of boron potassium nitrate (BPN). The condition of ignition for a proportionally increasing focal length with the working distance was quantified by the following measuring techniques: the minimum output power required so that ignition can occur; and the minimum pulse duration necessary for the pyrotechnic material to absorb the required critical energy so that ignition can occur.

According to MilStd1901, a specific mixture of BPN is one of the pyrotechnic materials that can be used without interruption of the pyrotechnic chain [2].

Thanks to its high heat of reaction, boron is often used as a reducer of energetic materials and in the composition of propellants. Its high enthalpy, high temperature of combustion, and low molar mass make it a choice candidate for applications such as pyrotechnics and propellants of rocket motors [3].

The sensitivity of pyrotechnic compositions and the critical laser energy density required to initiate them were investigated by [4–6]. It was concluded that laser initiation is a merely thermal process, instead of photochemical, electrical, or light impact mechanisms.

The physical factors affecting the sensitivity of Mg-based pyrotechnic compositions were studied by [7–9]. It was concluded that at short pulse durations, the sensitivity was characterized by a threshold ignition energy density (i.e. internal properties of the material, such as heat capacity and thermal conductivity); whilst at long pulse durations, the ignition was characterized by a threshold ignition power (i.e. sample area and internal and external parameters of the sample).

The relationship between laser initiation and pulse duration for Ti/KClO<sub>4</sub> was also studied by [10]. The results showed that at short pulse durations, ignition occurred as long as there was a minimum level of energy delivery rates (delivered power); whilst at long pulse durations, ignition was governed by heat loss rates from a critical volume in the composition.

The ignition of Ti/KClO<sub>4</sub> and Zr/KClO<sub>4</sub> was investigated by [11, 12], respectively. Their studies outlined the existence of the ignition energy/power map. Laser spot size was critical in determining the threshold energy and power levels [11].

It has been demonstrated that for TiHx/KClO<sub>4</sub> compositions in unsealed holders, the ignition power decreased with increasing laser pulse duration or increasing laser spot size [13].

Laser initiation is a thermal mechanism, implying that energy is absorbed in the material, and thus the absorption occurs at defects, such as cracks, clusters, or dislocations within the lattice [14]. These inhomogeneities could also lead to a laser beam focusing with high energy densities at particular local sites, which may lead to a number of initiation mechanisms.

Due to their high specific surface area to volume ratio, nanometer-sized boron particles produce more heat release than micrometer-sized particles. When it comes to handling and processing, nano-sized boron particles-based BPN is as safe as the micro-sized one. However, although nano-sized boron particles enhanced calorific value and pressurization rate, they did not contribute to the maximum pressure level [15].

Most studies were conducted in an open-air environment. In practical applications such as rocket motors, ignition takes place under confinement, accompanied by a rise in pressure, which regulates heat transfer and laser beam transmission. Under confinement, laser initiation is more efficient [16].

In addition to the originality of our work, by providing more flexibility in terms of distance covered, by allowing fine spot sizes with high power densities and longer focal lengths, our findings were in compliance with previous studies. In the next section, the laser key parameters on which laser system designs can be built for an effective laser initiation are presented and mathematically described. In Section 3, the experimental setup design used in this work to conduct the current investigation on laser initiation is described, and details on BPN features and composition as well as set up production cost and time are also provided. In Section 4, the obtained results are further discussed, such as varying key parameters and their related effects on sensitivity, ignition threshold, and combustion performance of BPN, and key variables with the most significant influence on the overall system are defined. Last but not least, in Section 5, outcomes are summarized, and conclusions are presented, a better apprehension of how an optimal and viable solution in terms of ignition delays, burning times, and combustion performance, considering laser wavelength, power, and energy densities, and the focal length displacement over a changing working distance is achieved.

## 2. Key parameters of laser systems

Laser systems can be defined by the key parameters shown in **Table 1**.

These laser key parameters are mathematically described. In our application, the laser beam is assumed to be Gaussian, and irradiance profiles are assumed to follow an ideal Gaussian distribution, being symmetric around the center of the beam and decrease as the radius of the laser beam increases. The ideal Gaussian distribution is expressed by Eq. (1):

Fundamental parameters	Beam parameters	Final system parameters
Power and Energy	Power or Energy Density	Spot Size
Pulse Duration	Beam diameter	Working Distance
Repetition Rate	Beam Profile	
Coherence Length	Divergence	
Wavelength		

**Table 1.**  
*Key parameters of laser systems.*

$$I(r) = I_0 \exp\left(\frac{-2r^2}{\omega(z)^2}\right) = \frac{2P}{\pi\omega(z)^2} \exp\left(\frac{-2r^2}{\omega(z)^2}\right) \quad (1)$$

Where  $I_0$  is the peak irradiance at the center of the beam,  $r$  is the radial distance away from the axis,  $\omega(z)$  is the radius of the laser beam where the irradiance is  $1/e^2$  of  $I_0$ ,  $z$  is the distance propagated from the plane where the wavefront is flat, and  $P$  is the total power of the beam.

The irradiance profile varies as the beam propagates through space, hence the dependence of  $\omega(z)$  on  $z$ . The beam waist is the location along the propagation direction of the laser beam where the beam radius is at its minimum. Due to diffraction, a Gaussian beam converges and diverges, by the divergence angle  $\theta$ , equally on both sides of the beam waist ( $\omega_0$ ). This is where the beam diameter reaches its minimum value. The beam waist and divergence angle are expressed as follows:

$$\omega_0 = \frac{\lambda}{\pi\theta} \quad (2)$$

$$\theta = \frac{\lambda}{\pi\omega_0} \quad (3)$$

Where  $\lambda$  is the wavelength of the laser and  $\theta$  is a far field approximation. From Eq. (3), it is noticeable that the smaller the beam waist, the larger the divergence angle, and vice-versa. Therefore, laser beam expanders can be applied to reduce beam divergence by increasing beam diameter. Variation of the beam diameter in the beam waist region is expressed by Eq. (4):

$$\omega(z) = \omega_0 \sqrt{1 + \left(\frac{\lambda z}{\pi\omega_0^2}\right)^2} \quad (4)$$

For a circular laser beam, the Rayleigh length is the distance from the beam waist to the point where the mode area is doubled, and the radius of the beam is increased by a factor of the square root of 2. The Rayleigh range of a Gaussian beam is defined as the value of  $z$  where the cross-sectional area of the beam is doubled. For focused laser beams, the effective Rayleigh length is an essential quantity in determining the depth of focus. The Rayleigh range ( $z_R$ ) is expressed by Eq. (5):

$$z_R = \frac{\pi\omega_0^2}{\lambda} \quad (5)$$

Thus,  $\omega(z)$  can also be related to  $z_R$ , as shown by Eq. (6):

$$\omega(z) = \omega_0 \sqrt{1 + \left(\frac{\lambda z}{\pi\omega_0^2}\right)^2} = \omega_0 \sqrt{1 + \left(\frac{z}{z_R}\right)^2} \quad (6)$$

Considering the quantitative deviation of the beam parameter product and from the characteristics of the Gaussian beam, the far field divergence is the ratio of the beam waist and the Rayleigh length. On the other hand, the Rayleigh length expressed by Eq. (5) is combined with the far field divergence expressed by Eq. (3), and a simpler expression can be obtained, which shows that the beam waist times the far field divergence is equal to a constant. The product of the far field divergence angle

Gaussian beams	Real laser beams
$\omega_{Gauss} = \omega_{0,Gauss} \sqrt{1 + \left(\frac{z}{z_{R,Gauss}}\right)^2}$	$\omega_{Real} = \omega_{0,Real} \sqrt{1 + \left(\frac{z}{z_{R,Real}}\right)^2}$
$z_{R,Gauss} = \frac{\pi \omega_{0,Gauss}^2}{\lambda}$	$z_{R,Gauss} = \frac{\pi \omega_{0,real}^2}{\lambda M^2} = \frac{\pi \omega_{0,real}^2 K}{\lambda}$
$BPP_{Gauss} = \omega_{0,Gauss} \theta_{Gauss} = \frac{\lambda}{\pi}$	$BPP_{Real} = \omega_{0,Real} \theta_{Real} = \frac{\lambda}{\pi} M^2 = \frac{\lambda}{\pi K}$

**Table 2.**  
 Real beam and Gaussian beam with respect to the propagation.

and the beam radius is minimum for a Gaussian beam and depends only on the wavelength of that corresponding laser. For a single laser, this beam parameter product is constant throughout all locations of the propagation of a laser beam in whatever optical system it is put into. The consequence is that this product is invariant under propagation and focusing.

$$BPP = \omega_0 \theta = \frac{\lambda}{\pi} = const. \tag{7}$$

When comparing real beams to Gaussian beams with respect to the propagation, some changes need to be introduced, because in the real case there is a less good beam quality and a less good focusability or a higher divergence at these lower-quality laser beams. The real laser beam is in relation to a theoretical best case, that is, the number  $M^2$  called beam quality/propagation factor, and which is always larger than 1. According to ISO Standard 11146,  $M^2$  is defined as the beam parameter product (BPP) divided by the ratio  $\lambda/\pi$  (Table 2).

The beam quality factor ( $M^2$ , or  $K$ ) can be expressed as follows:

$$M^2 = \frac{1}{K} = \frac{BPP_{Real}}{BPP_{Gauss}} = \frac{\omega_{0,Real} \theta_{Real}}{\omega_{0,Gauss} \theta_{Gauss}} > 1 \tag{8}$$

Laser beam parameters, namely, solid angle of divergence, wavelength, beam parameter product, beam quality factor, spot size, and laser power are major contributors to the laser beam brightness and are used to measure the brightness [17] and associated laser beam parameters [18, 19]. The brightness of a light source is defined as the power emitted per unit surface area per unit solid angle. The maximum brightness is achieved for a perfectly spatially coherent laser beam. The brightness can be expressed by:

$$Br = \frac{P_{out}}{A\Omega} \tag{9}$$

Where  $P_{out}$  is the laser power over the surface area  $A$  and  $\Omega$  is the solid angle of divergence. The solid angle is proportional to the square of the divergence angle  $\theta$ , that is, the smaller is the divergence the higher is the brightness. High brightness is usually characterized by a high-quality factor. The solid angle of divergence of a Gaussian beam is as follows:

$$\Omega = \pi \theta^2 = \frac{\lambda^2}{\omega_0^2} \tag{10}$$

Where  $\lambda$  is the wavelength and  $\omega_0$  is the beam radius at the beam waist. For a perfect Gaussian single mode TEM<sub>00</sub> beam condition,  $M^2$  equals 1. This also shows how small a beam waist can be focused. The propagation ratio for circular Gaussian laser beams is shown in Eq. (11):

$$M^4 = M_y^2 M_x^2 \quad (11)$$

Where  $M_y^2$  and  $M_x^2$  are the parameters of the beam profile. Finally, the brightness of the laser beam is once more expressed as follows:

$$Br = \frac{P_{out}}{M^4 \lambda^2} \quad (12)$$

The spot diameter is incorporated by including power density, which is a combination of power and the spot size for a particular Gaussian or non-Gaussian beam, as brightness is a function of output power, wavelength,  $M^2$ , the beam divergence and the spot diameter [20]. Thus, power density is expressed as:

$$Power\ density = \frac{252}{d^2} Output\ power \quad (13)$$

Where  $d$  is the laser beam diameter and 252 is for the Gaussian beam profile. Upon inclusion of the laser power density for determining radiance gives rise to Eq. (14) that takes into consideration the full laser beam parameters, that is, the radiance density (RD), which makes it suitable and accurate:

$$RD = \frac{PD}{M^4 \lambda^2} \quad (14)$$

Where radiance (R) replaces brightness (Br); whilst the radiance density (RD) takes into consideration the beam diameter as well as the power density (PD).

For the incident laser beam, laser energy absorption and diffusion are subject to the following process: absorption by free electrons, propagation through the electron subsystem, then transfer to the lattice. Energy absorption and diffusion is also influenced by the microstructure and electromagnetic properties of the pyrotechnic material; whilst heat conduction is influenced by thermal conductivity, density, heat capacity, and thermal diffusivity. At first, after turning the laser signal on, the temperature increases, the heat at the surface increasingly diffuses into the depth of the pyrotechnic material, that is, absorption at the surface followed by diffusion; therefore, convection simply means moving matter particles into the volume carrying heat and energy; and thus, contributing to the inner energy density of that volume. The diffusion accounts for the heat, which is deposited in the surface and then diffuses into that volume, whilst the thermal penetration depth is defined as the distance that the heat diffuses through. On the other hand, there is diffusion out of the considered volume, that is, at the boundaries, there is diffusion to the environment and loss of energy due to convection carrying energy out of that volume. There is also the change of temperature and its dependence on time, thus the energy changes in this volume are associated with the temperature. Finally, the change of temperature in time is a sum of all these inputs and losses in the corresponding volume. Next, the absorbed intensity can be put into the boundary condition, at the point  $z = 0$  at the surface of the absorbing material, the absorbed intensity can be considered as a source of energy flux.

**Boundary conditions.**

$$\begin{aligned} T(z, t < 0) &= T_0. \\ T(z \rightarrow \infty, t) &= T_0 \\ Q &= 0 \\ -\lambda_T \partial_z T(t)|_{z=0} &= AI \end{aligned}$$

where AI is the absorbed laser intensity, and  $\lambda_T$  is the thermal conductivity.

**Heat equation**

$$\partial_t T(z, t) = \kappa \partial_z^2 T(z, t) \tag{15}$$

Where  $\kappa$  is the temperature conductivity. The solution of the heat conduction equation is not trivial, it implies an integrated error function (ierfc), which is basically the integral of an exponential function where the variable is part of the integral limits. But the most important here is the definition of the thermal penetration depth. As it can be seen, the argument of the integrated error function scales with  $z$ , which is the distance from the surface and the thermal penetration depth.

$$T(z, t) = T_0 + \frac{AI}{\lambda_T} \delta_{th}(t) ierfc\left(\frac{z}{\delta_{th}(t)}\right) \tag{16}$$

The thermal penetration depth can be expressed as follows:

$$\delta_{th}(t) = \sqrt{4\kappa t} \tag{17}$$

and the integral of complementary error function can be expressed as follows:

$$ierfc(x) = \int_x^\infty erfc(z) dz \tag{18}$$

$$erfc(x) = \frac{2}{\sqrt{\pi}} \int_x^\infty \exp(-t^2) dt \tag{19}$$

The maximum temperature can be described by Eq. (20):

$$\Delta T_{max} = T(0, \tau) - T_0 = \frac{AI}{\lambda_T \sqrt{\pi}} \sqrt{4\kappa \tau} \tag{20}$$

Where  $\tau$  is the pulse duration of the laser pulse. Eq. (21) and Eq. (22) describe the threshold ignition energy density and the threshold ignition power [21–23]:

$$E_{ign} = \frac{\rho C_p}{\alpha} (T_{ign} - T_0) \tag{21}$$

$$P_{ign} = 2\lambda_T \omega_0 \sqrt{\pi} (T_{ign} - T_0) \tag{22}$$

Where  $\rho$  is the density,  $C_p$  is the specific heat capacity, and  $\alpha$  is the thermal diffusivity.

### 3. Experimental setup

A fiber coupled laser diode was used to generate the laser signal, with a divergence angle of 12.6 for the laser beam exiting FC/PC fiber. This laser beam was then collimated using a collimating lens. Next, the collimated beam was transmitted to the beam expander used in reverse mode to decrease its diameter by different inverted magnifying power values. After that, the laser beam exiting the beam expander was focused using an achromatic doublet, targeting the BPN for initiation. Finally, by controlling the magnifying power of the beam expander, the focal length was gradually changed over a specific working distance separating the achromatic doublet and the BPN (i.e., BPN positions were readjusted each time the magnifying power was modified so that the focal point would fall on the surface of the BPN). These experiments were conducted in an open-air environment.

A photodiode was used to measure the light emitted by the laser signal and the ignited BPN, then related to a benchtop oscilloscope to display and record the measured values. A power and energy laser measurement sensor and meter were used to measure and display the data, respectively.

#### 3.1 Laser diode, fiber-coupled model

The laser diode used in this experiment to produce the laser beam in order to target and initiate the BPN is a DS3-21312-203 diode laser system fiber-coupled model manufactured by BWT Beijing LTD, with a maximum input power of 2 W and a wavelength of 808 nm.

The experiment was conducted using different values of input power and pulse durations, with a changing focal length and working distance between the beam expander output and the BPN.

#### 3.2 Collimating lens

A C240 TMD-B molded glass mounted aspheric lens from Thorlabs was used to collimate the beam exiting the fiber without introducing spherical aberration into the transmitted wavefront, with broadband AR coating for 600–1050 nm,  $f = 8.00$  mm, and  $NA = 0.5$ . The diffraction-limited spot size is given by Eq. (23):

$$\Phi_{spot} = \frac{4\lambda f}{\pi D} \quad (23)$$

Where  $f$  is the focal length of the lens,  $\lambda$  is the wavelength of the input light, and  $D$  is the diameter of the collimated beam incident on the lens. Solving the equation for a desired focal length of the collimating lens yields to Eq. (24), with MFD being the mode field diameter:

$$f = \frac{\pi D(MFD)}{4\lambda} \quad (24)$$

#### 3.3 Beam expander in reverse mode

The beam expander BE-02-05-B from Thorlabs was used in reverse mode to decrease the diameter of the collimated beam by the lens C240 TMD-B (Table 3).



Expansion	Input aperture	Max input beam diameter ( $1/e^2$ )	AR coating range
2X–5X	Ø8.0 mm	Ø4.0 mm	650–1050 nm

**Table 3.**  
 Beam expander specifications.

Beam expanders in reverse mode decrease the beam area quadratically by inverting the magnifying power (iMP) without significantly affecting the total energy contained within the beam, but divergence will somehow be increased. This results in an increase of the beam’s power density and irradiance, which may also decrease the lifetime of laser components, by increasing the chances of laser induced damage.

### 3.4 Focusing lens

The laser beam exiting the beam expander was then focused using one or other of the two focusing lenses, AC254–60-B-ML and AC254–125-B-ML achromatic doublets from Thorlabs, with focal lengths of 60 mm—and 125 mm, respectively. Both lenses are AR coated for the 650–1050 nm range. The tighter the beam was focused, the higher was the power density.

Achromatic doublets are useful for controlling chromatic aberration and are frequently used to achieve a diffraction-limited spot when using a monochromatic source. Achromatic doublets are optimized to provide a nearly constant focal length across a broad bandwidth. Dispersion in the first (positive) element of the doublet is corrected by the second (negative) element, resulting in better broadband performance than spherical singlets or aspheric lenses.

### 3.5 Pyrotechnic material

The pyrotechnic material used in our experiments for laser initiation is boron potassium nitrate, as shown in **Table 4**. Its military specification is as follows: MIL-P-46994B(AR). Aerospace missions require that pyrotechnic compositions are able to withstand 180°C [24]. Boron is often used as a reducer of energetic materials and in the composition of propellants; thanks to its high heat of reaction, high enthalpy, high temperature of combustion, low molar mass, long shelf life, thermal stability, and output performance. BPN is also listed as a linear reference for the security of pyrotechnic agents [24].

Military specification	MIL-P-46994B(AR)	
Scope	This specification covers eight types of ignitor pellets/granules for use in rocket motors, fuzes, and payload ignition/expelling charges.	
Classification	Type I – Cylindrical	
Material composition requirements	Potassium nitrate	MIL-P-156 except particle size shall be 15 microns maximum
	Boron, amorphous	MIL-B-51092 except particle size shall be 1.5 microns maximum and the boron purity shall be 90–92%
	Polyester resin	MIL-R-7575 Grade A, Class O, Form K

<b>Military specification</b>	<b>MIL-P-46994B(AR)</b>	
	Peroxide, methyl ethyl ketone	MIL-P-81351
	Cobalt naphthenate	—
Materials formulation	Potassium nitrate, %	70.7 ± 2.0
	Boron, amorphous, %	23.7 ± 2.0
	Binders, %	5.6 ± 0.5
Binder composition	Polyester resin, %	98.0 ± 1.0
	Catalyst, %	1.5 ± 0.1
	Accelerator, %	0.5 ± 0.01
Physical properties	Type	I-E – Cylindrical
	Diameter, mm	4
	Height, mm	5
	Minimum weight, gm	0.1
Physical and ballistic properties	Minimum density, gm/cm <sup>3</sup>	N/A
	Maximum moisture content, %	0.75
	Burning rate, mm/s	31.75–44.45
	Minimum heat of reaction, calories/gm	1500
	Minimum crush strength, gm	5000 (axial) 500 (radial)
	Time to maximum pressure, ms	N/A

1. *The igniter compositions shall be a homogeneous blend of materials.*
2. *The igniter pellets shall be free of cracks or laminations.*
3. *All pellets and packaging material shall be free of dirt, grease, and other foreign matter.*

**Table 4.**  
*BPN specification, classification, composition, and properties.*

### 3.6 Photodiode

A Si-photodiode FDS1010 from Thorlabs, with 65 ns risetime, 350–1100 nm, and 10 x 10 active area was used in our experiments to measure the light signal and its duration related to the light emitted by the laser pulse at the activation and the light emitted during the ignition and combustion of the pyrotechnic material, that is, pulse duration, ignition delay time, and burning time.

### 3.7 Benchtop oscilloscope

The Benchtop oscilloscope TDS2024B model from Tektronix was used in our experiments to display and record the ignition delay and burning times.

### 3.8 Power and energy laser measurement sensor

The F150A-BB-26 from Ophir photonics, which is a general-purpose fan cooled thermal power and energy measurement sensor, was used to measure the output power and energy, and their respective densities. It has an aperture of 26 mm and can measure power from 50 mW to 150 W and energy from 20 mJ to 100 J. It has the spectrally flat broadband coating and covers the spectral range of 0.19–20  $\mu\text{m}$ .

### 3.9 Laser power and energy meter

Ophir Photonics Vega power and energy meter was used in our experiments to display the output power and energy measured values.

### 3.10 Experimental setup production cost and time

The total cost of our experimental setup and safety equipment, as well as the availability and delivery time, are detailed below (Table 5):

Item	Part number	Price/unit [CNY]
Laser diode, fiber-coupled model	DS3-21312-203	32,500.00
Collimating lens	C240 TMD-B	793.90
Beam expander	BE-02-05-B	11,145.70
Focusing lens	AC254-60-B-ML	1,073.77
	AC254-125-B-ML	1,073.77
Photodiode	FDS1010	498.16
Benchtop oscilloscope	TDS2024B	12,025.65
Power and energy laser meas. Sensor	F150A-BB-26	8,795.90
Laser power and energy meter	Ophir Photonics Vega	14,671.29
Personal protection equipment (laser safety glasses, respirators, gloves, protective clothing, safety boxes, inert containers, clamps, pliers, etc.)	—	3,000.00
Total cost		85,578.14

*Notes:*

1. The availability period of the devices could vary from 1 day to 1 month or more after the establishment of the order. It includes neither the delivery time (within mainland China, or from overseas), nor the delivery cost. The price of BPN is not available.
2. The total production time cannot be accurately estimated due to COVID-19 related delays that affected the acquisition time of the aforementioned equipment.
3. OSHA, HIOSH, and other internal process safety management guidelines and directives on manufacturing, storage, sale, handling, use, and display of pyrotechnic materials have been followed during the whole process of the experiment.

**Table 5.**  
 Experimental setup production cost and time.

### 4. Results and discussion

As described earlier in Section 3, the distance separating the focusing lens and the BPN at each value of the inverted magnifying power was measured and reported in **Figures 1** and **2**. As it can be seen, the working distance characterizing the focal length increased exponentially with the increasing inverted magnifying power, that is, the larger is the inverted magnifying power the longer is the focal length, whilst the energy and power densities remained unchanged, as proven in **Figures 4–13**. The laser beam waist variation over the working distance for AC254-60-B-ML due to changes in the inverted magnifying power was reported in **Figure 3**. Four cases were considered for simpler and better illustrations, that are  $iMP_1$ ,  $iMP_2$ ,  $iMP_3$ , and  $iMP_4$ . It can be noticed that the laser beam variations were not just in terms of working distance, but also in terms of beam waist minima that were different from a location to another. At first, the beam waist was at its minimum at  $iMP_1$ , then it increased between  $iMP_2$  and  $iMP_3$ , to finally decrease till it reached another minimum at  $iMP_4$ , and still larger than the one reached in the first place. By considering  $\omega_0(iMP_1)$ ,  $\omega_0(iMP_2)$ ,  $\omega_0(iMP_3)$ , and  $\omega_0(iMP_4)$  as the beam waists corresponding to  $iMP_1$ ,  $iMP_2$ ,  $iMP_3$ , and  $iMP_4$ ,

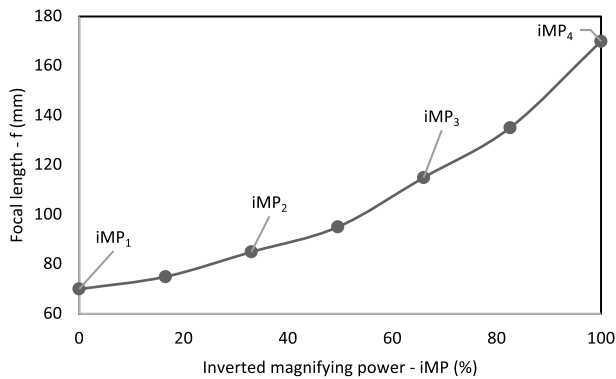


**Figure 1.** Focal length variation with the inverted magnifying power of the beam expander in reverse mode, with  $iMP_1$ ,  $iMP_2$ ,  $iMP_3$ , and  $iMP_4$  being equal to 0%, 33%, 66%, and 100%, respectively, using AC254-60-B-ML.

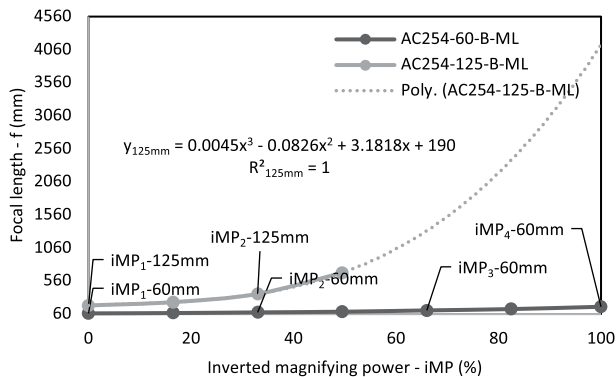


**Figure 2.** Focal length variation with the inverted magnifying power of the beam expander in reverse mode, with  $iMP_1$ ,  $iMP_2$ ,  $iMP_3$ , and  $iMP_4$  being equal to 0%, 33%, 66%, and 100%, respectively, with  $f_1 = 60$  mm and  $f_2 = 125$  mm.

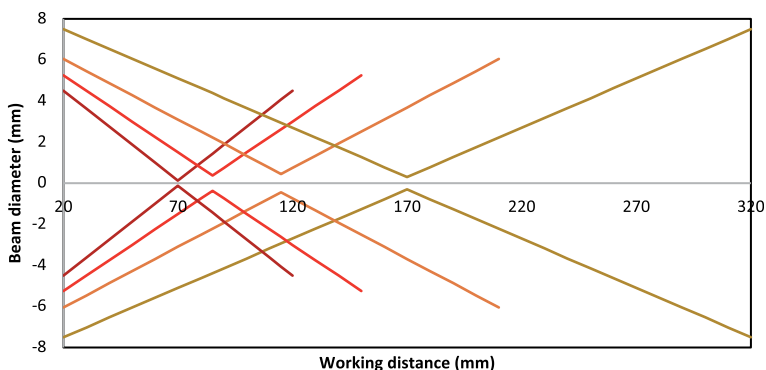


**Figure 3.** Beam diameter variation with the working distance for different inverted magnifying power values, with  $d_i$  equal to 0.25 mm, 0.75 mm, 0.89 mm, and 0.60 mm for  $iMP_1$ ,  $iMP_2$ ,  $iMP_3$ , and  $iMP_4$  respectively, using AC254-60-B-ML. The value  $y = 0$  represents the axis of the laser beam.

respectively, and rank them from smaller to larger, the following order was obtained:  $\omega_0(iMP_1) < \omega_0(iMP_4) < \omega_0(iMP_2) < \omega_0(iMP_3)$ .

We assume that the main reason for this is the focused spot size is diffraction limited, and when the spot size either increases or decreases under the control of the inverted magnifying power of the beam expander, it is influenced by contributions from diffraction and spherical aberration that characterize the internal lenses and optical elements of the beam expander. Another reason is related to the fact that the mechanism of the selected beam expander BE-02-05-B is a rotating focusing mechanism. Such a mechanism, in contrary to the sliding focusing mechanism, is somehow similar to threaded focusing tubes that rotate the optical elements during the translation, which in some cases may create the potential for beam wander during the rotation. Nevertheless, such beam expanders remain cost-effective than the sliding ones due to their simplified mechanism. In addition to changes in beam waists, changes in angles of divergence are also noticeable. These changes influence the interactions of the laser with the pyrotechnic material.

After conducting laser initiation of BPN, the following results were obtained (see **Figures 4–7**) and reproduced (see **Figures 8–13**).

As it can be seen from the benchtop oscilloscope recorded results and data, the first electric impulse measured in volt and displayed in **Figures 4–7** represents the light emission generated by the laser signal intended to initiate BPN. The second, larger impulse which follows the first impulse with a gap of dozens to hundreds of milliseconds represents the light emitted due to BPN ignition and combustion. But the most important remark is that of a third impulse which is less pronounced than the two previous impulses representing the laser signal and BPN ignition. However, this impulse comes only in cases where the pulse duration is larger than the ignition delays. Therefore, this third impulse represents the end of the laser pulse (or laser signal). Its significance lies in the fact that BPN does not necessarily ignite after that all the energy contained within one pulse is totally absorbed; however, energy is absorbed by BPN even after ignition influencing the combustion process. Therefore, this third pulse following BPN ignition can be noticed from the recorded data in the form of a sudden disruption (or a disruptive impulse) occurring during the combustion process, and its time duration is usually equal to the pulse duration starting from the time when the laser signal is turned on. In other words, ignition is a thermal process which

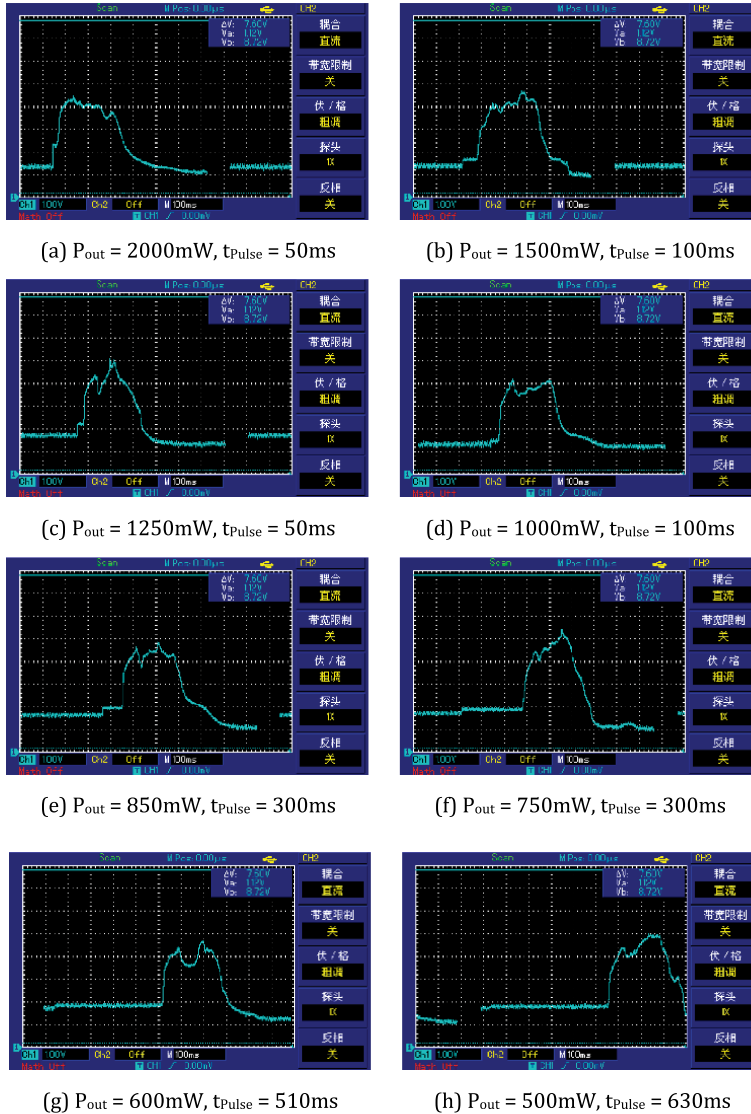


**Figure 4.** Laser initiation of BPN with a varying output power values and pulse durations at  $iMP_1$  using AC254-60-B-ML.

is not always dependent on the laser pulse duration, but rather on the threshold ignition energy and power, as mentioned earlier in the introduction. This can be noticed from the pulse durations that are in most of the cases higher than the ignition delays, particularly at lower output power, and almost equal to the ignition delays, particularly at higher output power.

Another noticeable fact from **Figures 4–7** is that of BPN ignitability or sensitivity dependance on the focal spot size. As mentioned earlier, BPN initiation recorded results related to  $iMP_1$ ,  $iMP_2$ ,  $iMP_3$ , and  $iMP_4$  and represented by **Figures 4–7**, respectively, are dependent on the spot size, that is, the smaller is the spot size the higher is the sensitivity, which in turns depends on power density, absorbed intensity, and thus brightness. Therefore, the sensitivity of BPN was higher for the cases

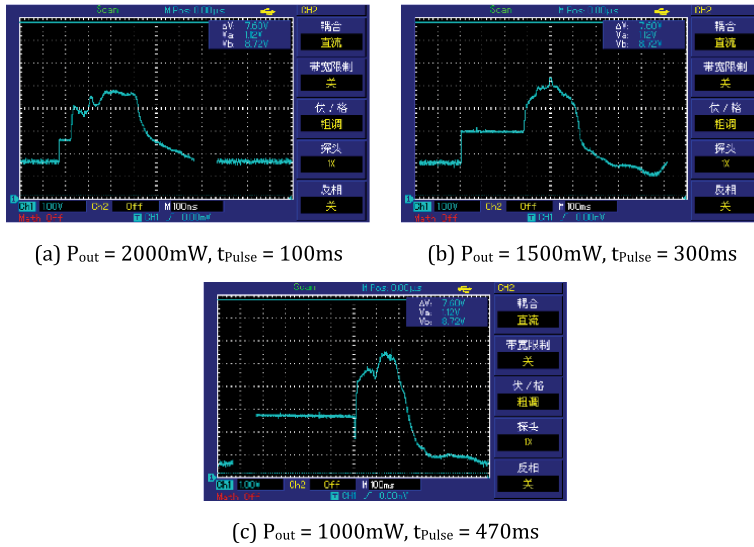


**Figure 5.** Laser initiation of BPN with a varying output power values and pulse durations at  $iMP_2$  using AC254-60-B-ML.

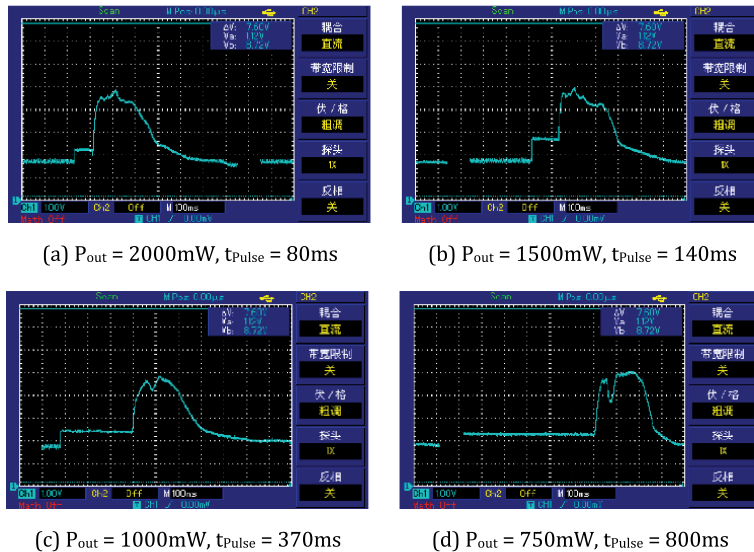


**Figure 6.** Laser initiation of BPN with a varying output power values and pulse durations at  $iMP_3$  using AC254-60-B-ML.

represented by **Figures 4** and **7**, and lower for the ones in **Figures 5** and **6**. The same applies to the lowest values of the output power required for the initiation, in **Figures 4** and **7**, even if the pulse durations increased up to 630 ms, ignition occurred at an output power as low as 500 mW, while in **Figures 5** and **6**, for pulse durations up to 800 ms, ignition occurred at higher output power, between 750 and 1000 mW.

As it can be seen from **Figures 8–11**, there is a clear tradeoff between the output power, the absorbed intensity, and the critical pulse duration at which the ignition occurs. This can be noticed from the gap existing between the ignition delay times and the pulse duration times; this gap is very small for higher values of output power but

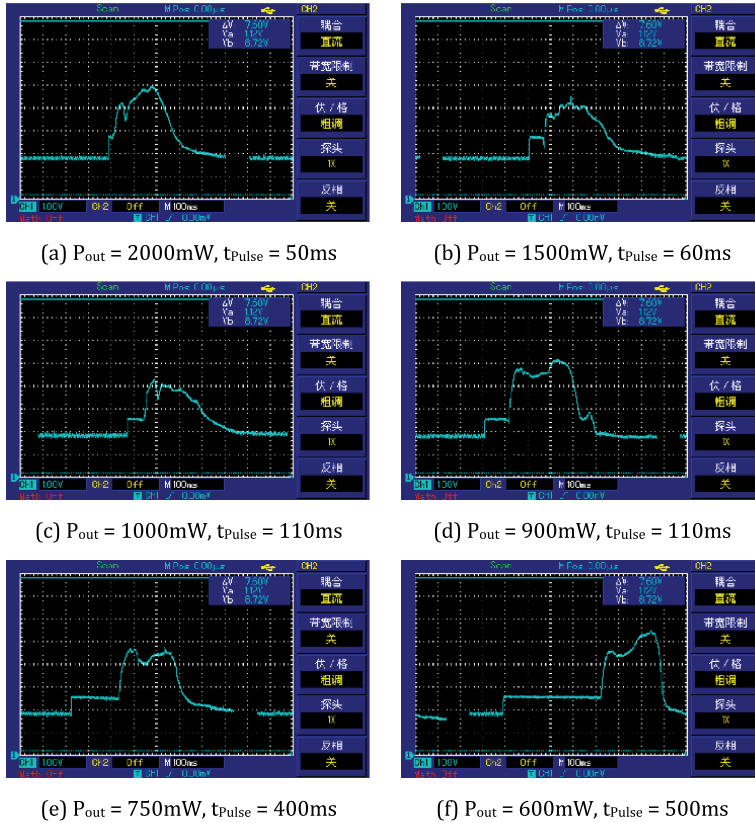


**Figure 7.** Laser initiation of BPN with a varying output power values and pulse durations at  $iMP_4$  using AC254-60-B-ML.

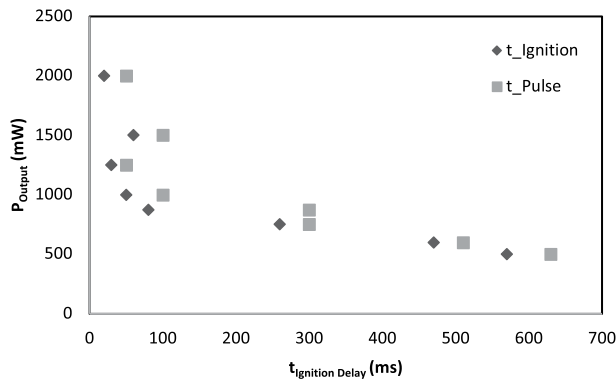


**Figure 8.** Minimum initiation power and pulse durations tradeoff at  $iMP_1$  using AC254-60-B-ML.

increases gradually with the decrease of the output power, that is, the threshold ignition energy required is higher at lower values of output power, which increases not only the ignition delay time, but also and especially the pulse duration. From **Figure 12**, we can notice that ignition delay times are shorter for  $iMP_1$  and  $iMP_4$ , while they are longer for  $iMP_2$  and  $iMP_3$ , and this either at high or low output power. The main reason is that the values of the beam waist are directly influencing the ignition,



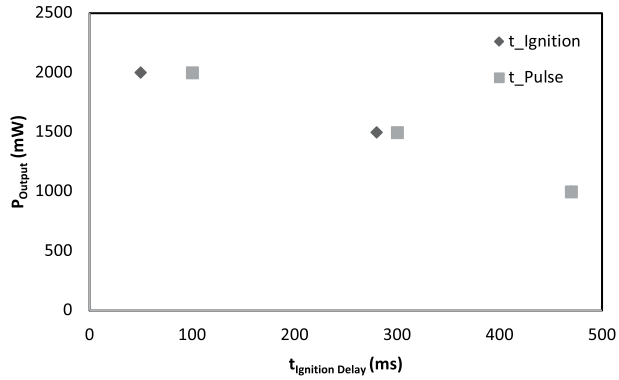


**Figure 9.**  
 Minimum initiation power and pulse durations tradeoff at  $iMP_2$  using AC254-60-B-ML.

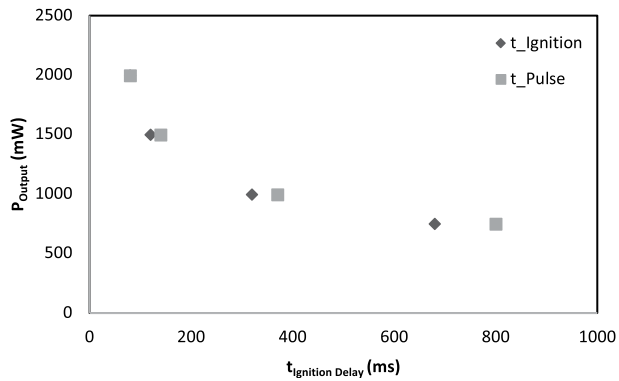


**Figure 10.**  
 Minimum initiation power and pulse durations tradeoff at  $iMP_3$  using AC254-60-B-ML.

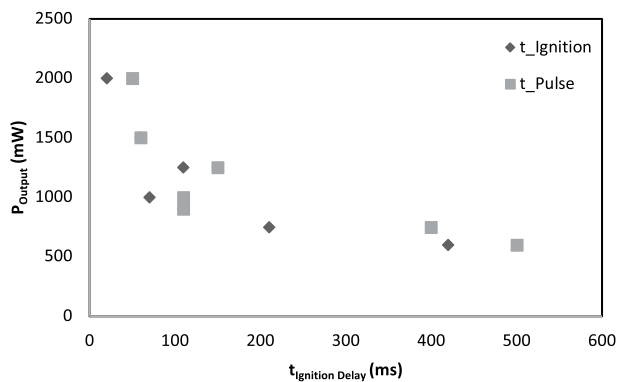


**Figure 11.**  
 Minimum initiation power and pulse durations tradeoff at  $iMP_4$  using AC254-60-B-ML.

and thus the tighter is the focus and the higher are the power densities. Also, after using a 125 mm focal length lens for the case of  $iMP_1$  and  $iMP_2$ , the obtained results were almost identical to those with similar working distances but with a 60 mm focal length lens. This means that, considering the setup produced in our experiments, no

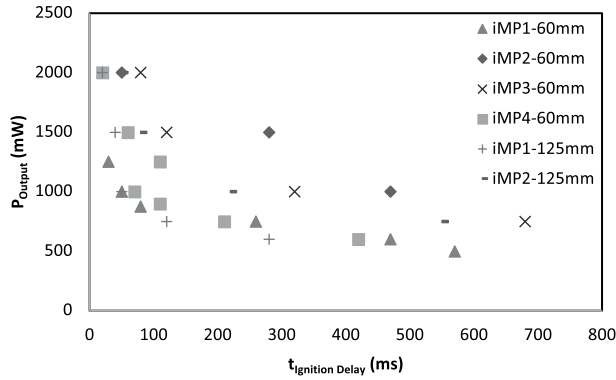


**Figure 12.** Minimum initiation power and pulse durations tradeoff at different magnifying power values using AC254-60-B-ML and AC254-125-B-ML.

matter what the working distance is, it will not affect power and energy densities, BPP,  $M^2$ , and the brightness as long as the beam waist remains unchanged.

To confirm the aforementioned findings, four cases with the same output power but different working distances were investigated, that is, changing the position of BPN to adjacent locations, whilst the focal length remained unchanged, only the spot size at the target changed. The results are presented in **Figure 13**, the increase in the spot size was inversely proportional to the increase in the working distance. Whilst the pulse duration and ignition delay times decreased proportionally with the decreasing spot size, as power densities were concentrated in smaller areas. However, it is noticeable that the required threshold ignition energy became higher with the increase of the working distance even if the spot size decreased, as the gap between pulse durations and ignition times increased.

There is a trade-off between the minimum laser power and the irradiation time [25]. Achieving maximum temperature rise and minimum threshold ignition power depends on various parameters. Under a quasi-steady state condition, the temperature rise depends inversely on the square root of the pulse duration. Thus, the criteria that

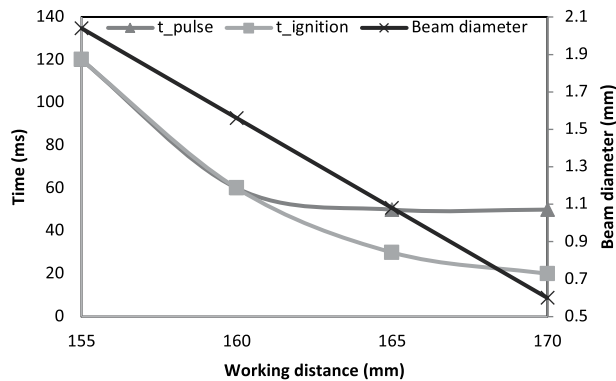


**Figure 13.** Beam diameters, pulse duration and ignition delay times variation at a 1500 mW output power at four different, but adjacent, working distances (155 mm, 160 mm, 165 mm, and 170 mm; the latter corresponds to the focal length at iMP<sub>4</sub> using AC254-60-B-ML).

need to be considered are high power density, highly focused beam, minimum reflection losses, long irradiation time, and high diffusivity.

Considering the same energy pulse, a comparison can be made in a way to describe a case with a certain amplitude and a certain time, and the other case with four times the amplitude but only one-fourth of the time. In other words, energy is unchanged, or the values of the integral of power over time remain unchanged, but in the first case four times the intensity and one-fourth of the time are obtained, and the opposite for the second case. The thermal penetration depth for the low intensity case is a factor of two longer when compared with the high intensity case because the time is a factor of four different and the thermal penetration depth must be the root of that which is a factor of two shorter. The same principle applies to the temperature, the lower intensity pulse generates half the temperature at the surface as the high intensity pulse and that scales with the root. The deposited energy in the short-pulse case should equal the deposited energy in the long-pulse case; therefore, if the penetration depth scales with the root of temperature, it is more plausible that the maximum temperature also scales with the root of the intensity of radiation. The shorter the pulse, the higher the temperature on the surface, and the less deep the thermal penetration. Thus, in terms of quantitative consequences, the shorter the pulses the smaller the penetration depth.

## 5. Conclusion

Laser diodes are high-reliability devices due to their exceptional energetic efficiencies and unsensitivity to magnetic disruption. Laser devices can be used either with optical fibers to drive the energy to the energetic material, or with lenses and other optical systems to concentrate energy on the surface of the energetic material.

The optimal wavelength for a given case is highly application-dependent because different pyrotechnic materials have unique wavelength-dependent absorption properties, leading to different interactions. Similarly, atmospheric absorption and interference affect certain wavelengths differently with a varying charging distance. Shorter wavelength laser systems are advantageous for creating minimal peripheral heating because of a smaller focused spot. However, they are prone to damage than lasers at longer wavelengths, that is, less cost-effective.

Higher power and energy lasers are typically more expensive, and they generate more waste heat. As power and energy increase, beam quality may decrease.

High power and energy densities are often ideal at the final output of a system, but low power and energy densities are often beneficial inside a system to prevent laser-induced damage.

Finally, the parameters affecting laser initiation can be summarized as follows (**Table 6**):

In this work, flexibility is achieved, and more distance is covered by allowing fine spot sizes with high power densities and longer focusing distances. Some of these findings were the perspectives suggested by refs. [26, 27]. The intensity obtained at the spot size is proportional to the brightness of the beam. This brightness is characterized [28, 29] as follows:

- Brightness is not affected by focusing or defocusing the beam.
- Changes in power, spot size,  $M^2$ , beam divergence, or the wavelength will lead to a change in the brightness.

<b>Laser parameters</b>	<b>Material parameters</b>
Wavelength	Spectral absorptivity
Average power	Thermal conductivity
Peak power	Chemical composition and morphology of the material
Power density	Ignition temperature of the material
Beam uniformity	
Duration of irradiation	
Dimension of focused spot	
Heat dissipation	

**Table 6.**  
*Parameters affecting laser initiation.*

- The brightness of a Gaussian beam does not change as it propagates as it is inversely proportional to solid angles of divergence. And the smaller the divergence the higher the brightness of the laser. High brightness beams, however, have the most idealized beam profile and tend to have a high-quality factor.

## **Acknowledgements**

The authors thank Professor Yan from Beijing Institute of Technology and Zhang Liang from Peking University and acknowledge their assistance with this effort and the support received from them in terms of provision of part of the experimental equipment and devices necessary for the completion of this work.

## **Conflict of interest**


The authors declare no conflict of interest.

## **Author details**

Ghedjatti Ilyes\*, Yuan Shiwei and Wang Haixing  
Aerospace Propulsion Laboratory, School of Astronautics, Beihang University,  
Beijing, China

\*Address all correspondence to: [ilyes.ghedjatti@buaa.edu.cn](mailto:ilyes.ghedjatti@buaa.edu.cn)

## **IntechOpen**

© 2022 The Author(s). Licensee IntechOpen. This chapter is distributed under the terms of the Creative Commons Attribution License (<http://creativecommons.org/licenses/by/3.0>), which permits unrestricted use, distribution, and reproduction in any medium, provided the original work is properly cited. 

## References

- [1] de Yong L, Nguyen T, Waschl J. Laser Ignition of Explosives, Pyrotechnics and Propellants: A Review [DSTO-TR-0068]. Weapons Systems Division, Aeronautical and Maritime Research Laboratory. Melbourne, Victoria, Australia; 1995
- [2] Sivan J, Haas Y. Laser ignition of various pyrotechnic mixtures - an experimental study. Mint: Propellants, Explosives, Pyrotechnics. 2015;**40**:755-758
- [3] Gillard P, Opdebeck F. Laser diode ignition of the B/KNO<sub>3</sub> pyrotechnic mixture: An experimental study. Mint: Combustion Science and Technology. 2007;**179**(8):1667-1699
- [4] Menichelli VJ, Yang LC. Sensitivity of explosives to laser energy [NASA technical report 32-1474]. Jet Propulsion Laboratory, California Institute of Technology; 1970
- [5] Brish A, Galeev A, Zaitsev BN, Sbirnev EA, Tatarintsev LV. Excitation of detonation in condensed high explosives by radiation from an optical quantum generator. Fizika Goreniya i Vzryva. 1966;**2**:132
- [6] Brish A, Galeev A, Zaitsev BN, Sbirnev EA, Tatarintsev LV. The mechanism of initiation of condensed high explosives by laser radiation. Fizika Goreniya i Vzryva. 1969;**5**:475
- [7] Oestmark H. Laser as a tool in the sensitivity testing of explosives. In: Proceedings of the 8th Symposium (International) on Detonation. Albuquerque, NM, USA.; 1985
- [8] Oestmark H. Laser ignition of explosives: Ignition energy dependence of particle size. In: Proceedings of the 12th International Pyrotechnics Seminar; 1987. Juan-les Pins, France;
- [9] Oestmark H, Roman N. Laser ignition of explosives: Pyrotechnic ignition mechanisms. Mint: Applied Physics. 1993;**73**(4):1993-2003
- [10] Kunz S, Salas F. Diode laser ignition of high explosives and pyrotechnics. In: Proceedings of the 13th International Pyrotechnics Seminar. Grand Junction, CO, USA; 1988
- [11] Jungst R, Salas F. Diode laser ignition of explosives and pyrotechnic components. In: OE 90 Symposium. USA. 1990
- [12] de Yong L, Valenta F. A Study of the Radiant Ignition of a Range of Pyrotechnic Materials Using a CO<sub>2</sub> Laser [MRL-TR-90-20]. Materials Research Laboratory; 1990
- [13] Holy J, Girman T. The effects of pressure on laser initiation of TiHx/KClO<sub>4</sub> and other pyrotechnics. In: Proceedings of the 13th International Pyrotechnics Seminar. Grand Junction, CO, USA; 1988
- [14] Hagan JT, Chaudhri M. Low energy laser initiation of single crystals of  $\beta$ -lead azide. Mint: Journal of Materials Science. 1981;**16**:2457-2466
- [15] Koc S, Ulas A, Yilmaz NE. Characterization of BPN pyrotechnic composition containing micro- and nanometer-sized boron particles. Mint: Propellants, Explosives, Pyrotechnics. 2015;**40**:735-742
- [16] Ahmad SR, Russell DA. Studies into laser ignition of confined pyrotechnics. Mint: Propellants, Explosives, Pyrotechnics. 2008;**33**:396-402
- [17] Shukla P. Viability and characterization of laser surface treatment of engineering ceramics

- [doctoral thesis]. Loughborough University; 2011
- [18] Ion JC. Laser Processing of Engineering Materials. Oxford, UK: Elsevier Butterworth Heinemann; 2005
- [19] Koechner W. Solid-State Laser Engineering. 5th ed. Berlin, Germany: Springer-Verlag; 1999
- [20] Shukla P, Lawrence J, Zhang Y. Understanding laser beam brightness: A review and new prospective in material processing. Mint: Optics & Laser Technology. 2015;75:40-51
- [21] O'Nei W. an K. High-quality micromachining of silicon at 1064 nm, using a high-brightness MOPA-based 20-W Yb fiber laser. Mint: IEEE Journal on Selected Topics in Quantum Electronics. IEEE. 2009;15(2):462-470
- [22] Almeida J, Liang D. Design of a high brightness solar-pumped laser by lightguides. Mint: Optics Communications. 2012;285:5327-5333
- [23] Liang D, Almeida J. Design of ultrahigh brightness solar-pumped disk laser. Mint: Applied Optics. Optica (formerly OSA). 2012;15(26):6382-6388
- [24] Li C, Yan N, Ye Y, Lv Z, He X, Huang J, et al. Thermal analysis and stability of boron/potassium nitrate pyrotechnic composition at 180°C. Mint: Applied Sciences. MDPI. 2019;9:3630
- [25] Ahmad SR, Cartwright M. Laser Ignition of Energetic Materials. 1st ed. Chichester: Wiley; 2015. p. 293
- [26] Sumf B, Hülsewede R, Erbert G, Dzionk C, Fricke J, Knauer A, et al. High brightness 735 nm tapered lasers-optimization of the laser geometry. Mint: Optical and Quantum Electronics. 2003; 35:521-532
- [27] Rudy P, Steele T, Vaissie L. More efficient and less complex-enhancing the spectral and spatial brightness of diode lasers, lasers technology, laser beam source. Mint: Laser and Photonics. 2008: 32-36
- [28] Milonni PW, Eberly JH. Lasers. New York: John Wiley & Sons; 1998
- [29] Chalupsky J, Bohacek HP, Hajkova V, Hau-Riege SP, Heimann PA, Juha L, et al. Comparing different approaches to characterization of focused X-ray laser beams. Mint: Nuclear Instruments and Methods in Physics Research – Section A (NIM-A). 2011;631: 130-133



*Edited by Konstantin Volkov*

Hypersonic flight vehicles have the potential to enable a range of future aviation and space missions. However, the extreme environmental conditions associated with high Mach number flight pose a major challenge for vehicle aerodynamics, materials and structures, and flight control, particularly within the hybrid ramjet/scramjet/rocket propulsion systems. The complexity of hypersonic vehicles requires closer coupling of aerodynamics and design principles with new materials development to achieve expanded levels of performance and structural durability. This book focuses on the fundamental disciplines and practical applications involved in the investigation, description, and analysis of super- and hypersonic aircraft flight including applied aerodynamics, aircraft propulsion, materials, and other topics.

Published in London, UK

© 2023 IntechOpen

© Floaria Bicher / iStock

**IntechOpen**

